micromachines

Frontiers in Ultra-Precision Machining

Edited by
Jiang Guo, Chunjin Wang and Chengwei Kang

Printed Edition of the Special Issue Published in *Micromachines*

www.mdpi.com/journal/micromachines

MDPI

Frontiers in Ultra-Precision Machining

Frontiers in Ultra-Precision Machining

Editors

Jiang Guo
Chunjin Wang
Chengwei Kang

MDPI • Basel • Beijing • Wuhan • Barcelona • Belgrade • Manchester • Tokyo • Cluj • Tianjin

Editors
Jiang Guo
Dalian University of Technology
China

Chunjin Wang
The Hong Kong Polytechnic University (PolyU)
China

Chengwei Kang
Xi'an Jiaotong University
China

Editorial Office
MDPI
St. Alban-Anlage 66
4052 Basel, Switzerland

This is a reprint of articles from the Special Issue published online in the open access journal *Micromachines* (ISSN 2072-666X) (available at: https://www.mdpi.com/journal/micromachines/special_issues/Ultra-Precision_Machining).

For citation purposes, cite each article independently as indicated on the article page online and as indicated below:

LastName, A.A.; LastName, B.B.; LastName, C.C. Article Title. *Journal Name* **Year**, *Volume Number*, Page Range.

ISBN 978-3-0365-3864-8 (Hbk)
ISBN 978-3-0365-3863-1 (PDF)

Contents

About the Editors

Jiang Guo is currently a professor at Dalian University of Technology (DUT). He received his Ph.D. from The University of Tokyo in 2013. After graduation, he joined RIKEN as a researcher. In October 2015, he became a scientist in A*STAR (Agency for Science, Technology and Research). He has been actively involved in precision machining related research for over a decade. His research interests include ultraprecision machining, polishing, actuators, mechatronics, and neutrons. He has published more than 30 journal papers in the top journals in mechanical engineering and holds several patents. His research work was highlighted in A*STAR Research. He is a member of European Society for Precision Engineering and Nanotechnology (EUSPEN), American Society for Precision Engineering (ASPE) and Asian Society for Precision Engineering and Nanotechnology (ASPEN). He is also the reviewer for over 30 SCI journals.

Chunjin Wang is currently a Research Assistant Professor in the Department of Industrial and Systems Engineering (ISE) at The Hong Kong Polytechnic University (PolyU). He received his B.Sc. and Ph.D. degree from Xiamen University in 2010 and 2015, respectively. He joined the State Key Lab of Ultra-precision Machining Technology in ISE at PolyU in 2015 as a postdoctoral fellow and then a research fellow in 2018. His research focuses on ultra-precision polishing technology, ultra-precision machining equipment and instrumentation, and advanced optics manufacturing.

Chengwei Kang is currently a professor at Xi'an Jiaotong University, China. He obtained his Ph.D. in the University of Queensland, Australia, one of the top universities (QS 2021 46th) worldwide. After graduation in 2016, he joined University College Dublin (UCD) as a post-doc research fellow and was promoted to be a Senior Research Engineer and Lab Supervisor in the research center of Micro/nano Manicuring Technology (MNMT-Dublin) in the year of 2018. In 2022, he joined school of mechanical engineering, Xi'an Jiaotong University. His research concerns the ultra-precision machining, high-speed grinding, manufacturing and post-processing of surface-microstructures. He has published over 30 papers in peer-reviewed journals with h-index of 11. Three of his publications were awarded 'Distinct Paper'by the journal of Advances in Manufacturing. He has been involved in several national research projects with total funding in excess of EUR 8 million, including Science Foundation Ireland (SFI) Professorship Project and Infrastructure Project, Australia Research Council (ARC) Engineering Project. His teaching activities have variously spanned all undergraduate and postgraduate levels. He is also an active member of International Society for Nanomanufacturing (ISNM).

micromachines

MDPI

Editorial

Editorial for the Special Issue on "Frontiers of Ultra-Precision Machining"

Jiang Guo [1,*], Chunjin Wang [2,*] and Chenwei Kang [3,*]

[1] School of Mechanical Engineering, Dalian University of Technology, Dalian 116024, China
[2] State Key Laboratory of Ultra-precision Machining Technology, Department of Industrial and Systems Engineering (ISE), the Hong Kong Polytechnic University (PolyU), Hong Kong 999077, China
[3] State Key Laboratory for Manufacturing Systems Engineering, School of Mechanical Engineering, Xi'an Jiaotong University, Xi'an 710049, China
* Correspondence: guojiang@dlut.edu.cn (J.G.); chunjin.wang@polyu.edu.hk (C.W.); chengwei.kang@outlook.com (C.K.)

Ultra-precision machining is a multi-disciplinary research area that is an important branch of manufacturing technology. It targets achieving ultra-precision form or surface roughness accuracy, forming the backbone and support of today's innovative technology industries in aerospace, semiconductors, optics, telecommunications, energy, etc. The increasing demand for components with ultra-precision accuracy has stimulated the development of ultra-precision machining technology in recent decades. Accordingly, this special issue showcases 17 research papers which focus on the frontiers of ultra-precision machining, including ultra-precision machining processes, process simulation and modelling, process optimization, the development of novel machining tools and processes, and surface integrity characterization.

1. Process simulation and modelling: Yuan et al. [1] presented a dynamic model of the cutting system for the characterization of surface topography variation in ultra-precision tool servo-based diamond cutting of a microlens array considering the tool-work vibration as an underdamped vibration. Du et al. [2] studied the ion beam sputtering process for single crystal aluminum with different crystallographic orientations by the molecular dynamics method, and the mechanism of morphology evolution of aluminum were revealed. Fu et al. [3] presented a piezoelectric hysteresis modeling method based on a generalized Bouc–Wen model, which can describe the piezoelectric hysteresis characteristics of the three axial subsystems of the three-dimensional elliptical vibration which effectively aided the cutting system and ensured higher modeling and fitting accuracy. Tian et al. [4] proposed the Coupled Eulerian–Lagrangian (CEL) method to simulate the high-shear low-pressure grinding process. Zhang et al. [5] established a two-phase flow field model based on the RANS k-ε turbulence mode to analyze the influence of vibration on the process of electrochemical machining, which is suitable for narrow flow field and high flow velocity.

2. Process optimization: Wang et al. [6] proposed a reasonable elementary approximation algorithm of dwell time on the basis of the theoretical requirement of a removal function in the subaperture polishing and single-peak rotational symmetry character of its practical distribution, which has obvious advantages for improving calculation efficiency and flatness and is of great significance for the efficient computation of large-aperture optical polishing. Yan et al. [7] proposed a new calculation method for the height of surface residual materials in ultra-precision grinding of Nano-ZrO2, and established the prediction model of the three-dimensional roughness *S*a and *S*q by using this calculation method. Rashedul et al. [8] investigated the influence of different electrode materials experimentally, namely titanium alloy (TC4), stainless steel (SS304), brass, and copper–tungsten (CuW) alloys (W70Cu30, W80Cu20, W90Cu10), on electrodes' electrical properties, aiming to select an appropriate electrode in the ECDM process. Zhao et al. [9] studied the critical machining parameters which affect the surface generation and surface quality in the machining of

Citation: Guo, J.; Wang, C.; Kang, C. Editorial for the Special Issue on "Frontiers of Ultra-Precision Machining". *Micromachines* **2022**, *13*, 220. https://doi.org/10.3390/mi13020220

Received: 24 January 2022
Accepted: 27 January 2022
Published: 29 January 2022

polar microstructures, so as to obtain optimized machining parameters and determine optimized cutting strategy for polar microstructures. Huang et al. [10] studied the self-aligning flanges based on piezoelectric actuators, and the average eccentricity value in the experiments decreased by 74%. Qiao et al. [11] investigated the optimum vertex angle and parameters for the preparation of atom probe tomography (APT) specimen, and the double interdiffusion relationship of the multilayer films was successfully observed by the local electrode APT.

3. Development of novel machining tools and processes: Fan et al. [12] developed an electrorheological (ER) polishing tool with an annular integrated electrode, and six influencing factors of ER polishing were analyzed experimentally. Jin et al. [13] presented a high-accuracy and high-efficiency surface topography manufacturing method for continuous phase plate, which demonstrates the potential of the atmospheric pressure plasma jet approach for the manufacturing of complex surface topographies. Zhou et al. [14] analyzed the machined surface morphology and cutting force in different lubricant machining environments, and the results indicated that the minimum quantity lubrication machining oil can suppress the formation of hard particles to improve the machining quality.

4. Surface integrity characterization: Deng et al. [15] carried out a study on the repair of fused silica damage using the magnetorheological removing method, and the repairing rate of small-scale damage was up to 90.4%. Yang et al. [16] designed experiments to investigate the influence of machining factors on subsurface damage, in order to reduce the subsurface damage depth generated during the grinding process by adjusting the process parameters. Guo et al. [17] proposed a new measurement method in order to accurately obtain the wall thickness of thin-walled spherical shell parts.

We wish to thank all authors who submitted their papers to this Special Issue. We would also like to acknowledge all the reviewers for dedicating their time to provide careful and timely reviews to ensure the quality of this Special Issue.

Conflicts of Interest: The author declares no conflict of interest.

References

1. Yuan, W.; Cheung, C.F. Characterization of surface topography variation in the ultra-precision tool servo-based diamond cutting of 3d microstructured surfaces. *Micromachines* **2021**, *12*, 1448. [CrossRef] [PubMed]
2. Du, C.; Dai, Y.; Guan, C.; Hu, H. Molecular dynamic investigation of the anisotropic response of aluminum surface by ions beam sputtering. *Micromachines* **2021**, *12*, 848. [CrossRef] [PubMed]
3. Fu, X.; Gong, H.; Lu, M.; Zhou, J.; Lin, J.; Du, Y.; Zhou, R. Piezoelectric hysteresis modeling of hybrid driven three-dimensional elliptical vibration aided cutting system based on an improved flower pollination algorithm. *Micromachines* **2021**, *12*, 1532. [CrossRef] [PubMed]
4. Tian, C.; Han, J.; Tian, Y.; Liu, B.; Gu, Z.; Hu, X. Simulation analysis of cluster effect of high-shear low-pressure grinding with flexible abrasive tools. *Micromachines* **2021**, *12*, 827. [CrossRef] [PubMed]
5. Zhang, J.; Song, S.; Zhang, J.; Chang, W.; Yang, H.; Tang, H.; Chen, S. Multi-physics coupling modeling and experimental investigation of vibration-assisted blisk channel ecm. *Micromachines* **2021**, *13*, 50. [CrossRef] [PubMed]
6. Wang, Y.; Zhang, Y.; Kang, R.; Ji, F. An elementary approximation of dwell time algorithm for ultra-precision computer-controlled optical surfacing. *Micromachines* **2021**, *12*, 471. [CrossRef] [PubMed]
7. Yan, Y.; Zhang, Z.; Liu, J.; Yan, H.; Wang, X. Study on the algorithm of three-dimensional surface residual material height of nano-zro2 ceramics under ultra-precision grinding. *Micromachines* **2021**, *12*, 1363. [CrossRef] [PubMed]
8. Rashedul, I.M.; Zhang, Y.; Zhou, K.; Wang, G.; Xi, T.; Ji, L. Influence of different tool electrode materials on electrochemical discharge machining performances. *Micromachines* **2021**, *12*, 1077. [CrossRef] [PubMed]
9. Zhao, C.Y.; Cheung, C.F.; Fu, W.P. An investigation of the cutting strategy for the machining of polar microstructures used in ultra-precision machining optical precision measurement. *Micromachines* **2021**, *12*, 755. [CrossRef] [PubMed]
10. Huang, X.; Wang, Z.; Shen, B.; Lei, P. Research on self-aligning flanges based on piezoelectric actuators applied to precision grinding machines. *Micromachines* **2021**, *12*, 1393. [CrossRef] [PubMed]
11. Qiao, Y.; Zhao, Y.; Zhang, Z.; Liu, B.; Li, F.; Tong, H.; Wu, J.; Zhou, Z.; Xu, Z.; Zhang, Y. Single-wedge lift-out for atom probe tomography Al/Ni multilayers specimen preparation based on dual-beam-fib. *Micromachines* **2021**, *13*, 35. [CrossRef] [PubMed]
12. Fan, C.; Chen, Y.; Xue, Y.; Zhang, L. Study on the electrorheological ultra-precision polishing process with an annular integrated electrode. *Micromachines* **2021**, *12*, 1235. [CrossRef] [PubMed]
13. Jin, H.; Tang, C.; Li, H.; Zhang, Y.; Li, Y. High-accuracy surface topography manufacturing for continuous phase plates using an atmospheric pressure plasma jet. *Micromachines* **2021**, *12*, 683. [CrossRef] [PubMed]

14. Zhou, M.; Wang, J.; Zhang, G. Influence of lubricant environment on machined surface quality in single-point diamond turning of ferrous metal. *Micromachines* **2021**, *12*, 1110. [CrossRef] [PubMed]
15. Deng, M.; Song, C.; Shi, F.; Zhang, Y.; Tian, Y.; Zhang, W. Rapid and non-destructive repair of fused silica with cluster damage by magnetorheological removing method. *Micromachines* **2021**, *12*, 274. [CrossRef] [PubMed]
16. Yang, W.; Li, Y. The influence of crystal orientation on subsurface damage of mono-crystalline silicon by bound-abrasive grinding. *Micromachines* **2021**, *12*, 365. [CrossRef] [PubMed]
17. Guo, J.; Xu, Y.; Pan, B.; Zhang, J.; Kang, R.; Huang, W.; Du, D. A new method for precision measurement of wall-thickness of thin-walled spherical shell parts. *Micromachines* **2021**, *12*, 467. [CrossRef] [PubMed]

micromachines

MDPI

Article

Characterization of Surface Topography Variation in the Ultra-Precision Tool Servo-Based Diamond Cutting of 3D Microstructured Surfaces

Wei Yuan and Chi-Fai Cheung *

State Key Laboratory in Ultra-Precision Machining Technology, Department of Industrial and Systems Engineering, The Hong Kong Polytechnic University, Hong Kong 999077, China; wer.yuan@connect.polyu.hk
* Correspondence: benny.cheung@polyu.edu.hk; Tel.: +852-2766-7905

Abstract: Previous models of the relative tool-work vibration are not generalized to represent the surface generation mechanism in the ultra-precision tool servo-based diamond cutting (UTSDC) of three-dimensional (3D) microstructured surfaces. This is due to the fact that the tool-work vibration in UTSDC is no longer a steady harmonic vibration with a constant amplitude but is influenced by the tool motion along the thrust direction. In this paper, dynamic modeling of the cutting system is presented for the characterization of surface topography variation in UTSDC of a microlens array considering the tool-work vibration as an underdamped vibration. The natural frequency and damping ratio of the cutting system are determined by the data-dependent systems (DDS) method. Based on the analysis of the surface profile and cutting force signals, it is found that the tool-work vibration is significantly enhanced in the cut-in process when the cutting speed increases. The simulation results show that the proposed dynamic model can well-determine root-mean-squares RMS values of the surface primary profile and the dynamic force acting on the force sensor. The dynamic model provides insight into the formation of the surface topography variation in UTSDC of 3D microstructured surfaces, and the model might be applied in self-optimized machining systems in the future.

Keywords: dynamic modeling; surface characterization; cutting forces; tool servo diamond cutting; data-dependent systems; surface topography variation; ultra-precision machining; microstructured surfaces; microlens array

Citation: Yuan, W.; Cheung, C.-F. Characterization of Surface Topography Variation in the Ultra-Precision Tool Servo-Based Diamond Cutting of 3D Microstructured Surfaces. *Micromachines* **2021**, *12*, 1448. https://doi.org/10.3390/mi12121448

Academic Editor: Aiqun Liu

Received: 17 October 2021
Accepted: 18 November 2021
Published: 26 November 2021

1. Introduction

Machining instability is a great obstacle to fine surface quality in ultra-precision machining. There has been a wealth of research on establishing an accurate surface topography model according to the cutting mechanics and the dynamics of the machining process. Surface topography in ultra-precision machining is mainly generated by the interaction of tool profiles with a workpiece. The surface finish is mainly characterized by process parameters, tool geometry, material properties and the vibrations arising in the material removal process [1]. Much work has been conducted to investigate the cutting mechanics at the micro/nanometer scales recently. Venkatachalam et al. [2] presented that the flow stress affected by the material grain size, grain boundary and crystallographic orientation contributes to the cutting forces in face-turning of polycrystalline brittle material. Yan et al. [3] proposed that the unsteadiness of side flow of material in the cutting region causes surface waviness perpendicular to the cutting direction when cutting a microgroove array on an electroless-plated NiP surface. In micro-grooving experiments, Guo et al. [4] found that the loss of harder particles in rapidly solidified aluminum due to a high-stress concentration around the straight cutting edges leads to surface and subsurface damage. Rahman et al. [5,6] investigated the cutting-edge radius effect on the surface generation mechanisms and concluded that when the relative tool sharpness is less than 1, the material

removal transfers from shearing to extrusion, ploughing and rubbing. Due to the effects of cutting edge, the workpiece surface improves in 2D vibration-assisted machining (VAM) because ploughing increases significantly in 2D VAM [6].

The analysis of the surface data and cutting force signal provides insightful understanding on the formation of surface topography variation. Kim [7] proposed a 3D surface topography simulation model for face-turning aluminum alloy and copper alloy based on the frequency domain information obtained by the Fast Fourier Transform analysis method. Wang et al. [8] pointed out that the Fast Fourier Transform (FFT) method has no access to the localized details of the surface profile. They employed the wavelet method to evaluate the amplitude and frequency of the surface profile signal along the cutting direction. By applying the data-dependent systems (DDS) approach to analyze the surface profile, Pandit [9] found that the relative tool-work vibration plays a dominant role in the surface generation in ultra-precision diamond turning. Takasu et al. [10] pointed out that the relative tool-work vibration commonly has a small amplitude and low frequency. The surface roughness in the tool feed direction can be much smaller than the amplitude of tool-work vibration by optimizing the phase shift of the vibration to one spindle revolution. Cheung and Lee [11] proposed that the spindle run-out and machine vibration are the major sources of the tool-work vibration in ultra-precision diamond turning. The decomposition of the surface roughness profile indicated that the cutting dynamics of the surface roughness have a strong correlation with the surface generation mechanisms. The natural frequency component which results from the tool-work vibration contributes to more than 67% of the total surface roughness. The feed and tool geometry component contributes to much less percentage of the total roughness as compared to conventional machining [12]. Chen and Zhao [13] pointed out that the actual tool-work vibration during the turning process is different from the measured vibration before turning, and the actual relative vibration is almost impossible to measure directly in the cutting process.

The above-mentioned studies mainly focus on the simple cutting operation, where the depth of the cut does not change in the whole material removal process. The tool-work vibration is assumed to be a steady harmonic vibration with a constant amplitude and frequency, which produces periodic patterns on a machined surface [14], while in the ultra-precision tool servo-based diamond cutting (UTSDC), 3D microstructures such as microlens arrays are cut by the servo-controlled motion of the diamond tool. The force in the thrust direction, which is significantly affected by the cut-in and cut-out process, may cause extra material to be indented beneath the tool. The indentation force and the tool servo motion lead to the instability in machining and result in surface topography variation. Slowing down the cutting velocity is found to be one solution to reduce the surface topography variation [15]. However, there is still a lack of a dynamic model to determine the effect of machine dynamics on the surface topography variation and how it is affected by the cutting speed.

This paper aims to investigate the surface generation mechanism in UTSDC considering the effect of the servo motion in the thrust direction and the thrust force corresponding to the material being indented as the diamond tool cuts into the surface. A dynamic model is proposed for analyzing the surface topography variation in the UTSDC of a microlens array. The model is built by the identification of the dynamic parameters of the system based on the DDS method and the estimation of the contact force in the thrust direction during machining. Hence, the equation of motion of the cutting system is derived to determine the transient response of the diamond tool. The simulation results are presented and validated by a series of cutting experiments and the analysis of the surface profiles of machined surfaces.

2. Characterization Method for Surface Topography Variation

Figure 1 shows a framework for the characterization of the surface topography variation in the UTSDC of microstructured surfaces. To eliminate the potential spindle vibration, the microstructures are cut only by two slides of the machine tool, i.e., the y-axis and z-axis.

In this case, the surface profile along the cutting direction provides a faithful signature of the machining instability. The primary profile is obtained by subtracting the form from the measured surface profile. The natural frequency and damping ratio of the tool-work vibration are determined by a DDS model which provides component-by-component wavelength decomposition of the surface primary profile of the workpiece. During the machining process, the cutting force along the thrust direction is determined when the cutting speed is low so that the vibration is insignificant. The measured thrust force is used as an input of the dynamic cutting system. Hence, a dynamic model of the cutting system is built. The variation of surface topography and the dynamic force in the condition of higher cutting speed are predicted by solving the dynamic equation.

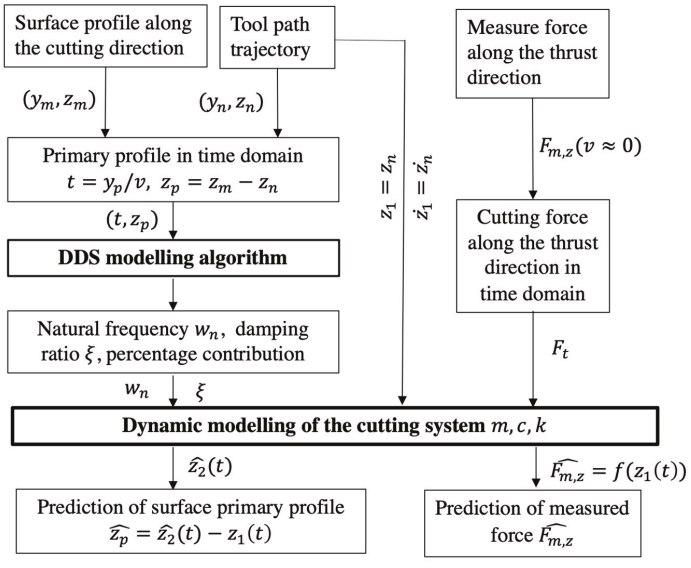

Figure 1. Framework for the characterization of the surface topography variation in ultra-precision tool servo-based diamond cutting (UTSDC).

2.1. Theoretical Background of the Data-Dependent Systems Analysis Method

The surface primary profile (y_p, z_p) of the workpiece is the sum of all the deviations of the measured profile (y_m, z_m) from the nominal profile. The nominal profile (y_n, z_n) is assumed to be the vertical projection of the ideal tool path trajectory on the designed surface for UTSDC. Thus,

$$(y_p, z_p) = (\, y_n, z_m - z_n) \tag{1}$$

The measured surface profile is an unmodified profile, which is composed of a wide range of frequency components. For example, the profile that only contains the high-frequency components of the surface profile is denoted as the surface roughness profile. To determine the effect of the tool-work vibration on the surface roughness components or the waviness components, the surface profile is used as raw data for analyzing the natural frequency and damping ratio of the tool-work vibration.

Data-dependent systems (DDS) is a comprehensive methodology for the modeling and characterization of surfaces, which can relate the surface topography to the manufacturing process [16]. DDS is developed based on the Fundamental Theorem [17] that any stochastic system can be represented by the response of an n-pole–zero transfer function to white noise. Thus, the differential equation for the system response, $X(t)$, is expressed as:

$$\frac{d^n X(t)}{dt^n} + \alpha_{n-1}\frac{d^n X(t)}{dt^n} + \ldots + \alpha_0 X(t) = b_{n-1}\frac{d^{n-1} Z(t)}{dt^{n-1}} + \ldots + b_1\frac{d^1 Z(t)}{dt^1} + Z(t) \tag{2}$$

where $Z(t)$ is white noise, α_i is an autoregressive (AR) parameter and b_i is a moving average (MA) parameter. Equation (2) is denoted by ARMA$(n, n-1)$. If some b_i are zero, the ARMA$(n, n-1)$ model can be simplified as an ARMA (n, m) model, where $m \leq n-1$. According to the Uniform Sampling Theorem theory [17], an ARMA$(n, n-1)$ system can be represented by the following stochastic difference equation as long as the data are sampled at a uniform interval of Δ:

$$X_t - \phi_1 X_{t-1} - \ldots - \phi_n X_{t-n} = a_t - \theta_1 a_{t-1} - \theta_{n-1} a_{t-n+1} \tag{3}$$

With the backstep notation $BX_t = X_{t-1}$, the autoregressive part of the ARMA$(n, n-1)$ model, i.e., the left-hand side of Equation (3), can be expressed in the form of backward shift operator B,

$$\left(1 - \phi_1 B - \phi_2 B^2 - \ldots - \phi_n B^n\right) X_t \equiv (1 - \lambda_1 B)(1 - \lambda_2 B) \ldots (1 - \lambda_n B) X_t \tag{4}$$

where λ_i are the roots of the characteristic equation, given by:

$$\lambda^n - \phi_1 \lambda^{n-1} - \phi_2 \lambda^{n-2} \ldots - \phi_n = 0 \tag{5}$$

Similarly, the right-hand side of Equation (3) can be expressed as:

$$a_t - \theta_1 a_{t-1} - \theta_{n-1} a_{t-n+1} \equiv \left(1 - \theta_1 B - \theta_2 B^2 - \ldots - \theta_n B^n\right) a_t \tag{6}$$

Substituting Equations (4) and (6) into Equation (3), then:

$$X_t = \frac{\left(1 - \theta_1 B - \theta_2 B^2 - \ldots - \theta_n B^n\right)}{(1 - \lambda_1 B)(1 - \lambda_2 B) \ldots (1 - \lambda_n B)} a_t \tag{7}$$

Equation (7) can also be expressed by a group of Green's functions, G_j:

$$X_t = \sum_{j=0}^{\infty} G_j a_{t-j} \tag{8}$$

$$G_j = g_1 \lambda_1^j + g_2 \lambda_2^j + \ldots + g_n \lambda_n^j \tag{9}$$

$$g_i = \frac{\lambda_i^{n-1} - \theta_1 \lambda_i^{n-2} - \ldots - \theta_{n-1}}{\prod_{j=1, j \neq i}^{n} (\lambda_i - \lambda_j)} \tag{10}$$

The characteristic root, λ_i, can be either a real number or a complex number. A real λ_i represents a decaying exponential dynamic mode, while a pair of complex roots, λ_i, λ_i^*, describes a damped or undamped harmonic vibration mode. The natural frequency, ω_i, and damping ratio, ζ_i, corresponding to the pair of complex roots, λ_i, λ_i^*, are obtained as [18]:

$$\omega_i = \sqrt{\sigma_i^2 + \Omega_i^2} \tag{11}$$

$$\zeta_i = -\frac{\sigma_i}{\sqrt{\sigma_i^2 + \Omega_i^2}} \tag{12}$$

where σ_i and Ω_i are defined by:

$$\sigma_i = \frac{1}{2\Delta} In(\lambda_i \lambda_i^*) \tag{13}$$

$$\Omega_i = \frac{1}{\Delta} \arctan\left[\frac{Im(\lambda_i)}{Re(\lambda_i)}\right] \tag{14}$$

The power of a root, λ_i, is expressed by d_i:

$$d_i = \sum_{j=1}^{n} \frac{g_i g_j}{1 - \lambda_i \lambda_j} \tag{15}$$

If λ_i is a real root, the percentage contribution of the total power is given by:

$$P = \frac{d_i}{\sum_{j=1}^{n} d_j} \times 100 \tag{16}$$

If λ_i and λ_{i+1} are a pair of complex conjugate roots, the percentage contribution of the power of this vibration mode to the total power is expressed by:

$$P = \frac{d_i + d_{i+1}}{\sum_{j=1}^{n} d_j} \times 100 \tag{17}$$

In practice, ARMA$(2n, 2n-1)$ models are used to represent an n-degrees-of-freedom vibration system. The order $2n$ is found by an iterative, least-squares procedure until the increase in order fails to significantly reduce the residual sum of squares [18]. The significant improvement in fit is checked by the F-test:

$$F = \frac{(E_1 - E_0)/S}{E_0/(N-r)} \sim F(S, N-r) \tag{18}$$

where N is the number of the input data, E_0 is the residual sum of squares of the ARM$(2n+2,\ 2n+1)$ model and E_1 is the residual sum of squares of the ARMA$(2n, 2n-1)$ model. The F distribution has two degrees of freedom, denoted by S and $N-r$, respectively. The values of S and r are expressed as:

$$S = 4 \tag{19}$$

$$r = 4n + 3 \tag{20}$$

The F-test starts with the ARMA$(2,1)$ and ARMA$(4,3)$ models. If the F value is less than the value of $F(S, N-r)$ at a 5% level of significance, then ARMA$(2,1)$ is adequate to represent the system. Otherwise, ARMA$(2,1)$ is not sufficient, so an F-test comparing ARMA$(4,3)$ and ARMA$(6,5)$ would be conducted to check whether ARMA$(4,3)$ is adequate. The iterative procedure is carried on until the F value does not exceed the value of $F(S, N-r)$ at a 5% level of significance.

2.2. Dynamic Modeling of Relative Tool-Work Vibration

Figure 2 shows the mechanical structure of the cutting system. The workpiece is mounted on the spindle which moves along the y-axis during the UTSDC operation. The displacement of the moving part of the slide, the diamond tool and workpiece are z_1, z_2 and y_1, respectively. The moving part of the slide is regarded as a base, which is assumed to precisely follow the commands consisting of the tool path trajectory. A force transducer is placed between the diamond tool system and the moving part of the slide.

The dynamic system is simplified as a single-degree-of-freedom system with a moving base. Based on Newton's second law, the equation of the motion of the diamond tool system is given by:

$$m\ddot{z}_2(t) + c\big(\dot{z}_2(t) - \dot{z}_1(t)\big) + k(z_2(t) - z_1(t)) = F_t(t) \tag{21}$$

where $z_1(t)$ can be obtained from the commanded tool path. The thrust force, $F_t(t)$, in the z-axis direction is not actually the measured force, $F_{m,z}$, obtained by the force sensor. $F_{m,z}$ is the total force applied on the force transducer, which is expressed by:

$$F_{m,z}(t) = F_t(t) - c\left(\dot{z}_2(t) - \dot{z}_1(t)\right) - k(z_2(t) - z_1(t)) \tag{22}$$

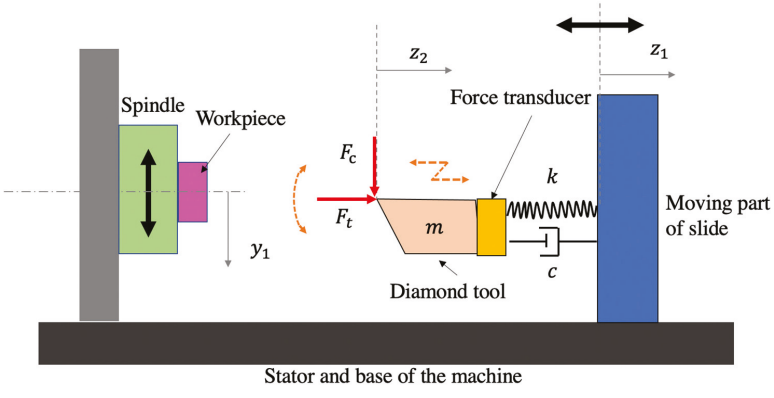

Figure 2. The mechanical structure of the cutting system.

The initial condition $(z_2(t=0), \dot{z_2}(t=0))$ is determined by the tool path and operation parameters.

When the cutting speed is extremely low, the system can be regarded as a "semi-static" system, where no obvious vibration signal can be detected. Under such condition, the measured force, $F_{m,z}(t)$, is close to the thrust force, $F_t(t)$.

$$F_t(t) \approx F_{m,z}(t, v \approx 0) \tag{23}$$

The solution of Equation (21) can be solved by a numerical method. It is noted that (y_1, z_1) is assumed to be equal to the generated tool path (y_n, z_n), and (y_1, z_2) is assumed to be equal to the actual measured profile (y_m, z_m). Thus, the simulated primary profile, z_p, is obtained by:

$$z_p = z_2 - z_1 = z_m - z_n \tag{24}$$

3. Experimental Setup

To investigate the characteristics of the UTSDC process for 3D microstructured surfaces, a set of microlens arrays was fabricated on a Moore Nanotech 350FG(Moore Nanotechnology Systems, LLC, Keene, NH, USA), as shown in Figure 3. The workpiece material is aluminum 6061-T6(Alcoa Corporation, Alcoa, TN, USA). Table 1 shows the designed parameters of the microlens arrays and the process parameters in the experiment. The diamond tool has a round nose of 0.32 mm. The tool edge radius of the diamond tool is around 0.2 μm. Four lines of microlens arrays were cut with different cutting velocities. The cutting forces were measured by a Kistler 9256C1 force transducer (Kistler Group, Winterthur, Switzerland). The sampling rate was set to 50 kHz. The surface topography was measured using a Zygo Nexview™ 3D Optical Surface Profiler (Zygo Corporation, Middlefield, CT, USA).

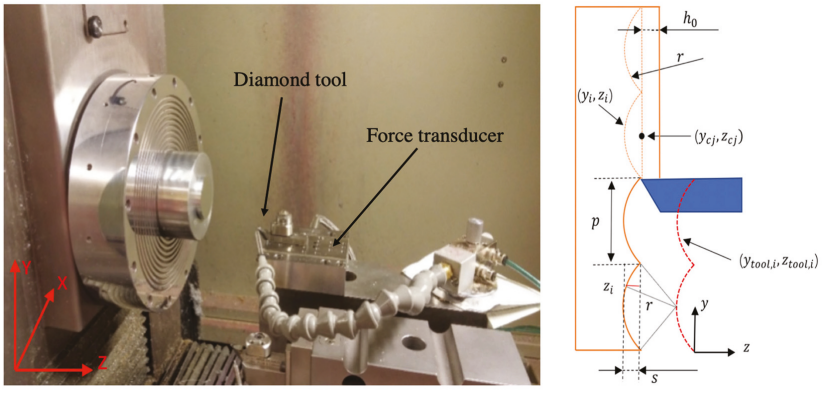

(**a**) (**b**)

Figure 3. (**a**) Experiment setup. (**b**) Tool path for cutting a microlens array.

Table 1. The designed parameters of microlens arrays and the process parameters.

Parameter	Value
Pitch (μm)	100
Sag (μm)	3.93
Lens radius (μm)	320
Workpiece material	Aluminum 6061-T6
Cutting velocity (mm/min)	5, 10, 15, 20
Tool nose radius (μm)	320
Nominal rake angle (°)	0
Nominal clearance angle (°)	10
Constant depth of cut (μm)	5
Coolant	No

Microlens arrays were cut utilizing the servo motion of the y- and z-axes of the machine tool. The corresponding tool path was determined as follows. The tool trajectory of the turning microlens arrays is shown in Figure 3b. The tool path $(y_{n,\,i}, z_{n,\,i})$ was determined by a set of cutting points denoted by (y_i, z_i) and the increment of y_i was set at Δy mm. It is assumed that the length of a compound lens array is l, the pitch is p and the radius of each lens unit is the same as the tool radius, r, while the center of the j-th eyelet (y_{cj}, z_{cj}) in the machine tool coordinate is expressed as:

$$y_{cj} = j \times p;\ j = 1, 2, 3 \ldots, \frac{l}{p} \tag{25}$$

In each eyelet, there are $\frac{p}{\Delta y}$ sampling points, and the cutting points (y_i, z_i) for the j-th microlens are derived as:

$$(y_i, z_i) = \left(y_{k+j\times p/\Delta y},\ \sqrt{r^2 - \left(y_{cj} - \left(y_{k+j\times p/\Delta y}\right)\right)^2} \right) k = 1, 2, 3, \ldots, \frac{p}{\Delta y} \tag{26}$$

The tool path $(y_{n,\,i}, z_{n,\,i})$ can be derived from cutting point positions:

$$(y_{n,\,i}, z_{n,\,i}) = (y_i, r - s - h_0 - z_i) \tag{27}$$

where s is the sag value of the eyelet, such that:

$$s = r - \sqrt{r^2 - \left(r - \left(\frac{p}{2}\right)\right)^2} \tag{28}$$

and $y_{k+j\times p/\Delta y}$ satisfies Equation (29):

$$y_{k+j\times p/\Delta y} = k \times \Delta y + j \times p;\ k = 1, 2, 3, \ldots, \frac{p}{\Delta y} \tag{29}$$

In the cutting experiments, the actual uncut chip thickness is the summation of z_i and the constant depth, h_0. h_0 is set to 5 µm, which is more than ten times larger than the tool edge radius. As a result, the tool edge effect can be ignored during the machining.

4. Results and Discussion

4.1. Surface Profile Analysis

The measured surfaces are shown in Figure 4. The surface profile $\widehat{AB}$ is extracted from the surface along the axis of symmetry. Hence, the surface primary profile is obtained by removing the form of each microlens.

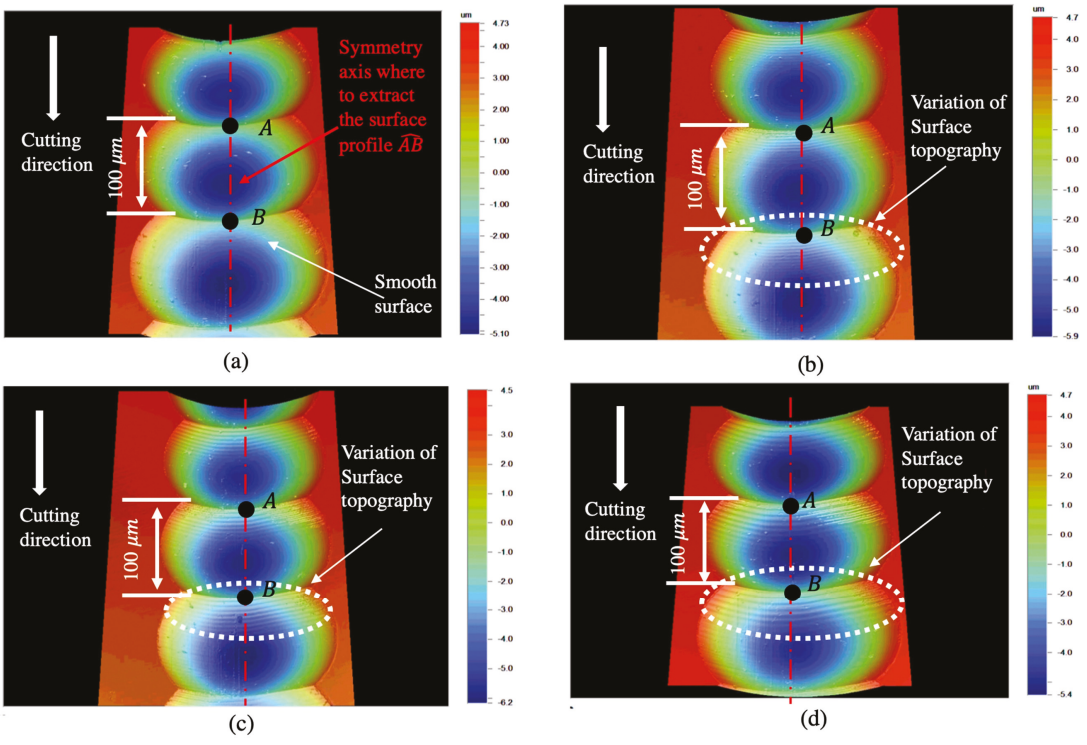

Figure 4. Measured surfaces: (**a**) 5 mm/min, (**b**) 10 mm/min, (**c**) 15 mm/min, (**d**) 20 mm/min.

The surface primary profiles corresponding to different cutting conditions are shown in Figure 5. The variation of surface primary profiles is not obvious in the profile corresponding to the relatively low cutting velocity of 5 mm/min. However, periodic components can be clearly seen in the profiles when the cutting velocity is equal to or above 10 mm/min. The wavelength (*wl*) of the surface topography variation can be roughly estimated by measuring the peak-to-peak distances, which are 2.5, 4.0 and 5.1 µm, as shown in Figure 5b–d, respectively. By dividing the cutting speed by the corresponding wavelength, the frequencies of the relative vibration were found to be around 60 Hz, regardless of the cutting speed. As a result, the frequency around 60 Hz was identified as the characteristic frequency of the relative tool-work vibration. The theoretical peak-to-peak distance corresponding to the characteristic frequency was around 1.4 µm when the cutting

velocity was 5 mm/min. Considering that the lateral resolution of the surface profiler is around 0.2 µm, the profiler would have captured the surface variation if the relative tool-work vibration was noticeable. As shown in Figure 5c,d, the periodic components exhibit apparent damping behavior. Hence, the tool-work vibration should not be modeled as a simple undamped harmonic vibration in UTSDC. Apart from the periodic components, the material spring-back can be seen in Figure 5a,b. This coincides with Reference [19], which showed that spring-back is significant when the cutting speed is low and it contributes to the increase of the thrust force.

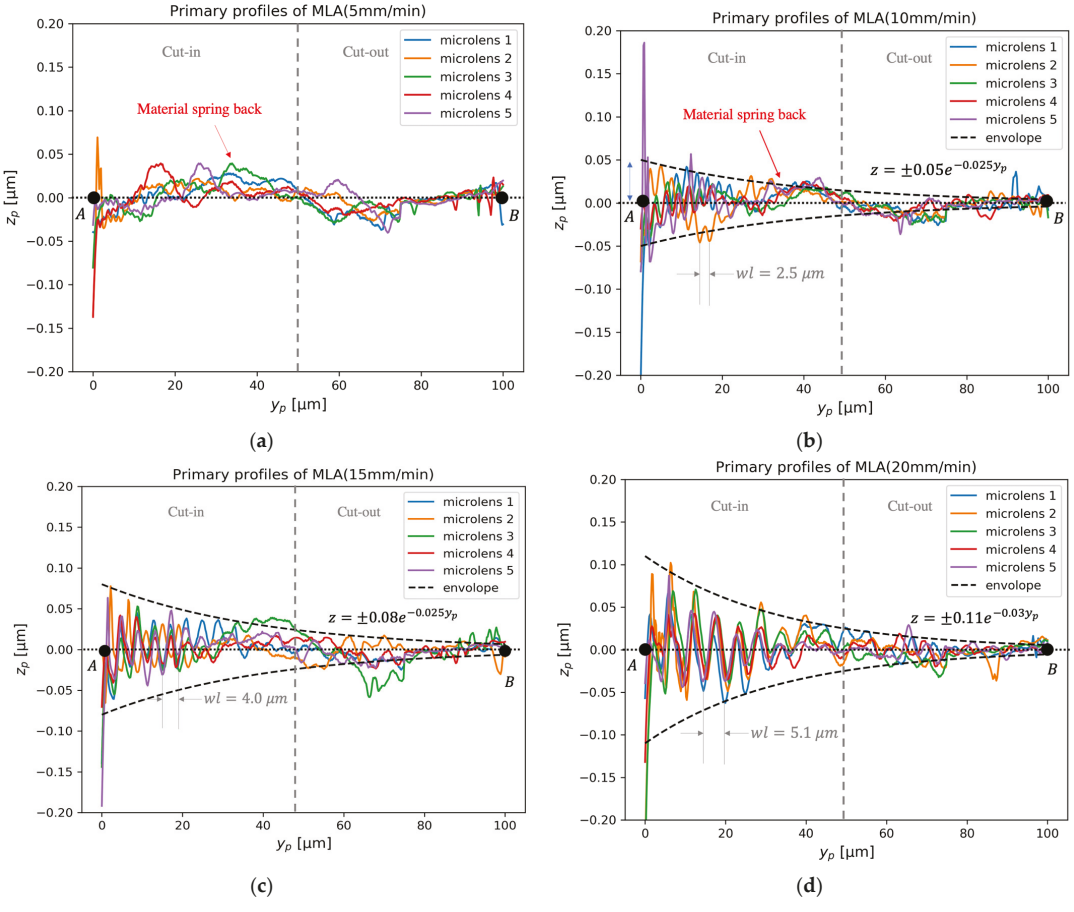

Figure 5. Primary profiles of microlens array corresponding to nominal cutting velocity: (**a**) 5 mm/min, (**b**) 10 mm/min, (**c**) 15 mm/min, (**d**) 20 mm/min.

The DDS analysis of the surface profiles under different cutting conditions is shown in Table 2. ARMA models of order (4,3) to (12,11) are fitted to the profiles. When the cutting speed is 5 mm/min, the characteristic frequency component only contributes less than 13% of the total power of the primary profile. A pair of real roots were detected, whose percentage contribution to total power was more than 60%. The real roots represent strong break frequency with a high damping ratio ($\xi > 0.7$). This is similar to the ultra-precision face-turning operation, where the contribution of the break frequency components was found to be above 67% of the total surface roughness [20]. As a result, the effect of relative

tool-work vibration is considered to be insignificant in UTSDC when the cutting speed is less than 5 mm/min.

Table 2. Results of data-dependent systems (DDS) analysis for the tool-work vibration component along the surface primary profile.

Cutting Velocity (mm/min)	Characteristic Roots	Characteristic Frequency (Hz)	Damping Ratio	Percentage Contribution to Total Power
5	$0.6139 \pm 0.8486j$	59.84	0.049	12.63%
10	$0.9032 \pm 0.4712j$	61.39	0.039	25.97%
15	$0.9560 \pm 0.3333j$	63.88	0.037	79.63%
20	$0.9819 \pm 0.2396j$	60.03	0.045	97.98%

When the cutting speed increased from 10 to 20 mm/min, the characteristic frequencies were found to be around 62 Hz and the damping ratio, ξ, was about 0.04. The frequencies and damping ratios appear to be independent when the cutting velocity varies in the range of 10 to 20 mm/min. However, the percentage contributions to total power were 25.97%, 79.63% and 99.12%, when the cutting speed was increased from 10 to 20 mm/min. This indicates that the relative tool-work vibration is significantly enhanced when the cutting speed increases.

4.2. Estimation of the Thrust Force

Figure 6 shows the measured thrust forces, $F_{m,z}$, along the thrust direction. Under the condition that the cutting speed was 5 mm/min, $F_{m,z}$ jumped from 0.06 to 0.27 N at the beginning of the cut-in process. At this stage, a certain amount of work material is indented and generates an extra resistance force on the clearance face of the diamond tool. $F_{m,z}$ then remains at a relatively stable value until the end of the cut-in process, suggesting that the volume of the indented material becomes stable. In the cut-out process, $F_{m,z}$ decreased almost linearly with increasing cutting distance. Since the vibration component is not obvious when the cutting speed is low, the spring force and damping force can be ignored. As a result, the thrust force, F_t, can be modeled by $F_{m,z}$ when $v = 5$ mm/min,

$$F_t(y_p) = F_{m,z}(y_p, v = 5) = \begin{cases} 70y_p & y_p \in [0,\ 0.003) \\ 0.27 & y_p \in [0.003,\ 0.05) \\ 0.48 - 4.2y_p & y_p \in [0.05,\ 0.1] \end{cases} \quad (30)$$

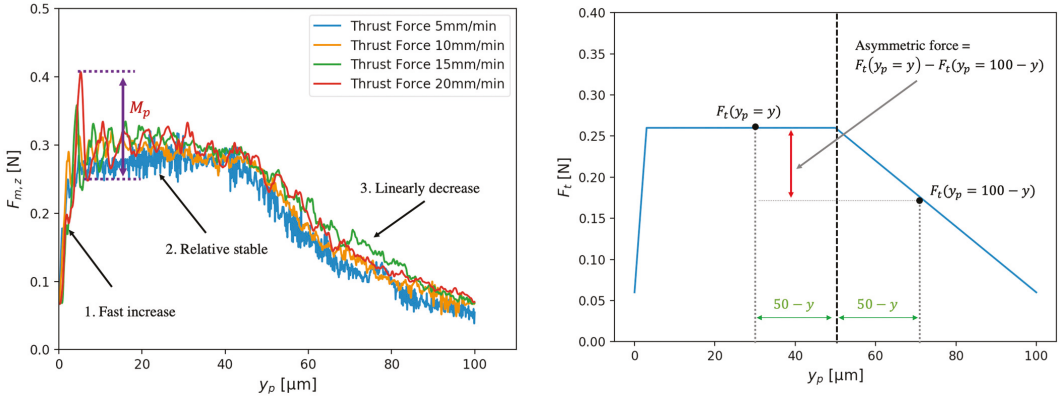

(**a**) (**b**)

Figure 6. (**a**) The measured forces, $F_{m,z}$, along the thrust direction. (**b**) The thrust force, F_t, used in the dynamic model.

For an arbitrary speed v,

$$y_p = \frac{vt}{60} \tag{31}$$

By combining Equations (30) and (31), the thrust force is derived as a function of time t. When v is larger, $F_{m,z}$ exhibits overshoot at the beginning of the cut-in process and the dynamic component decays as the diamond tool moves forward in the cutting direction. Although a larger cutting speed results in larger overshoot, the primary shape of $F_{m,z}$ is the same despite different cutting speeds. The frequency of the measured force, $F_{m,z}$, was around 60 Hz, which is close to the characteristic frequency identified from the surface primary profile. Since the force sampling frequency is much larger than 60 Hz, the force signal can also reflect the amplitude of the tool-work vibration.

4.3. Verification of the Proposed Dynamic Cutting Model

The dynamic equation of the cutting system can be derived after the w_n, ζ and F_t are obtained from the surface profile data and thrust force data. Due to the complexity of the second-order differential equation, the numerical solution is computed using the Python scipy.integrate package.

The root-mean-squares (RMS) value of the measured primary profile and the predicted profile, i.e., $\hat{z}_p$, are shown in Figure 7. The *RMS* values reflect the overall deviation of the machining error along the surface profile. It can be seen that the theoretical *RMS* value is close to the measured value when the cutting speed is 15 and 20 mm/min. Under such cutting conditions, the tool-work vibration of the diamond tool system is the major source of the surface topography variation.

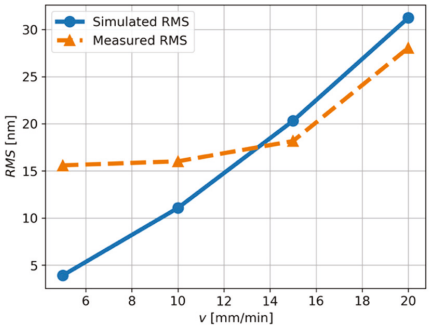

Figure 7. The relationship between the cutting velocity, v, and root-mean-squares (RMS) of the primary profile.

When the cutting speed is smaller than 10 mm/min, the theoretical *RMS* value is smaller than the measured value because the vibration component only contributes to a small portion of the total power of the profile, as demonstrated in Table 2. As shown in Figure 5a,b, z_p drops in the center of a microlens, where the cutting state changes from cut-in to cut-out. Therefore, the major error source is probably the material spring-back.

In the cut-in state, part of the material beneath the cutting tool tip is compressed and elastically recovered at the clearance face of the tool, generating an extra indentation force in the thrust direction. The extra force can be roughly measured by the asymmetric force illustrated in Figure 6b. In the cut-out process, the motion of the diamond tool is in the positive z-axis direction, which pushes the majority of material ahead of the tool's rake face to the free surface. Hence, a small amount of material flows under the tool tip and the thrust force decreases. The resultant force acting on the force sensor, $F_{m,z}(t)$, can be predicted by the proposed dynamic cutting model based on Equation (21) once m, c, k, tool path trajectory and the theoretical thrust force, $F(t)$, are known. Figure 8 shows the good

agreement between the maximum overshoot, M_p, of the theoretical force acting on the force sensor and the actual measured force.

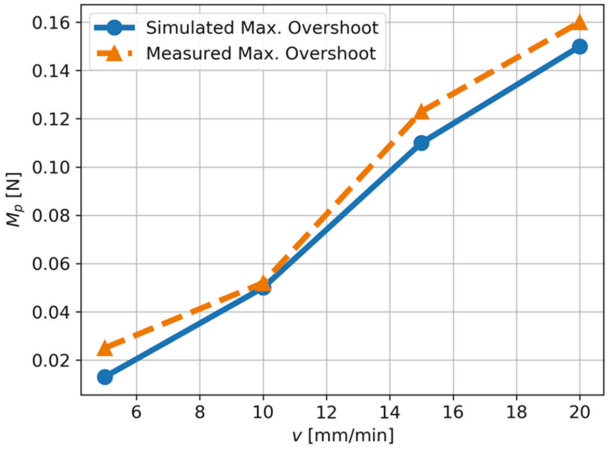

Figure 8. The relationship between the cutting velocity, v, and the maximum overshoot of the thrust force.

Overall, the dynamic model provides insight into the formation of the surface topography variation in the UTSDC of 3D microstructured surfaces. The slide motion in the thrust direction and the sudden increase of the thrust force at the beginning of the cut-in process leads to a disturbance in the dynamic cutting system, generates an underdamped vibration of the diamond tool in the thrust direction and leaves a wavy profile in the machined surface. The effect of the cutting speed on the *RMS* of the surface primary profile and the maximum overshoot of thrust force are quantified based on the proposed dynamic cutting model. To strike a balance between a fine surface finish and machining efficiency, the velocity of 15 mm/min is preferred to fabricate the microlens arrays. Although the proposed method is limited by the lateral resolution of the surface profiler, and the thrust force, F_t, used as an input for the dynamic model needs to be obtained from experiments, the theoretical analysis and experimental results provide potential benefits in predicting the dynamic forces and surface topography variation in the UTSDC of microstructured surfaces. Further work is needed to calculate F_t based on the theory of metal shearing and the tool indentation effect. The proposed dynamic model can be used in the self-optimization machining system [21], providing essential information on the process–machine interactions and machining quality inspection.

5. Conclusions

In this paper, the characteristics of the surface topography variation in ultra-precision tool servo-based diamond cutting (UTSDC) of 3D microstructured surfaces were investigated. Conclusions are drawn as follows:

(1) In UTSDC, the relative tool-work vibration exhibited apparent damping behavior. The vibration cannot be simplified as a steady harmonic vibration with a constant amplitude and frequency.

(2) The characteristic frequency and the damping ratio of the surface topography variation were obtained based on the data-dependent systems approach. The percentage contribution of characteristic frequency to total power of the surface topography variation increased from 12.63% to 97.98% when the cutting speed increased from 5 to 20 mm/min.

(3) Based on the analysis of the machined surface profile and thrust force, it was found that the surface topography variation in UTSDC was mainly affected by the tool-work

vibration when the cutting speed was over 10 mm/min, and the variation increased with an increase of cutting speed.

(4) A dynamic model has been purposely developed which takes into account the tool path, cutting speed and the dynamics of the machining system. The model can well-predict the *RMS* values of the surface primary profile and the dynamic force acting on the force sensor.

Author Contributions: Conceptualization, methodology, investigation, formal analysis, writing—original draft preparation, W.Y.; Conceptualization, supervision, funding acquisition, resources, writing—review and editing, C.-F.C. All authors have read and agreed to the published version of the manuscript.

Funding: The work described in this paper was supported by a grant from the Ministry of Science and Technology of China (Project Code: 2017YFE0191300) and a PhD studentship (project account code: RUK0) from The Hong Kong Polytechnic University.

Conflicts of Interest: The authors declare no conflict of interest.

Nomenclature

(y_p, z_p)	Surface primary profile
(y_m, z_m)	Measured profile
(y_n, z_n)	Nominal profile/Tool path
(y_i, z_i)	Cutting location points
t	Time
α_i	Autoregressive (AR) parameter
b_i	Moving average (MA) parameter
Δ	Sampling interval
λ_i, λ_i^*	A pair of complex roots
ω_i	Natural frequency
ζ_i	Damping ratio
P	The percentage contribution of the total power
h_0	The constant depth
z_1	The displacement of the moving part of the slide along the z-axis
z_2	The displacement of the diamond tool along the z-axis
y_1	The displacement of the workpiece of the slide along the y-axis
$F_{m,z}$	The measured force along the z-axis
F_t	The thrust force

References

1. Zhang, S.J.; To, S.; Wang, S.J.; Zhu, Z.W. A review of surface roughness generation in ultra-precision machining. *Int. J. Mach. Tools Manuf.* **2015**, *91*, 76–95. [CrossRef]
2. Venkatachalam, S.; Fergani, O.; Li, X.; Yang, J.G.; Chiang, K.N.; Liang, S.Y. Microstructure effects on cutting forces and flow stress in ultra-precision machining of polycrystalline brittle materials. *J. Manuf. Sci. Eng. Trans. ASME* **2015**, *137*, 21020. [CrossRef]
3. Yan, J.; Oowada, T.; Zhou, T.; Kuriyagawa, T. Precision machining of microstructures on electroless-plated NiP surface for molding glass components. *J. Mater. Process. Technol.* **2009**, *209*, 4802–4808. [CrossRef]
4. Guo, J.; Zhang, J.; Wang, H.; Liu, K.; Kumar, A.S. Surface quality characterisation of diamond cut V-groove structures made of rapidly solidified aluminium RSA-905. *Precis. Eng.* **2018**, *53*, 120–133. [CrossRef]
5. Rahman, M.A.; Amrun, M.R.; Rahman, M.; Kumar, A.S. Variation of surface generation mechanisms in ultra-precision machining due to relative tool sharpness (RTS) and material properties. *Int. J. Mach. Tools Manuf.* **2017**, *115*, 15–28. [CrossRef]
6. Arefin, S.; Zhang, X.Q.; Neo, D.W.K.; Kumar, A.S. Effects of cutting edge radius in vibration assisted micro machining. *Int. J. Mech. Sci.* **2021**, *208*, 106673. [CrossRef]
7. Kim, K. Prediction and Characterization of Machined Surface Topography in the Frequency Domain. Ph.D. Thesis, Northwestern University (Evanston, Ill.), Evanston, IL, USA, June 2000.
8. Wang, H.X.; Zong, W.J.; Sun, T.; Liu, Q. Modification of three dimensional topography of the machined KDP crystal surface using wavelet analysis method. *Appl. Surf. Sci.* **2010**, *256*, 5061–5068. [CrossRef]
9. Pandit, S.M.; Revach, S. A Data Dependent Systems Approach to Dynamics of Surface Generation in Turning. *J. Eng. Ind.* **1981**, *103*, 437–445. [CrossRef]

10. Takasu, S.; Masuda, M.; Nishiguchi, T.; Kobayashi, A. Influence of Study Vibration with Small Amplitude Upon Surface Roughness in Diamond Machining, CIRP Ann. *Manuf. Technol.* **1985**, *34*, 463–467. [CrossRef]
11. Cheung, C.F.; Lee, W.B. A theoretical and experimental investigation of surface roughness formation in ultra-precision diamond turning. *Int. J. Mach. Tools Manuf.* **2000**, *40*, 979–1002. [CrossRef]
12. Cheung, C.F.; Lee, W.B. Multi-spectrum analysis of surface roughness formation in ultra-precision machining. *Precis. Eng.* **2000**, *24*, 77–87. [CrossRef]
13. Chen, J.; Zhao, Q. A model for predicting surface roughness in single-point diamond turning. *Measurement* **2015**, *69*, 20–30. [CrossRef]
14. Wang, H.; To, S.; Chan, C.Y. Investigation on the influence of tool-tip vibration on surface roughness and its representative measurement in ultra-precision diamond turning. *Int. J. Mach. Tools Manuf.* **2013**, *69*, 20–29. [CrossRef]
15. Brinksmeier, E.; Gläbe, R.; Schönemann, L. Diamond Micro Chiseling of large-scale retroreflective arrays. *Precis. Eng.* **2012**, *36*, 650–657. [CrossRef]
16. Pandit, S.M.; Shaw, M.C. Characteristic Shapes and Wavelength Decomposition of Surfaces in Machining. *CIRP Ann. Manuf. Technol.* **1981**, *30*, 487–492. [CrossRef]
17. Pandit, S.M.; Systems, D.D. Stochastic Linearization by Data Dependent Systems. *J. Dyn. Sys. Meas. Control* **1977**, *99*, 221–226. [CrossRef]
18. Pandit, S.M.; Mehta, N.P. Data dependent systems approach to modal analysis Part 1: Theory. *J. Sound Vib.* **1988**, *122*, 413–422. [CrossRef]
19. Zhao, Z.; To, S.; Zhu, Z.; Yin, T. A theoretical and experimental investigation of cutting forces and spring back behaviour of Ti6Al4V alloy in ultraprecision machining of microgrooves. *Int. J. Mech. Sci.* **2020**, *169*, 105315. [CrossRef]
20. Cheung, C.F.; Chan, K.C.; Lee, W.B. Surface characterization in ultra-precision machining of Al/SiC metal matrix composites using data dependent systems analysis. *J. Mater. Process. Technol.* **2003**, *140*, 141–146. [CrossRef]
21. Möhring, H.C.; Wiederkehr, P.; Erkorkmaz, K.; Kakinuma, Y. Self-optimizing machining systems. *CIRP Ann.* **2020**, *69*, 740–763. [CrossRef]

micromachines

MDPI

Article

Molecular Dynamic Investigation of the Anisotropic Response of Aluminum Surface by Ions Beam Sputtering

Chunyang Du [1,2,3], Yifan Dai [1,2,3], Chaoliang Guan [1,2,3] and Hao Hu [1,2,3,*]

[1] College of Intelligence Science, National University of Defense Technology, Changsha 410073, China; nature_cydu@vip.sina.com (C.D.); dyf@nudt.edu.cn (Y.D.); gchl_nudt@163.com (C.G.)
[2] Laboratory of Science and Technology on Integrated Logistics Support, National University of Defense Technology, Changsha 410073, China
[3] Hu'nan Key Laboratory of Ultra-Precision Machining Technology, Changsha 410073, China
* Correspondence: tiny_hh@139.com

Abstract: Aluminum optics are widely used in modern optical systems because of their high specific stiffness and high reflectance. With the applied optical frequency band moving to visible, traditional processing technology cannot meet the processing precision. Ion beam sputtering (IBS) provides a highly deterministic technology for high-precision aluminum optics fabrication. However, the surface quality is deteriorated after IBS. The interaction between the bombard atoms and the surface morphology evolution mechanism are not clear, and systematic research is needed. Thus, in this paper, the IBS process for single crystal aluminum with different crystallographic orientations are studied by the molecular dynamics method. The ion beam sputter process is firstly demonstrated. Then, the variation of sputter yield of the three crystal faces is analyzed. The sputter yield difference of different crystal surfaces causes the appearance of the relief structure. Then, the gravel structure generates on the single crystal surfaces and dominates the morphology evolution. The state of the atom diffusion of the specific crystal surfaces will determine the form of the gravel structure. Furthermore, the form and distribution of subsurface damage and stress distribution of three different crystal surfaces are analyzed. Although there are great differences in defect distribution, no stress concentration was found in three workpieces, which verifies that the ion beam sputter is a stress-free machining method. The process of IBS and the mechanism of morphology evolution of aluminum are revealed. The regularity and mechanism will provide a guidance for the application of IBS in aluminum optics manufacture fields.

Keywords: aluminum; ion beam sputtering; morphology evolution; subsurface damage; molecular dynamics

Citation: Du, C.; Dai, Y.; Guan, C.; Hu, H. Molecular Dynamic Investigation of the Anisotropic Response of Aluminum Surface by Ions Beam Sputtering. *Micromachines* **2021**, *12*, 848. https://doi.org/10.3390/mi12070848

Academic Editors: Jiang Guo, Chunjin Wang and Chengwei Kang

Received: 15 June 2021
Accepted: 19 July 2021
Published: 20 July 2021

1. Introduction

With fine mechanical properties, light weight and high reflectivity, aluminum is widely used in optical systems in recent years, especially in the micro-satellites with extreme requirements for weight and volume [1–3]. Currently, the applied optical frequency band of aluminum optics is moving from infrared (IR) to visible (VIS), which brings a great challenge to fabrication [4]. For application in visible band, the aluminum optics should possess nanometer scale surface profile precision and subnanometer scale surface roughness. Usually, single-point diamond turning (SPDT) and magnetorheological finishing (MRF) are widely used in the fabrication of aluminum optics [5,6]. However, the precision of these methods cannot meet the requirements for visible light usage. Moreover, due to the properties of high chemical reactivity and low surface hardness, contact machining will cause the contamination of the aluminum surface, which is often associated with a reduction in the surface quality [7].

As a high-determined machining method, ion beam sputtering (IBS) achieves surface profile correction by removing materials through physic sputtering effects [8,9]. When re-

ceiving enough energy from bombarded atoms, the surface atoms will be sputtered from the surface. IBS is believed to possess the highest machining precision. Moreover, the whole process is conducted in a near-vacuum environment which will not cause contamination [10,11]. All the advantages show that IBS can be a better polishing method for visible range aluminum optics compared with contact polishing methods such as MRF. In recent years, more researches have been focused on the roughness and surface morphology revolution during IBS. Remarkable experimental work is conducted to demonstrate the formation of specific micro-topographies, such as ripples [12,13] and nanoparticles [14,15]. However, most researches are conducted on amorphous materials such as fused silica. There is a great lack of studies about aluminum. A systematic experiment on roughness evolution of different materials during IBS was carried out by C.M. Egert [16]. Aluminum shows poor performance on the decrease in roughness. The same phenomenon is also observed in the experiments conducted by our research group. Unlike traditionally used materials in IBS, peculiar relief and gravel structure emerge on the aluminum surface during IBS [17]. In order to realize the regulation of surface microscopic morphology and surface roughness, the process of IBS and mechanism of morphology evolution need to be revealed. However, experimentalists face the daunting task of characterizing the material removal and surface evolution of aluminum at nanoscale time and space. Thus, the mechanism is still unrevealed.

Molecular dynamics (MD) simulations play a key role in understanding the experimental results, revealing mechanism and predicting outcomes [18–20]. Remarkable works have been successfully conducted, revealing the mechanism of interaction between energy particles and many other materials. Using MD, Wang et al. reveal the elastoplastic transformation process of monocrystalline silicon material induced by ion implantation [21]. By optimizing the ion implantation, amorphous layer with microns' scale can be generated. Xiao et al. have studied the surface damage evolution of nanoscale silicon caused by Ga-focused ion beam machining. Simulation results are in good agreement with the experimental results [22]. Xiao et al. have successfully revealed the material removal process and surface morphology evolution of single crystal silicon during IBS [23]. However, there is limited work related to the metal materials such as aluminum [24–29]. Moreover, the aluminum used in the IBS are usually in an alloy state. There are multiple crystal faces on the surface. In order to realize the regulation of surface microscopic morphology of aluminum, it is necessary to fully understand the mechanism in each crystallographic orientation through MD.

In this work, the IBS process and surface morphology evolution of three kinds of crystal surfaces are studied. In Section 2, the method of MD simulation, defect analysis, and visualization techniques are presented. In Section 3, the results of ion beam sputtering process and its mechanism, surface morphology evolution, sputtering yield, and subsurface damage are analyzed and discussed. Finally, a conclusion is summarized in Section 4. The results of this study will be beneficial to understanding the IBS of aluminum and promoting the application of IBS in the field of aluminum optics manufacture, which will significantly improve the machining efficiency and precision of aluminum optics.

2. Simulation Method

2.1. Simulation Description

The MD model of Ar ion sputtering consists of a single crystal aluminum workpiece and Ar atoms, as indicated in Figure 1. The aluminum workpiece has a dimension of 15, 15, and 38 nm in X, Y, and Z directions, respectively. To investigate the influence of crystal orientation, three aluminum workpieces with Al(110), Al(111), and Al(001) free surface in Z direction are considered. Ar atoms bombard the workpiece vertically in the Z direction. Because IBS is conducted in a near-vacuum environment, the influence of the environment can be ignored. As shown in Figure 1, the aluminum sample is divided into three regions: the region of boundary atoms to fix the sample in space, the region of thermostat atoms to imitate the heat dissipation, and the region of Newtonian atoms which

obeys Newton's second law [30–33]. The thickness of thermostat layer and boundary layer are both 1 nm. The initial temperature of the aluminum sample is maintained at 293 K. The periodic boundary condition is applied on the direction of X and Y to elimination of size effect.

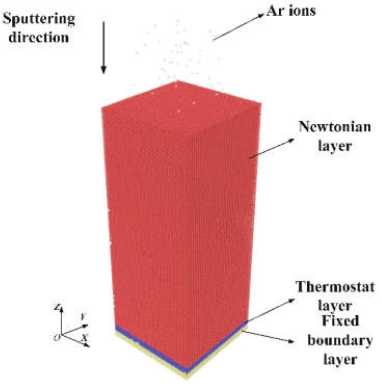

Figure 1. MD model of ion beam sputtering of single crystal aluminum.

During IBS, Ar is firstly ionized in the cavity and accelerated by screen-grid voltage. Then, a neutralizer is applied to the generated electron to neutralize the charge of Ar^+. Thus, the Ar atoms will have the same bombardment speed as shown in Table 1. The Ar will bombard the workpiece surface in a steady stream. Thus, in this study, we adopt a continuous bombardment situation. First, k Ar atoms are distributed randomly in a $10 \times 10 \times 1$ nm^3 box to simulate specific ionic concentration in the cavity. Then, the $10 \times 10 \times 1$ box will expand n times in the Z direction. For each $10 \times 10 \times 1$ nm^3 box, the Ar atoms in the box are randomly distributed. The total Ar atoms bombarding on the surface will be $k \times n$. All the MD simulations are based on LAMMPS developed by Sandia National Laboratory (PO Box 5800, Albuquerque, NM, USA). The Ovito is utilized to perform visualization of MD simulation of the IBS process. The velocity-Verlet algorithm is applied to integrate Newton's equations of motion with the time step of 1 fs. The common neighbor analysis (CNA) is used to identify the crystal structure during the ion sputtering. Firstly, the energy minimization is carried out by the conjugate gradient method to avoid the overlap of atomic position. Then, the temperature of workpiece is equilibrated to 293 K by the Nose–Hoover thermostat for 70 ps. Both the relaxation stage and sputtering simulation are performed in a microcanonical ensemble (NVE) [34–36]. The Ar atoms are placed at the height of 2 nm above the initial top surface of workpiece. Considering the commonly process parameters of IBS, the ion energy is chosen to be 500 eV and the incident angle is 90°. The total number of bombarded Ar atoms is 50. The ion dose is defined as the total number of Ar atoms trapped in workpiece divided by the upper surface area of workpiece. The simulated parameters are represented in Table 1.

Table 1. Simulation parameters of ion beam sputtering.

Material	Aluminum
Dimension	$15 \times 15 \times 38$ nm^3
Number of atoms	554,040
Time step	1 fs
Initial temperature	293 k
Incident angle	90°
Ion energy (Ion velocity)	500 eV (491 Å/fs)
Lattice plane	(110) (111) (001)
Ion dose	2.2×10^{13} ion/cm^2

2.2. Potential Description

The mixing potentials are used in the ion beam sputtering simulation. The interaction potentials between atoms are described as follow:

(1) For Ar–Ar atomic interaction, the Ziegler–Biersack–Littmark (ZBL) potential is adopted, which can be expressed as follow [37]:

$$E_{ij}^{ZBL} = \frac{1}{4\pi\varepsilon_0} \cdot \frac{Z_i Z_j e^2}{r_{ij}} \phi(r_{ij}/a) + S(r_{ij}), \quad (1)$$

$$a = \frac{0.46850}{Z_i^{0.23} + Z_j^{0.23}}, \quad (2)$$

$$\phi(x) = 0.18175e^{-3.19980x} + 0.50986e^{-0.94229x} + 0.28022e^{-0.40290x} + 0.02817e^{-0.20162x}. \quad (3)$$

where e is the electron charge, ε_0 is the electrical permittivity of vacuum, and Z_i and Z_j are the nuclear charges of the two atoms. $S(r)$ is the switching function.

(2) For Al–Al atomic interaction, the embedded-atom method (EAM) potential is adopted, which can be expressed as follow [38]:

$$E_i = F_\alpha\left(\sum_{j \neq i} \rho_\beta(r_{ij})\right) + \frac{1}{2}\sum_{j \neq i} \phi_{\alpha\beta}(r_{ij}). \quad (4)$$

where E_i is the total energy, F is the embedding energy which is a function of the atomic electron density ρ, ϕ is a pair potential interaction, α and β are the element types of atoms i and j.

(3) For Al–Ar atomic interaction, the splicing potentials are adopted. ZBL, the second order polynomial function and Lennard–Jones (*LJ*) potentials are used for different atomic spacing, respectively, to construct the Ar–Al potential function. The *LJ* potential is expressed as follow:

$$U_{ij}^{LJ}(r_{ij}) = 4\varepsilon\left[\left(\frac{\sigma}{r_{ij}}\right)^{12} - \left(\frac{\sigma}{r_{ij}}\right)^{6}\right] \quad (5)$$

where ε is the depth of the potential well, σ is the distance of zero potential. ZBL potential is used in the range of 0~0.31 nm and *LJ* potential in the range of 0.37~∞ nm. In the range of 0.31~0.37 nm, a second order polynomial function is used to join the two potentials [39].

3. Results and Discussion

3.1. Ion Beam Sputtering Mechanism

The IBS can be a complicated process. The Ar atoms bombard on the surface and perturb the Al atoms. The Al atoms receive enough energy and will be sputtered from the workpiece surface. During IBS, there will be two types of Ar ion behaviors: ion bounce and ion implantation, which are shown in Figures 2 and 3, respectively. For ion bounce, the Ar atoms impact the aluminum surface and embed into the substrate. Few surface Al atoms are disturbed, as shown in Figure 2d. Then, the Ar ion collides with Al atom, with a rapid transfer of kinetic energy. The Ar ion bounces back and the recoil Al atom will continue the movement, as shown in Figure 2f. For ion bounce, few Al atoms are exposed by Ar atoms during the bombardment and there is a rapid exchange of kinetic energy during the impact.

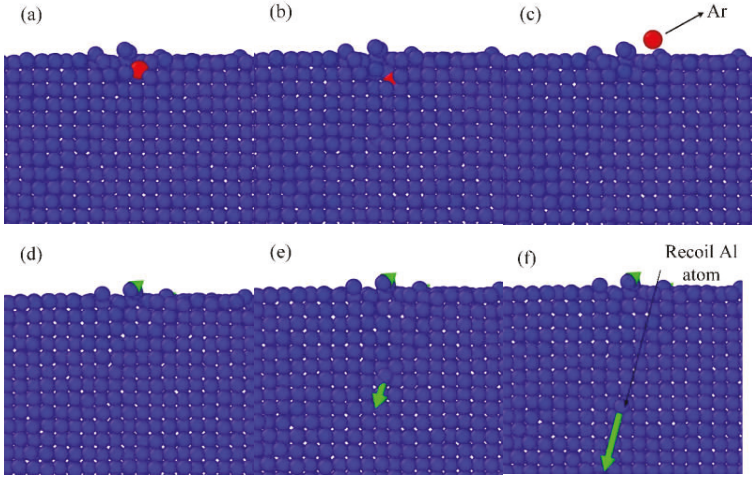

Figure 2. Scheme of Ar ion bounce, (**a**–**c**) process of bounce, (**d**–**f**) corresponding motion of Al atoms.

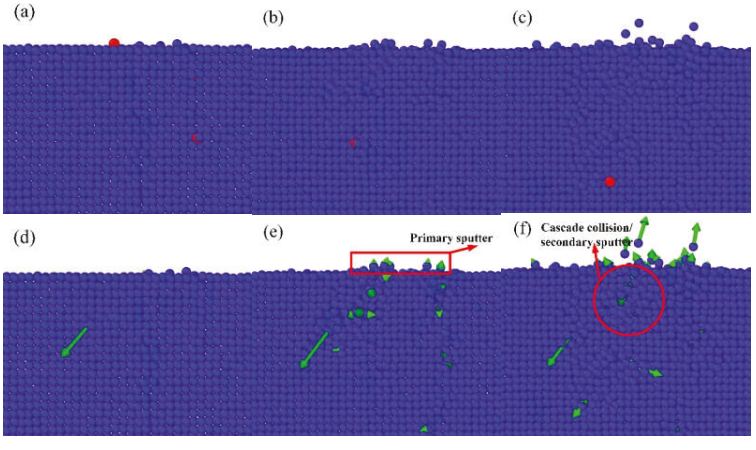

Figure 3. Scheme of Ar ion implantation, (**a**–**c**) process of implantation, (**d**–**f**) corresponding motion of Al atoms.

Ion implantation will occur for most of the Ar atoms. As shown in Figure 3a,d, the implantation will cause the perturbation of the deeper Al atoms. With the motion of the Ar atoms, large numbers of Al atoms in the bombardment area gain kinetic energy. Some atoms are directly sputtered out after colliding with Ar atoms, as shown in Figure 3e, which is referred as primary sputter phenomenon. The Al atoms with kinetic energy will bump into other atoms in a cascade collision, which will cause secondary sputter phenomenon, as shown in Figure 3f.

3.2. Sputter Yield Analysis

IBS is believed to possess the highest machining precision. The steady erosion rate of IBS can be expressed as follow:

$$v_0 = \Omega J Y_0 \tag{6}$$

where J is the ion current, Ω is the atomic volume, and Y_0 is the sputter yield. In order to achieve high precision material removal, it is necessary to acquire precise sputtered

yield for corresponding materials. Usually, Monte Carlo methods are used to simulate sputter yields, which have a high accuracy for isotropic materials such as fused silica. However, the simulation setup of many Monte Carlo methods is relatively simple, which cause great deviation from experimental results. Commonly used Monte Carlo simulations for IBS are based on SRIM. Figure 4 shows the Monte Carlo simulation results of IBS of aluminum. With same simulation parameters, the Ar atoms mainly distribute in the depth of around 58 Å or less. The displacements and vacancies have the same distributions, which is similar to the Ar distribution. The sputter yield calculated by SRIM is 0.6707 Atoms/Ions. However, the IBS process of different crystal orientations cannot be revealed by SRIM, which slightly limits the application of the Monte Carlo simulation.

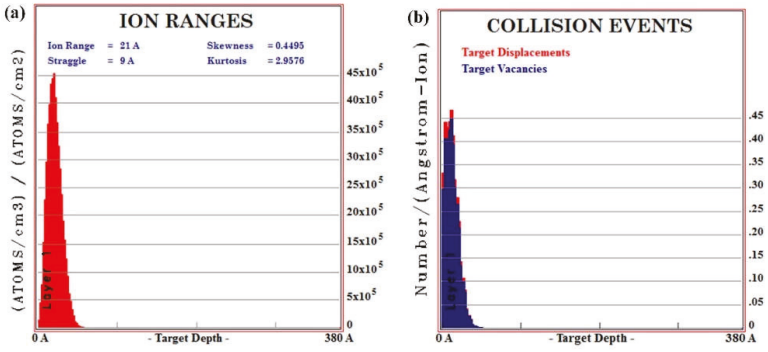

Figure 4. Monte Carlo simulation results of IBS process, (**a**) Ar atoms distribution, (**b**) damage distribution.

Based on MD simulation, the Ar atoms distribution and corresponding Gaussian distribution fitting in the z direction are presented in Figure 5. For Al(001), the average depth of bombardment is around 70 Å. As the depth increases, the number of Ar atoms decreases, which conforms to the actual processing conditions. Al(111) shares the same regularity with Al(001). However, according to the expectation and variance, the distribution of Ar atoms is more concentrated and the depth is shallower. For Al(110), Ar atoms are more evenly distributed relatively. The average depth of bombardment is 146 Å, which is the deepest among the three crystal orientations.

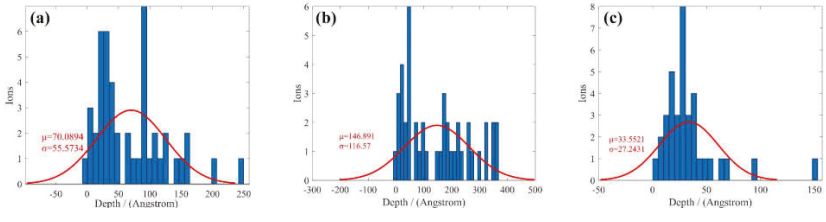

Figure 5. Ar atoms distribution and corresponding Gaussian distribution fitting of, (**a**) Al(001), (**b**) Al(110), (**c**) Al(111).

The sputter yield can be calculated by the division of sputtered Al atoms and Ar ions. The sputter yields of Al(001), Al(110), and Al(111) are 1.24 atoms/ions, 0.84 atoms/ions, and 1.7 atoms/ions, respectively. The sputter yield of Al(111) is nearly twice that of the Al(110). The experimental result of IBS of polycrystalline aluminum is shown in Figure 6. The experiment is conducted on a ϕ100 mm planar aluminum surface. The surface is polished to roughness of 2 nmRa with no particular micro morphology. The processing parameters in Table 1 are used. The incident angle is 90°. When the processing time is short, the sputtering

yield difference of different crystal surfaces will cause the obvious relief structure. The size of relief structure is similar to aluminum grains, which also verifies our analysis. Compared with Monte Carlo simulations, MD simulations are closer to the experiments, and are more comprehensive and accurate.

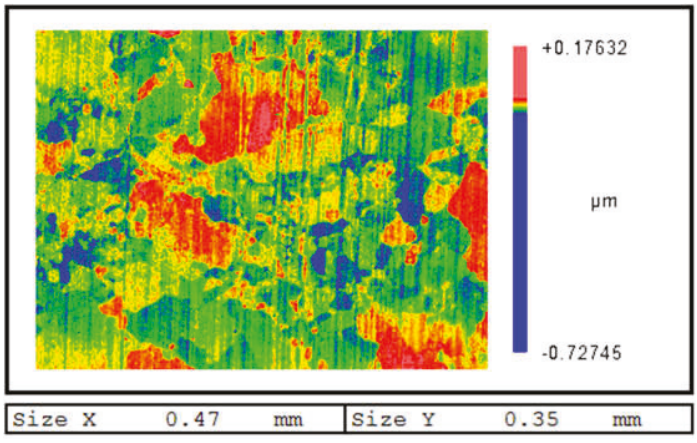

Figure 6. Surface morphology of aluminum with short time IBS.

3.3. Surface Morphology and Roughness Evolution

Due to its highest machining precision, IBS is usually used in optics fabrication as the final process. Thus, the surface quality and morphology evolution are important concerns during IBS. Normally speaking, the surface quality can be preserved during IBS for many non-metallic materials such as fused silica and monocrystalline silicon. However, for aluminum, the surface quality deteriorates significantly during IBS in our previous experiments. Figure 7 shows the surface morphology evolution of different crystal surfaces. For Al(001), the evolution of morphology can be divided into four stages. Firstly, as shown in Figure 7a, the Ar atoms bombardment causes obvious pits on the surface. The surface atoms are disturbed and the fluctuation appears on the surface. The atoms outside the sputtering area are also affected by the bombardment and deviate from the original position. However, the bombardment and cascade collision process will end after few ps. Thus, the form of the morphology varies, as shown in Figure 7b. The atoms in the sputtering area are disturbed and an embossment is formed. Meanwhile, most of the atoms outside the sputtering area present a tendency to restore to the original state, which leads to the surface of an unbombarded area to flatten out. Then, with increasing relaxation time, the atoms diffusion dominates the evolution of surface morphology. The atoms outside the sputtering area are subject to secondary perturbation. The height of the embossment decreases with the diffusion and specific morphology emerging gradually. Finally, with long-time relaxation, the surface morphology with local gravel structures is formed and stabilized. As for the crystal surfaces of Al(110) and Al(111), the evolution of morphology can also be expressed by the same four stages. However, at the same stage, there is difference for different crystal surfaces. For Al(110), the atoms outside the sputtering area do not restore after disturbance, which highly affects the subsequent atoms diffusion. Thus, the surface morphology of Al(110) shows no obvious specific structure after stabilization. For Al(111), the atoms outside the sputtering area are barely affected by the bombardment and diffusion. By comparison, the stabilized morphology of Al(111) has the most obvious morphological features. With the processing time increasing, the crystal surface begins to coarse with the increasing bombardment atoms. The relief structure will gradually disappear and evolve into gravel structure, as shown in Figure 8. In Figure 8, the regionalization of morphology is also obvious. The number of gravels at a specific area are significantly larger than other

areas. Based on above analysis, different crystal surfaces will have a large difference on the generation of gravels, which is in good agreement with experimental results.

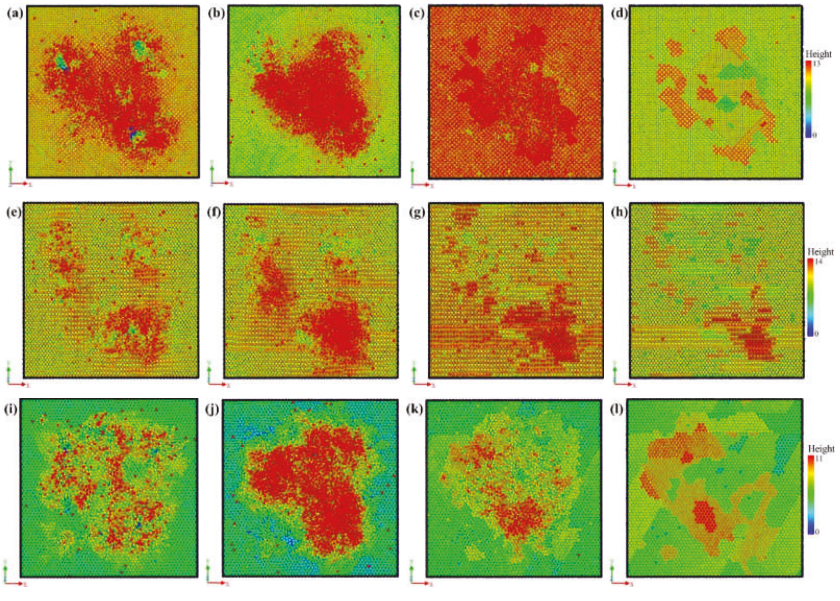

Figure 7. Surface morphology evolution of aluminum crystal surface of; Al(001) (**a**) 6 ps, (**b**) 9 ps, (**c**) 28 ps, (**d**) 100 ps; Al(110) (**e**) 6 ps, (**f**) 9 ps, (**g**) 28 ps, (**h**) 100 ps; Al(111) (**i**) 6 ps, (**j**) 9 ps, (**k**) 28 ps, (**l**) 100 ps.

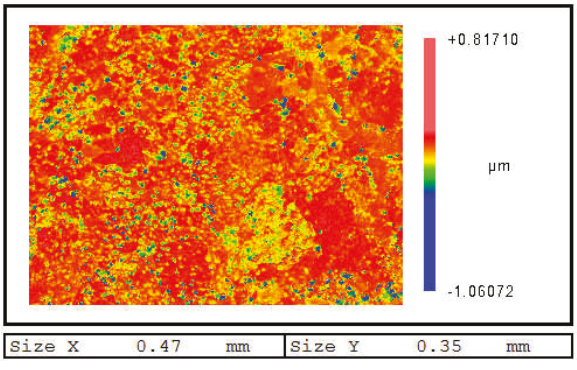

Figure 8. Surface morphology of aluminum with long time IBS.

The surface roughness is an important characteristic for optical components. The surface contour arithmetic mean deviation R_a is usually used to evaluate surface roughness, which can be expressed as follow:

$$R_a = \frac{1}{l_r}\int_0^{l_r} |y_i| dx \tag{7}$$

where y_i is the height of sampling point, and l_r is the sampling length. After stabilization of system, the surface roughness is calculated for each crystal surface, as shown in Figure 9. The Al(110) has the lowest surface roughness of 2.02 Å. Al(111) and Al(001) have the surface

roughness of 3.4 Å and 3.8 Å, respectively. For Al(110), the surface pits caused by bombardment is not obvious and the surface state is relatively uniform after surface disturbed. Thus, the final surface roughness of Al(110) is relatively better than the other two crystal surfaces. Comparing with Al(111), the atoms outside the sputtering area of Al(001) are easily disturbed and are harder to stabilize during relaxation, which will cause resistance to atom diffusion and surface roughness deterioration. Based on the above analysis, the surface-disturbed state and atom diffusion state will dominate the final surface roughness. The surface roughness of different crystal surfaces varies greatly. In actual IBS process of aluminum alloy, the surface is comprised of various crystal surfaces. Thus, the surface roughness of aluminum alloy is harder to maintain during the IBS process, which is quite consistent with the experimental results.

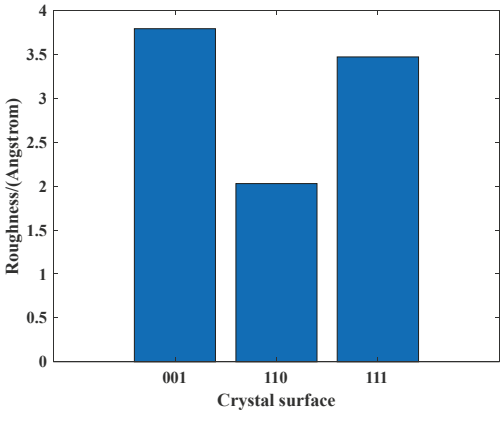

Figure 9. Roughness comparison of different crystal surfaces.

3.4. Subsurface Damage and Machining Stress Analysis

The subsurface damage and machining stress are important concerns in optics fabrication. The subsurface damage in the aluminum optics may cause the surface corrosion, which will severely destroy the surface quality. The subsurface damage evolution processes of the different crystal surfaces are displayed in Figure 10. The lattice defects are identified by the CNA method. The evolution of the subsurface damage can be roughly divided into four stages. Take Al(001) as an example, the bombarded Ar atoms firstly causes the disturbance of the subsurface. The bombardment will end quickly in less than 0.1 ps. The cascade collision of Al atoms will affect the deeper atoms, as shown in Figure 10b. Then, the stacking fault (SF) will generate with the system stabilizing. The disturbed Al atoms are reduced and the system can finally reach a stable state in Figure 10d. Comparing with Al(001), the disturbance layer of Al(110) and Al(111) are obviously deeper, which is consistent with the analysis in Section 3.3. The appearance of SFs in Al(110) and Al(111) is earlier than that of Al(001). After stabilization, the distribution of SFs in the Al(110) and the Al(111) are deeper than in the Al(001). The style of defects in the three crystal surface are consistent which is mainly SFs, but the distribution feature is quite different. For the Al(001), the SFs mainly concentrate in the bombardment area and have a shallow distribution. However, the SFs exist in a grid pattern and extend to a deeper location in the Al(110). For the Al(111), the SFs appear in the laminated structure and their amount is obviously highest.

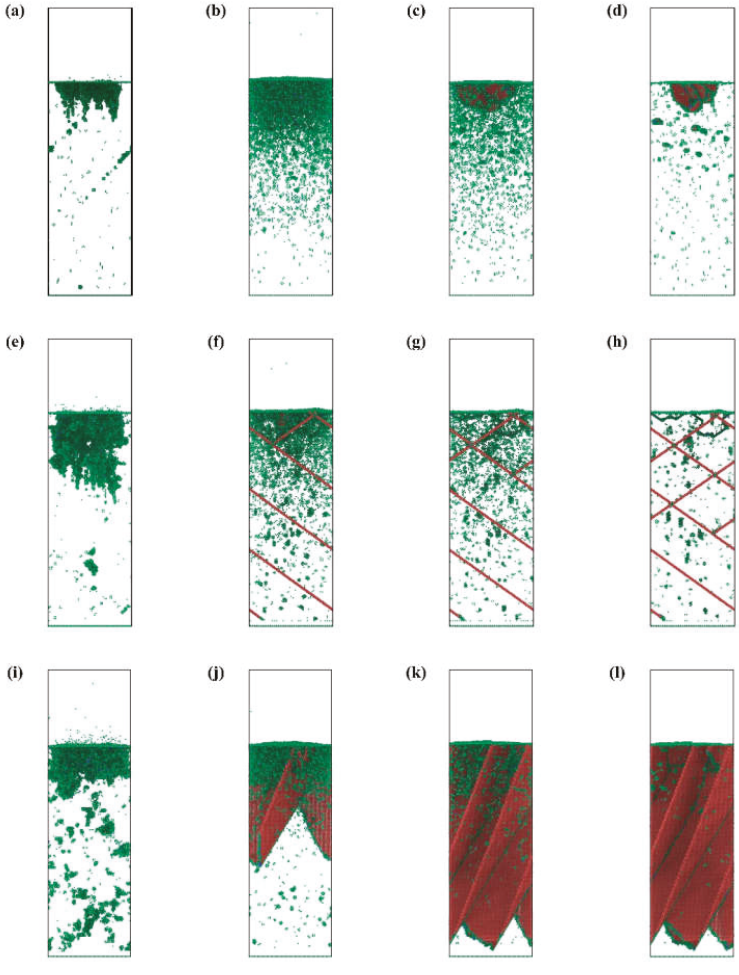

Figure 10. The evolution of subsurface damage, of Al(001) (**a**) 200 fs (**b**) 20,900 fs (**c**) 80,000 fs (**d**) 240,000 fs, of Al(110) (**e**) 200 fs (**f**) 20,900 fs (**g**) 80,000 fs (**h**) 240,000 fs, of Al(111) (**i**) 200 fs (**j**) 20,900 fs (**k**) 80,000 fs (**l**) 240,000 fs.

Figure 11 gives the evolution of dislocation length and atom number in the Al(001), Al(110), and Al(111) during total IBS machining. The IBS mainly induces the Shockley dislocation and stair-rod dislocation generated in the Al(001), Al(110), and Al(111). It can be observed from Figure 11a–c that the dislocation length firstly increases and then tends to stabilize. Comparing the stable stages in the Figure 11a–c, the Shockley dislocations are more obvious in the Al(111) than in the Al(001) and Al(110), while the stair-rod dislocations are relatively more in the Al (111). The phenomenon demonstrates that, after IBS, the density of dislocations in the Al(111) is largest, thereby bringing about significant dislocation strengthening for the Al(111).

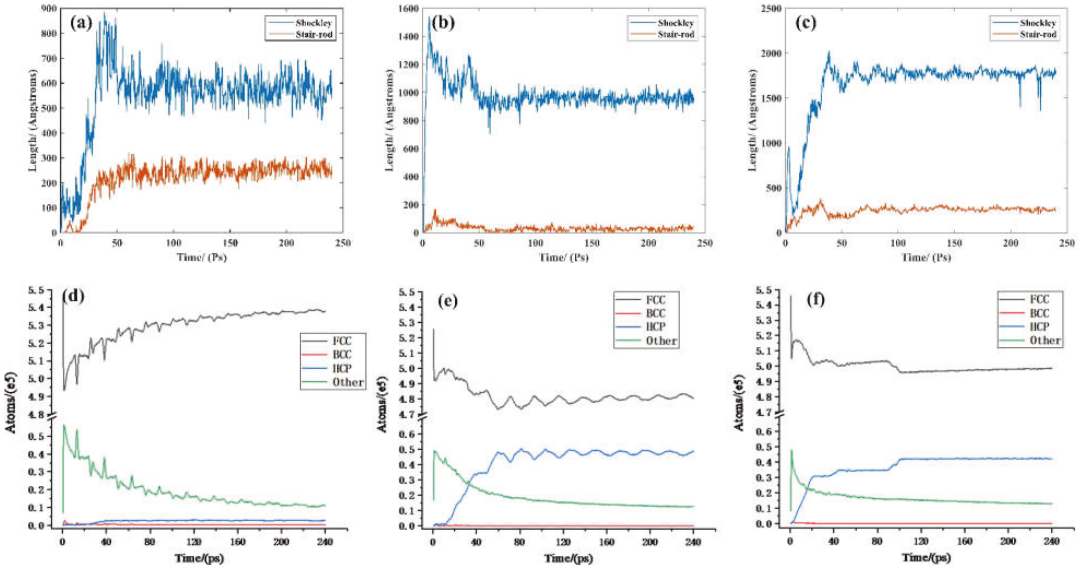

Figure 11. Dislocation statistics of, (**a**) Al(001), (**b**) Al(110), (**c**) Al(111); and atomic type statistics of, (**d**) Al(001), (**e**) Al(110), (**f**) Al(111).

In addition, it can be seen from Figure 11d–f that the number of face-centered cubic (FCC) atoms rapidly increases with the abrupt decrease in the number of other atoms, which reveals that the FCC atoms in the workpiece are mainly turned into the other atoms due to the high speed intrusion of Ar atoms. The result is consistent with the phenomena shown in Figure 10a,e,i. With the time increasing, it is observed that the number of other atoms decreases gradually when that of hexagonal closepacked structure (HCP) atoms increases, indicating that the other atoms are further translated into the HCP atoms. As a result, the numbers of FCC, Other and HCP atoms obtain certain values. The number of HCP atoms is highest in the Al(111), which is consistent with the results in Figure 10.

The above phenomena indicate that the crystal orientation of a machined surface exert an apparent influence on the subsurface damage. For the three surfaces of Al(001), Al(110), and Al(111), the subsurface damage of Al(111) is severest, because the numerous SFs are generated and distributed in the deepest part of the workpiece.

Figure 12a–c show the stress distribution of the three crystal surface after IBS. There is no significant concentration of stress after IBS. In addition, Figure 12d–f display the cross section of stress distribution in the Al(001), Al(110), and Al(111) after IBS. Similarly, hardly any stress concentration is introduced to the workpiece by the IBS machining. The phenomenon demonstrates that the Ar ion beam bombardment causes no additional stress in the workpiece. In addition, it can also be used to release stress caused by other processing methods. Therefore, the IBS is believed to be stress-free machining in the optical fabrication field. The simulation results are quite consistent with the experimental results [17].

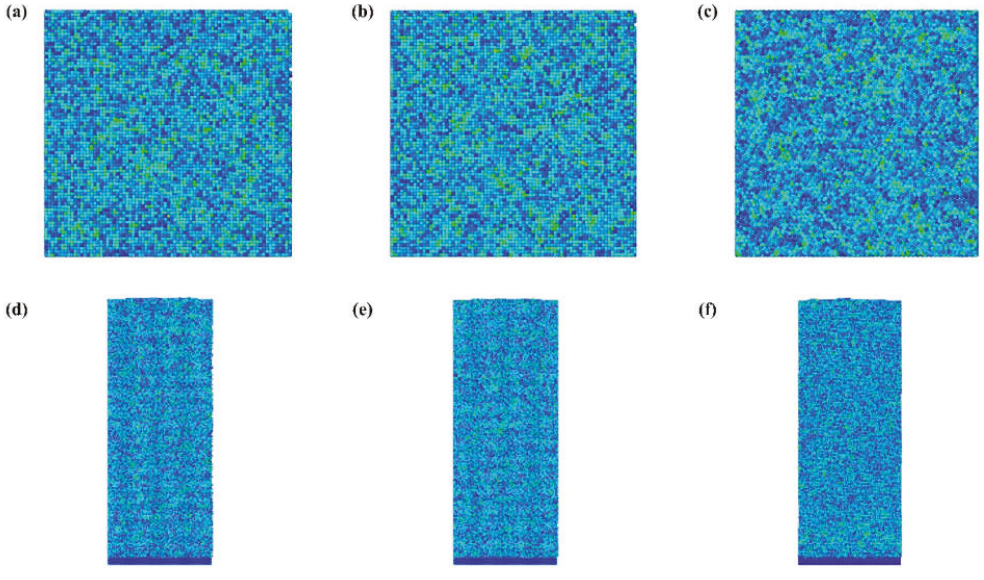

Figure 12. The stress distribution after relaxation, of Al(001) (**a**)surface (**d**) cross section, of Al(110) (**b**) surface (**e**) cross section, of Al(111) (**c**) surface (**f**) cross section.

4. Conclusions

In this paper, the MD simulation of IBS process of aluminum with different crystal orientation is studied. Influences of different crystallographic orientations on IBS process and manufactured results are revealed.

Firstly, the ion beam sputtering mechanism is exposed. Two states of Ar atoms (implantation and bounce) are observed. The implantation of Ar atoms causes massive disturbance of the shallow Al atoms, which leads to primary sputtering effect. The shallow Al atoms will cause cascade collision and lead to secondary sputtering effect. The simulation results are consistent with the traditional sputtering theory, which verify the validity of the MD simulation.

Secondly, the sputter yield, morphology evolution, and surface roughness are revealed by simulation results. Three crystal surfaces show great variety. The sputter yield of Al(111) is nearly twice that of Al(110). When the processing time of IBS is short, the varied sputter yield of different crystal surfaces will cause the emergence of the relief structure. With increased bombard time, the gravel structure of single crystal surface will dominate the morphology evolution. The state of atom diffusion (during the bombardment and during the relaxation) determines the final morphology and roughness of specific crystal surfaces. With easier atom diffusion, Al(110) has the lowest roughness. However, with poor atom diffusion during the bombardment and large disturbance during relaxation, the roughness of Al(001) is nearly twice that of Al(110).

Finally, the subsurface damage and machining stress are analyzed. The main defects for different crystal surfaces are identical, which are stacking fault, Shockley dislocation, and stair-rod dislocation. However, the form and distribution show great difference. For Al(001), the defects generate on the bombardment area and have a shallow distribution. The defects are in a grid pattern and extend to a deeper location in Al(110). For Al(111), the defects have a laminated structure and have the highest amount. IBS is believed to be stress-free machining in the optical fabrication field. There are no significantly concentrations of stress after IBS for all three crystal surfaces, which is consistent with the experimental results.

The process of IBS and mechanism of morphology evolution of aluminum are revealed. The regularity and mechanism will lay a foundation for the application of IBS in aluminum optics manufacture fields.

Author Contributions: Conceptualization and investigation, C.D. and Y.D.; Modeling and debugging, C.D. and H.H.; Formal analysis and experiments, C.G. and C.D.; Manuscript writing, C.D.; Manuscript review and revision, Y.D. All authors have read and agreed to the published version of the manuscript.

Funding: This study was funded by Major Programs of the National Natural Science Foundation of China (Grant No. 51991371) and the Postgraduate Scientific Innovation Fund of Hunan Province.

Conflicts of Interest: The authors declare no conflict of interest.

References

1. Wang, Y.; Li, Z.; Liu, X.; Fang, F.Z. Freeform-objective Chernin multipass cell: Application of a freeform surface on assembly simplification. *Appl. Opt.* **2017**, *56*, 8541–8546. [CrossRef]
2. Li, Z.; Liu, X.; Fang, F.; Zhang, X. Integrated manufacture of a freeform off-axis multi-reflective imaging system without optical alignment. *Opt. Express* **2018**, *26*, 7625–7637. [CrossRef]
3. Wamboldt, L.; Roy, B.; Crifasi, J.; Stephens, S.; Hanninen, D.; Woodard, K.; Felock, R.; Polczwartek, S.; Parenteau, J. An ultra-low surface finish process for 6061-Al mirrors. *Proc. SPIE* **2015**, *9451*, 94511X1–94511X9.
4. Ahn, Y.; Yoon, J.Y.; Baek, C.W.; Kim, Y.K. Chemical mechanical polishing by colloidal silica-based slurry for micro-scratch reduction. *Wear* **2004**, *257*, 785–789. [CrossRef]
5. Harvey, J.E. Parametric analysis of the effect of scattered light upon the modulation transfer function. *Opt. Eng.* **2013**, *52*, 073110. [CrossRef]
6. Dumas, P.; Golini, D.; Tricard, M. Improvement of figure and finish of diamond turned surfaces with magneto-rheological finishing. *Proc. SPIE* **2005**, *5786*, 296–304.
7. Wang, Y.L.; Wu, J.; Liu, C.W.; Wang, T.C.; Dun, J.W. Material characteristics and chemical-mechanical polishing of aluminum alloy thin films. *Thin Solid Film.* **1998**, *332*, 397–403. [CrossRef]
8. Drueding, T.W.; Bifano, T.G.; Fawcett, S.C. Contouring algorithm for ion figuring. *Precis. Eng.* **1995**, *17*, 10–21. [CrossRef]
9. Weiser, M. Ion beam figuring for lithography optics. *Nucl. Instrum. Methods Phys. Res. Sect. B* **2009**, *267*, 1390–1393. [CrossRef]
10. Yuan, Z.; Dai, Y.F.; Zhou, L.; Feng, S.R. Cleaning of iron powders embedded into the surface of KDP crystal by ion beam figuring. *J. Synth. Cryst.* **2013**, *42*, 582–586.
11. Dai, Y.F.; Liao, W.L.; Zhou, L.; Chen, S.S.; Xie, X.X. Ion beam figuring of high-slope surfaces based on figure error compensation algorithm. *Appl. Opt.* **2010**, *49*, 6630–6636. [CrossRef]
12. Bradley, R.M.; Harper, J.M.E. Theory of ripple topography induced by ion bombardment. *J. Vac. Sci. Technol. A* **1998**, *6*, 2390–2395. [CrossRef]
13. Keller, A.; Facsko, S.; Moller, W. Evolution of ion-induced ripple patterns on SiO2 surfaces. *Nucl. Instrum. Meth. B* **2009**, *267*, 656–659. [CrossRef]
14. Xu, M.J.; Dai, Y.F.; Zhou, L.; Peng, X.Q.; Chen, S.S.; Liao, W.L. Evolution mechanism of surface roughness during ion beam sputtering of fused silica. *Appl. Opt.* **2018**, *57*, 5566–5573. [CrossRef] [PubMed]
15. Chkhalo, N.I.; Churin, S.A.; Mikhaylenko, M.S.; Pestov, A.E.; Polkovnikov, V.N.; Salashchenko, N.N.; Zorina, M.V. Ion-beam polishing of fused silica substrates for imaging soft x-ray and extreme ultraviolet optics. *Appl. Opt.* **2016**, *55*, 1249–1256. [CrossRef]
16. Egert, C.M. Roughness evolution of optical materials induced by ion beam milling. *Proc. SPIE* **1992**, *1752*, 63–72.
17. Du, C.Y.; Dai, Y.F.; Hu, H.; Guan, C.L. Surface Roughness Evolution Mechanism of Optical Aluminum 6061 Alloy during Low Energy Ar+ Ion Beam Sputtering. *Opt. Express* **2020**, *28*, 34054–34068. [CrossRef] [PubMed]
18. Papanikolaou, M.; Salonitis, K. Fractal roughness effects on nanoscale grinding. *Appl. Surf. Sci.* **2019**, *467*, 309–319. [CrossRef]
19. Liu, B.; Xu, Z.; Wang, Y.; Gao, X.; Kong, R. Effect of ion implantation on material removal mechanism of 6H-SiC in nano-cutting: A molecular dynamics study. *Comp. Mater. Sci.* **2020**, *174*, 109476. [CrossRef]
20. Chavoshi, S.Z.; Xu, S.; Luo, X. Dislocation-mediated plasticity in silicon during nanometric cutting: A molecular dynamics simulation study. *Mat. Sci. Semicon. Proc.* **2016**, *519*, 60–70. [CrossRef]
21. Wang, J.S.; Zhang, X.D.; Fang, F.Z.; Chen, R.T. Diamond cutting of micro-structure array on brittle material assisted by multi-ion implantation. *Int. J. Mach. Tool. Manuf.* **2019**, *137*, 58–66. [CrossRef]
22. Xiao, Y.J.; Fang, F.Z.; Xu, Z.W.; Hu, X.T. Annealing recovery of nanoscale silicon surface damage caused by Ga focused ion beam. *Appl. Surf. Sci.* **2015**, *343*, 56–69. [CrossRef]
23. Xiao, H.; Dai, Y.F.; Duan, J.; Tian, Y.; Li, J. Material removal and surface evolution of single crystal silicon during ion beam polishing. *Appl. Surf. Sci.* **2021**, *544*, 148954. [CrossRef]
24. Turowski, M.; Jupé, M.; Melzig, T.; Pflug, A.; Ristau, D. Multiple scale modeling of Al2O3 thin film growth in an ion beam sputtering process. *Proc. SPIE* **2015**, *27*, 96271M.

25. Tetsuya, O.; Kiyoshi, M.; Kenya, O. Molecular dynamics simulation of non-equilibrium low energy (1–100 eV) ion beam deposition processes. *Nucl. Instrum. Meth. B* **1994**, *91*, 593–596. [CrossRef]
26. Mäkinen, J.; Vehanen, A.; Hautojärvi, P.; Huomo, H.; Nieminen, R.M.; Valkealahti, S. Vacancy-type defect distributions near argon sputtered Al(110) surface studied by variable-energy positrons and molecular dynamics simulations. *Surf. Sci.* **1986**, *175*, 385–414. [CrossRef]
27. Pogorelko, V.V.; Krasnikov, V.S.; Mayer, A.E. High-speed collision of copper nanoparticles with aluminum surface: Inclined impact, interaction with roughness and multiple impact. *Comp. Mater. Sci.* **2018**, *142*, 108–121. [CrossRef]
28. Pogorelko, V.V.; Mayer, A.E.; Krasnikov, V.S. High-speed collision of copper nanoparticle with aluminum surface: Molecular dynamics simulation. *Appl. Surf. Sci.* **2016**, *390*, 289–302. [CrossRef]
29. Gen, I.; Rei, K.; Kimiya, K.; Hiroyuki, K. Incident angle dependence of reflected particles in low-energy xenon-ion impacts on metal surfaces. *Comp. Mater. Sci.* **2021**, *186*, 109989.
30. Zhu, P.; Li, R. Study of nanoscale friction behaviors of graphene on gold substrates using molecular dynamics. *Nano Res. Lett.* **2018**, *13*, 1–8. [CrossRef]
31. Liu, L.; Xu, Z.; Tian, D.; Hartmaier, A.; Luo, X.; Zhang, J.; Fang, F. MD simulation of stress-assisted nanometric cutting mechanism of 3C silicon carbide. *Ind. Lubr. Tribol.* **2019**, *71*, 686–691. [CrossRef]
32. Li, B.; Li, J.; Zhu, P.; Xu, J.; Li, R.; Yu, J. Influence of crystal anisotropy on deformation behaviors in nanoscratching of AlN. *Appl. Surf. Sci.* **2019**, *487*, 1068–1076. [CrossRef]
33. Tian, Y.Y.; Fang, Q.H.; Li, J. Molecular dynamics simulations for nanoindentation response of nanotwinned FeNiCrCoCu high entropy alloy. *Nanotechnology* **2020**, *31*, 465701. [CrossRef]
34. Goel, S.; Luo, X.; Agrawal, A.; Reuben, R.L. Diamond machining of silicon: A review of advances in molecular dynamics simulation. *Int. J. Mach. Tools Manuf.* **2015**, *88*, 131–164. [CrossRef]
35. Liu, L.; Xu, Z.W.; Li, R.R.; Zhu, R.; Xu, J.; Zhao, J.L.; Wang, C.; Nordlund, K.; Fu, X.; Fang, F.Z. Molecular dynamics simulation of helium ion implantation into silicon and its migration. *Nucl. Instrum. Methods Phys. Res. Sect. B.* **2019**, *456*, 53–59. [CrossRef]
36. Tian, Y.Y.; Feng, H.; Li, J.; Fang, Q.H.; Zhang, L.C. Nanoscale sliding friction behavior on Cu/Ag bilayers influenced by water film. *Appl. Surf. Sci.* **2021**, *545*, 148957. [CrossRef]
37. Korsunsky, A.M.; Guenole, J.; Salvati, E.; Sui, T.; Mousavi, M.; Prakash, A. Quantifying eigenstrain distributions induced by focused ion beam damage in silicon. *Mater. Lett.* **2016**, *185*, 47–49. [CrossRef]
38. Sheng, H.W.; Kramer, M.J.; Cadien, A.; Fujita, T.; Chen, M.W. Highly optimized embedded-atom-method potentials for fourteen fcc metals. *Phys. Rev. B* **2011**, *83*, 134118. [CrossRef]
39. Wu, H.; Zhang, N.; He, M.; Shih, C.Y.; Zhu, X.N. Calculation of Argon-Aluminum Interatomic Potential and its application in molecular dynamics simulation of femtosecond laser ablation. *Chin. J. Las.* **2016**, *43*, 0802004.

micromachines

MDPI

Article

A New Method for Precision Measurement of Wall-Thickness of Thin-Walled Spherical Shell Parts

Jiang Guo [1], Yongbo Xu [1], Bo Pan [1], Juntao Zhang [1], Renke Kang [1], Wen Huang [2] and Dongxing Du [2,*]

[1] Key Laboratory for Precision and Non-Traditional Machining Technology of Ministry of Education, Dalian University of Technology, Dalian 116024, China; guojiang@dlut.edu.cn (J.G.); xuyongbo130@163.com (Y.X.); panbo723@mail.dlut.edu.cn (B.P.); 15207144627@163.com (J.Z.); kangrk@dlut.edu.cn (R.K.)

[2] Institute of Mechanical Manufacturing Technology, China Academy of Engineering Physics, Mianyang 621999, China; huangw0673@yinhe596.cn

* Correspondence: ddx4142@126.com

Abstract: Thin-walled parts are widely used in shock wave and detonation physics experiments, which require high surface accuracy and equal thickness. In order to obtain the wall thickness of thin-walled spherical shell parts accurately, a new measurement method is proposed. The trajectories, including meridian and concentric trajectories, are employed to measure the thickness of thin-walled spherical shell parts. The measurement data of the inner and outer surfaces are unified in the same coordinate system, and the thickness is obtained based on a reconstruction model. The meridian and concentric circles' trajectories are used for measuring a spherical shell with an outer diameter of Φ210.6 mm and an inner diameter of Φ206.4 mm. Without the data in the top area, the surface errors of the outer and inner surfaces are about 5 μm and 6 μm, respectively, and the wall-thickness error is about 8 μm with the meridian trajectory.

Keywords: spherical shell; thin-walled part; wall-thickness; benchmark coincidence; data processing

Citation: Guo, J.; Xu, Y.; Pan, B.; Zhang, J.; Kang, R.; Huang, W.; Du, D. A New Method for Precision Measurement of Wall-Thickness of Thin-Walled Spherical Shell Parts. *Micromachines* **2021**, *12*, 467. https://doi.org/10.3390/mi12050467

Academic Editor: Kai Cheng

Received: 30 March 2021
Accepted: 18 April 2021
Published: 21 April 2021

1. Introduction

Thin-walled parts are widely used in aerospace equipment, such as rocket tank panels, rocket nozzles and aircraft skins [1,2]. Spherical thin-walled parts have typical geometric shapes, and the mathematical description of their deformation and failure is easy to express. In terms of physical design, spherical thin-walled parts take advantage of "high energy efficiency and low energy consumption", and the spherical thin-walled parts are often used in shock wave physics, and are used to develop the mechanism of various physical, chemical and mechanical phenomena [3]. For example, spherical thin-walled parts are mostly used in the design of explosive physics experiment parts, where structures gather energy easily. By studying the deformation and destruction of the parts before and after the experiment, the important parameters that characterize the implosion process of the weapon are obtained. In order to improve the accuracy and reliability of important scientific experimental data of shock wave physics and detonation physics, the surface shape accuracy and wall-thickness uniformity of thin-walled parts of the spherical shell put forward extremely high requirements [3,4]. The machining of thin-walled freeform components has many challenges in terms of the geometrical complexity, high-requirement accuracy, and especially low rigidity [5]. The thin-walled parts have low rigidity and are difficult to clamp, and therefore it is hard to measure the thickness. For the wall-thickness measurement of curved parts, the main problem is that the wall-thickness information of the part needs to be obtained in the normal direction of a certain point.

At present, researchers have explored the wall-thickness measurement. The methods of measuring wall-thickness are divided into two kinds: direct measurement method and indirect measurement method. The main principle of the direct measurement method is to directly measure the distance between the inner and outer walls in the normal direction of

the corresponding point as the point's wall-thickness. Cao et al. [6] proposed a dual-probe contact sensor measurement scheme. By constructing a theoretical curve, the articulation center is established to always move along the motion curve, so that the connection between the fixed contact and the sensor probe is always in the normal direction of the inner wall to obtain the wall-thickness value of the workpiece.

Wei et al. [7] proposed a method to measure the wall-thickness of seamless steel pipes in the normal direction using resistance strain sensors. Zhang et al. [8] used a photoelectric sensor probe to obtain wall-thickness information by ensuring that the line of the measuring clamp between the contact point on the inner wall and the contact point on the outer wall is always in the normal direction of the measured point. Guo et al. [9] developed a special geometric parameter measuring instrument based on the photoelectric micro-displacement sensor, which can directly measure the normal geometric thickness of thin-walled parts with deep holes. Lyssakow et al. [10] used two laser sensors to successfully obtain the geometric defects and thickness defects of the cylindrical structure. Jin et al. [11] proposed a tubing wall-thickness measurement method based on a measurement sensor and designed an online tubing wall-thickness measurement system with a wall-thickness measurement accuracy of ± 0.05 mm. The indirect measurement method is mainly based on the principle of eddy current measurement and ultrasonic measurement, and the wall-thickness information is calculated by the indirect quantity related to the wall-thickness. Generally, the use of eddy current to measure the wall-thickness of a part is to obtain the thickness information by extracting the peak value and peak time in the pulse eddy current response. Fan et al. [12] proposed the spectral pulse eddy current response of Hall sensors to obtain wall-thickness information. Mao et al. [13] proposed a method of using eddy currents to estimate the thickness of the pipeline, mainly by placing the excitation electromagnetic coil outside the pipeline to be tested, determining the relationship between the relative capacitance of the excitation coil and the pipe wall-thickness, and estimating the wall-thickness. Nishino et al. [14] proposed a method of measuring tube wall-thickness using ring wave resonance generated by a piezoelectric ring sensor, and verified through experiments that the wall-thickness error obtained by this method is less than 1.5%. Li et al. [15] proposed a pulse eddy current signal processing thickness measurement method for metal parts based on the Laplace wavelet characteristic frequency, and used 304 stainless steel specimens with a wall-thickness of 12 mm to 30 mm for experimental verification. The error of wall-thickness measurement results within the range of 0 mm to 120 mm in height is within 8%. Ultrasonic pulse echo technology is widely used in thickness measurement. Wu et al. [16] used the principle of ultrasonic reflection to measure the thickness of the pipeline by calculating the difference in the arrival time of the echo signal according to the arrival time of the echo signal. Jaime et al. [17] proposed a method where two orthogonally polarized shear waves were excited in the metal material by two mutually orthogonal coils, and the material thickness and crack defects were measured simultaneously in the pulse echo mode. Durongsak et al. [18] used the gamma rays obtain the wall-thickness information of the carbon steel pipe according to the energy change of the reflected ray. Levesque et al. [19] made the ultrasonic wave emit perpendicular to the surface. After the ultrasonic wave was reflected by the inner wall of the pipe, the wall-thickness of the pipe was obtained by detecting the wave caused by the reflected ultrasonic wave on the outer surface. Liu et al. [20] designed an ultrasonic scanning device to measure the thickness of large aerospace thin-walled parts, and used large aerospace aluminum alloy grid plates to verify the practicability of the device. In order to evaluate the measurement uncertainty of ultrasonic wall-thickness measurement, Morana et al. [21] used the Monte Carlo simulation method to establish a mathematical model for the estimation of ultrasonic measurement thickness uncertainty. In order to reduce the influence of the measurement environment on ultrasonic measurement, Adamowski et al. [22] proposed a temperature correction strategy for an ultrasonic measurement system, which can obtain the loss of micron wall-thickness due to internal corrosion of the pipeline, and monitor the corrosion of the pipeline for a long time. Rees et al. [23] obtained the thickness information of the glass furnace by measuring

the microwave signal round-trip path, and improved the stability of the measurement by enhancing the echo signal at the receiving end.

The direct method is widely used to measure the wall-thickness, but the process is cumbersome and takes a long time. During the measurement, the connection between the inner and the outer wall contact point must always be in the normal direction of the measured point, which makes achieving a high-precision measurement difficult. The eddy current method to measure the wall-thickness needs a large amount of calculation and complex equipment. The measurement environment and the strength of the ultrasonic echo signal have a greater impact on the measurement result, and the cost of the ultrasonic device is relatively high. For spherical shell parts with micron-level precision, the above method is not suitable for the wall-thickness detection of spherical shell parts.

This paper proposes a method for measuring the wall-thickness of thin-walled spherical shell parts. The method is based on the three-coordinate measuring machine (CMM) with sub-micron measurement accuracy to obtain measurement data points. The measurement trajectory is planned for thin-walled spherical shell parts. By establishing a measurement reference coincidence model under the spatial coordinate system, the data on the inner and outer surfaces are unified to the same coordinate system. Based on the reconstruction model method of spherical shell parts, the wall-thickness information is obtained.

2. Methodology

2.1. The Method of Measuring Wall-Thickness

The thin-walled spherical shell parts are shown in Figure 1. During the measurement, the workpiece experiences the overturn process, which will cause the inner and outer surfaces to have different axes. Furthermore, it will induce an error in the wall-thickness. Thus, to obtain the wall-thickness accurately, the rotation and movement along the x-axis, y-axis, and z-axis between the two positions shown in Figure 2 should be modified. Therefore, a new method for measuring the wall-thickness of thin-walled spherical shell parts is proposed. In the process of measuring the inner and outer surfaces of the spherical shell, the flange circumference is employed as the measurement benchmark. The model for the measurement benchmark coincidence in one spatial coordinate system is established. The reconstruction model of the spherical shell part is built based on the benchmark, and the wall-thickness is obtained. The measurement process is shown in Figure 3.

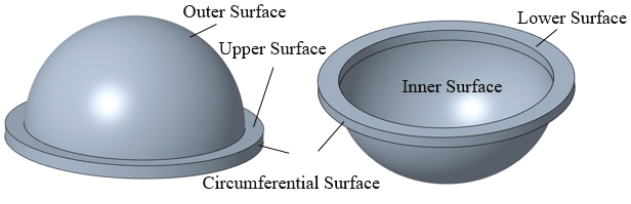

Figure 1. The spherical shell part.

2.2. Measurement Trajectory

During the measurements, the spherical shell parts are placed on the measuring platform. The data on spherical shell parts and the points (x_{wc}, y_{wc}, z_{wc}) on the flange circumference are obtained based on a precision coordinate measuring machine. As shown in Figure 4, the trajectory includes a circular trajectories, and the equation of the n_{wc}-th circular trajectory can be expressed as:

$$\begin{cases} x^2 + y^2 = {R_1}^2 \\ z = h_1 + (n_{wc} - 1) * h_2 \end{cases}, 0 \le z \le h \quad (1)$$

where R_1 is the radius of the flange circumference, h_1 is the distance between the lower end of the flange and the first circular track, h_2 is the distance between each circular track, and h is the distance between the upper end of the flange and the lower end of the flange distance.

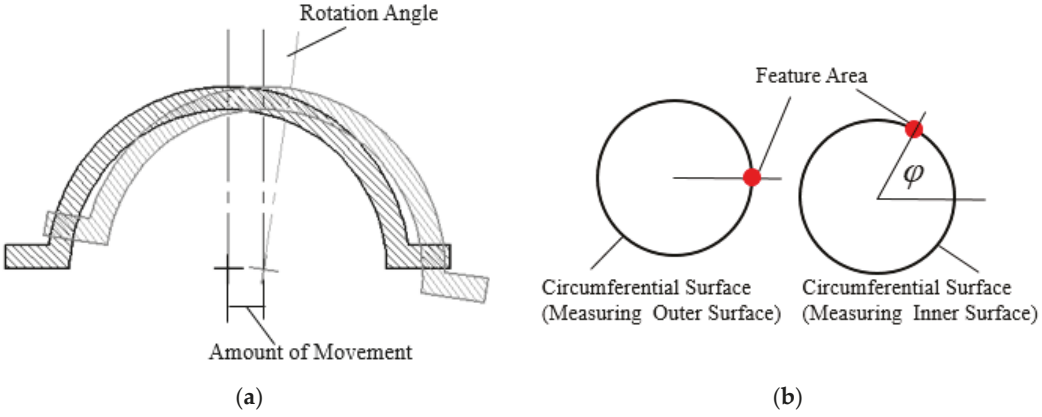

Figure 2. The schematic: (**a**) the amount of rotation and movement; (**b**) the rotation angle.

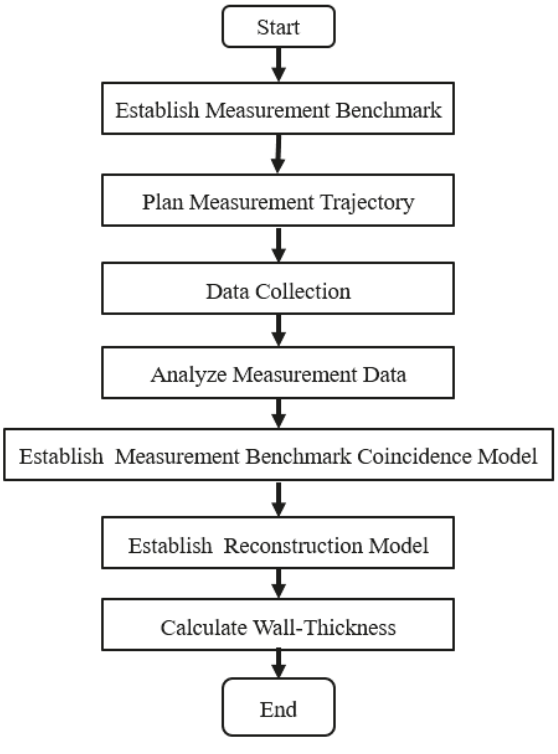

Figure 3. The measurement process.

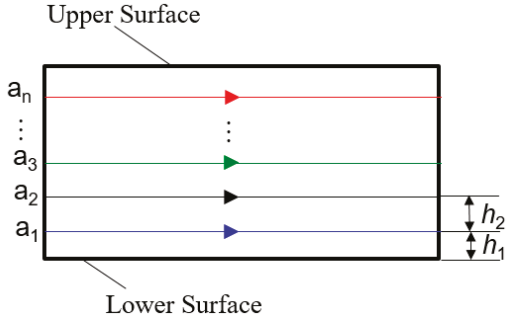

Figure 4. The circular measurement trajectory.

The meridian trajectory and concentric trajectory are shown in Figures 5 and 6, respectively. The data points on the outer surface are (x_{ww1}, y_{ww1}, z_{ww1}) and (x_{wt1}, y_{wt1}, z_{wt1}); the equation of the n_{ww1} ($\leq b$)-th meridian measurement track is:

$$\begin{cases} x^2 + y^2 + z^2 = {R_2}^2 \\ y = x * \tan\left[\frac{2\pi(n_{ww1}-1)}{b}\right] \end{cases}, 0 \leq x^2 + y^2 \leq {R_3}^2 \quad (2)$$

Figure 5. The meridian trajectory.

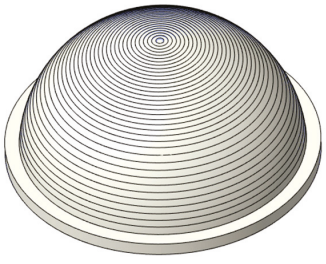

Figure 6. The concentric trajectory.

The n_{wt1} ($\leq c$)-th concentric circle measurement trajectory equation is:

$$\begin{cases} x^2 + y^2 + z^2 = {R_2}^2 \\ z = h_{n_{wt1}} \end{cases}, 0 \leq x^2 + y^2 \leq {R_3}^2 \quad (3)$$

where $h_{n_{wt1}}$ is the distance of the n_{wt1}-th concentric circle measuring track from the lower end of the flange, R_2 is the radius of the outer surface of the spherical shell, and R_3 is the radius of the intersection of the outer surface of the spherical shell and the upper end of the flange.

Secondly, the workpiece is turned over and placed on the measuring platform with the inner surface facing upwards. Then, the circumference of the flange is measured, of which tracks are circular trajectories, and data points (x_{nc}, y_{nc}, z_{nc})on the flange circumference are obtained.

The trajectories are d meridian trajectory and e concentric trajectories, respectively. The data points are (x_{nw1}, y_{nw1}, z_{nw1}) and (x_{nt1}, y_{nt1}, z_{nt1}); the equation of the n_{nw1} ($\leq d$)-th meridian measurement track in the workpiece coordinate system is:

$$\begin{cases} x^2 + y^2 + z^2 = {R_4}^2 \\ y = x * \tan\left[\frac{2\pi(n_{nw1}-1)}{d}\right] \end{cases}, 0 \leq x^2 + y^2 \leq {R_4}^2 \tag{4}$$

Among them, the equation of the n_{nt1} ($\leq e$)-th concentric circle measuring track is:

$$\begin{cases} x^2 + y^2 + z^2 = {R_4}^2 \\ z = h_{n_{nt1}} \end{cases}, 0 \leq x^2 + y^2 \leq {R_4}^2 \tag{5}$$

where $h_{n_{nt1}}$ is the distance of the n_{nw1}-th concentric circle measurement track from the lower end of the flange, and R_4 is the radius of the inner surface of the spherical shell.

Before obtaining the surface shape distribution, the measurement data of the inner and outer surfaces of the spherical shell need to be preprocessed. The preprocessing includes removing the singular items in the data and smoothing. The data points obtained after preprocessing are (x_{ww2}, y_{ww2}, z_{ww2}), (x_{nw2},y_{nw2},z_{nw2}), (x_{wt2}, y_{wt2}, z_{wt2}) and (x_{nt2}, y_{nt2}, z_{nt2}). According to the data points after preprocessing, the sphere center of the outer surface of the meridian spherical shell is recorded as (x_{ww}, y_{ww}, z_{ww}), the sphere radius is R_{ww}, the center of the sphere on the inner surface of the meridian spherical shell is recorded as (x_{nw}, y_{nw}, z_{nw}), and the sphere radius is R_{nw}. The center of the sphere on the outer surface of the concentric spherical shell is recorded as (x_{wt}, y_{wt}, z_{wt}), the radius of the sphere is R_{wt}, the center of the sphere on the inner surface of the concentric spherical shell is recorded as (x_{nt}, y_{nt}, z_{nt}) and the radius of the sphere is R_{nt}. The error of the i-th data point position is on the surface. To obtain the surface error, the surface error formula is as follows:

$$\begin{cases} d_{ww}(i) = \sqrt{(x_{ww2} - x_{ww})^2 + (y_{ww2} - y_{ww})^2 + (z_{ww2} - z_{ww})^2} - R_{ww} \\ d_{nw}(i) = \sqrt{(x_{nw2} - x_{nw})^2 + (y_{nw2} - y_{nw})^2 + (z_{nw2} - z_{nw})^2} - R_{nw} \\ d_{wt}(i) = \sqrt{(x_{wt2} - x_{wt})^2 + (y_{wt2} - y_{wt})^2 + (z_{wt2} - z_{wt})^2} - R_{wt} \\ d_{nt}(i) = \sqrt{(x_{nt2} - x_{nt})^2 + (y_{nt2} - y_{nt})^2 + (z_{nt2} - z_{nt})^2} - R_{nt} \end{cases} \tag{6}$$

2.3. Measuring Benchmark Coincidence Model

In the process of obtaining data points on the inner and outer surfaces of spherical shell parts, the data points on the inner and outer surfaces are not in the same coordinate system due to the flip of the spherical shell. In order to calculate the wall-thickness information of spherical shell parts, it is necessary to make the data points in the same coordinate system.

When measuring the inner and outer surfaces, there may be rotations along the x-axis, y-axis and z-axis between the two spherical shell positions, which are α, β and θ respectively. Moreover, there is a rotation angle φ around its own axis. The movement along the x-axis and y-axis between the two spherical shell positions cannot be ignored. Since the reference in the z direction does not move during the turnover process, the movement between the x-axis and the y-axis can be acquired, which are and, respectively. In order to obtain these six parameters, it is necessary to obtain the rotation corresponding to the flange circumference data points (x_{wc}, y_{wc}, z_{wc}) when measuring the outer surface, and the flange circumference data points (x_{nc}, y_{nc}, z_{nc}) when measuring the inner surface. The new data points (x_{wc1}, y_{wc1}, z_{wc1}) and (x_{nc1}, y_{nc1}, z_{nc1}) are obtained by eliminating singularities in data points (x_{wc}, y_{wc}, z_{wc}) and (x_{nc}, y_{nc}, z_{nc}). The movement amounts m, n are obtained by processing the data. The points (x_{wc1}, y_{wc1}, z_{wc1}) contain a circular trajectory and the

points of the i-th circular trajectory are (x_{wc1i},y_{wc1i}, z_{wc1i}). The circle center (x_{wci}, y_{wci}, z_{wci}) of the i-th circle track is obtained by fitting. The same method is used to obtain the circle center (x_{nc1}, y_{nc1}, z_{nc1}). The horizontal and vertical coordinates of the flange axis for the first and second times are m_1, n_1, m_2 and n_2, respectively, which can be expressed as:

$$\begin{cases} m_1 = \frac{1}{a} * \sum_{i=1}^{a} x_{\mathrm{wc}}(i) \\ n_1 = \frac{1}{a} * \sum_{i=1}^{a} y_{\mathrm{wc}}(i) \\ m_2 = \frac{1}{a} * \sum_{i=1}^{a} x_{\mathrm{nc}}(i) \\ n_2 = \frac{1}{a} * \sum_{i=1}^{a} y_{\mathrm{nc}}(i) \end{cases} \tag{7}$$

where $h_{n_{\mathrm{nt1}}}$ is the distance of the n_{nw1}-th concentric circle measurement track from the lower end of the flange, and R_4 is the radius of the inner surface of the spherical shell.

The amount of movement between x-axis and y-axis can be expressed as:

$$\begin{cases} m = m_1 - m_2 \\ n = n_1 - n_2 \end{cases} \tag{8}$$

The direct method is used to obtain the rotation angles α, β and θ. The direct method refers to matching the pre-processed flange data points (x_{wc1i}, y_{wc1i}, z_{wc1i}) and (x_{nc1i}, y_{nc1i}, z_{nc1i}) without fitting. The ranges of α, β are $[\alpha_1, \alpha_2]$, $[\beta_1, \beta_2]$, respectively. Take a points in the $[\alpha_1, \alpha_2]$ range, and the i point is α_i; in the $[\beta_1, \beta_2]$ range, take b points, and the j point is β_j. Take α_i and β_j as a set of data and record them as (α_i, β_j) and $a * b$ can be taken in total group data, where:

$$\begin{cases} \alpha_i = \alpha_1 + \frac{1}{\alpha} * (i-1) * (\alpha_2 - \alpha_1) \\ \beta_i = \beta_1 + \frac{1}{\beta} * (j-1) * (\beta_2 - \beta_1) \end{cases} \tag{9}$$

The flange data points (x_{nc3i}, y_{nc3i}, z_{nc3i}) are obtained by coordinate conversion. The formula is as follows:

$$\begin{bmatrix} x_{\mathrm{nc2i}} \\ y_{\mathrm{nc2i}} \\ z_{\mathrm{nc2i}} \end{bmatrix} = \begin{pmatrix} 1 & 0 & 0 \\ 0 & \cos\alpha_i & \sin\alpha_i \\ 0 & \sin\alpha_i & \cos\alpha_i \end{pmatrix} \begin{bmatrix} x_{\mathrm{nc1i}} \\ y_{\mathrm{nc1i}} \\ z_{\mathrm{nc1i}} \end{bmatrix} \tag{10}$$

$$\begin{bmatrix} x_{\mathrm{nc3i}} \\ y_{\mathrm{nc3i}} \\ z_{\mathrm{nc3i}} \end{bmatrix} = \begin{pmatrix} \cos\beta_j & 0 & -\sin\beta_j \\ 0 & 1 & 0 \\ \sin\beta_j & 0 & \cos\beta_j \end{pmatrix} \begin{bmatrix} x_{\mathrm{nc2i}} \\ y_{\mathrm{nc2i}} \\ z_{\mathrm{nc2i}} \end{bmatrix} \tag{11}$$

After the rotation of α_i and β_j, the coincidence error between the corresponding points is recorded as t_{ij}. The formula is as follows:

$$t_{ij} = \sum_{i=1}^{u} \sqrt{(x_{\mathrm{wc1i}} - x_{\mathrm{nc3i}})^2 + (y_{\mathrm{wc1i}} - y_{\mathrm{nc3i}})^2 + (z_{\mathrm{wc1i}} - z_{\mathrm{nc3i}})^2} \tag{12}$$

The minimum value t_0 is obtained by comparing $t_{11}, t_{12} \ldots t_{\mathrm{ab}}$. Under this condition, the rotation angle α_i around the x axis is recorded as α, the rotation angle β_j around the y axis is recorded as β_0, and (x_{nc4i}, y_{nc4i}, z_{nc4i}) is recorded as (x_{nc5i}, y_{nc5i}, z_{nc5i}).

Data points (x_{wc1i}, y_{wc1i}, z_{wc1i}) and (x_{nc5i}, y_{nc5i}, z_{nc5i}) contain u data points. The distance d_{w} from each data point in (x_{wc1i},y_{wc1i},z_{wc1i}) to the center (x_{wci}, y_{wci}, z_{wci}) in the data is recorded as d_{w1}, d_{w2} … … d_{wu}. The distance d_{n} from each data point in (x_{nc5i}, y_{nc5i}, z_{nc5i}) to the center (x_{nci}, y_{nci}, z_{nci}) in the data is recorded in turn as $d_{\mathrm{n1}}, d_{\mathrm{n2}} \ldots d_{\mathrm{nu}}$. To calculate the arithmetic sum of squares of the errors in different correspondences, the formula is as follows:

$$\begin{cases} \Delta_1 &= (d_{w1} - d_{n1})^2 + (d_{w1} - d_{n1})^2 + \cdots + (d_{wu} - d_{nu})^2 \\ \Delta_2 &= (d_{w1} - d_{n2})^2 + (d_{w1} - d_{n3})^2 + \cdots + \left(d_{w(u-1)} - d_{nu}\right)^2 + (d_{wu} - d_{n1})^2 \\ & \cdots \\ \Delta_{u-1} &= (d_{w1} - d_{nu})^2 + (d_{w2} - d_{n1})^2 + \cdots + \left(d_{w(u-1)} - d_{n(u-2)}\right)^2 + \left(d_{wu} - d_{n(u-1)}\right)^2 \end{cases} \tag{13}$$

The minimum value Δ_i is obtained by comparing $\Delta_1, \Delta_2 \ldots \Delta_{u-1}$, and the rotation angle φ along the z-axis is obtained as follows:

$$\varphi = \frac{i}{u} * 2\pi \tag{14}$$

2.4. Reconstruction Model and Method of Obtaining Wall-Thickness

In order to obtain the wall-thickness of spherical shell parts, it is necessary to move and rotate the measurement data so that the inner and outer surfaces are unified under the same coordinate system. The subsequent processing method is the same, whether the meridian or concentric trajectory are used in the measurement. Thus, the meridian trajectory was taken as an example for wall-thickness processing. First, the external surface data points (x_{ww2}, y_{ww2}, z_{ww2}) were processed. The formula is as follows:

$$\begin{bmatrix} x_{ww3} \\ y_{ww3} \\ z_{ww3} \end{bmatrix} = \begin{bmatrix} x_{ww2} \\ y_{ww2} \\ z_{ww2} \end{bmatrix} - \begin{bmatrix} m_1 \\ n_1 \\ 0 \end{bmatrix} \tag{15}$$

After preprocessing, the inner surface data points (x_{nw2}, y_{nw2}, z_{nw2}) and (x_{nt2}, y_{nt2}, z_{nt2}) are translated and rotated. The formula is as follows:

$$\begin{bmatrix} x_{nw3} \\ y_{nw3} \\ z_{nw3} \end{bmatrix} = \begin{bmatrix} x_{nw2} \\ y_{nw2} \\ z_{nw2} \end{bmatrix} - \begin{bmatrix} m \\ n \\ 0 \end{bmatrix} \tag{16}$$

$$\begin{bmatrix} x_{nw4} \\ y_{nw4} \\ z_{nw4} \end{bmatrix} = \begin{pmatrix} 1 & 0 & 0 \\ 0 & \cos\alpha_0 & \sin\alpha_0 \\ 0 & -\sin\alpha_0 & \cos\alpha_0 \end{pmatrix} \begin{bmatrix} x_{nw3} \\ y_{nw3} \\ z_{nw3} \end{bmatrix} \tag{17}$$

$$\begin{bmatrix} x_{nw5} \\ y_{nw5} \\ z_{nw5} \end{bmatrix} = \begin{pmatrix} \cos\beta_0 & 0 & -\sin\beta_0 \\ 0 & 1 & 0 \\ \sin\beta_0 & 0 & \cos\beta_0 \end{pmatrix} \begin{bmatrix} x_{nw4} \\ y_{nw4} \\ z_{nw4} \end{bmatrix} \tag{18}$$

$$\begin{bmatrix} x_{nw6} \\ y_{nw6} \\ z_{nw6} \end{bmatrix} = \begin{pmatrix} \cos\theta_0 & \sin\theta_0 & 0 \\ -\sin\theta_0 & \cos\theta_0 & 0 \\ 0 & 0 & 1 \end{pmatrix} \begin{bmatrix} x_{nw5} \\ y_{nw5} \\ z_{nw5} \end{bmatrix} \tag{19}$$

The outer surface points (θ_w, ϕ_w, r_w) and the inner surface points (θ_n, ϕ_n, r_n) are obtained by coordinate conversion. The conversion formula is as follows:

$$\begin{cases} r = \sqrt{x^2 + y^2 + z^2} \\ \theta = \cos^{-1}\left(\frac{z}{\sqrt{x^2+y^2+z^2}}\right) \\ \phi = \tan^{-1}\frac{y}{x} \end{cases} \tag{20}$$

In the interpolation, θ is $-180°$~$180°$, the interpolation interval is $\Delta\theta$; ϕ is $0°$~$90°$, and the interpolation interval is $\Delta\phi$; The outer surface interpolation point (θ_e, ϕ_e, r_{we}) and the inner surface interpolation point (θ_e, ϕ_e, r_{ne}) are obtained according to data points (θ_w, ϕ_w, r_w) and (θ_n, ϕ_n, r_n), and the wall-thickness difference formula as:

$$h_e = r_{we} - r_{ne} \tag{21}$$

3. Experimental Setup

A spherical shell with an outer diameter of Φ210.6 mm and an inner diameter of Φ206.4 mm is used for the measurement test. As shown in Figure 7, the processing machine is an ultra-precision single-point diamond machine made by Precitech in the United States. The machine parameters are shown in Table 1. The cemented carbide tool (KC5010) is used for processing and the constant speed is used for machining. The specific parameters are shown in Table 2. The spherical shell is measured with CMM by Zeiss, Germany. The maximum allowable error of the size measurement is $\pm 0.5 + L/500$ μm, and L is the length to be measured. For the most part, the measurement accuracy is about 1 μm. A ruby probe with a diameter of 5 mm is used in the processing.

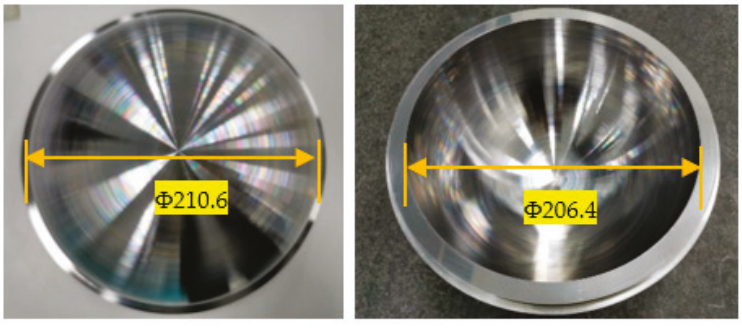

(**a**) (**b**)

Figure 7. The processed spherical shell: (**a**) the outer surface; (**b**) the inner surface.

Table 1. The machine parameters.

Parameter Type	Parameter Value
X Stroke (mm)	350
Z Stroke (mm)	300
Position Feedback Accuracy (nm)	0.032
X Horizontal Straightness (μm/25 mm)	0.05
Z Horizontal Straightness (μm/25 mm)	0.05
Spindle Load (kg)	85
Spindle Radial Runout (nm)	≤15
Spindle Axial Runout (nm)	≤15
Maximum Spindle Speed (rpm)	7000

Table 2. The processing related parameters.

Parameter Type	Parameter Value
Tool Radius (mm)	0.2
Spindle Speed (rpm)	200
F (mm/min)	20
ap (μm)	10
Adsorption Pressure (kPa)	50

The circular trajectory on the circumferential surface of the spherical shell flange is measured first, and the spherical shell is placed on the three-coordinate platform with the outer surface facing upwards, as shown in Figure 8. The data point (x_{wc}, y_{wc}, z_{wc}) is measured according to the trajectory of the flange circumferential surface, which takes four circular trajectories. In the circular trajectory Equation (1), R_1 is 115 mm, h_1 is 4 mm, h_2 is 2 mm, and h is 12 mm.

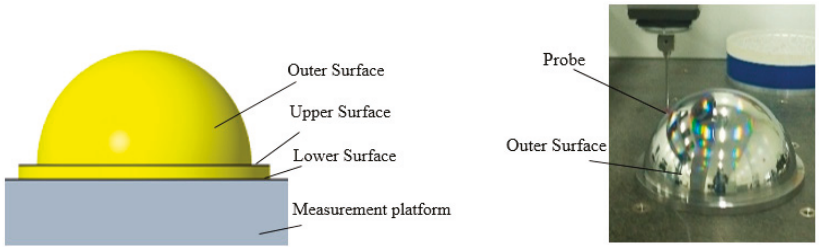

Figure 8. The outer surface measurement: (**a**) the measurement model; (**b**) measuring the real object.

The outer surface is measured according to the meridian and concentric circles. The meridian measurement of the outer surface takes 18 meridian trajectories. In Equation (2), R_2 is 105.3 mm, R_4 is 103.2 mm, and b is 18. The obtained data points are (x_{ww1}, y_{ww1}, z_{ww1}). Concentric circle traces of 28 concentric circles are taken to obtain data point (x_{wt1}, y_{wt1}, z_{wt1}). Then the spherical shell is placed on the three-coordinate platform with the inner surface facing upwards, as shown in Figure 9. The data points (x_{nc}, y_{nc}, z_{nc}) on the circumferential surface of the flange are obtained. Finally, the inner surface is measured according to the meridian and concentric circles. The meridian measurement of the inner surface takes 18 meridian trajectories to obtain the measurement data points (x_{nw1}, y_{nw1}, z_{nw1}). The concentric circular measurement of the inner surface takes 29 measurement trajectories to obtain the measurement data points (x_{nt1}, y_{nt1}, z_{nt1}).

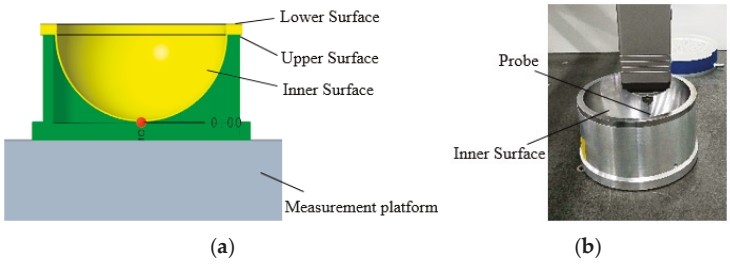

Figure 9. The inner surface measurement: (**a**) the measurement model; (**b**) measuring the real object.

4. Results and Discussion

4.1. Spherical Shell Surface Shape

The surface errors of the outer and inner surface of the spherical shell near the top are about 22 μm and 27 μm respectively by the meridian trajectory, while the outer and inner surface errors near the top are about 8 μm and 14 μm by concentric circles. Due to the large error near the top, the surface error was evaluated without the points near the top. The results revealed that the errors of the inner and outer surfaces are 5 μm and 6 μm respectively by the meridian trajectory. Similar to the meridian trajectory, the inner and outer surfaces are 5 μm and 8 μm using concentric circles, as shown in Figure 10.

4.2. Wall-Thickness of Spherical Shell

When evaluating the wall-thickness, it is necessary to make the measurement benchmark coincide. According to Formula (7) and Formula (8), m_1, m_2, n_1, n_2, m and n are obtained, as shown in Table 3.

The direct method was used to obtain the rotation angles α, β and θ along the x-axis, y-axis and z-axis, which is $\alpha_0 = 0.07°$, $\beta_0 = 0.26°$, $\varphi = 17.67°$. After moving the second flange data, the distance between the corresponding points was calculated as the error

based on the rotation. The error of the flange circumference is less than 2 μm obviously, as shown in Figure 11.

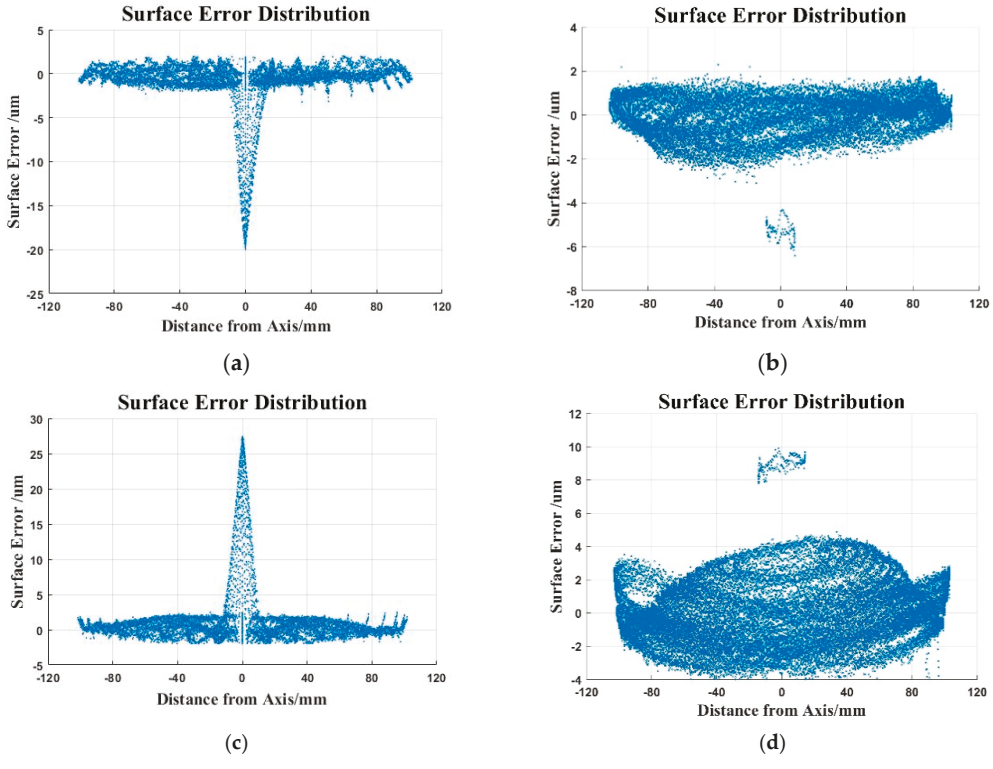

Figure 10. The surface error distribution: (**a**) Surface error distribution of the outer surface (the meridian trajectory); (**b**) surface error distribution of the outer surface (the concentric trajectory); (**c**) surface error distribution of the inner surface (the meridian trajectory); (**d**) surface error distribution of the inner surface (the concentric trajectory).

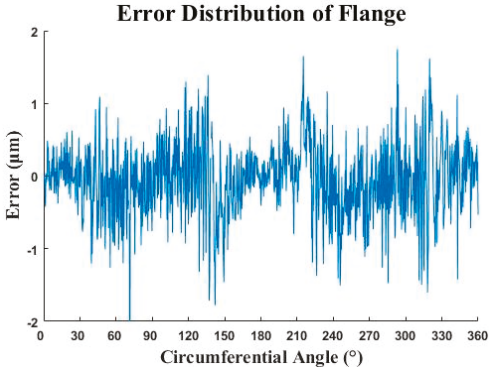

Figure 11. The error distribution of flange.

Table 3. The related parameters.

Parameter	m_1	m_2	n_1	n_2	m	n
(μm)	−2.9486	1.7417	−0.4585	−0.1361	−4.6903	−0.3224

The inner and outer surface data were rotated and translated according to Equations (15)–(19), and then interpolated in the inner and outer surfaces. The interpolation interval $\Delta\theta$ is 0.01° and $\Delta\phi$ is 0.01°. According to Formula (21), the wall-thickness h_e of each point is obtained. (θ_e, ϕ_e, h_e) are used as the data points to draw the spherical shell wall-thickness error distribution, as shown in Figure 12. The meridian measurement track is used to measure the wall-thickness error of about 45 μm. The concentric circle measurement track used to measure the wall-thickness error is about 16 μm.

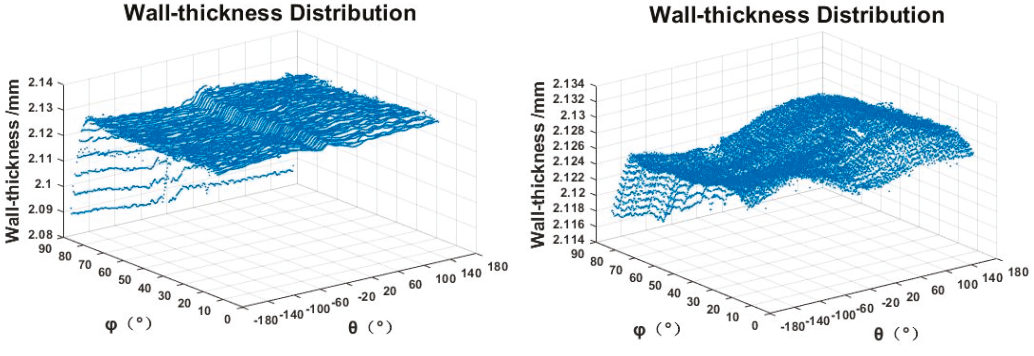

(**a**) (**b**)

Figure 12. The wall-thickness distribution (polar coordinates): (**a**) the wall-thickness distribution (the meridian trajectory); (**b**) the wall-thickness distribution (the concentric trajectory).

In order to describe the wall-thickness clearly, the interpolation data point (θ_w, ϕ_w, r_w) on the outer surface of the spherical shell is converted into rectangular coordinates (x_w, y_w, z_w), and the (x_w, y_w, h_e) is used as the data point to draw the spherical shell wall-thickness distribution, as shown in Figure 13.

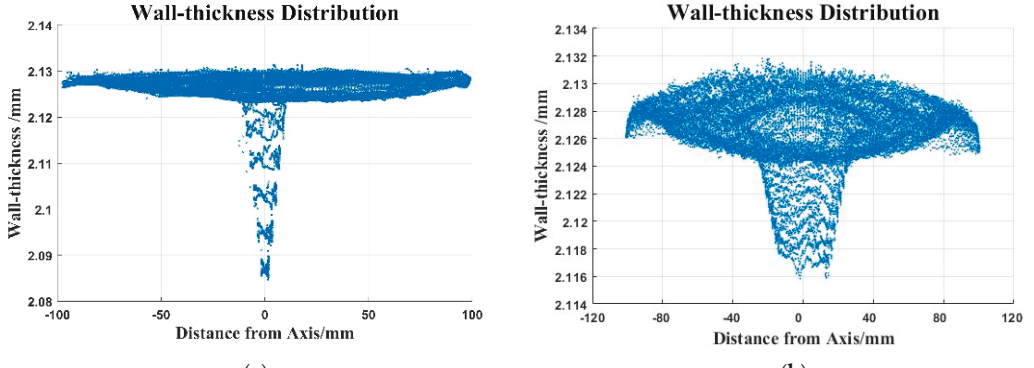

(**a**) (**b**)

Figure 13. The wall-thickness distribution (Cartesian coordinates): (**a**) the wall-thickness distribution (the meridian trajectory); (**b**) the wall-thickness distribution (the concentric trajectory).

4.3. Discussion

The surface error of the top by the meridian trajectory is larger than that of the concentric circles. This is because the measurement of the concentric circles fails to collect the top data information. In actual processing, due to the poor cutting conditions at the top area, the presence of entangled chips and a long distance from the positioning surface (flange) will cause a large wall-thickness error, and the uniformity of the wall-thickness at the top is more difficult to achieve. The meridian trajectory can reflect the wall-thickness information accurately. Hence, the meridian trajectory is more suitable for measuring the spherical shell part thickness than the concentric circle trajectory measurement. The wall-thickness difference is large near the top, and the error increased simultaneously. During the actual processing of the inner and outer surfaces, the workpiece is always machined from the flange position to the top, and the rigidity is weak in the top area. Thus, the surface error of the spherical shell is large and the wall-thickness uniformity is poor. There are several reasons for causing the problem, including built-up edge in the processing process, the deviation of tool installation center and rotation center of the workpiece, tool setting errors in the x and z directions, the harsh processing conditions, etc.

5. Conclusions

This paper proposes a method for measuring the wall-thickness of thin-walled spherical shell parts. Experiments are conducted on a spherical shell part with an outer diameter of Φ210.6 mm and an inner diameter of Φ206.4 mm. The meridian track and the concentric circle track are used to measure the spherical shell.

1. Thin-walled spherical shell parts thickness is obtained by measuring the surface of inner and outer surface respectively.
2. The surface error of the outer and inner surfaces of the spherical shell are about 5 μm and 6 μm, and the wall-thickness error is about 8 μm.
3. The meridian trajectory is verified as a better method to obtain the wall-thickness of spherical shell parts.

The measurement method is suitable for the wall-thickness of thin-walled spherical shell parts, and it has certain significance for subsequent scholars to study the thickness of thin-walled parts.

Author Contributions: Conceptualization, J.G.; methodology, J.G.; software, D.D.; data analysis, Y.X.; original draft writing, Y.X. and B.P.; review and editing, W.H. and J.Z.; supervision, R.K. All authors have read and agreed to the published version of the manuscript.

Funding: This work was supported by the Science Challenge Project (No. TZ2016006).

Informed Consent Statement: Not applicable.

Data Availability Statement: No new data were created or analyzed in this study. Data sharing is not applicable to this article.

Conflicts of Interest: The authors declare no conflict of interest.

References

1. Liu, H.-B.; Wang, Y.-Q.; Jia, Z.-Y.; Guo, D.-M. Integration strategy of on-machine measurement (OMM) and numerical control (NC) machining for the large thin-walled parts with surface correlative constraint. *Int. J. Adv. Manuf. Technol.* **2015**, *80*, 1721–1731. [CrossRef]
2. Naveed, A.; Muhammad, A.-N.; Ateekh, U.-R.; Madiha, R.; Usama, U.; Adham, E.-R. High Aspect Ratio Thin-Walled Structures in D2 Steel through Wire Electric Discharge Machining (EDM). *Micromachines* **2021**, *12*, 1.
3. Huang, X.-C. *Analysis of Mechanical States and Failure Modes of Shells Subjected to Implosive and Explosive Loadings*; Institute of Engineering China Academy of Engineering Physics: Mianyang, China, 2010.
4. Zhao, F.; Tan, H.; Wu, Q.; Cai, L.-C.; Tan, D.-W.; Zhu, W.-J. Shock wave and detonation physics research in the Chinese Academy of Engineering Physics. *Physics* **2009**, *38*, 894–899.
5. Zha, J.; Chu, J.; Li, Y.-P.; Chen, Y.-L. Thin-walled Double Side Freeform Component Milling Process with Paraffin Filling Method. *Micromachines* **2017**, *8*, 332. [CrossRef] [PubMed]

6. Cao, G.-Q. *The Research of Instrument for Measurement of Wall-Thickness and Wall-Thickness Difference of Thin-Wall Parts of Variation Curvature Revolving Body*; National University of Defense Technology: Changsha, China, 2005.
7. Wei, P.; Zhao, J.-X.; Sun, Z.-J. Measuring and Computerized Data Processing System for W.T. of Seamless Steel Tubes. *Steel Pipe* **2002**, *31*, 40–42.
8. Zhang, Y.; Lin, B. Error Analysis and Data Processing in the Measurement of Wall Thickness of Missile Radom. *Electr. Autom.* **2013**, *35*, 96–98.
9. Guo, D.-M.; Wang, X.-M.; Jia, Z.-Y.; Xu, Z.-X. Researches on the Geometric Parameter Measuring Instrument for Radome. *Chin. J. Mech. Eng.* **2000**, *36*, 41–46. [CrossRef]
10. Lyssakow, P.; Friedrich, L.; Krause, M.; Dafnis, A.; Schröder, K.-U. Contactless geometric and thickness imperfection measurement system for thin-walled structures. *Measurement* **2020**, *150*, 107038. [CrossRef]
11. Jin, J.-H.; Kang, Y.-H.; Yang, S.-Z. Magnetic Leakage Flux Method for Wall Thickness Measurement in Oil Well Tubing. *Chin. J. Sci. Instrum.* **2001**, *22*, 469–472.
12. Fan, M.-B.; Cao, B.-H.; Sunny, A.-I.; Li, W.; Tian, G.-Y.; Ye, B. Pulsed eddy current thickness measurement using phase features immune to liftoff effect. *NDT E Int.* **2017**, *86*, 123–131. [CrossRef]
13. Mao, X.-F.; Lei, Y.-Z. Thickness measurement of metal pipe using swept-frequency eddy current testing. *NDT E Int.* **2016**, *78*, 10–19. [CrossRef]
14. Nishino, H.; Iwata, K.; Ishikawa, M. Wall thickness measurement using resonant phenomena of circumferential Lamb waves generated by plural transducer elements located evenly on girth. *Jpn. J. Appl. Phys.* **2016**, *55*, 07KC07. [CrossRef]
15. Li, W.; Duan, S.-Y.; Song, Y.; Wu, X.-J. An pulse eddy current thickness measurement method of stainless steel plate based on Laplace wavelet's characteristic frequency. *Chin. J. Sci. Instrum.* Available online: http://kns.cnki.net/kcms/detail/11.2179.TH.20201223.0905.002.html (accessed on 23 December 2020).
16. Wu, A.; Zhu, J.-H.; He, F.-Y.; Hu, J.-D.; Wang, L. Measuring System for the Wall Thickness of Pipe Based on Ultrasonic Multisensory. In Proceedings of the 2009 9th International Conference on Electronic Measurement & Instruments, Beijing, China, 16–19 August 2009; Institute of Electrical and Electronics Engineers: New York, NY, USA, 2009; pp. 641–644.
17. Jaime, P.; Pouyan, K.; Frederic, C. Shear waves with orthogonal polarisations for thickness measurement and crack detection using EMATs. *NDT E Int.* **2020**, *111*, 102212.
18. Durongsak, K.; Yenjai, C.; Rassamee, S. Development of remaining wall thickness measurement system for boiler wall tube using gamma scattering technique. *J. Phys. Conf. Ser.* **2017**, *860*, 12040. [CrossRef]
19. Levesque, D.; Kruger, S.-E.; Lamouche, G.; Kolarik, R., II; Jeskey, G.; Choquet, M.; Monchalin, J.-P. Thickness and grain size monitoring in seamless tube-making process using laser ultrasonics. *NDT E Int.* **2006**, *39*, 622–626. [CrossRef]
20. Liu, H.-B.; Wang, Y.-Q.; Lian, M.; Zhang, T.-Y.; Liu, B.-L. Thickness Measurement Using Ultrasonic Scanning Method for Large Aerospace Thin-Walled Parts. In Proceedings of the 2019 IEEE 5th International Workshop on Metrology for AeroSpace (MetroAeroSpace), Turin, Italy, 19–21 June 2019; IEEE: New York, NY, USA, 2019; pp. 243–247.
21. Morana, M.; Damir, M.; Biserka, R.; Zdenka, K. Measurement uncertainty evaluation of ultrasonic wall thickness measurement. *Measurement* **2019**, *137*, 179–188.
22. Adamowski, J.-C.; Buiochi, F.; Tsuzuki, M.; Pérez, N. Ultrasonic Measurement of Micrometric Wall-Thickness Loss Due to Corrosion Inside Pipes. In Proceedings of the 2013 IEEE International Ultrasonics Symposium (IUS), Prague, Czech Republic, 21–25 July 2013; Institute of Electrical and Electronics Engineers: New York, NY, USA, 2014; pp. 1881–1884.
23. Rees, J.; Hobsont, G.-S.; Tozert, R.C.; Busby, T.-S. Microwave measurement of furnace wall thickness. *Trans. Inst. Meas. Control* **1986**, *8*, 91–99. [CrossRef]

micromachines

MDPI

Article

High-Accuracy Surface Topography Manufacturing for Continuous Phase Plates Using an Atmospheric Pressure Plasma Jet

Huiliang Jin [1,*], Caixue Tang [1], Haibo Li [1], Yuanhang Zhang [1] and Yaguo Li [2,*]

[1] Research Center of Laser Fusion, China Academy of Engineering Physics, Mianyang 621900, China; ispwr@foxmail.com (C.T.); feel612@163.com (H.L.); yuanhang_zhang@126.com (Y.Z.)
[2] Chengdu Fine Optical Engineering Research Center, Chengdu 610041, China
* Correspondence: jinhl09@sina.com (H.J.); yargolee@163.com (Y.L.); Tel.: +86-028-8514-1138 (H.J.)

Abstract: The continuous phase plate (CPP) is the vital diffractive optical element involved in laser beam shaping and smoothing in high-power laser systems. The high gradients, small spatial periods, and complex features make it difficult to achieve high accuracy when manufacturing such systems. A high-accuracy and high-efficiency surface topography manufacturing method for CPP is presented in this paper. The atmospheric pressure plasma jet (APPJ) system is presented and the removal characteristics are studied to obtain the optimal processing parameters. An optimized iterative algorithm based on the dwell point matrix and a fast Fourier transform (FFT) is proposed to improve the accuracy and efficiency in the dwell time calculation process. A 120 mm × 120 mm CPP surface topography with a 1326.2 nm peak-to-valley (PV) value is fabricated with four iteration steps after approximately 1.6 h of plasma processing. The residual figure error between the prescribed surface topography and plasma-processed surface topography is 28.08 nm root mean square (RMS). The far-field distribution characteristic of the plasma-fabricated surface is analyzed, for which the energy radius deviation is 11 μm at 90% encircled energy. The experimental results demonstrates the potential of the APPJ approach for the manufacturing of complex surface topographies.

Keywords: atmospheric pressure plasma jet; continuous phase plate; surface topography; high accuracy and efficiency

Citation: Jin, H.; Tang, C.; Li, H.; Zhang, Y.; Li, Y. High-Accuracy Surface Topography Manufacturing for Continuous Phase Plates Using an Atmospheric Pressure Plasma Jet. *Micromachines* **2021**, *12*, 683. https://doi.org/10.3390/mi12060683

Academic Editors: Chengwei Kang, Chunjin Wang and Jiang Guo

Received: 8 May 2021
Accepted: 7 June 2021
Published: 10 June 2021

1. Introduction

High-powered laser systems require precise control of the laser beam shape and energy distribution in the target plane [1]. The continuous phase plate (CPP), as a beam-shaping optical element, can manipulate the incident laser to allow beam shaping and smoothing with complex surface topographies [2]. The surface topography of the CPP, having multiple spatial scales, high peak-to-valley (PV) values, large gradients, and high accuracy, causes much difficulty in fabrication [3].

Subaperture technology is mainly used to imprint the topography deterministically to obtain CPP elements [4]. Menapace et al. [5] developed the magnetorheological finishing (MRF) technique to fabricate large-aperture CPPs for the National Ignition Facility (NIF), in which the spatial periods of the surface topography are usually larger than 4 mm and the PV values are as high as 8.6 μm [6,7]. Microstructures with smaller spatial periods are difficult to process with MRF due to the limitations of tool sizes. Ion beam figuring (IBF) has the potential to process smaller period structures, as the beam sizes can be changed easily with a shielding diaphragm to as small as 1 mm. Xu et al. [8,9] used the ion beam figuring (IBF) approach with different beam diameters based on the frequency filtering method to improve the machining accuracy and efficiency of CPPs. However, the low removal rate limits its application for large-aperture CPPs.

The atmospheric pressure plasma jet (APPJ) approach is an efficient manufacturing technology with the advantages of high material removal efficiency, adjustable tool function

size, and no subsurface damage. It is based on the chemical reaction removal mechanism, involving a chemically reactive plasma jet driven with radio frequency (RF) power under atmospheric pressure conditions. The plasma jet is fed by a mixture of fluorine-containing reactive gases (NF_3, CF_4, SF_6). The reactive gases dissociate in the plasma, producing chemically reactive fluorine radicals that react with the workpiece surface to form volatile products. In the case of silicon-based materials, SiF_4 is formed and exhausted as a waste product. It has been shown that plasma jet technology is a very efficient tool for the treatment of optical surfaces made of silicon, silicon-based materials such as fused silica for damage-free optics in high-powered laser systems, and silicon carbide for space applications.

The plasma jet technology combines the advantages of a non-contact machining technique with material removal rates comparable to traditional polishing methods. As a key advantage, subsurface damage is avoided owing to the material being removed by plasma-assisted chemical etching without any mechanical or physical contribution. The high-density distribution of reactive species can allow high material removal rates. Furthermore, the lateral dimensions of the plasma jets can be adjusted easily from around 14 mm down to the sub-mm range. Thus, these plasma jets are suitable for pre-shaping with high machining depths and for deterministic shape correction with high spatial resolution. Due to the pure chemical removal mechanism, the surface roughness increases while surface contaminants are efficiently removed the during processing. At present, the disadvantage of the plasma jet approach is solved by using a combined processing chain.

Several fluorine-plasma-based machining techniques have been developed for optical surface fabrication and freeform manufacturing. Castelli et al. [10,11] adopted the reactive atom plasma (RAP) approach for large-optics rapid surface figuring, bringing the figure error corrections down to 30 nm RMS on a ULE workpiece measuring 400 mm in diameter with a 3 m radius of curvature (ROC). Yamamura et al. [12,13] developed the plasma chemical vaporization machining (PCVM) approach to correct thickness deviations of quartz crystal wafer, whereby the thickness distribution for 14.4 nm PV was obtained after two correction steps. Arnold et al. [14–16] proposed plasm jet machining (PJM) and investigated the effects of the surface temperature on the etching rate. A three-dimensional finite element heat transfer model was built to assess the spatiotemporal variations of the surface temperature and temperature-dependent material removal. Su et al. [17] applied atmospheric pressure plasma processing (APPP) to CPP fabrication, whereby 320 mm × 320 mm CPP of B33 with 2.78 μm PV was fabricated and the RMS of the form error was 96 nm. Li [18,19] proposed a multiaperture plasma processing method to structure a 30 mm × 30 mm CPP, for which the peak-to-valley error was 163.4 nm. The potential of plasma processing for manufacturing CPP has been proven but the fabrication accuracy and efficiency need to be further improved to meet the performance requirements.

In this paper, an optimized iterative algorithm for high-accuracy and high-efficiency CPP manufacturing is presented. The APPJ system and surface topography processing are first introduced and the removal function characteristics are investigated to obtain the optimal processing parameters. Then, an optimized iterative algorithm based on the dwell point matrix and FFT is proposed to improve the accuracy and efficiency of the APPJ processing. The experimental processing is carried out to validate the accuracy and efficiency of the APPJ in fabricating CPP. Finally, the far-field distribution characteristics of the processed CPP are calculated.

2. Experiment

2.1. Experiment Setup

The APPJ made use of a radio frequency inductively coupled plasma (ICP) torch as a tool to generate the plasma jet. The plasma jet source consisted of three coaxially arranged conducting tubes guiding the plasma gas Ar and reactive gas CF_4 together to a nozzle. The plasma jet was generated through the excitation energy (radio frequency at 13.56 MHz) and the CF_4 was decomposed into active fluorine atoms. These reactive fluorine atoms

acted as the main reactant, which was carried by plasma jet and reacted with the substrate to form the volatile reaction products SiF_4 and CO_2. A schematic diagram of the APPJ used for CPP processing is shown in Figure 1.

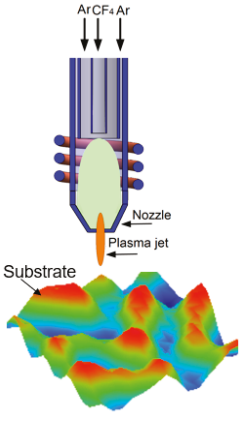

Figure 1. Schematic diagram of the APPJ used for CPP processing.

The lateral dimensions of the primary plasma discharge can be modified within a range between 2 mm and 14 mm by varying the inner diameter of the exit nozzle or by adding additional beam-shaping nozzles and apertures. In this way, the material removal rates of 0.01 to 10 mm^3/min are achieved.

2.2. APPJ Processing of Surface Topography

The fundamentals of the APPJ processing flow chart include targeted removal, dwell time calculations, plasma processing, and testing, as shown in Figure 2. First, the prescribed surface data were inverted and superimposed with the existing measured surface figure and the targeted removal map was obtained. Then, the dwell time and residual error were calculated through the removal function and the targeted surface deconvolution iteration, while the CNC program was also generated according to the dwell time and path. After this, the APPJ processing was performed to structure the phase topography on the optic substrate. The residual error was obtained by comparing the measured surface topography with the prescribed surface. Several plasma processing iterations were required until effective convergence of the residual error was achieved.

The APPJ approach uses the removal function and dwell time to differentially remove material from areas of an optic so that the desired surface can be obtained. Two main aspects in the plasma surface topography processing deserve mention, namely the size and removal rate of the removal function used to structure the topography. The physical characteristics of the removal function determine the accuracy and success of the plasma processing on the surface topography. The dwell time calculation is another key aspect during APPJ processing, in which the APPJ process integrates interferometry and a computer algorithm to generate the required instrument stage motions to deterministically remove material surfaces. The algorithm attempts to converge to a solution that minimizes the RMS of the residual error between the prescribed surface and plasma processing surface.

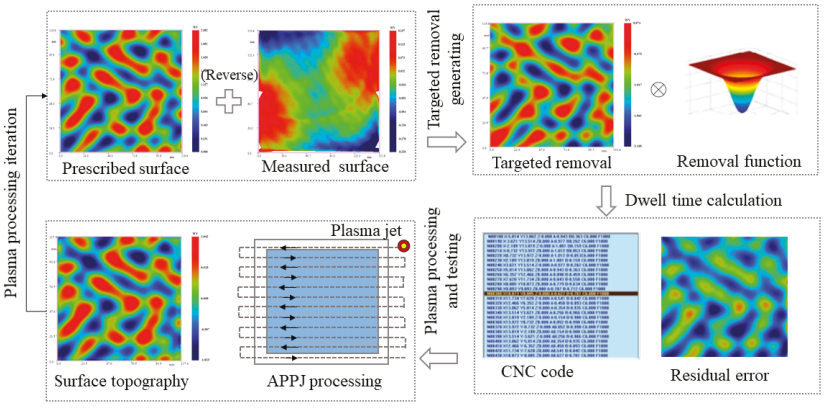

Figure 2. The fundamentals of APPJ processing.

3. Methods

3.1. Removal Function

The most important factor to achieve precise etch depths for phase plate fabrication is well-founded knowledge of the etch rate and its stability during the etching process. Therefore, the peak removal rates were investigated closely as functions of the plasma RF power and the CF_4–Ar gas mixture flow and ratio. The key experimental parameters and variation range for removal characteristic groups are listed in Table 1. In practical plasma processing, the plasma jet stability, shape of the influence function, and material removal efficiency need to be considered. Combined with the experimental results, the processing parameters were determined. As the cooling gas, Ar is immitted through the external tube with a tangential inlet at a flow of 16 slm (standard liter per minute). The plasma gas, also Ar, is immitted through the intermediate tube at a rate of 1 slm, whereas the reactive gas CF_4 is kept at a flow rate of 5–70 sccm (standard cubic centimeter per minute, 1 sccm = 10^{-3} slm) when entering the center tube. The effects of the plasma parameters on the peak removal rates are shown in Figure 3.

Table 1. Experimental parameters used for investigation of the removal characteristics.

Parameter	Value
Ar flow rate	16 slm
RF power	800~1300 W
CF_4 flow rate	5~70 sccm
Ratio of O_2 and CF_4	0~100%
Processing distance	12 mm
Dwell time	3 s

Figure 3a shows the peak removal rates with the RF power values ranging from 800 W to 1300 W. It can be seen that the peak removal rates significantly increase with the increase of RF power, which provides reactive species to promote material remove. Figure 3b shows the peak removal rates with the flow rates of the reactive gas CF_4 ranging from 5 sccm to 70 sccm. It is clear that the peak removal rates increase linearly with the CF_4 flow, reaching 48 μm/min at 60 sccm; when the CF_4 flow rate exceeded 70 sccm, the plasma discharge became unstable. Figure 3c shows the peak removal rates with the O_2/CF_4 ratio, whereby the addition of O_2 to CF_4 gas leads to fluorine-rich plasma, which can improve the removal rate, while the peak removal rate reaches a peak value at about 40% of O_2/CF_4 and then decreases upon the addition of O_2. Figure 3d shows the repeatability of the removal function with processing parameters at 1100 W RF power, 60 sccm CF_4 flow, and

40% O_2/CF_4 ratio, where five removal functions are etched with the same parameters and the maximum deviation of the peak removal rate is about 6.3%.

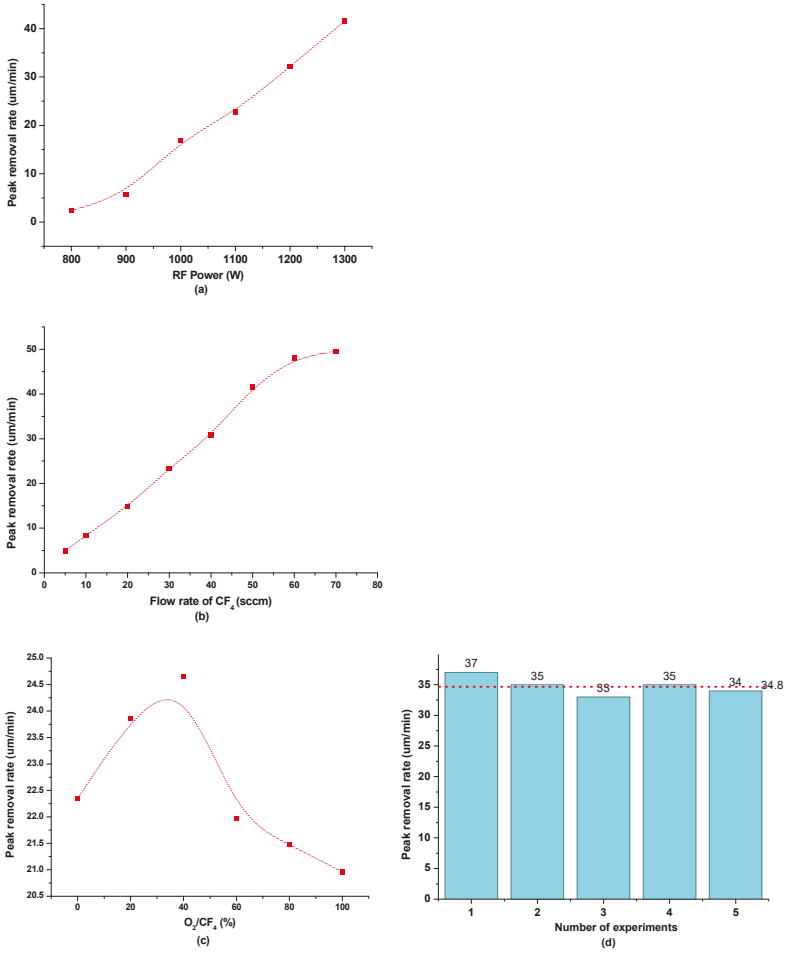

Figure 3. Influence on peak removal rates of plasma parameters. (**a**) RF power. (**b**) Flow rate of CF_4. (**c**) O_2/CF_4 ratio. (**d**) Repeatability of the removal function.

3.2. Dwell Time Algorithm

The dwell time is the input control for surface topography structure configuration, meaning the dwell time algorithm is the key issue in APPJ processing. For a conventional dwell time calculation, the removed material $F(x, y)$ is equal to the convolution of the removal function $R(x, y)$ and the dwell time $T(x, y)$ is given as follows:

$$F(x, y) = R(x, y) * T(x, y) \quad (1)$$

The dwell time $T(x, y)$ can be obtained by calculating the deconvolution of the removed material $F(x, y)$ and the removal function $R(x, y)$ [20]. However, with this deconvolution calculation process, it is difficult to achieve convergence for the prescribed surface topography and the calculation process is also time-consuming, especially for complex structure components, for which the calculation scale is large and the accuracy and efficiency of con-

ventional calculations are difficult to match with the processing requirements. Therefore, an iterative algorithm based on the dwell point matrix and fast Fourier transform (FFT) was proposed to achieve high accuracy and efficiency in the dwell time calculation.

During plasma processing, the plasma jet scanning follows the raster path. A schematic of the plasma jet with the raster path is shown in Figure 4.

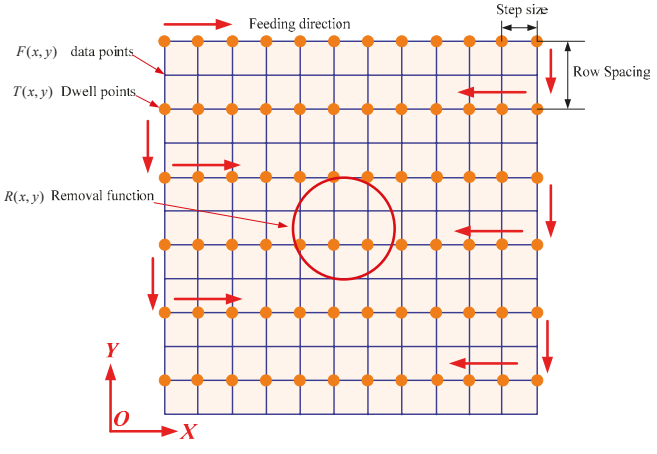

Figure 4. Schematic diagram of the material removal during plasma processing.

Assuming that the number of original surface data points is M × N and the number of dwell time points is U × V, the material removal convolution equation can be converted into the matrix-based form as follows:

$$\begin{bmatrix} f_{11} & f_{12} & \cdots & f_{1N} \\ f_{21} & f_{22} & \cdots & f_{2N} \\ \vdots & \vdots & \ddots & \vdots \\ f_{M1} & f_{M2} & \cdots & f_{MN} \end{bmatrix} = \begin{bmatrix} r_{11} & r_{12} & \cdots & r_{1Q} \\ r_{21} & r_{22} & \cdots & r_{2Q} \\ \vdots & \vdots & \ddots & \vdots \\ r_{P1} & r_{P2} & \cdots & r_{PQ} \end{bmatrix} * \begin{bmatrix} t_{11} & t_{12} & \cdots & t_{1V} \\ t_{21} & t_{22} & \cdots & t_{2V} \\ \vdots & \vdots & \ddots & \vdots \\ t_{U1} & t_{U2} & \cdots & t_{UV} \end{bmatrix} \quad (2)$$

Generally, the number of dwell points is less than that of the surface data points (U < M, V ≤ N) and the size of the dwell time matrix $\boldsymbol{D}$ is not equal to the original data matrix $\boldsymbol{P}$, so the dwell time matrix $\boldsymbol{D}$ and the removal function matrix $\boldsymbol{R}$ cannot be directly used for the convolution operation to obtain the matrix $\boldsymbol{P}$ [21].

To achieve fast calculation without loss of accuracy when calculating the dwell time, the concept of the dwell point matrix $\boldsymbol{DP}$ is proposed in this paper. The size of matrix $\boldsymbol{DP}$ is M × N, which is equal to the original data matrix $\boldsymbol{P}$, while the value of the dwell point is 1 and of the non-dwell point is 0. The dwell time matrix $\boldsymbol{T}$ performs the matrix Hadamard product operation [22,23] with the dwell point matrix $\boldsymbol{DP}$, as shown in Equation (3), so that the value of the non-dwell point in the dwell time matrix is equal to zero, which ensures that the amount of material removal is calculated only when the removal function is at the dwell point. The standard convolution method can be used to calculate the amount of material removal with the dwell point matrix $\boldsymbol{DP}$:

$$T = \begin{bmatrix} t_{11} & t_{12} & \cdots & t_{1V} \\ t_{21} & t_{22} & \cdots & t_{2V} \\ \vdots & \vdots & \ddots & \vdots \\ t_{U1} & t_{U2} & \cdots & t_{UV} \end{bmatrix} \bullet \begin{bmatrix} 1 & 1 & \cdots & 1 \\ 0 & 0 & \cdots & 0 \\ 1 & 1 & \cdots & 1 \\ \vdots & \vdots & \ddots & \vdots \\ 0_{M1} & 0_{M2} & \cdots & 0_{MN} \end{bmatrix} = \begin{bmatrix} t_{11} & t_{12} & \cdots & t_{1N} \\ t_{21} & t_{22} & \cdots & t_{2N} \\ \vdots & \vdots & \ddots & \vdots \\ t_{M1} & t_{M2} & \cdots & t_{MN} \end{bmatrix} \quad (3)$$

When the calculation scale is large, the calculation speed of the matrix convolution according to the definition of the convolution is slow. To improve the speed of the convolution calculation, as the spatial domain convolution calculation is equal to the frequency domain product operation, in this paper we propose using a fast Fourier transform (FFT) algorithm for convolution calculations.

$$\boldsymbol{T} * \boldsymbol{R} = IFFT(FFT(\boldsymbol{T}) \bullet FFT(\boldsymbol{R})) \tag{4}$$

In Equation (4), FFT represents the fast Fourier transform and IFFT represents the inverse fast Fourier transform. In the convolution calculation, first we perform the FFT transformation on the matrix and then separately perform the Hadamard product operation on the results of the FFT transformation. Finally, we perform the inverse FFT on the multiplied result to obtain the final convolution calculation result. The convolution calculation based on the FFT has a very fast calculation speed compared to the convolution calculation according to the definition in the large-scale calculation.

A flow chart of the dwell time algorithm is shown in Figure 5. The dwell point matrix ***DP*** is established according to various parameters, such as the line spacing and step length. Once the necessary parameters have been chosen, the initial value of the dwell time, the permission iteration error Err_{max}, and the maximum iteration number it_{max} are set. Then, the dwell time matrix $\boldsymbol{T}$ is calculated with the main iterative loop, then the dwell time matrix $\boldsymbol{T}$ is multiplied by the Hadamard product matrix ***DP*** and the residual error matrix $\boldsymbol{E}$ is calculated using a multicore parallel FFT convolution calculation. Finally, the iterative loop is terminated when the calculated residual error is less than the permission error and the dwell time $\boldsymbol{T}_{k+1}$ and residual error $\boldsymbol{E}_{k+1}$ can be obtained.

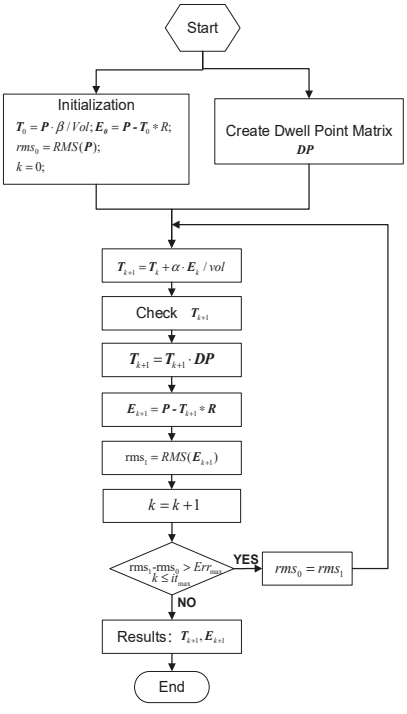

Figure 5. Flow chart of the dwell time algorithm.

4. Results

The dwell time iterative calculation was used to fabricate a 120 mm × 120 mm × 5 mm CPP substrate. The prescribed surface of the CPP has a random surface topography with 1326.2 nm PV and 292.2 nm RMS, as shown in Figure 6a. All figuring experiments were performed in our self-developed APPJ system. After the experiment, the 4D interferometer was used to measure the CPP and the specified evaluation aperture for the CPP was 100 mm × 100 mm. After four plasma iteration steps, the surface topography measurements for the CPP were 1306.4 nm PV and 286.5 nm RMS, as shown in Figure 6b. The interferometer measurements and a photo of the substrate after the APPJ process are shown in Figure 6c. The actual residual error after the plasma process was 28.08 nm, as shown in Figure 6d.

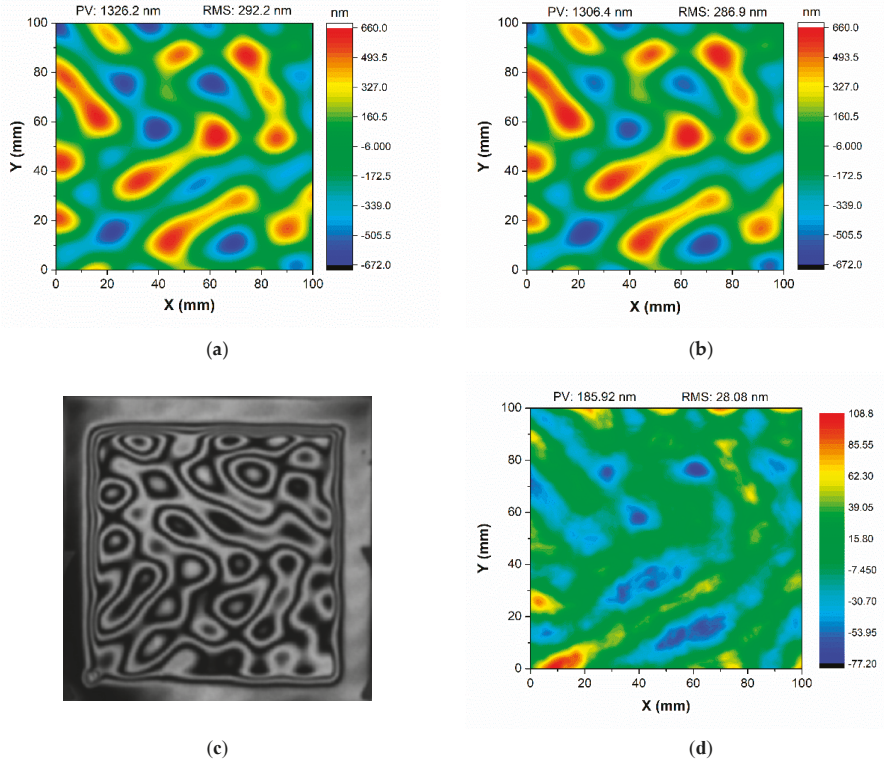

Figure 6. Machining example of a CPP substrate: (**a**) prescribed surface: PV = 1326.2 nm, RMS = 292.2 nm; (**b**) plasma-processed surface, PV = 1306. 4 nm, RMS = 286.5 nm; (**c**) interferometer measurement; (**d**) plasma-processed residual errors of the CPP.

During plasma processing, further iteration steps comprise the dwell time matrix calculation using the modified topography. Several iterations are performed until the residual error obtained from the difference between the measured topography and the designed topography is less than that required by the specifications. The topographical profiles have RMS errors of <30 nm relative to the idealized CPP prescription. Figure 7 shows the convergence of the residual error of the material removal at four iteration steps for the CPP shape. After the first plasma processing stage, the surface topography was generated and a residual figure error of 115.413 nm remained, after which a further three correction steps were applied, resulting in a residual figure error of 28.08 nm.

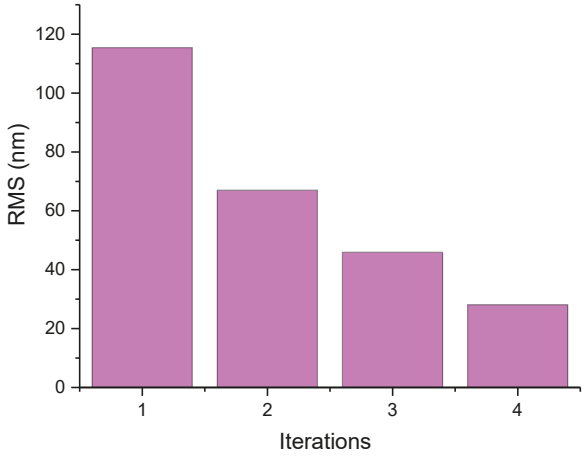

Figure 7. Convergence of the residual error at the four plasma processing iteration steps.

5. Discussion

The far-field characteristics of the surface shape can be analyzed using numerical simulation, whereby an ideal plane shines light through the component, making the far field of the modulated beam a direct reflection of the far-field characteristics of the CPP component, for which the wavelength λ = 633 nm and the focal distance d = 200 mm are used in the calculation. Figure 8 shows the far-field focal spot distribution of the prescribed surface and the plasma-processed surface, respectively. From the simulation results, the fabricated plasma has a reasonable beam-shaping function as the prescribed surface.

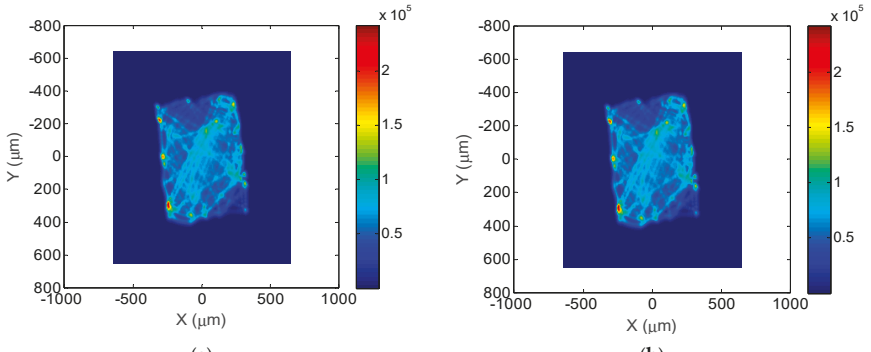

Figure 8. Far field distribution of the prescribed surface and plasma-processed surface: (**a**) Far-field distribution of prescribed surface; (**b**) Far-field distribution of plasma-processed surface.

To provide more information on the far-field distribution, the one-dimensional distributions of the far field focal spot are plotted in Figure 9. It can be seen from the figure that for the phase plate, the one-dimensional distribution of the focal spot is regular and the energy is concentrated. The cross-section profile of the plasma-processed surface is mainly consistent with prescribed surface profile, while the waveform of the intensity indicates non-uniformity of the energy distribution.

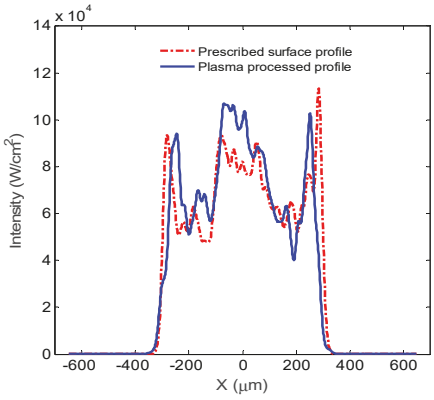

Figure 9. One-dimensional distribution of the focal spot.

The non-uniformity is scaled by the focal spot contrast in a circle with the energy included. The relationship between the energy proportion and the diameter from the centroid are given in Figure 10. The 90% encircled energy radius values for the prescribed surface and plasma-fabricated surface are 374 and 363 μm, respectively. The energy radius deviation is 11μm, which is less than the specification of 15 μm.

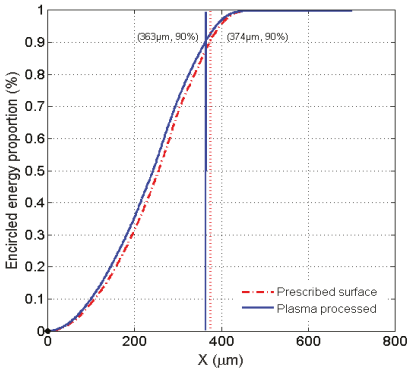

Figure 10. The relationship between the energy proportion and the diameter from the centroid.

6. Conclusions

In this paper, the figuring capability of the atmospheric pressure plasma jet technology for the spatial surface topography was proven at 28.08 nm RMS. An optimized iterative algorithm based on the dwell point matrix combined with the FFT convolution calculation method was proposed in order to improve the convergence accuracy and efficiency of the dwell time calculation. The experimental results verified that this optimized method could efficiently imprint a prescribed surface topography of 120 mm × 120 mm CPP with a residual figure error of 28.08 nm (RMS) after 1.6 h of plasma processing. Comparing the far-field focal spots of the prescribed CPP and fabricated CPP, the energy radius deviation was 11μm at 90% encircled energy. Meanwhile, the peak removal rate of the APPJ system reached 48 μm/min, showing the high efficiency of the system for large-aperture optics. This study provides a new technical option for the fabrication of large-aperture optics with complex surface topographies. Ongoing process development for the APPJ process is expected to confirm its effectiveness for surface structures of wide spatial wavelength ranges and its advantages for lightweight optical components such as SiC.

Author Contributions: Conceptualization, H.J.; investigation, C.T., H.L.; methodology, Y.Z.; resources, H.J., Y.L.; supervision, Y.L.; writing—original draft, H.J.; writing—review and editing, H.J., Y.Z., H.L. All authors have read and agreed to the published version of the manuscript.

Funding: This research was funded by the National Natural Science Foundation of China, grant number: 51505443, and Youth Talent Fund of Laser Fusion Research Center, China Academy of Engineering Physics, grant number: LFRC-PD006.

Acknowledgments: The authors would like to thank Wenhui Deng for the assistance in dwell time calculation, and Hongjun Liu for the assistance in APPJ processing. The authors also would like to sincerely thank the reviewers for their valuable comments on this work.

Conflicts of Interest: The authors declare no conflict of interest.

References

1. Baisden, P.A.; Atherton, L.J.; Hawley, R.A.; Land, T.; Menapace, J.A.; Miller, P.E.; Runkel, M.J.; Spaeth, M.L.; Stolz, C.J.; Suratwala, T.I.; et al. Large Optics for the National Ignition Facility. *Fusion Sci. Technol.* **2016**, *69*, 295–351. [CrossRef]
2. Moses, E.I.; Lindl, J.D.; Spaeth, M.L.; Patterson, R.W.; Sawicki, R.H.; Atherton, L.J.; Baisden, P.A.; Lagin, L.J.; Lar-son, D.W.; MacGowan, B.J.; et al. Overview: Development of the National Ignition Facility and the Transition to a User Facility for the Ignition Cam-paign and High Energy Density Scientific Research. *Fusion Sci. Technol.* **2016**, *69*, 1–24. [CrossRef]
3. Yang, C.; Yan, H.; Wang, J.; Zhang, R. A novel design method for continuous-phase plate. *Opt. Express* **2013**, *21*, 11171–11180. [CrossRef]
4. Hou, J.; Chen, X.H.; Li, J.; Zhong, B.; Deng, W.H. Processing technology of magnetorheological finishing for large-aperture optical components. In Proceedings of the Optical Design and Fabrication, OSA Technical Digest, Washington, DC, USA, 10–12 June 2019; p. JT5A.22.
5. Menapace, J.A.; Davis, P.J.; Steele, W.A.; Hachkowski, M.R.; Nelson, A.; Xin, K. MRF applications: On the road to making large-aperture ultraviolet laser resistant continuous phase plates for high-power lasers. In Proceedings of the Boulder Damage Symposium XXXVIII: Annual Symposium on Optical Materials for High Power Lasers, Boulder, CO, USA, 25–27 September 2006; p. 64030N.
6. Lindl, J.; Landen, O.; Edwards, J.D.M.; Moses, I.E.; NIC Team. Review of the National Ignition Campaign 2009–2012. *Phys. Plasmas* **2014**, *21*, 020501. [CrossRef]
7. Menapace, J.A.; Ehrmann, P.E.; Bayramian, A.J.; Bullington, A.; Di Nicola, J.G.; Haefner, C.; Jarboe, J.; Marshall, C.; Schaffers, K.I.; Smith, C. Imprinting high-gradient topographical structures onto optical surfaces using magnetorheo-logical finishing: Manufacturing corrective optical elements for high-power laser applications. *Appl. Opt.* **2016**, *55*, 5240–5248. [CrossRef] [PubMed]
8. Xu, M.; Dai, Y.; Xie, X.; Zhou, L.; Peng, W. Fabrication of continuous phase plates with small structures based on recursive frequency filtered ion beam figuring. *Opt. Express* **2017**, *25*, 10765. [CrossRef]
9. Xu, M.; Dai, Y.F.; Xie, X.; Zhou, L.; Li, S.; Peng, W. Ion beam figuring of continuous phase plates based on the fre-quency filtering process. *Front. Mech. Eng.* **2017**, *12*, 110–115. [CrossRef]
10. Jourdain, R.; Castelli, M.; Shore, P.; Sommer, P.; Proscia, D. Reactive atom plasma (RAP) figuring machine for meter class optical surfaces. *Prod. Eng.* **2013**, *7*, 665–673. [CrossRef]
11. Yu, N.; Yang, Y.; Jourdain, R.; Gourma, M.; Bennett, A.; Fang, F. Design and optimization of plasma jet nozzles based on computational fluid dynamics. *Int. J. Adv. Manuf. Tech.* **2020**, *108*, 2559–2568. [CrossRef]
12. Yang, X.; Kawai, K.; Arima, K.; Yamamura, K. Highly efficient planarization of sliced 4H–SiC (0001) wafer by slurry-less electrochemical mechanical polishing. *Int. J. Mach. Tool Manuf.* **2019**, *144*, 103431. [CrossRef]
13. Sun, R.; Yang, X.; Watanabe, K.; Miyazaki, S.; Fukano, T.; Kitada, M.; Arima, K.; Kawai, K.; Yamamura, K. Etching Characteristics of Quartz Crystal Wafers Using Argon-Based Atmospheric Pressure CF4 Plasma Stabilized by Ethanol Addition. *Nanomanuf. Metrol.* **2019**, *2*, 168–176. [CrossRef]
14. Arnold, T.; Böhm, G.; Fechner, R.; Meister, J.; Nickel, A.; Frost, F.; Hänsel, T.; Schindler, A. Ultra-precision surface finishing by ion beam and plasma jet techniques—Status and outlook. *Nucl. Instrum. Methods Phys. Res. Sect. A Accel. Spectrometers Detect. Assoc. Equip.* **2010**, *616*, 147–156. [CrossRef]
15. Kazemi, F.; Boehm, G.; Arnold, T. Development of a model for ultra-precise surface machining of N-BK7 using mi-crowave-driven reactive plasma jet machining. *Plasma Process Polym.* **2019**, *e1900119*, 1–14.
16. Arnold, T.; Bohm, G.; Kazemi, F. Advances in precision freeform manufacturing by plasma jet machining-INVITED. *EPJ Web Conf.* **2020**, *238*, 03001. [CrossRef]
17. Su, X.; Zhang, P.; Liu, K.; Xia, L.G.; Li, P.; Zhao, R.C.; Wang, B. Fabrication of continuous phase plate using atmos-pheric pressure plasma processing. *Int. J. Adv. Manuf. Technol.* **2019**, *105*, 4559–4570. [CrossRef]
18. Li, D.; Li, N.; Su, X.; Liu, K.; Ji, P.; Wang, B. Continuous Phase Plate Structuring by Multi-Aperture Atmospheric Pressure Plasma Processing. *Micromachines* **2019**, *10*, 260. [CrossRef]
19. Li, D.; Li, N.; Su, X.; Liu, K.; Ji, P.; Wang, B. Modelling of removal characteristics and surface morphology formation in capacitively coupled atmospheric pressure plasma processing of fused silica optics. *Opt. Mater. Express* **2019**, *9*, 1893–1906. [CrossRef]

20. Wang, C.J.; Yang, W.; Wang, Z.Z.; Yang, X.; Hu, C.L.; Zhong, B.; Guo, Y.B.; Xu, Q. Dwell-time algorithm for pol-ishing large optics. *Appl. Optics.* **2014**, *53*, 4752–4760. [CrossRef] [PubMed]
21. Li, L.X.; Xue, D.L.; Deng, W.J. Positive dwell time algorithm with minimum equal extra material removal in determin-istic optical surfacing technology. *Appl. Opt.* **2017**, *56*, 9098–9104. [CrossRef]
22. Huang, T.; Zhao, D.; Cao, Z.-C. Trajectory planning of optical polishing based on optimized implementation of dwell time. *Precis. Eng.* **2020**, *62*, 223–231. [CrossRef]
23. Wang, Y.; Zhang, Y.; Kang, R.; Ji, F. An Elementary Approximation of Dwell Time Algorithm for Ultra-Precision Computer-Controlled Optical Surfacing. *Micromachines* **2021**, *12*, 471. [CrossRef] [PubMed]

micromachines

MDPI

Article

Multi-Physics Coupling Modeling and Experimental Investigation of Vibration-Assisted Blisk Channel ECM

Juchen Zhang [1,2,*], Shasha Song [1], Junsheng Zhang [1], Weijie Chang [1], Haidong Yang [1], Huohong Tang [1] and Shunhua Chen [1]

[1] School of Mechanical Engineering, Hefei University of Technology, Hefei 230009, China; 2020110218@mail.hfut.edu.cn (S.S.); zhangjunsheng90@126.com (J.Z.); changwj1981@163.com (W.C.); yanghaidonghfut@126.com (H.Y.); tanghh@ustc.edu.cn (H.T.); shchen@hfut.edu.cn (S.C.)

[2] College of Mechanical and Electrical Engineering, Nanjing University of Aeronautics & Astronautics, Nanjing 210016, China

* Correspondence: zhangjuchen@hfut.edu.cn

Abstract: Due to its advantages of good surface quality and not being affected by material hardness, electrochemical machining (ECM) is suitable for the machining of blisk, which is known for its hard-to-machine materials and complex shapes. However, because of the unstable processing and low machining quality, conventional linear feeding blisk ECM has difficulty in obtaining a complex structure. To settle this problem, the vibration-assisted ECM method is introduced to machine blisk channels in this paper. To analyze the influence of vibration on the process of ECM, a two-phase flow field model is established based on the RANS k-ε turbulence model, which is suitable for narrow flow field and high flow velocity. The model is coupled with the electric field, the flow field, and the temperature field to form a multi-physics field coupling model. In addition, dynamic simulation is carried out on account of the multi-physics field coupling model and comparative experiments are conducted using the self-developed ECM machine tool. While a shortcut appeared in the contrast experiment, machining with vibration-assisted channel ECM achieved fine machining stability and surface quality. The workpiece obtained by vibration-assisted channel ECM has three narrow and straight channels, with a width of less than 3 mm, an aspect ratio of more than 8, and an average surface roughness *Ra* in the hub of 0.327 μm. Compared with experimental data, the maximum relative errors of simulation are only 1.05% in channel width and 8.11% in machining current, which indicates that the multi-physics field coupling model is close to machining reality.

Keywords: vibration-assisted electrochemical machining (ECM); blisk; narrow channel; high aspect ratio; multi-physics coupling simulation; machining stability

Citation: Zhang, J.; Song, S.; Zhang, J.; Chang, W.; Yang, H.; Tang, H.; Chen, S. Multi-Physics Coupling Modeling and Experimental Investigation of Vibration-Assisted Blisk Channel ECM. *Micromachines* **2022**, *13*, 50. https://doi.org/10.3390/mi13010050

Academic Editor: Jiang Guo

Received: 14 December 2021
Accepted: 26 December 2021
Published: 29 December 2021

Publisher's Note: MDPI stays neutral with regard to jurisdictional claims in published maps and institutional affiliations.

1. Introduction

Blisk is an important part of an advanced aeroengine [1]. However, owing to its extremely complex structure, difficult-machined material, and high manufacturing precision requirement, blisk machining has been an enormous challenge for the manufacturing industry [2]. As an advanced processing method removing materials in the form of ions, electrochemical machining (ECM) is accessible to achieve high surface quality, being free from the influence of the material hardness [3]. Therefore, ECM has become the main machining method of blisk [4]. Generally, blisk ECM is divided into two steps. That is, the cascade channel is pre-machined firstly in channel ECM and then the blisk surface is finished in profile ECM [5]. Due to the impact of memory error, a distribution of allowance before processing will seriously affect the profile ECM precision [6]. Thus, if the distribution of machining allowance after channel ECM is not uniform, it has a serious influence on the machining stability and accuracy in the following machining step [7]. Hence, blisk channel machining is a key machining process of blisk ECM.

Over the past few years, a considerable amount of research has been done in the blisk ECM process. Xu et al. proposed an efficient machining method of blisk channel ECM and presented an experimental system with the synchronous movement of three tool tubes, which can process multiple channels at the same time [8]. Zhu et al. proposed a method called rotating-cathode feeding electrochemical trepanning to homogenize the allowance distribution of twisted blades on a blisk in the roughing stage [9]. Wang et al. established a method of variable feed rate mode to process the cascade channel. This method could effectively reduce the difference of allowance in machining the blisk channel [10]. Klocke et al. constructed a simulation model of the ECM process for the engine blades and analyzed the changes of flow rate, gas volume fraction, temperature, and conductance in the ECM process [11]. Ernst et al. present an inverse approach for the tool optimization, and the tool shape for the desired vane geometry is calculated using a self-developed algorithm. The experimental validation of the simulated tool shape showed good results, especially for the forming of the flow surfaces and the leading edge [12].

Because of serious stray corrosion of non-machining surfaces in conventional linear or rotation feeding, it is difficult to get a complex curved surface with high precision. Numerous studies have focused on the application of electrode vibration in the ECM process to improve machining quality and stability. Hewidy et al. proposed a mathematical model for studying the mechanism of metal removal. The model shows that the hybrid ECM with low-frequency tool vibration has a positive effect on changing the physical conditions in the electrode gap [13]. Wang et al. processed a narrow slit by cathode compound feeding and proved that compound feeding can obtain a narrow slit with a more uniform average width [14]. Yue et al. showed that cathode vibration feed can improve the machining accuracy of micro-hole [15]. Bhattacharyya et al. studied the effect of the cathode vibration frequency on the machining accuracy of small holes [16]. Uhlmann et al. presented a new approach for modeling the development of surface roughness during vibratory finishing processes [17].

To reveal the coupling mechanism between the multiple physical fields and analyze the forming process of ECM, lots of researchers have established various theoretical models. For example, Klink et al. studied the formation of cavitation in ECM by investigating the electrolyte flow in narrow openings [18]. Zhao et al. optimized the hollow slice cathode structure and vibrating parameters by simulating the flow field [19]. Qu et al. proved that progressive pressure flow gives a high electrolyte flow rate through simulation, allowing a high cathode feed rate without a shortcut [20]. Tang et al. applied the electrolyte flow field mathematics models and the 3D gap flow field simulation geometric model to carry out the simulation research [21].

Blisk channel ECM has a narrow and twisted machining gap, in which parameters such as temperature, gas volume fraction, and electrolyte velocity change tremendously. Therefore, it is difficult to keep the process steady and obtain a high machining quality [22]. Vibration may be an effective way to improve machining stability and quality. So, this study adopted a cathode vibration feed ECM method for machining blisk channels. A cathode feeds towards the workpiece with a vibration movement of a cosine function curve, thereby improving the allowance uniformity of the machined blisk channel [23]. To analyze the influence of vibration on the forming process of ECM, the multi-physical field coupling model is established and the dynamic simulation is carried out based on the parameter transfer law of ECM. The effects of vibration ECM on electrolyte flow rate, bubble rate, conductivity, and stability were studied. The influence of each physical field on blisk channels ECM is analyzed, which provides theoretical guidance for experiments. Finally, experiments were carried out using the self-developed ECM machine tool to verify simulation results. To evaluate machining quality, the surface profile and workpiece geometrical size were measured.

2. Geometric Model of Blisk Channel Electrochemical Machining (ECM)

Figure 1 shows a schematic diagram of the blisk channel ECM process. During the channel ECM process, the workpiece is connected to the positive pole of the power supply and the cathode is connected to the negative pole of the power supply to form a closed circuit. Normally, a reduction reaction occurs on the surface of the cathode, and an oxidation reaction takes place on the surface of the workpiece. Electrolyte flows through the machining gap between the cathode and the workpiece at a high speed to take away the hydrogen, electrolytic products and remove the heat generated in the ECM process. After the channel machining is finished, the cathode returns to its initial position and the workpiece rotates for a certain angle to process the next channel.

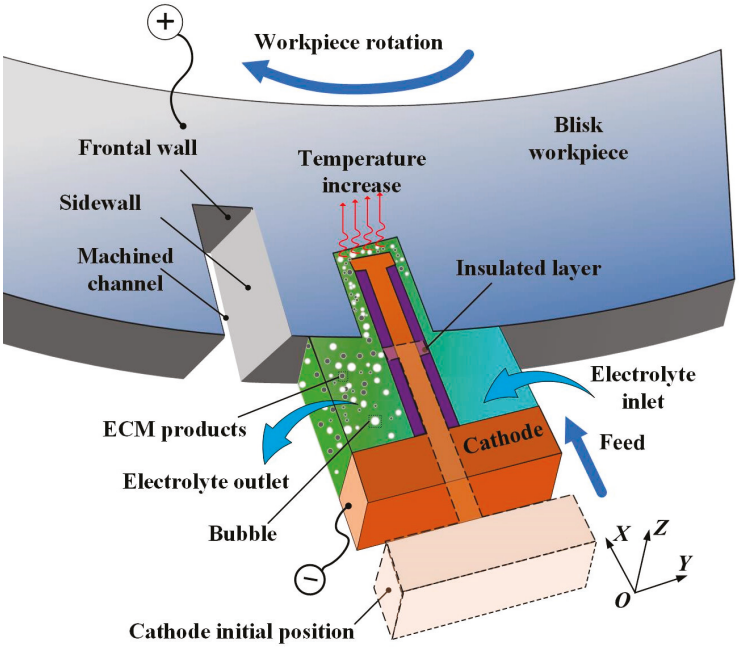

Figure 1. Principle of blisk channel electrochemical machining (ECM).

3. Establishment of the Multi-Physical Coupling Model

3.1. The Interaction of Physical Fields in Electrochemical Machining (ECM)

This paper studies the influence of cathode vibration feed on electrochemical machining. The coupling relations among the physical fields in channel ECM are shown in Figure 2. ECM is a complex machining process, including the electric field, the flow field, and the temperature field, these physical fields coupling each other and affecting the material removal on the workpiece. The change of a single physical field factor often affects the rest of the physics parameters and machining stability, resulting in the change of final machining stability and workpiece profiles. Therefore, it is of great significance to explore the dynamic forming process of ECM under coupling multi-physics.

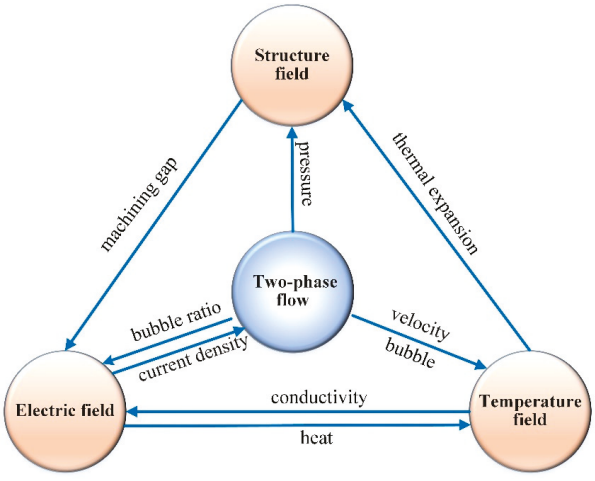

Figure 2. Multi-physical coupling relationship of ECM.

3.2. Electric Field Modeling

To simplify electric field modeling, the following assumptions are made in the model:

(1) Electrolyte concentration polarization and electrochemical polarization are not considered in the ECM process, and the surface of the anode material is always assumed to be in an activated state [24].

(2) ECM process has entered an equilibrium state, which is only a function of position space and belongs to a steady-state current field [25].

(3) The machining products are uniformly corroded from the material surface, and the products have only a certain valence [26].

(4) The electrolyte used in ECM is isotropic and, therefore, the potential distribution of the electric field conforms to Laplace's equation [27]. The model is established as follows:

$$\frac{\partial^2 \varphi}{\partial x^2} + \frac{\partial^2 \varphi}{\partial y^2} = 0 \tag{1}$$

where φ is the potential in the inter-electrode gap, x and y are the coordinate values of each point in the model.

In the electric field simulation of ECM, the cathode is connected with the negative pole of the power supply and the anode is connected with the positive pole of the power supply. The potential of the anode surface is defined as U and the potential of the cathode surface is 0. Therefore, the first kind of boundary condition is satisfied in the electric field model [28]:

$$\begin{cases} \varphi|\tau_1 = 0 \\ \varphi|\tau_8 = U \end{cases} \tag{2}$$

For the other boundary, the second boundary condition is satisfied:

$$\left.\frac{\partial \varphi}{\partial n}\right|\tau_{2,3,4,5,6,7,9,10,11,12} = 0 (\text{Insulation boundary}) \tag{3}$$

The electric field intensity of each point in the processing zone is equal to the negative value of the potential gradient of the point [29]:

$$\vec{E} = -\nabla \varphi \tag{4}$$

For the electrolyte in the processing area, the relation between the current density, the electric field strength, and conductivity is as follows [30]:

$$\vec{i} = \kappa \vec{E} \tag{5}$$

where i is current density, κ is the electrolyte conductivity and E is electric field strength. The above formulas are the electric field mathematical model of ECM, which can be introduced into the Laplace equation to solve the electric field distribution at any point in the machining area. Combined with the Lagrange-Euler (ALE) method, the dynamic simulation under the action of the electric field can be completed.

3.3. Flow Field Modeling

In the process of ECM, hydrogen and hydroxide products are generated near the cathode surface and anode surface, respectively. Since it is reasonable to neglect the influence of the hydroxide products, a two-phase flow is adopted in the model. In the turbulent bubble flow module, it is assumed that the gas produced by electrolysis follows the ideal gas state equation and the current efficiency is approximately constant.

The flow field in the gap of the machining area is a typical gas-liquid two-phase flow. The continuous equation of liquid phase mass in the gap of electrochemical machining area is shown in Equation (6); the mass equation of hydrogen gas phase is shown in equation:

$$(1 - \beta)\Delta u = \Delta_0 u_0 \tag{6}$$

$$\frac{p}{R_g T}\beta \Delta u = \eta_g k_g i x \tag{7}$$

in which β is bubble rate, p is pressure, η_g is current efficiency of hydrogen evolution, k_g is hydrogen evolution mass electrochemical equivalent, and R_g is hydrogen gas state parameter.

The influence of the bubble and temperature distributions on the electrolyte conductivity is expressed as follows [31]:

$$\kappa = \kappa_0[1 + \alpha(T_k - T_0)][1 - \beta]^n \tag{8}$$

in which κ_0 is the initial electrolyte conductivity, α is the temperature coefficient of conductivity, T_k is the electrolyte temperature, and T_0 is the initial electrolyte temperature. β is the void fraction, n is the influence coefficient of bubble rate on conductivity, usually 1.5–2. On the one hand, the bubble rate increases in the ECM process, which leads to a decrease in electrolyte conductivity. On the other hand, the increase in electrolyte temperature will cause an increase in electrolyte conductivity.

According to Faraday's law, the amount of hydrogen produced per unit of time and per unit of area on the surface of the cathode can be obtained [32]:

$$\beta = \frac{Mi\eta}{2F} \tag{9}$$

where M is the molar mass of hydrogen, i is current density, F is Faraday's constant, F = 96,500 [A·s·mol], and η is current efficiency.

According to the existing actual processing conditions, electrolyte velocity is u = 16 m/s, the hydraulic diameter is D_h = 0.97 mm, and the kinematic viscosity of 10% sodium nitrate solution is ν = 0.80 × 10^{-6} m^2/s under the condition of 30 °C. The Reynolds number is calculated by the equation:

$$R_e = \frac{uD_h}{\nu} = 1.94 \times 10^4 \tag{10}$$

According to the Reynolds number, the electrolyte is in a turbulent state (R_e >> 2300) [33]. Considering the influence of bubbles, the RANS *k*-ε turbulence model is suitable for the current situation and is adopted to simulate the flow field in this study [34].

$$\frac{\partial_k}{\partial_T} + \nabla\left[k\vec{u} - \left(v + \frac{v_T}{\sigma_k}\right)\nabla k\right] = P_k + S_k - \varepsilon \tag{11}$$

$$\frac{\partial_\varepsilon}{\partial_t} + \nabla\left[\varepsilon\vec{u} - \left(v + \frac{v_T}{\sigma_\varepsilon}\right)\nabla\varepsilon\right] = \frac{\varepsilon}{k}(C_1P_k + C_\varepsilon S_k - C_2\varepsilon) \tag{12}$$

$$P_k = \frac{v_T}{2}|\nabla_{\vec{u}} + \left(\nabla_{\vec{u}}\right)^T|^2 \tag{13}$$

$$S_k = -\beta C_k|\nabla_p|^2 \tag{14}$$

where k is the turbulent energy, ε is the turbulent dissipation, P_k is the generating term of turbulent energy, σ_k and σ_ε are Prandtl numbers corresponding to "k" and "ε", u is the flow velocity, and C_1, C_2, C_ε, C_k, δ_ε is the model constant.

3.4. Temperature Field Modeling

The temperature distribution in the machining gap can be calculated by the convection–diffusion equation [35]:

$$d_z\rho C_P\frac{\partial T}{\partial t} + d_z\rho C_P u\nabla T + d_z\nabla(-\lambda\nabla T) = d_z H + q_0 \tag{15}$$

where d_z is the thickness of the boundary layer, C_p is the electrolyte-specific heat capacity, λ is the electrolyte thermal conductivity, q_0 is initial heat flux, u is velocity field of the liquid phase of electrolyte, ρ is the density of the electrolyte, and H is the heat source, the Joule heat generated in the flow channel.

The Joule heat H generated in the flow channel is as follows [36]:

$$H = E \times j \tag{16}$$

where E is electric field strength, j is the local current density.

The convective heat flux at the surface boundary of cathode and anode is as follows:

$$q_1 = h \times (T_{ext} - T_k) \tag{17}$$

where q_1 is convective heat flux, h is heat transfer coefficient and T_{ext} is external temperature.

3.5. Deformation Field

There are two main feeding methods in ECM: linear feed and cathode vibration feed. In the linear feed mode, the cathode moves in a straight line at a constant speed and its feed trajectory is linear, which can be expressed by the equation:

$$s = B_0 + V_1 \times t \tag{18}$$

The cathode vibration feed makes a periodic vibration with a certain amplitude while making a linear feed motion, and its trajectory is a sinusoidal motion of continuous feed, which can be expressed by the equation:

$$s = B_0 + V_1 \times t - A_0\cos wt \tag{19}$$

where s is cathode position, B_0 is initial machining clearance, V_1 is the cathode feed rate, t is the machining time, A_0 is the amplitude of the displacement of the tool cathode, and ω is angular velocity.

Figure 3 is a comparison of the cathode movement law in the two feed modes. The cathode vibration feed mode is developed from the linear feed method, with an auxiliary back and forth movement. When the vibration frequency is 0, it is the linear feed mode.

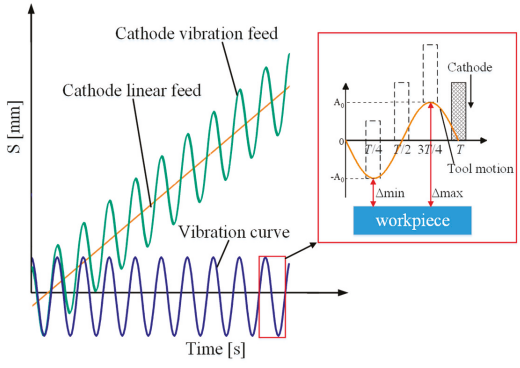

Figure 3. The law of cathode movement.

4. Simulation Analysis

4.1. Model Description

It is shown in Figure 1 that the cross-sectional shape is approximately the same when its normal direction of the section is *Z*. Therefore, a two-dimensional cross-sectional shape is employed to simplify the research problem, thus reducing the amount of calculation in the simulation process and improving the simulation efficiency.

Based on the above multi-field coupling model, COMSOL Multiphysics 5.4 is used to carry out a multi-physics simulation of the ECM process of the blisk channel. The 2D model and mesh division of the simulation is shown in Figure 4. Since the dynamic simulation will lead to a large deformation on the anode surface, the partial mesh at the anode boundary area with large deformation is refined locally to ensure the accuracy of the simulation results.

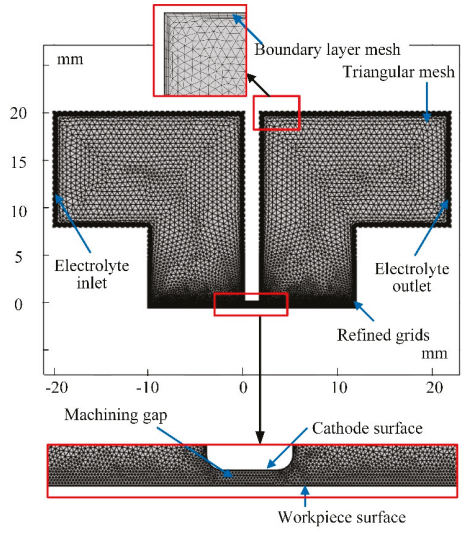

Figure 4. Mesh generation of the model.

4.2. Parameters Setting

The relevant parameters should be set before the simulation analysis. The simulation parameters of the multi-physical field coupling model are consistent with the actual machining. The process parameters are shown in Table 1.

Table 1. Simulation parameters.

Symbol	Definition	Value	Unit
T_0	Initial temperature	303.15	K
P_0	Inlet pressure	0.3	MP_a
P_1	Outlet pressure	0	MP_a
V_0	Feed rate	0.5	mm/min
k_0	Electrolyte conductivity	7.6	S·m
U	Processing voltage	22	V
f	Frequency of oscillation and pulse	5	Hz
A	Amplitude	0.2	mm

4.3. Boundary Condition

The dynamic simulation under the action of ECM multi-physical field coupling is carried out by using COMSOL software's four modules: primary current distribution, deformation geometry, bubble flow *k*-*ε* (RANS *k*-*ε*), and fluid heat transfer. The simulation model of ECM multi-physical field coupling is shown in Figure 5 and the boundary conditions are shown in Table 2.

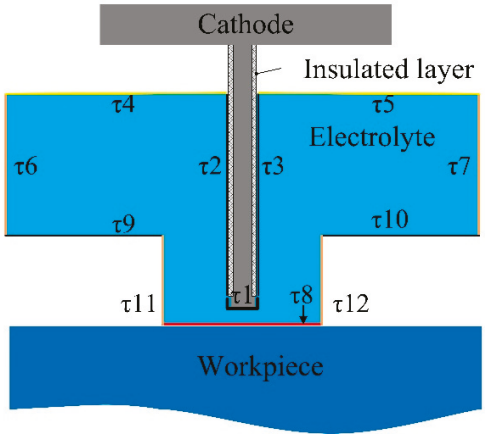

Figure 5. Boundary distribution in simulation.

4.4. Simulation Results and Discussion

The cathode vibrates according to the cosine curve and the machining gap changes periodically. In a single vibration cycle, three cathode positions under the balance state of vibrational feed ECM are selected, which are the nearest cathode position to the anode ($t = T/4$), cathode at the middle position ($t = T/2$), and cathode at its farthest position to the anode ($t = 3T/4$).

Table 2. Boundary conditions setting of multiple physical fields.

	Boundary	Condition Setting
Flow Field	$\tau 1$	The gas flux $V_H = (H_2 \cdot cd.IlMag)/(2 \cdot F)$
	$\tau 2$, $\tau 3$, $\tau 4$, $\tau 5$, $\tau 8$, $\tau 9$, $\tau 10$, $\tau 11$, $\tau 12$	No sliding wall and no gas flux at the boundary
	$\tau 6$	Electrolyte inlet, pressure boundary (0.3 MPa)
	$\tau 7$	Electrolyte outlet, pressure boundary (0 MPa)
Temperature Field	M	Heat source, total power density
	$\tau 1$, $\tau 8$	Boundary heat source of electrochemical reaction
	$\tau 2$, $\tau 3$, $\tau 4$, $\tau 5$, $\tau 9$, $\tau 10$, $\tau 11$, $\tau 12$	Natural convection heat flux
	$\tau 6$, $\tau 7$	Temperature boundary, 303.15 K
Electric Field	$\tau 1$	Cathode surface, $U = 0$
	$\tau 8$	Anode surface, $U = 20$ V
	$\tau 2$, $\tau 3$, $\tau 4$, $\tau 5$, $\tau 6$, $\tau 7$, $\tau 9$, $\tau 10$,$\tau 11$, $\tau 12$	$\frac{\partial \varphi}{\partial n}\Big\vert_{\tau 2,3,4,5,6,7,9,10,11,12} = 0$ (Insulation boundary)
	M	$\kappa = \kappa_0[1 + \alpha(T_k - T_0)][1 - \beta]^n$

Figure 6 shows the velocity distributions at different times in the ECM simulation. In the maps of velocity distribution at different times, it can be seen intuitively that the flow of electrolyte in the machining area is 0.179 L/s at $T/4$. With the retreat of the cathode caused by vibrational motion, the maximum flow reaches 0.219 L/s at $T/2$ and 0.256 L/s at $3T/4$. Therefore, the renewal of the electrolyte and the exhaustion of the electrolysis products are improved by the increase of electrolyte flow velocity. The improvement in the flow field is beneficial to reinforce the machining stability and accuracy of blisk channels machining.

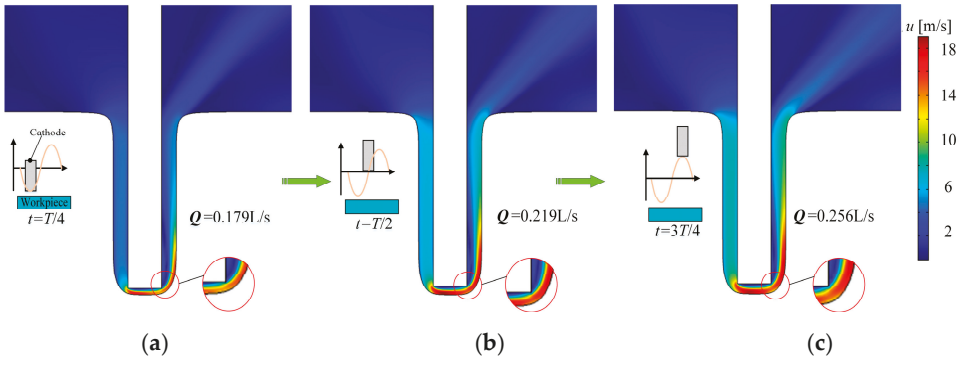

Figure 6. Distributions of electrolyte velocity over time; (**a**) $t = T/4$. The nearest cathode position to the anode, the maximum flow is 0.179 L/s; (**b**) $t = T/2$. Cathode at the middle position, the maximum flow increases to 0.219 L/s; (**c**) $t = 3T/4$. Cathode at its farthest position to the anode, the maximum flow reaches 0.256 L/s.

The temperature distributions in the machining area in a unit cycle are obtained through transient simulation, as shown in Figure 7. The heat generated in the ECM process gradually accumulates and the temperature in the machining gap gradually increases along the flow direction. Due to the small machining gap and increasing machining depth, the heat is difficult to eliminate. The temperature is 303 K in the inlet wall and increases to 308 K to the side of the outlet at $T/4$, as shown in Figure 7a. Figure 7b,c indicate that when the cathode moves far away from the workpiece, the machining gap becomes larger, and therefore, the flushing electrolyte quickly takes away the heat and reactants.

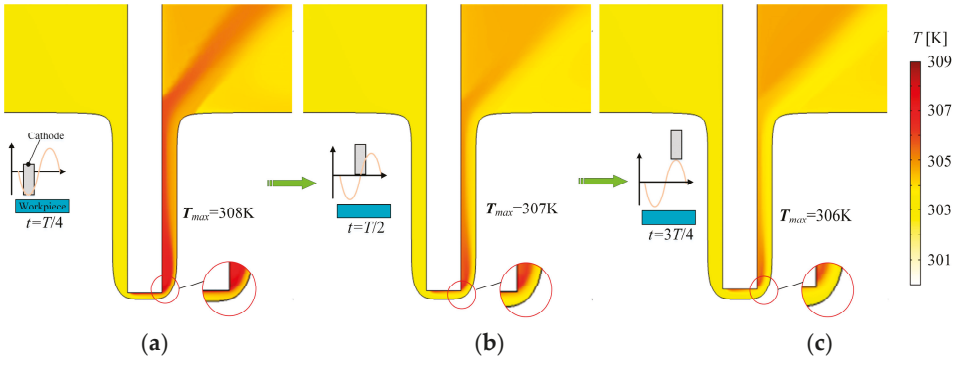

Figure 7. Distributions of electrolyte temperature over time; (**a**) $t = T/4$. The maximum temperature is 308 K at the cathode's nearest position to anode; (**b**) $t = T/2$. The maximum temperature drops to 307 K at the middle position; (**c**) $t = 3T/4$. The maximum temperature is 306 K at the farthest position.

To study the temperature evolution more exactly, the line between the cathode and the anode is used as a reference line. We plotted the curves of temperature along this line in Figure 8. It is observed that the temperature near the inlet is much lower than that near the outlet. Thus, the temperature in the channel increases along the direction of electrolyte flow. The maximum temperature appears on the outlet side and its value is 307.5 K at $T/4$. The temperature in the whole line has an evident drop at $T/2$ and $3T/4$. The maximum temperature in this line drops to 305.5 K and it still appears at the outlet side at $3T/4$. This is consistent with the result shown in Figure 7.

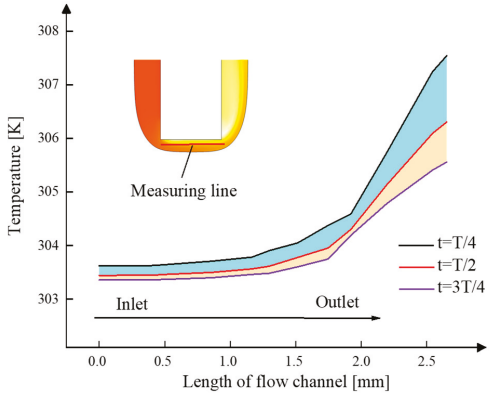

Figure 8. Temperature distribution of electrolyte near the cathode.

The evolution of gas-phase volume fraction in the machining area in a unit cycle is obtained through a transient simulation shown in Figure 9. The volume fraction of gas in the whole gap increases over time and its content becomes higher along the flow direction, as shown in Figure 9a. The volume fraction of hydrogen bubble rises to 0.12 at $T/4$. In comparison, when the cathode moves away from the anode, it drops dramatically. As shown in Figure 9b,c, when the cathode moves away from the anode, the maximum value of the bubble volume fraction drops to 0.09. Therefore, the gas volume fraction drops greatly and thus the flow field of electrolyte in the inter-electrode gap is optimized obviously.

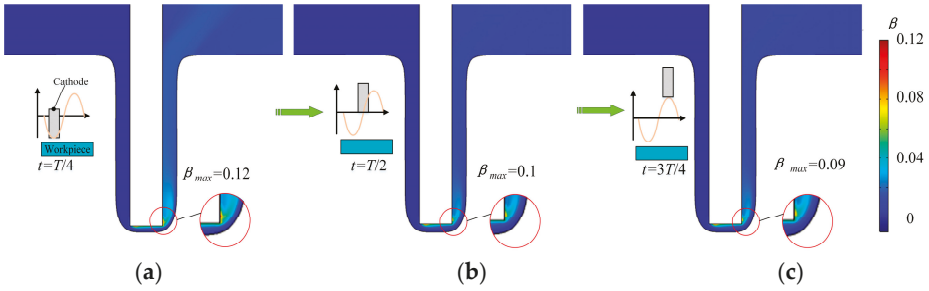

Figure 9. Distributions of gas-phase volume fraction over time; (**a**) $t = T/4$. The maximum volume fraction of hydrogen bubble is 0.12 at the cathode's nearest position to anode; (**b**) $t = T/2$. The maximum volume fraction of the hydrogen bubble is 0.1 at the middle position; (**c**) $t = 3T/4$. The maximum volume fraction of the hydrogen bubble is 0.1 at the cathode's farthest position.

Figure 10 presents the curves of electrolyte volume fraction along the flow direction during one period. The volume fraction of hydrogen increases along the direction of electrolyte flow in the machining area. The vibration of the tool cathode has a significant influence on the diffusion of gas bubbles. As the cathode moves away from the workpiece, the gas volume fraction starts to drop. The maximum gas fraction drops from 8.2% at $T/4$ to 1.9% at $3T/4$. The drop of the gas fraction is of great benefit to improve the machining stability and quality.

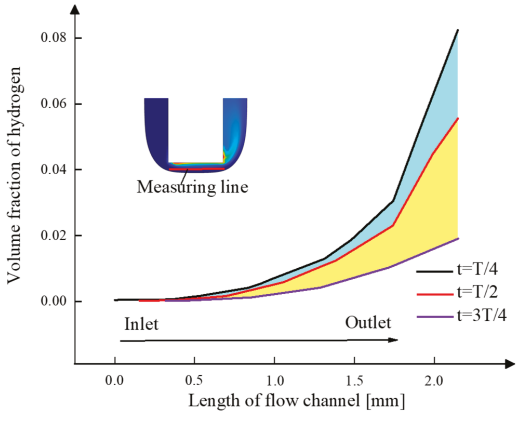

Figure 10. The volume fraction of hydrogen distribution of electrolyte.

5. Experiment Analysis

5.1. Experimental Design

To verify the simulation results, machining experiments are conducted with an ECM machine tool, as shown in Figure 11. This system comprises the rotary platform, feed and vibration system, power supply, electrolyte circulation and filtration system, processing fixture, and integrated control system. The processing fixture and its flow field are shown in Figure 12. The ECM fixture provides a sealed flow channel with the cathode and workpiece. The electrolyte flow form is a side flow type, in which the electrolyte inlet and the electrolyte outlet are at the different sides of the fixture. The high-speed electrolyte flows into the machining area from the electrolyte inlet pipe, passes through the inter-electrode gap, and returns to the electrolyte circulation system for filtering and recycling.

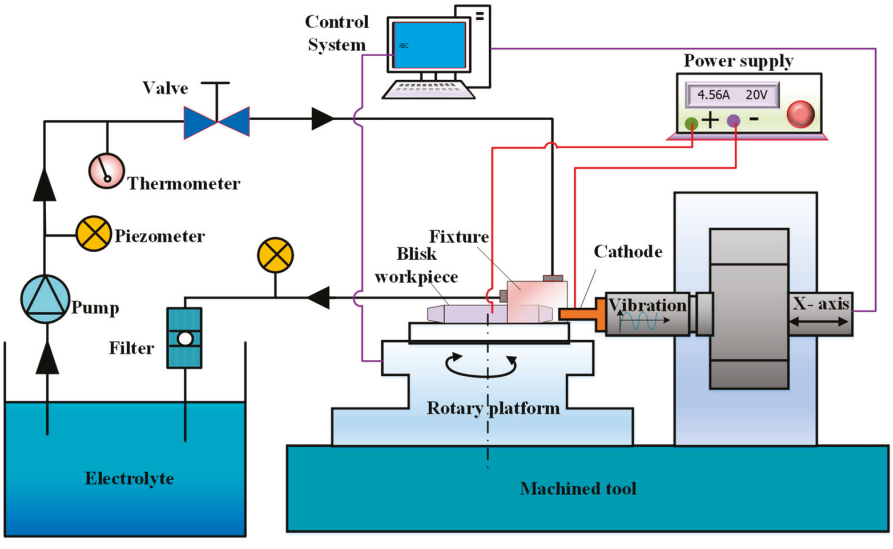

Figure 11. The set-up for electrochemical machining.

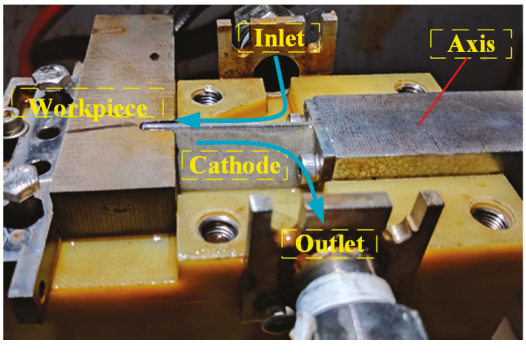

Figure 12. Electrochemical machining fixture.

In the experiments, samples of Inconel 718 superalloy are chosen as the workpiece (anode). The electrolyte is 10% $NaNO_3$ and its temperature is 30 °C. The electrolyte is pumped through the channel at a high speed by the constant pressure pump and the electrolyte pressure at the inlet is 0.3 MPa. The power supply is 22 V. To investigate the influence of the cathode feed mode on the machining stability, contrast experiments using a cathode linear feed are also performed. Workpieces have the same feed velocity of 0.5 mm/min in the two modes. After machining, the width of the machined channel is measured along the depth direction.

5.2. Analysis of Experimental Results

Figure 13 shows the variation of the channel width in different feed modes. The average width of the blisk channel processed through vibration-assisted channel ECM is slightly wider than that processed through the linear feed ECM without vibration. Figure 14 shows the morphologies of the channel in the two types of feed modes.

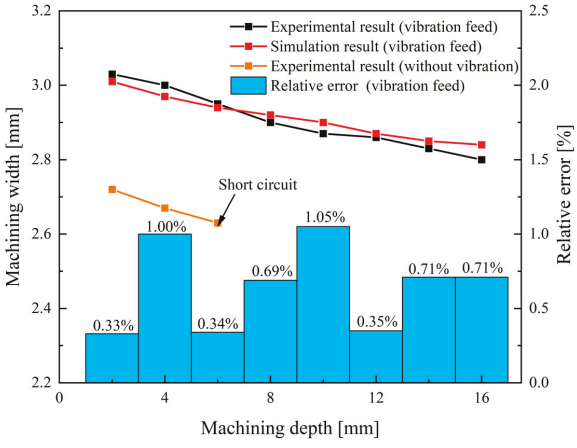

Figure 13. Variation of the channel width with different feed modes.

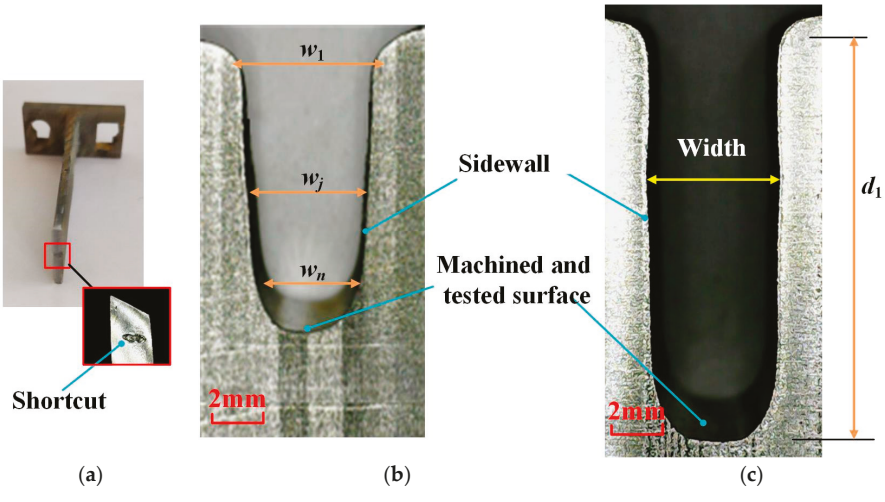

Figure 14. Morphology of blisk channels under different feed modes; (**a**) shortcut region of the cathode; (**b**) workpiece obtained in contrast experiment; (**c**) workpiece obtained by the vibration-assisted channel ECM.

A short circuit occurs between the anode and cathode when the machined depth is 7 mm in the contrast experiment. The shortcut region is located at the front of the cathode, shown in Figure 14a. Since electrolytic products and heat are generated in the machining process, it requires high-speed flowing electrolyte to take them away from the machining area. As machining depth grows, the narrow flow channel becomes longer and the pressure loss in the flow passage increases. As a result, when the electrolyte flow speed decreases more and more dramatically, products and heat cannot be completely removed from the machining area, affecting the stability of machining.

In the vibration-assisted channel ECM experiment, the sidewalls are close to straight lines and the width of the channel has no obvious change, as shown in Figure 14c. The vibration produces a strong suction effect in the machining gap. Moreover, when the cathode goes back, it is helpful to update the electrolyte and accelerate the heat exchange,

which can effectively avoid the occurrence of a short circuit phenomenon. Therefore, compared with the linear feed mode, the machining stability and the machining quality of the ECM of the blisk channel are improved in the vibration feed mode.

In this paper, sidewall taper θ of the channel is defined as follows [37]:

$$\text{Taper}(\theta) = \frac{\text{atan}(w_1 - w_n)}{2d_1} \tag{20}$$

where d_1 is the depth of the machined channel, w_1 is the width of a machined channel on the outside position, and w_n is the width of a machined channel on the inside position. The sidewall taper of the blisk channel processed through the cathode linear feed is 0.86°. When the cathode was fed by vibration, the width of a channel was enlarged, while the taper was 0.82° and the change of taper is not obvious.

The effects of the cathode feed mode on the machining accuracy are investigated by analyzing the average of the machined channel width $\overline{w}$, the standard deviation width of the machined channel σ_a and σ_b. The average machined channel width $\overline{w}$ is defined as follows:

$$\overline{w} = \frac{w_1 + w_2 + \ldots w_n}{n} \tag{21}$$

The standard deviation of the machined channel width σ_1 and σ_2 are defined as follows:

$$\sigma_a = \sqrt{\frac{\sum_{\Sigma=1}^{n} \left(w_j - \overline{w}\right)^2}{n}} \tag{22}$$

$$\sigma_b = \sqrt{\frac{\sum_{\Sigma=1}^{n} \left(w_j - w_{\theta j}\right)^2}{n}} \tag{23}$$

$$w_{\theta j} = w_1 - 2 \times D_{1j} \times \tan\theta \tag{24}$$

where w_j is the width of a machined channel in the j position, $w_{\theta j}$ is the width of a machined channel in the j position on the taper line, and D_{1j} is the distance between position 1 and position j. The standard deviation of the machined channel width σ_a reflects the straightness of the sidewall, which is affected by the taper to some extent. The standard deviation width σ_b eliminates the influence of taper. Table 3 demonstrates the average of the machined channel width and the standard deviation width with different feed modes. The channel obtained by the vibration-assisted channel ECM method was wider than that obtained in the contrast experiment. Since a short circuit appeared in the contrast experiment, the depth of the channel obtained in the contrast experiment was shorter than the other one. For that, the value of σ_a (=0.0076 mm) is much higher than σ_b (=0.0027 mm), thus taper of the channel has an obvious influence on the channel profile. The value of σ_b is only 0.0027 mm in the whole channel (with a depth of 16 mm), which also indicates that the process is very stable.

Table 3. Evaluation of the machined channel width.

	Experimental Result (Vibration)	**Simulation Result (Vibration)**	**Experimental Result (without Vibration)**
θ (°)	0.82°	0.61°	0.86°
$\overline{w}$ (mm)	2.905	2.912	2.673
σ_a (mm)	0.076	0.056	0.037
σ_b (mm)	0.027	0.024	0.012

Figure 15 demonstrates the machined workpiece with vibration-assisted channel ECM. The workpiece obtained by the cathode vibration feed method has three narrow channels, with a width of less than 3 mm and an aspect ratio of more than 8. Figure 16 shows the changes of current in the machining area recorded in the experiment and simulation over

time. The current in channel machining rose from 13.01 A at the beginning to 35.94 A at 211 s (current rising period) and then kept almost constant (stable machining state). The current achieved a stable state during processing in the balance period, which indicates the process is reliable. It was obvious that the trend of change of experimental current and simulation current density is roughly the same, with the maximum relative error of only 8.11%, as shown in Figure 16.

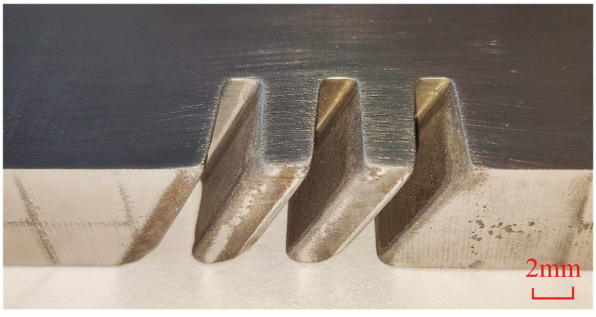

Figure 15. Machined specimen with the channels.

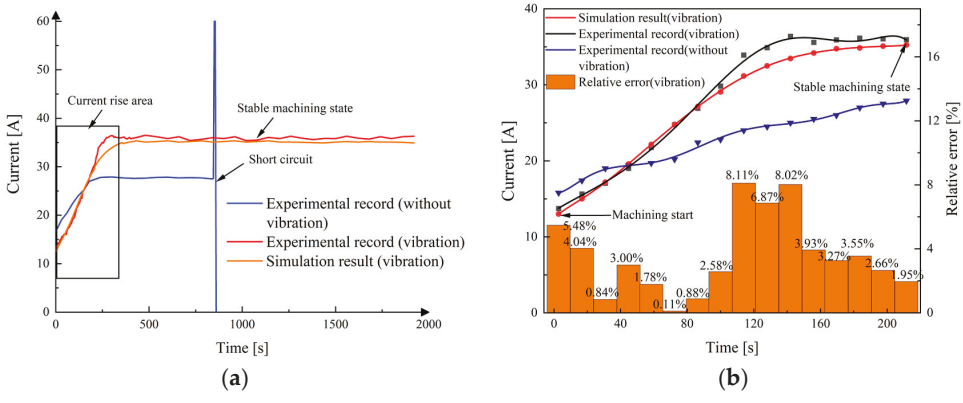

Figure 16. The changes of machining current experiment and simulation over time; (**a**) whole machining time; (**b**) enlarged view of current in rising time.

To evaluate the surface quality, the JD-520 roughness tester was used to measure the roughness of the hub, electrolyte inlet wall, and outlet wall. The machined surfaces of the specimens were measured using the roughness tester. Then, the surface profile curves were obtained, as shown in Figure 17. The values of roughness *Ra* are listed in Figure 18. The average surface roughness *Ra* in the hub, the sidewall close to the inlet, and the sidewall close to the outlet are 0.327 µm, 1.197 µm, and 1.992 µm, respectively. The value of *Ra* at the hub is lower than that at the sidewalls. One of the reasons is that the electrolyte flow rate near the hub is higher than that near the electrolyte inlet and outlet. The other reason is that secondary corrosion occurs at the machined sidewall, resulting in the decreases of the surface roughness and surface quality of the sidewall. At the same time, it is observed that the value of *Ra* in the sidewall close to the inlet is less than the sidewall close to the outlet. The reason for the different machining quality is that when most products and bubbles are generated in the hub of the blisk channel, the electrolyte carries the electrolytic products to the outlet, resulting in uneven changes in conductivity and affecting the surface quality.

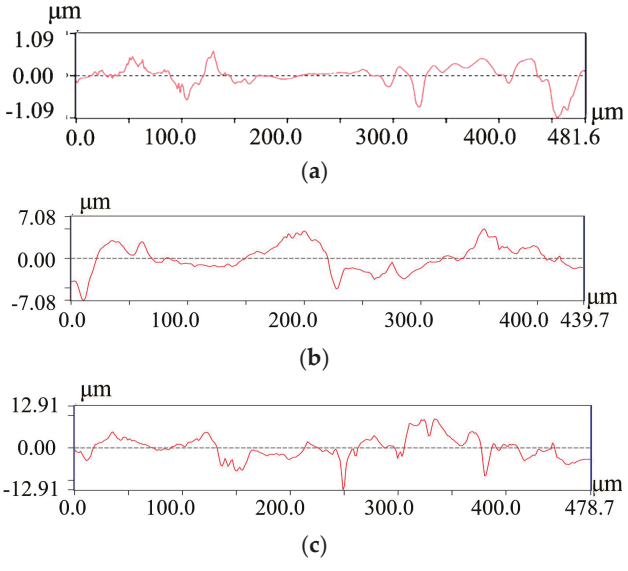

Figure 17. The profile curve of Inconel 718 the channel machining; (**a**) the channel hub; (**b**) the sidewall close to the inlet; (**c**) the sidewall close to the outlet.

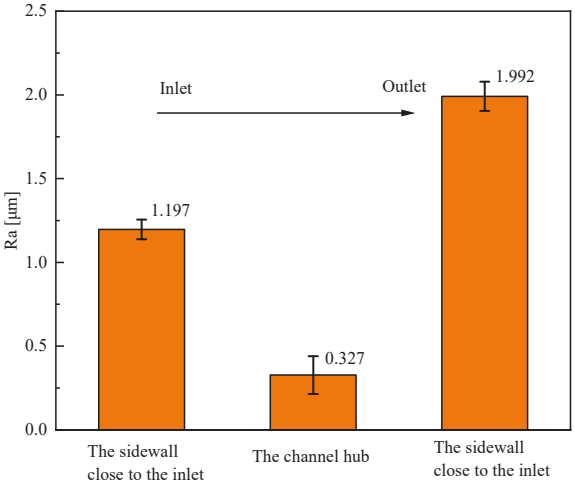

Figure 18. Surface roughness *Ra* of the channels.

The surface topographies of the channel hub, the electrolyte inlet wall, and the outlet wall were scanned by scanning electron microscope (SEM), shown in Figure 19. The surface of the hub is much smoother. There is a certain degree of uneven corrosion on the sidewalls of the channel, presenting block discrete distribution morphology. In addition, the uneven corrosion degree of the sidewall close to the outline is higher than that of the sidewall close to the inlet. Therefore, the surface quality of the sidewall at the electrolyte inlet is slightly better than that at the outlet, which is consistent with the roughness data measured in Figure 18.

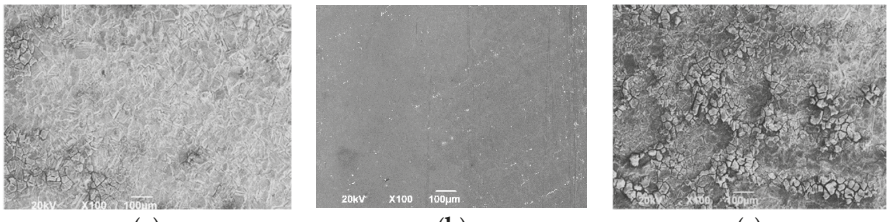

(**a**) (**b**) (**c**)

Figure 19. Surface morphology of the machined Inconel 718 channel; (**a**) the sidewall close to the inlet; (**b**) the channel hub; (**c**) the sidewall close to the outlet.

6. Conclusions

In the present research, a theoretical model of multi-field coupling is established to analyze the influence of vibration on the blisk channel ECM. Based on the multi-physical field simulation results and experimental investigations, the conclusions are summarized as follows:

(1) A multi-physical field coupling model, including temperature field, flow field, electric field, is established for the blisk channel ECM based on the transmission relationship of machining parameters. The model is used to obtain the spatial distribution of temperature, hydrogen volume fraction, electrolyte conductivity, and other parameters.

(2) Simulations show that vibration-assisted channel ECM can effectively promote the exclusion of electrolytic products and the renewal of the electrolyte in the machining gap. As the cathode moves away from the workpiece, the gas volume fraction and electrolyte temperature have an evident drop. The drops of gas fraction and electrolyte temperature are of great benefit to improve the machining stability and quality.

(3) The variation trend of the workpiece contour shape obtained by the experiment and simulation is consistent. Comparing the channel width between simulation and experiment, the maximum relative error is only 1.05%. A comparison of the currents between the simulation and experiment was also conducted, with the maximum relative error of only 8.11%.

(4) An Inconel 718 alloy blisk with three narrow channels has been successfully manufactured by vibration-assisted channel ECM. The experimental results show that the cathode vibration significantly improves the machining stability and surface quality. The width of the narrow channels is less than 3 mm and the aspect ratio is more than 8. The average surface roughnesses *Ra* of the hub is 0.327 μm.

Author Contributions: J.Z. (Juchen Zhang): conceptualization, resources, project administration, methodology, funding acquisition, writing—review and editing. S.S.: investigation, validation, writing—original draft. J.Z. (Junsheng Zhang): formal analysis, investigation, writing—review and editing. W.C.: investigation, writing—review and editing. H.Y.: writing—review and editing. H.T.: writing—review and editing. S.C.: resources, methodology, writing—review and editing. All authors have read and agreed to the published version of the manuscript.

Funding: The work described in this paper was supported by the Natural Science Foundation of Anhui Province (2008085QE250), the Natural Science Foundation of Jiangsu Province (BK20190419), and the China Postdoctoral Science Foundation (2018M642246).

Conflicts of Interest: The authors declare no conflict of interest.

References

1. Bewlay, B.P.; Weimer, M.; Kelly, T.; Suzuki, A.; Subramanian, P.R. The science, technology, and implementation of TiAl alloys in commercial aircraft engines. *Mater. Res. Soc. Symp. Proc.* **2013**, *1516*, 49–58. [CrossRef]
2. Li, X.Y.; Ren, J.X.; Tang, K.; Zhou, Y.K. A Tracking-based numerical algorithm for efficiently constructing the feasible space of tool axis of a conical ball-end cutter in five-axis machining. *Comput. Aided Des.* **2019**, *117*, 102756. [CrossRef]

3. Ren, Z.; Wang, D.; Cui, G.; Cao, W.; Zhu, D. Optimize the flow field during counter-rotating electrochemical machining of grid structures through an auxiliary internal fluid flow pattern. *Precis. Eng.* **2021**, *72*, 448–460. [CrossRef]
4. El-Hofy, H. Vibration-assisted electrochemical machining: A review. *Int. J. Adv. Manuf. Technol.* **2019**, *105*, 579–593. [CrossRef]
5. Hu, X.Y.; Zhu, D.; Li, J.B.; Gu, Z.Z. Flow field research on electrochemical machining with gas film insulation. *J. Mater. Process. Technol.* **2019**, *267*, 247–256. [CrossRef]
6. Zhang, J.C.; Zhu, D.; Xu, Z.Y.; Zhang, K.L.; Liu, J.; Qu, N.S. Improvement of trailing edge accuracy in blisk electrochemical machining by optimizing the electric field with an extended cathode. *J. Mater. Process. Technol.* **2016**, *231*, 301–311. [CrossRef]
7. Zong, Y.W.; Liu, J.; Zhu, D. Study of voltage regulation strategy in electrochemical machining of blisk channels using tube electrodes. *Int. J. Adv. Manuf. Technol.* **2021**, *114*, 3489–3501. [CrossRef]
8. Xu, Z.Y.; Xu, Q.; Zhu, D.; Gong, T. A high efficiency electrochemical machining method of blisk channels. *CIRP Ann.* **2013**, *62*, 187–190. [CrossRef]
9. Lei, G.P.; Zhu, D.; Zhu, D. Feeding strategy optimization for a blisk with twisted blades in electrochemical trepanning. *J. Manuf. Process.* **2021**, *62*, 591–599. [CrossRef]
10. Wang, J.; Xu, Z.Y.; Wang, J.T.; Zhu, D. Electrochemical machining on blisk channels with a variable feed rate mode. *Chin. J. Aeronaut.* **2021**, *34*, 151–161. [CrossRef]
11. Klocke, F.; Zeis, M.; Klink, A. Interdisciplinary modelling of the electrochemical machining process for engine blades. *CIRP Ann.-Manuf. Technol.* **2015**, *64*, 217–220. [CrossRef]
12. Ernst, A.; Heib, T.; Hall, T.; Schmidt, G.; Bähre, D. Simulation of the tool shape design for the electrochemical machining of jet engine vanes. *Proc. CIRP* **2018**, *68*, 762–767. [CrossRef]
13. Hewidy, M.; Ebeid, S.; El-Taweel, T.; Youssef, A. Modelling the performance of ECM assisted by low frequency vibrations. *J. Mater. Process. Technol.* **2007**, *189*, 466–472. [CrossRef]
14. Wang, F.; Zhao, J.S.; Zhang, X.L.; Yang, Z.W.; Gan, W.M.; Tian, Z.J. Electrochemical machining of a narrow slit by cathodic compound feeding. *Int. J. Adv. Manuf. Technol.* **2017**, *90*, 971–978.
15. Pan, Y.; Xu, L.Z. Vibration analysis and experiments on electrochemical micro-machining using cathode vibration feed system. *Int. J. Precis. Eng. Manuf.* **2015**, *16*, 143–149. [CrossRef]
16. Bhattacharyya, B.; Malapati, M.; Munda, J.; Sarkar, A. Influence of tool vibration on machining performance in electrochemical micro-machining of copper. *Int. J. Mach. Tools Manuf.* **2007**, *47*, 335–342. [CrossRef]
17. Uhlmann, E.; Dethlefs, A.; Eulitz, A. Investigation into a geometry-based model for surface roughness prediction in vibratory finishing processes. *Int. J. Adv. Manuf. Technol.* **2014**, *75*, 815–823. [CrossRef]
18. Klink, A.; Heidemanns, L.; Rommes, B. Study of the electrolyte flow at narrow openings during electrochemical machining. *CIRP Ann.* **2020**, *69*, 157–160. [CrossRef]
19. Zhao, J.S.; Lv, Y.M.; Wang, F.; Yang, Z.W.; Liu, D.M.; Fan, Y.T. Experimental research on process stability in pulsed electrochemical machining of deep narrow grooves with high length-width ratio. *Int. J. Adv. Manuf. Technol.* **2018**, *96*, 2245–2256. [CrossRef]
20. Qu, N.S.; Hu, Y.; Zhu, D.; Xu, Z.Y. Electrochemical machining of blisk channels with progressive-pressure electrolyte flow. *Mater. Manuf. Process.* **2014**, *29*, 572–578. [CrossRef]
21. Tang, L.; Zhu, Q.L.; Zhao, J.S.; Fan, Z.J. Research on the cathode design and experiments of electrochemical machining a closed impeller internal flow channel. *Int. J. Adv. Manuf. Technol.* **2016**, *88*, 2517–2525. [CrossRef]
22. Wang, J.; Xu, Z.Y.; Wang, J.T.; Xu, Z.L.; Zhu, D. Electrochemical machining of blisk channels with rotations of the cathode and the workpiece. *Int. J. Mech. Sci.* **2021**, *208*, 106655. [CrossRef]
23. Wang, F.; Zhao, J.S.; Lv, Y.M.; Yang, Z.W.; Yao, J.; He, Y.F. Electrochemical machining of deep narrow slits on TB6 titanium alloys. *Int. J. Adv. Manuf. Technol.* **2017**, *92*, 3063–3071. [CrossRef]
24. Shenoy, R.V.; Datta, M.; Romankiw, L.T. Investigation of island formation during through-mask electrochemical micromachining. *J. Electrochem. Soc.* **1996**, *143*, 2305–2309. [CrossRef]
25. Ghoshal, B.; Bhattacharyya, B. Influence of vibration on micro-tool fabrication by electrochemical machining. *Int. J. Mach. Tools Manuf.* **2013**, *64*, 49–59. [CrossRef]
26. Toshiaki, F.; Kazuaki, I.; Kato, D.; Makoto, Y. Multiphysics simulation of electrochemical machining process for three-dimensional compressor blade. *J. Fluids Eng.* **2008**, *130*, 081602.
27. Qian, S.Q.; Ji, F.; Qu, N.S.; Li, H.S. Improving the localization of surface texture by electrochemical machining with auxiliary anode. *Mater. Manuf. Process.* **2014**, *29*, 1488–1493. [CrossRef]
28. Liu, G.; Tong, H.; Li, Y.; Zhong, H. Novel structure of a sidewall-insulated hollow electrode for micro electrochemical machining. *Precis. Eng.* **2021**, *72*, 356–369. [CrossRef]
29. Collett, D.; Hewson-Browne, R.; Windle, D. A complex variable approach to electrochemical machining problems. *J. Eng. Math.* **1970**, *4*, 29–37. [CrossRef]
30. Li, D.L.; Zhu, D.; Li, H.S. Microstructure of electrochemical micromachining using inert metal mask. *Int. J. Adv. Manuf. Technol.* **2011**, *55*, 189–194. [CrossRef]
31. Deconinck, D.; Hoogsteen, W.; Deconinck, J. A temperature dependent multi-ion model for time accurate numerical simulation of the electrochemical machining process. Part III: Experimental validation. *Electrochim. Acta* **2013**, *103*, 161–173. [CrossRef]
32. Jiang, X.C.; Liu, J.; Zhu, D.; Wang, M.M.; Qu, N.S. Research on stagger coupling mode of pulse duration and tool vibration in electrochemical machining. *Appl. Sci.* **2018**, *8*, 12. [CrossRef]

33. Zhu, D.; Zhang, J.C.; Zhang, K.L.; Liu, J.; Chen, Z.; Qu, N.S. Electrochemical machining on blisk cascade passage with dynamic additional electrolyte flow. *Int. J. Adv. Manuf. Technol.* **2015**, *80*, 637–645. [CrossRef]
34. Li, Z.L.; Cao, B.R.; Dai, Y. Research on multi-physics coupling simulation for the pulse electrochemical machining of holes with tube electrodes. *Micromachines* **2021**, *12*, 18. [CrossRef]
35. Damme, S.; Nelissen, G.; Bossche, B.; Deconinck, J. Numerical model for predicting the efficiency behaviour during pulsed electrochemical machining of steel in $NaNO_3$. *J. Appl. Electrochem.* **2005**, *36*, 1–10. [CrossRef]
36. Deconinck, D.; Van, D.S.; Albu, C.; Hotoiu, L.; Deconinck, J. Study of the effects of heat removal on the copying accuracy of the electrochemical machining process. *Electrochim. Acta.* **2011**, *56*, 5642–5649. [CrossRef]
37. Chen, X.L.; Zhu, J.J.; Xu, Z.Z.; Su, G.K. Modeling and experimental research on the evolution process of micro through-slit array generated with masked jet electrochemical machining. *J. Mater. Process. Technol.* **2021**, *298*, 117304. [CrossRef]

micromachines

MDPI

Article

Single-Wedge Lift-Out for Atom Probe Tomography Al/Ni Multilayers Specimen Preparation Based on Dual-Beam-FIB

Yi Qiao [1,*], Yalong Zhao [1], Zheng Zhang [2], Binbin Liu [1], Fusheng Li [1], Huan Tong [1], Jintong Wu [3], Zhanqi Zhou [3], Zongwei Xu [3,*] and Yue Zhang [1,*]

[1] State Key Laboratory for Advanced Metals and Materials, University of Science and Technology, Beijing 100083, China; zhaoyalong0123@163.com (Y.Z.); bbliu@ustb.edu.cn (B.L.); 18810562702@163.com (F.L.); tonghuan416@163.com (H.T.)

[2] School of Materials Science and Engineering, University of Science and Technology, Beijing 100083, China; zhangzheng@ustb.edu.cn

[3] State Key Laboratory of Precision Measuring Technology & Instruments, Laboratory of Micro/Nano Manufacturing Technology, Tianjin University, Tianjin 300072, China; 13352407489@163.com (J.W.); zzqtd@tju.edu.cn (Z.Z.)

* Correspondence: qiaoyi@ustb.edu.cn (Y.Q.); zongweixu@tju.edu.cn (Z.X.); yuezhang@ustb.edu.cn (Y.Z.)

Abstract: Atomic probe tomography (APT) samples with Al/Ni multilayer structure were successfully prepared by using a focused ion beam (FIB), combining with a field emission scanning electron microscope, with a new single-wedge lift-out method and a reduced amorphous damage layer of Ga ions implantation. The optimum vertex angle and preparation parameters of APT sample were discussed. The double interdiffusion relationship of the multilayer films was successfully observed by the local electrode APT, which laid a foundation for further study of the interface composition and crystal structure of the two-phase composites.

Keywords: atom probe tomography (APT); single-wedge; lift-out; focused ion beam (FIB); Al/Ni multilayers

Citation: Qiao, Y.; Zhao, Y.; Zhang, Z.; Liu, B.; Li, F.; Tong, H.; Wu, J.; Zhou, Z.; Xu, Z.; Zhang, Y. Single-Wedge Lift-Out for Atom Probe Tomography Al/Ni Multilayers Specimen Preparation Based on Dual-Beam-FIB. *Micromachines* **2022**, *13*, 35. https://doi.org/10.3390/mi13010035

Academic Editor: Jiang Guo

Received: 13 December 2021
Accepted: 24 December 2021
Published: 27 December 2021

Publisher's Note: MDPI stays neutral with regard to jurisdictional claims in published maps and institutional affiliations.

1. Introduction

Atomic probe tomography (APT) is the highest spatial resolution element analysis and testing equipment [1]. It mainly involves materials, physics, chemistry, biology and other research fields. The instrument is mainly used for atomic scale microanalysis in materials science research: in particular, measurement and analysis methods used in the research and development of materials. It provides researchers with a three-dimensional image of the material's internal structure with atomic resolution. The sensitivity is close to one millionth. It is especially suitable for the study of nanoscale microstructure (precipitation, cluster, etc.), and various internal interfaces (grain boundary (GB), phase boundary, interlayer interface in multilayer structure, etc.) can be used to observe and study the segregation behavior, size and distribution of elements on the interface, and the distribution and composition of micro precipitates.

APT analysis has strict requirements on the shape of the sample: the shape of the sample is a symmetrical tip, the diameter of the tip top is less than 50 nm, the diameter of the tip bottom is less than 200 nm, and the effective analysis height is about 100–1000 nm. Although electrochemical methods are the dominant technique for preparing APT specimens [2,3], it is not easy for them to put the site-specific area (precipitation, cluster, GB, etc.) on the top of the APT needle specimens [4–10]. Scientists have taken decades years to figure out several basic tools for FIB-based specimen preparation used today for this challenge [11], known as the annular milling method [12,13], low-energy modification [14–16], site-specific lift-out method [17,18].

The FIB method is used to refine APT samples from top to bottom. When there is a huge phase structure difference between the two materials, the preparation of a multilayer

structure is very difficult. At the same time, the Ga ion source for FIB cutting will induce an amorphous damage layer on the sample surface [19,20], while the resistance of the films to ion beam amorphous damage is weak. How to reduce or avoid the amorphous damage in the process of ion beam processing has become another difficulty in the preparation of APT multilayer composite materials.

Al/Ni multilayers are composed of alternating layers of Al and Ni, which have the characteristics of high chemical energy storage, fast energy release and fast combustion. They have potential application prospects in the following reaction ignition, thermal battery ignition and local heating. They are mainly used for welding and bonding [21]. A small thermal pulse will cause atoms to diffuse into the layer and lead to a rapid exothermic reaction, thus further establishing the self-propagating reaction [22]. In order to understand these behaviors, people have devoted themselves to basic research, such as final products, phase transition sequences and high concentration gradient effects. Particularly, the intermixing region in the interfaces not only changes the phase sequence, but also reduces stored chemical energy, especially as the modulation period drops below 50 nm. For instance, Al_9Ni_2 was observed as the primary phase in the multilayers with a modulation period larger than 25 nm, which could be explained by a nucleation model based on thermodynamics and diffusional intermixing. In this paper, Al/Ni multilayers APT sample were successfully prepared by the focused ion beam technique, which reduced the amorphous damage layer of Ga ions.

2. Experimental

Al/Ni multilayers with thickness of 4 μm were magnetron sputter-deposited from Al (99.999%) and Ni (99.999%) targets on a substrate of sapphire at a base pressure of 5×10^{-4} Pa. The modulation period was set to be 500 nm, while the relative thickness of Al and Ni layers was maintained at a 3:2 ratio. The temperature of the substrate was below 373 K during deposition. Both Al and Ni layer were deposited at 90 W, then the deposition rates for Al and Ni were about 15 nm/min and 10 nm/min, respectively.

Al/Ni multilayers were fixed on the FIB special sample preparation platform with silver glue. APT samples were prepared by Auriga focused ion beam field emission scanning double beam electron microscopy (FIB/SEM) produced by Zeiss (Oberkochen, Germany). APT samples were welded on the special Si column of APT by Pt welding, and the three-dimensional elements of APT samples were analyzed by the three-dimensional atomic probe system leap 5000 xr. The FIB system uses Ga ion as the ion source, the accelerating voltage is 3–30 kV, the working current is 50 pA to 20 nA, the minimum beam spot diameter is less than 3 nm; the acceleration voltage of the SEM system is 5 kV, and the image resolution is 1 nm.

3. Standard Lift-Out

When people are concerned about the three-dimensional distribution of special structural elements, such as the interface, precipitation, nanotubes and nanospheres, the typical lift-out method is usually used to prepare APT samples for analysis. This method was developed on the basis of Giannuzzi et al. (1997) [23], and Giannuzzi and Stevie (1999) [24], and then developed by Miller et al. (2005) [17], Miller and Russell (2007) [18], and Thompson et al. (2005–2007) [14–16]. The method is used as the main sampling method for region of interest (ROI). Taking the block interface material as an example, the sample preparation process of the standard method is shown in Figure 1: (a) platinum deposition, i.e., deposition of 20 μm × 2 μm × 1 μm platinum on the surface of the sample to protect the selected area of sample preparation; (b) cutting, that is, the thickness of the sample preparation area is reduced to 1 μm thickness by a small beam; (c) U-cut, that is, U-shaped separation between the thin sample and the matrix, but keeping a tiny connection; (d) lift-out, that is, thin samples are extracted from the matrix using nano-manipulators; (e) welding, that is, using Pt to weld the thin samples on an APT special holder; (f) separation, which is the separation of nano-manipulators and the sample; (g) annular milling, that is, sharpening

the sample to a cone of 50–100 nm by annular beam flow; (h) cleaning, that is, cleaning the amorphous layer on the sample surface with a low voltage and low current ion beam; (i) confirmation, that is, the final shape of the sample should be tip configuration, with a tip top diameter less than 50 nm and a tip bottom diameter less than 200 nm. In this method, the parameters of centering during welding and the following annular milling/cleaning are the key to the success of the sample preparation.

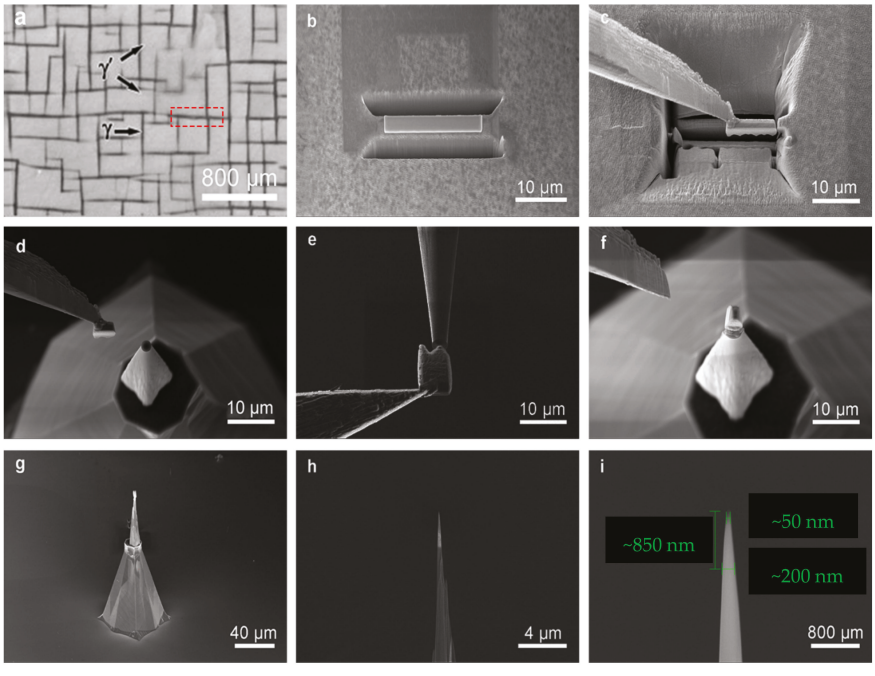

Figure 1. Example of the standard lift-out APT specimen preparation. (**a**) Platinum deposition; (**b**) cutting; (**c**) fine cutting; (**d**) lift-out; (**e**) welding; (**f**) separation; (**g**) annular milling; (**h**) cleaning; (**i**) fonfirmation.

4. Single-Wedge Lift-Out

4.1. Experimental Considerations

In the standard lift-out method, the sample is proposed to be a wedge-shaped square column, as shown in Figure 2a. In the process of manual milling, the ion beam is perpendicular to the upper surface of the sample, and the area of the upper surface of the sample is larger than that of the lower surface of the sample, so it is difficult to determine the welding center. During the practical manufacture process, the welding center of the sample is easy to produce deviation, thus cutting out the PT for welding, as shown in Figure 2a, which makes welding the joint very fragile, resulting in the sample fracture in APT analysis as shown in Figure 3. Therefore, we hope to find a suitable sample shape so that the solder joint between the sample and the holder can be easily determined during manual milling so as to strengthen the welding. Our new design strategy is to change the wedge lift sample into a single wedge, as shown in Figure 2b. In this way, when the ion beam is observed, the welding point between the sample and the bracket can be easily obtained, and enough welding platinum can be reserved during the encircling process to strengthen the welding stiffness of the sample.

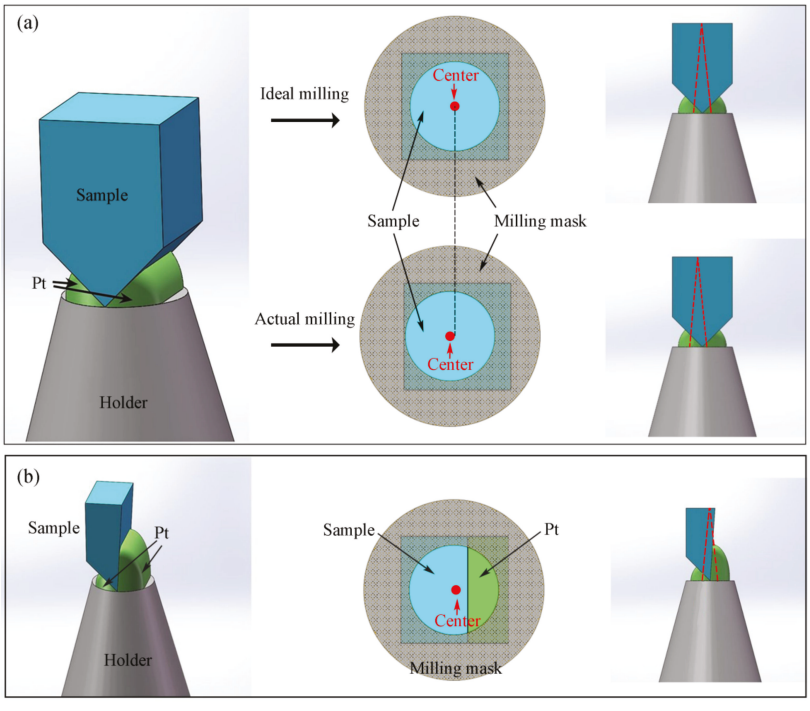

Figure 2. Welding process of standard lift-out and single-wedge lift-out. (**a**) Welding process of standard lift-out; (**b**) welding process of single-wedge lift-out.

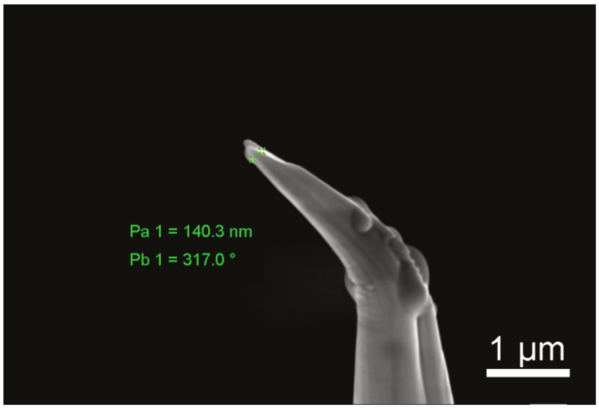

Figure 3. Example of the fractured APT sample.

4.2. Single-Wedge Lift-Out Tip Fabrication

4.2.1. Single-Wedge Milling

In the standard lifting method, we use Auriga fiber reinforced plastics produced by Zeiss. When the tilt angle of the sample stage is 54°, the ion beam is perpendicular to the upper surface of the sample. When milling, the tilt angle of the sample table is 54 ± 2° and the bottom of the double wedge specimen is thin, which can shorten the U-shaped cutting time and avoid the phenomenon of re deposition welding. In the single wedge ejection method, considering that the focusing plane of the ion beam is the upper surface of the

sample, there is defocusing phenomenon from the ion beam to the bottom of the sample. In order to eliminate the defocusing effect and obtain the vertical plane, the tilt angle of the sample table is 55° during milling. At the same time, in order to keep the advantage of easy separation between the standard lift-out sample and the matrix during U-shaped cutting, it is necessary to increase the milling angle of the wedge side to 51°.

4.2.2. Off-Center Welding

The APT sample holder we used is the APT special holder of CAMECA Company. It is a Si conical cylinder with a 2 µm upper surface, as shown in Figure 4. In the standard lifting-out method, the wedge tip of the sample is welded to the center of the upper surface of the silicon column to facilitate alignment, while in the single-wedge-ejection method, the wedge tip of the sample is welded at two thirds of the upper surface of the silicon column, with the vertical plane inside and the wedge body outside, as shown in Figure 5.

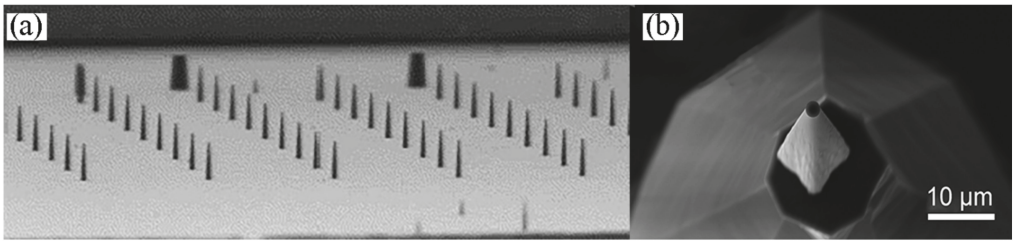

Figure 4. APT Si holder. (**a**) APT Si holders; (**b**) single APT Si holder.

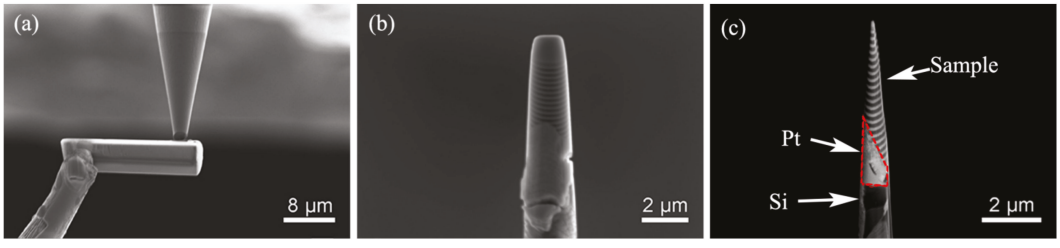

Figure 5. Welding process of single-wedge lift-out. (**a**) Welding; (**b**) sample enlarged view; (**c**) sample fine profile.

4.2.3. Annular Milling

SRIM-2013 is used to qualitatively analyze the Ga ion induced damage distribution in Al/Ni substrate from the perspective of Monte Carlo simulation, as shown in Figure 6. Among them, the Ga ion induced damage peaks are at ~2.2 nm, ~3.1 nm and ~8.5 nm, corresponding to 3 keV, 5 keV and 30 keV, respectively. It can be seen that the damage peaks ranging from 2 nm to above 10 nm with an impact energy ranges from 3 keV to 30 keV, showing a significantly increasing trend of damage concentration. In experimental studies, the tip shape is also an important factor in APT analysis. It is well known that there are many defects, such as vacancies, at the interface between the grain boundary and the phase boundary in the three-dimensional atomic probe experiment, which can lead to the fracture of the interface tip. As shown in Figure 7, we take the uniform silicon sample as the research object, and improve the stability of the sample by controlling the shape of the tip so as to avoid the tip fracture at the interface. The results show that when the taper is greater than 12° and in order to consider the sample collection amount of APT, the optimal cone angle of the tip is about 20° as shown in Figure 7e. In order to obtain the taper angle, it is necessary to control the diameter D2 and D1 of the grinding mask. After the inner

ring is determined, if the outer ring diameter is reduced, the cutting area will be greatly reduced, and the cutting efficiency will be improved, but the needle tip will also become steep and vulnerable to brittle fracture; if the outer ring diameter is larger, the cutting area will be larger, and the cutting efficiency will be reduced, but the cone angle of the needle tip will be significantly larger, and there will be burr on the outside of the needle tip, which will affect the APT analysis results.

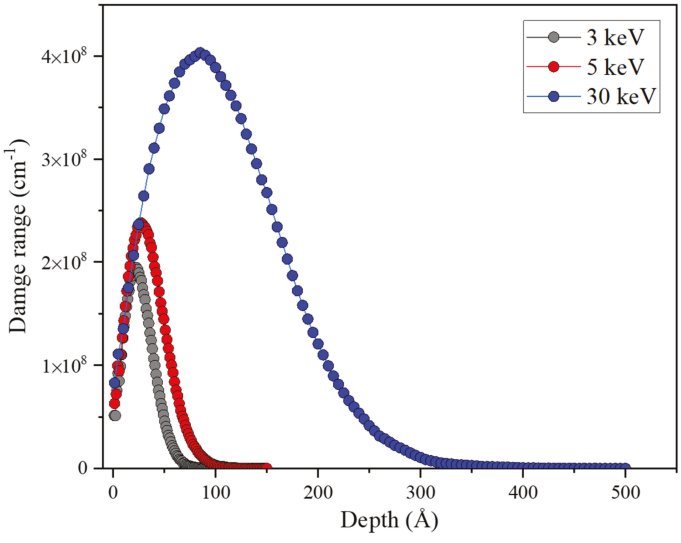

Figure 6. SRIM results for Ga ion induced recoil damage distribution in Al/Ni substrate under different ion energies.

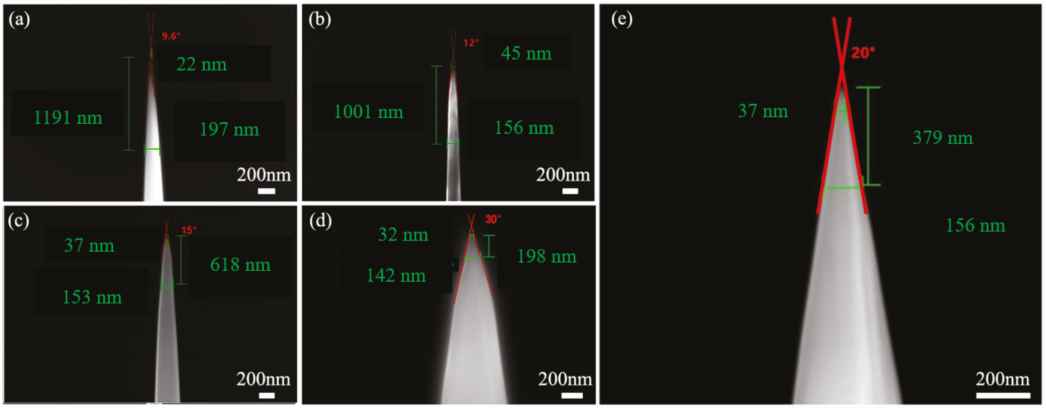

Figure 7. Example of the single-wedge lift-out APT specimen tip shape. (**a**) Tip 9°; (**b**) tip 12°; (**c**) tip 15°; (**d**) tip 30°; (**e**) tip 20°.

When the cutting current of the Ga ion beam is about 30 kV, the amorphous layer is about 20–30 nm. When the cutting beam voltage drops to 3 kV and 5 kV, the thickness of the amorphous layer can be reduced to 1–5 nm. Therefore, in order to reduce the thickness of the amorphous layer of Al/Ni multilayers, the hierarchical voltage dilution method is used in the manual milling process, as shown in Table 1. Finally, the diluted sample is

cleaned with 5 kV and 3 kV low pressure for 2–3 min, and the cleaning effect is good, as shown in Figure 8. The results of the APT analysis are shown in Figure 9.

Table 1. The sample diameter versus FIB process parameter.

Tip Diameter D/nm	Ion Beam Voltage U/kV	Ion Beam Current I/pA
1000	30	240
200	15	120
100	10	20
50	10	2

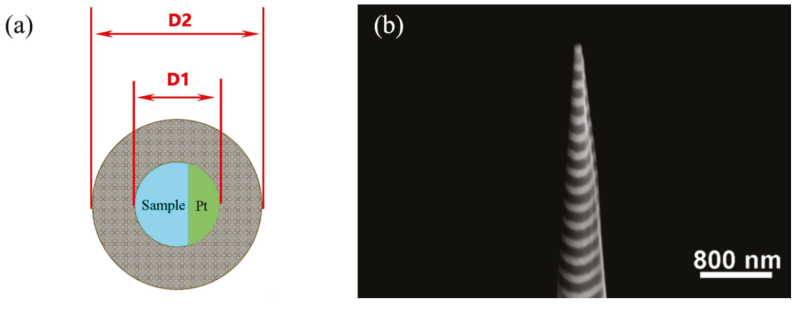

Figure 8. Example of annular milling and the APT specimen tip shape of the Al/Ni multilayers. (**a**) Schematic diagram of annular milling; (**b**) the APT specimen tip shape of the Al/Ni multilayers.

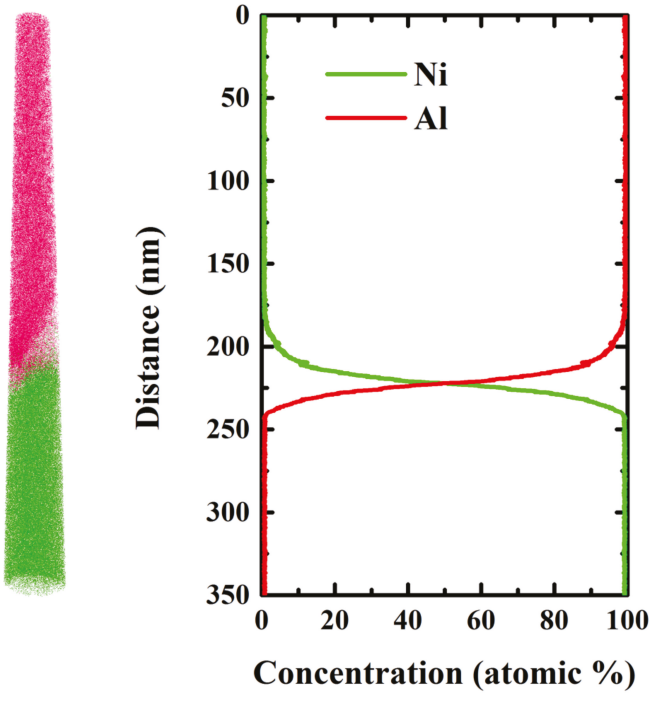

Figure 9. Reconstruction of atomic distribution and concentration profiles of the as-deposited Al/Ni multilayers.

5. Conclusions

In this paper, the nanofabrication technology of APT sample preparation of biphasic composites was studied by focused ion beam field emission scanning electron microscope, by improving the lift-out method with eccentric welding, tip angle control and step voltage thinning. The visualization of the welding between the wedge bottom and the holder was realized, so that the wedge and the holder were welded firmly, and the sample was on the back side, so it was not easy to fracture in the preparation of manual milling and APT analysis. The optimum vertex angle and preparation parameters of APT sample were discussed. APT samples with the Al/Ni multilayer structure with the reduced amorphous damage layer of Ga ions were successfully prepared. It is of great significance to study the interface composition, crystal structure and diffusion mechanism of Al/Ni dual phase composites.

Author Contributions: Conceptualization, Y.Q., Z.X. and Y.Z. (Yue Zhang); methodology, Y.Q.; software, J.W.; formal analysis, Y.Q.; resources, Y.Z. (Yalong Zhao), Z.Z. (Zheng Zhang), B.L., F.L. and H.T.; data curation, Y.Q.; writing—original draft preparation, Y.Q.; writing—review and editing, Z.Z. (Zhanqi Zhou); funding acquisition, Y.Q., Z.X. and Y.Z.(Yue Zhang) All authors have read and agreed to the published version of the manuscript.

Funding: The study is supported by the National Natural Science Foundation of China (No. 51871015, 51575389), 2020 Mobility Program of the Sino-German Center for Research Promotion (M-0396), the State key laboratory of precision measuring technology and instruments (Pilt2107).

Conflicts of Interest: The authors declare no conflict of interest.

References

1. Panitz, J.A.; Mclane, S.B.; Müller, E. Calibration of the Atom Probe FIM. *Rev. Sci. Instruments* **1969**, *40*, 1321–1324. [CrossRef]
2. Müller, E.; Tsong, T.T. *Field Ion Microscopy: Principles and Applications*; Elsevier: New York, NY, USA, 1969; pp. 109–127.
3. Melmed, A.J. The art and science and other aspects of making sharp tips. *J. Vac. Sci. Technol. B* **1991**, *9*, 601. [CrossRef]
4. Prosa, T.J.; Larson, D.J. Modern Focused-Ion-Beam-Based Site-Specific Specimen Preparation for Atom Probe Tomography. *Microsc. Microanal.* **2017**, *23*, 194–209. [CrossRef] [PubMed]
5. Alexander, K.B.; Angelini, P.; Miller, M.K. Precision ion milling of field-ion specimens. *J. Phys. Colloques.* **1989**, *50*, C8-549–C8-554. [CrossRef]
6. Cojocaru-Mirédin, O.; Choi, P.P.; Abou-Ras, D.; Schmidt, S.S.; Raabe, D. Characterization of Grain Boundaries in Cu(In,Ga)Se2 Films Using Atom-Probe Tomography. *IEEE J. Photovolt.* **2011**, *1*, 207–212. [CrossRef]
7. Eichfeld, C.M.; Gerstl, S.S.A.; Prosa, T.; Ke, Y.; Redwing, J.M.; Mohney, S.E. Local electrode atom probe analysis of silicon nanowires grown with an aluminum catalyst. *Nanotechnology* **2012**, *23*, 215205. [CrossRef]
8. Bran, J.; Jean, M.; Lardé, R.; Sauvage, X.; Breton, J.-M.L.; Pautrat, A. Elaboration and characterization of Cu/Co multilayered nanowires. *J. Korean Phys. Soc.* **2013**, *62*, 1744–1747. [CrossRef]
9. Blumtritt, H.; Isheim, D.; Senz, S.; Seidman, D.N.; Moutanabbir, O. Preparation of nanowire specimens for laser-assisted atom probe tomography. *Nanotechnology* **2014**, *25*, 435704. [CrossRef]
10. Chen, Y.; Rice, K.P.; Prosa, T.J.; Marquis, E.A.; Reed, R.C. Integrated APT/t-EBSD for Grain Boundary Analysis of Thermally Grown Oxide on a Ni-Based Superalloy. *Microsc. Microanal.* **2015**, *21*, 687–688. [CrossRef]
11. Estivill, R.; Audoit, G.; Barnes, J.-P.; Grenier, A.; Blavette, D. Preparation and Analysis of Atom Probe Tips by Xenon Focused Ion Beam Milling. *Microsc. Microanal.* **2016**, *22*, 576–582. [CrossRef]
12. Larson, D.J.; Miller, M.K.; Ulfig, R.M.; Matyi, R.J.; Camus, P.P.; Kelly, T.F. Field ion specimen preparation from near-surface regions. *Ultramicroscopy* **1998**, *73*, 273–278. [CrossRef]
13. Larson, D.J.; Foord, D.T.; Petford-Long, A.K.; Liew, H.; Blamire, M.G.; Cerezo, A.; Smith, G.D.W. Field-ion specimen preparation using focused ion-beam milling. *Ultramicroscopy* **1999**, *79*, 287–293. [CrossRef]
14. Thompson, K.; Gorman, B.; Larson, D.J.; Leer, B.V.; Hong, L. Minimization of Ga Induced FIB Damage Using Low Energy Clean-up. *Microsc. Microanal.* **2006**, *12*, 1736–1737. [CrossRef]
15. Mathew, P.T.; Rodriguez, B.J.; Fang, F. Atomic and Close-to-Atomic Scale Manufacturing: A Review on Atomic Layer Removal Methods Using Atomic Force Microscopy. *Nanomanuf. Metrol.* **2020**, *3*, 167–186. [CrossRef]
16. Thompson, K.; Lawrence, D.; Larson, D.J.; Olson, J.D.; Kelly, T.F.; Gorman, B. In Situ Site-Specific Specimen Preparation for Atom Probe Tomography. *Ultramicroscopy* **2007**, *107*, 131–139. [CrossRef]
17. Miller, M.K.; Russell, K.F.; Thompson, G.B. Strategies for fabricating atom probe specimens with a dual beam FIB. *Ultramicroscopy* **2005**, *102*, 287–298. [CrossRef]
18. Miller, M.K.; Russell, K.F.; Thompson, K.; Alvis, R.; Larson, D.J. Review of Atom Probe FIB-Based Specimen Preparation Methods. *Microsc. Microanal.* **2007**, *13*, 428–436. [CrossRef]

19. Zhongdu, H.; Zongwei, X.; Mathias, R.; Boteng, Y.; Tao, L.; Ying, S.; Fengzhou, F. Investigation of Ga ion implantation-induced damage in single-crystal 6H-SiC. *J. Micromanuf.* **2018**, *1*, 115–123. [CrossRef]
20. Yexin, F.; Zongwei, X.; Ying, S.; Bing, D.; Zhifu, X.; Bing, L.; Lei, L.; Dongyu, T. Nano material removal mechanism of 4H-SiC in ion implantation-assisted machining. *Comput. Mater. Sci.* **2021**, *200*, 110837. [CrossRef]
21. Zhang, Y.; Zhang, H.L.; Wu, J.H.; Wang, X.T. Enhanced thermal conductivity in copper matrix composites reinforced with titanium-coated diamond particles. *Scr. Mater.* **2011**, *65*, 1097–1100. [CrossRef]
22. Qiu, X.; Wang, J. Experimental evidence of two-stage formation of Al3Ni in reactive Ni/Al multilayer foils. *Scr. Mater.* **2007**, *56*, 1055–1058. [CrossRef]
23. Giannuzzi, L.A.; Drown, J.L.; Brown, S.R.; Irwin, R.B.; Stevie, F.A. Focused Ion Beam Milling and Micromanipulation Lift-Out for Site Specific Cross-Section Tem Specimen Preparation. *MRS Proc.* **1997**, *480*, 19. [CrossRef]
24. Giannuzzi, L.A.; Stevie, F.A. A review of focused ion beam milling techniques for TEM specimen reparation. *Micron* **1999**, *30*, 197–204. [CrossRef]

micromachines

MDPI

Article

Piezoelectric Hysteresis Modeling of Hybrid Driven Three-Dimensional Elliptical Vibration Aided Cutting System Based on an Improved Flower Pollination Algorithm

Xifeng Fu, Hong Gong *, Mingming Lu *, Jiakang Zhou, Jieqiong Lin, Yongsheng Du and Ruiqi Zhou

Key Laboratory of Micro/Nano and Ultra-Precision Manufacturing of Jilin Province, School of Mechatronic Engineering, Changchun University of Technology, Changchun 130012, China; fxf201418@163.com (X.F.); zhoujiakang07@163.com (J.Z.); linjieqiong@ccut.edu.cn (J.L.); dys19961015@163.com (Y.D.); Z16688213919@163.com (R.Z.)

* Correspondence: gonghong@ccut.edu.cn (H.G.); lumm@ccut.edu.cn (M.L.)

Abstract: Three-dimensional elliptical vibration assisted cutting technology has been widely used in the past few years. The piezoelectric stack drive structure is an important part of the three-dimensional elliptical vibration aided cutting system. Its piezoelectric hysteresis characteristics affects the final output of the elliptical trajectory. Aiming at this problem, a piezoelectric hysteresis modeling method based on a generalized Bouc–Wen model is presented in this paper. An improved flower pollination algorithm (IFPASO) was used to identify Bouc–Wen model parameters. Standard test result shows that IFPASO has better algorithm performance. The model identification effect experiment proved that the Bouc–Wen model obtained by IFPASO identification, the highest modeling accuracy of the three axial subsystems, can reach 98.86%. Therefore, the model can describe the piezoelectric hysteresis characteristics of the three axial subsystems of the 3D-EVC system effectively and has higher modeling accuracy and fitting accuracy.

Keywords: three-dimensional elliptical vibration cutting; piezoelectric hysteresis; Bouc–Wen model; flower pollination algorithm; dynamic switching probability strategy; parameter identification

Citation: Fu, X.; Gong, H.; Lu, M.; Zhou, J.; Lin, J.; Du, Y.; Zhou, R. Piezoelectric Hysteresis Modeling of Hybrid Driven Three-Dimensional Elliptical Vibration Aided Cutting System Based on an Improved Flower Pollination Algorithm. *Micromachines* **2021**, *12*, 1532. https://doi.org/10.3390/mi12121532

Academic Editor: Jiang Guo

Received: 10 November 2021
Accepted: 6 December 2021
Published: 9 December 2021

1. Introduction

With the rapid development of precision and ultra-precision machining technology, elliptical vibration cutting technology has the advantages of reducing cutting force, suppressing burrs and extending tool life. Since the end of the 1980s, this technology has received extensive attention from many experts and scholars. In order to improve the processing problems encountered by traditional cutting methods in processing certain difficult-to-machine materials, Shamoto and Moriwaki [1] proposed elliptical vibration cutting based on one-dimensional vibration cutting, namely, two-dimensional elliptical vibration cutting (EVC). The working principle is that the tool makes an elliptical movement in an orthogonal plane perpendicular on the machined surface. After adopting the elliptical vibration cutting method for difficult-to-machine materials, the mechanical machinability of such difficult-to-machine materials is improved and the cutting force and cutting heat can be reduced as much as possible during the cutting process and tool wear can be reduced. Therefore, this technology greatly improves the surface processing quality.

In the past few years, experts and scholars have made much progress and discoveries in EVC. Kim et al. [2] have done relevant research on difficult-to-machine materials and cutting shapes in elliptical vibration cutting and conducted machining experiments; Zhang C et al. [3] established a mechanical analysis model and also conducted cutting experiments on ceramic materials, which proved the effectiveness of elliptical vibration cutting. On this basis, experts and scholars proposed three-dimensional elliptical vibration cutting (3D-EVC) on the basis of two-dimensional elliptical vibration cutting and divided it into

resonant type and non-resonant type. Lu et al. [4,5] studied the processing of Ti-6Al-4V alloy using a non-resonant 3D-EVC device and compared three processing methods including traditional cutting methods, thusproving the non-resonant 3D-EVC technology has better processability; Lu et al. [6] used an improved memetic algorithm to identify the nonlinear system of the three-dimensional elliptical vibration cutting system. Lin et al. [7] modeled and analyzed chip formation and transient cutting force during elliptical vibration cutting and their calculation results proved its feasibility. Compared with one-dimensional vibration cutting and EVC, 3D-EVC not only has the advantages of suppressing sharp tool wear, suppressing tool brittleness and obtaining excellent machining quality, but also obtaining higher machining efficiency. At the same time, 3D-EVC is also more beneficial to the outflow of chips and has a series of advantages of reducing friction wear between tool and workpiece.

However, there are few studies on the hysteresis and nonlinear characteristics of the piezoelectric stack structure in the non-resonant 3D-EVC system. The piezoelectric stack structure is composed of piezoelectric ceramic material and the piezoelectric ceramic material has piezoelectric hysteresis characteristics. Therefore, the inherent hysteresis and nonlinearity of the piezoelectric stack structure will directly affect the performance of the 3D-EVC device, which will also reduce the accuracy of the control system and cause instability within the device. Therefore, it is necessary to select an appropriate piezoelectric hysteresis model to describe the relationship between the axial displacement and the input voltage of 3D-EVC for accurate parameter identification.

At present, experts and scholars have proposed many mathematical models to describe the nonlinear phenomenon of piezoelectric hysteresis. For example: Arindam Bhattacharjee et al. [8] use the Preisach model, which mainly uses multiple Preisach operators and weighted superposition to describe the hysteresis characteristics; Zhou et al. [9] use the KP model to describe and model the hysteresis characteristics of piezoelectric materials; Kim et al. [10] used the Bouc–Wen model to describe the relationship between the restoring force and displacement of the hysteresis system to describe the piezoelectric hysteresis characteristics; Naser M F et al. [11] used the Duhem model, which has clear equations. The hysteresis nonlinearity can be described by adjusting the parameters of the equation; Qing et al. [12] proposes a PI mathematical model based on the improvement of the traditional Preisach model to describe the hysteresis characteristics of the piezoelectric actuator. In summary, there are many models used to describe the hysteresis characteristics, but in face of complex mathematical modeling and in order to better describe the piezoelectric hysteresis nonlinearity of the 3D-EVC system, it is necessary to choose an effective and simple hysteresis model.

Bouc–Wen model is a typical mathematical model that uses differential equations to describe hysteresis. With the continuous research of the hysteresis characteristics of piezoelectric actuators by experts and scholars, Bouc–Wen model has been gradually applied and studied with its concise and intuitive expression.

There are many parameter identification methods of Bouc–Wen model. Nowadays, experts adopt various types of intelligent algorithms to identify the parameters of this model. For example, Rakotondrabe et al. [13] proposed a method to identify the model parameters by using nonlinear filtering system; Charalampakis et al. [14] proposed an improved particle swarm optimization algorithm to identify the model parameters; Fujii et al. [15]. used the least square algorithm to identify the parameters of the improved model. It can be seen that there are many parameter identification methods for the Bouc–Wen model and they are all carried out on the basis of certain improvements to improve the identification ability.

Yang et al. [16] proposed a flower pollination algorithm in 2012. As a new type of meta-heuristic algorithm, due to its simple structure parameters and strong optimization ability, it has recently received attention from many experts and scholars. However, the flower pollination algorithm still contains the problems of early maturity and poor convergence performance of the traditional algorithm. Therefore, it is necessary to improve the flower

pollination algorithm. However, there has been relatively little research on it and its application in practical problems. Nabil et al. [17] proposed a hybrid clonal selection algorithm for flower pollination algorithm to improve the performance of the algorithm; Abdel-Basset et al. [18] proposed an improved version of a cross-based flower pollination algorithm to solve the multidimensional knapsack problem; Fouad et al. [19] improved the algorithm by improving the global orientation and the best solution vector; Yang et al. [20] used a two-way learning strategy and a greedy strategy to improve the algorithm; Chen et al. [21] proposed an innovative flower pollination algorithm based on cloud mutation.

In this study, the Bouc–Wen model will be used to describe the hysteresis nonlinearity exhibited by the 3D-EVC system and an improved flower pollination algorithm will be used to identify the parameters of the model. The improved flower pollination algorithm introduces the early particle swarm optimization and dynamic switching probability strategy to improve the accuracy of model parameter identification and uses the standard test function to test the algorithm performance. Finally, the identification of the model parameters and the verification of the identification effect are carried out.

2. Establishment of Piezoelectric Hysteresis Model for Three-Dimensional Elliptical Vibration Cutting (3D-EVC)

For the non-resonant 3D-EVC device, the realization of its final elliptical trajectory output is achieved through the piezoelectric driver output displacement and then through the structural transmission and synthesis. The target system studied in this paper is a stack type piezoelectric actuator. Similarly, as a piezoelectric material, the hysteresis characteristic is part of its inherent nature. Its main manifestation is that the rising voltage-driven output displacement curve applied to the piezoelectric material does not completely coincide with the drop voltage-driven output displacement curve, thus forming a hysteresis loop. Since the piezoelectric stack is a vital component in the entire non-resonant 3D-EVC system, the piezoelectric hysteresis characteristics of the piezoelectric material will seriously affect the output of the final elliptical trajectory and the control of the entire processing system accuracy. In summary, in this section, we will consider the use of a piezoelectric hysteresis model to describe the axial motion of the non-resonant 3D-EVC system.

2.1. The Structure of the 3D-EVC System

The research in this paper is based on a self-designed non-resonant three-dimensional elliptical vibration aided cutting system, which is driven by three piezoelectric stacks with a "two parallel and one vertical" positional relationship, which is mainly composed of two flexible systems perpendicular to each other composition. The system can adjust various processing parameters in three-dimensional elliptical vibration cutting, thereby obtaining higher and good processing performance.

The specific structure of the system is shown in Figure 1. Three piezoelectric stacks are respectively distributed on the upper flexible hinge and the lower flexible hinge and each piezoelectric stack is placed in parallel with a displacement sensor. Each piezoelectric stack in a single direction will drive the corresponding flexible hinge to produce slight deformation after receiving a certain signal drive, thereby driving the entire 3D-EVC system to produce various axial displacements. There is a certain phase difference between the drive signals in each direction, so the axial displacement generated by these drives will work together to promote the tool tip to form a three-dimensional elliptical motion track, so as to achieve the purpose of three-dimensional elliptical motion assisted cutting.

2.2. Bouc–Wen Model

The Bouc–Wen model is a phenomenological mathematical model that uses differential equations to describe hysteresis. Compared with other operator-based models, the Bouc–Wen model has fewer parameters and a more expressive form, which exists as a form of nonlinear differential equations. For the intuitive advantage, it can not only characterize the mathematical characteristics of hysteresis, but also describe the dynamic characteristics of the piezoelectric actuator. It is precisely because the Bouc–Wen model has the ability to

simulate various hysteresis behaviors, it is widely used in structural materials and systems with hysteresis franchise.

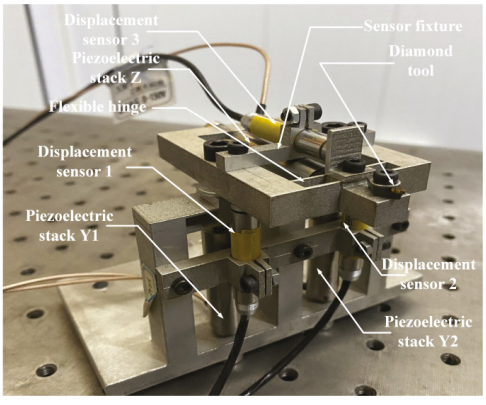

Figure 1. The structure of the 3D-EVC system.

It can be known from the working principle of the 3D-EVC system that the unidirectional sub-motion of the 3D-EVC system is the relationship between the input voltage and the output displacement of the piezoelectric stack actuator. This nonlinear relationship between voltage and displacement can be used as a piezoelectric hysteresis model to describe. In this paper, we will choose the Bouc–Wen model to describe.

The early Bouc–Wen model is a basic and simple form of first-order differential equation [22]. In recent years, with the research on smart material drive mechanisms, the Bouc–Wen model has gradually been used to describe the hysteresis and nonlinear characteristics of smart material actuators such as piezoelectric ceramic actuators and giant magnetostrictive actuators [13]. The mathematical expression of the Bouc–Wen model commonly used at present is represented by the following equation:

$$\begin{cases} Mx''(t) + Bx'(t) + kx(t) = C[Du(t) - h(t)] \\ h'(t) = Au'(t) - \beta|u'(t)|h(t)|h(t)|^{n-1}, \ h(0) = 0 \end{cases} \tag{1}$$

Considering that in this paper, the Bouc–Wen model describes the hysteresis characteristics based on the non-resonant 3D-EVC. Therefore, both from the experimental point of view and the identification in the next chapter, they are all performed at low frequencies. Therefore, $Mx''(t)$ in Equation (1) can be ignored. At the same time, the initial displacement $x(t)$ can be processed by recalibrating the displacement sensor. Based on the above factors and at the same time to facilitate subsequent identification, we simplified and organized the structure of the Bouc–Wen model to get the following equation:

$$\begin{cases} x'(t) = c_0 + c_1 u(t) + c_2 h(t) \\ h'(t) = Au'(t) - \beta|u'(t)|h(t)|h(t)|^{n-1} - \gamma u'(t)|h(t)|^n \\ y(t) = x(t) \end{cases} \tag{2}$$

In summary, in order to use the simplified Bouc–Wen model to describe the piezoelectric hysteresis behavior, we need to use a suitable and excellent algorithm to identify some unknown parameters in the model. From Equation (2), we can see that the identification of parameter is $c_0, c_1, c_2, A, \beta, \gamma, n$. The specific identification methods and identification results will be introduced in the subsequent chapters.

3. Improved Flower Pollination Algorithm (IFPASO)

As we all know, even the most advanced and complete algorithms cannot produce the most satisfactory results for all optimization problems. Flower pollination algorithm is a meta-heuristic algorithm proposed in recent years. It has the advantages of easy implementation, fewer parameters and strong optimization ability.

However, the flower pollination algorithm also has some shortcomings of the traditional meta-heuristic algorithm, such as the low accuracy of the later optimization and the shortcomings of being easy to fall into local extreme values. For the above defects existing in FPA, this paper will improve the traditional FPA.

3.1. Flower Pollination Algorithm (FPA)

Inspired by the flower pollination process of flowering plants, Yang proposed a new swarm intelligence optimization algorithm in 2012 to solve related practical problems and named the intelligent optimization algorithm as flower pollination algorithm [16].

Flower pollination algorithms need to be based on the following types of premises:

(1) Biological cross-pollination is considered to be a global pollination process and pollinators use Lévy flight to pollinate;
(2) Non-biological self-pollination is considered local pollination;
(3) Flower constancy is considered to be the probability of reproduction, which is proportional to the similarity of the two flowers participating in pollination;
(4) The conversion between local pollination and global pollination is controlled by the transition probability $p \in [0, 1]$. Due to the influence of physical conditions and other factors, local pollination should have a significant bias p in the overall pollination process.

In order to better express the above rules, we will express the above rules in the form of mathematical formulas. For example, in the global pollination stage, pollen is carried and spread by pollinators such as insects, because pollinators can carry pollen in a larger search range, so pollen can be spread over a longer distance. Equation (3) is used to express flowers' global pollination and flower constancy:

$$x_i^{t+1} = x_i^t + \gamma L(\lambda)(x_i^t - g_{best}^*) \tag{3}$$

$L(\lambda)$ is the parameter corresponding to the pollination intensity, that is, the flight step length. Since pollinators may move long distances in different steps, Lévy flight can be used to effectively express this feature, $L(\lambda)$ is expressed by Equation (4) and $L(\lambda) > 0$:

$$L(\lambda) \sim \frac{\lambda\Gamma(\lambda)\sin(\pi\lambda/2)}{\pi}\frac{1}{S^{1+\lambda}}, (S > S_0 > 0) \tag{4}$$

According to the Mantegna algorithm, S can be described by two Gaussian distributions of U, V:

$$S = \frac{U}{|V|^{1/\lambda}},\ U \sim N(0, \sigma^2),\ V \sim N(0, \sigma^2) \tag{5}$$

$$\sigma^2 = \left\{\frac{\Gamma(1+\lambda)}{\lambda\Gamma[(1+\lambda)/2} \cdot \frac{\sin(\pi\lambda/2)}{2^{(\lambda-1)/2}}\right\}^{1/\lambda} \tag{6}$$

Under the assumptions of rules (3) and (4), local pollination can be expressed by Equation (7):

$$x_i^{t+1} = x_i^t + \varepsilon(x_j^t - x_k^t) \tag{7}$$

The pseudo-code of the standard flower pollination algorithm is shown as following Algorithm 1:

Algorithm 1. Standard flower pollination algorithm.

1: Define the objective function $f(x), x = (x_1, x_2, \ldots, x_d)$
2: Initialize a population of n flowers/pollen gametes with random solutions
3: Evaluate each flower or solution in the population
4: Extract the best solution in the population
5: Find the best solution g^*_{best} in the initial population
6: Define a switch probability $p \in [0, 1]$
7: Define fixed number of iterations *Max_generation*
8: **While** $t <$ *Max_generation*
9: **for** i = 1:n (each flower in the population)
10: **if** (rand < p)
11: Draw a (d-dimensional) step vector L which obeys a Lévy distribution
12: Global pollination via $x_i^{t+1} = x_i^t + \gamma L(\lambda)(x_i^t - g^*_{best})$
13: **else**
14: Draw ε from a uniform distribution in [0, 1]
15: Do local pollination via $x_i^{t+1} = x_i^t + \varepsilon(x_j^t - x_k^t)$
16: **end if**
17: Evaluate each new solution x_i^t
18: **If** new solution is better, update it in the population
19: **end for**
20: Find the current best solution g^*_{best}
21: **end While**
22: Output the best solution found

3.2. Dynamic Switching Probability Strategy

In FPA, the local search and global search are adjusted by the conversion probability, which is a fixed value in the standard flower pollination algorithm. However, during the whole process of the algorithm operation, we prefer to perform more global searches at the beginning of the search to expand the search space and to enhance the execution of local searches in the later stage to speed up the speed of finding the best solution. By introducing a dynamic switching probability strategy in the later stage, the algorithm can adaptively adjust the ratio of local search and global search, so that the algorithm is no longer easy to fall into the range of partial optimal values when searching for optimization. Therefore, we adopt a dynamic conversion probability strategy to adjust the proportion of global search and local search in the entire search process. The switching probability is expressed by Equation (8):

$$0.8 - 0.1 * \frac{Max\_T - t}{Max\_T} \tag{8}$$

3.3. Early-Stage Particle Swarm Optimization

The initial solution of the algorithm plays a vital role in the quality of the optimization results and the initial solution of the FPA algorithm is generated randomly in the feasible region. When the value of one of the solutions deviates too much from the theoretical optimal value, it not only increases the search difficulty of the algorithm, but also greatly affects the convergence speed of the algorithm. Particle swarm optimization (PSO) is a search algorithm used to solve optimization in computational mathematics and it is also one of the most classic intelligent algorithms [23]. The goal of particle swarm optimization is to make all particles find the optimal solution in a multi-dimensional hyper-volume [24].

Suppose that in a D-dimensional target search space, there is a particle population with a population size of N, that is, there are a total of particles in the population. The position of the *i*-th particle is expressed as an N-dimensional vector $X_i = (x_{i1}, x_{i2}, \ldots x_{iD})$ $(i = 1, 2 \ldots N)$ and its flight speed can be expressed as $Vi = (v_{i1}, v_{i2}, \ldots v_{iD})(i = 1, 2, \ldots N)$. The position of each particle represents a feasible solution to a problem in the target search space. At the beginning of the algorithm, the population is initialized as a set of random

solutions, that is, randomly distributed in the entire search space. When the algorithm is executed, the state of the particles is updated mainly through Equations (9) and (10):

$$v_{t+1}^i = w_t v_t^i + c_1 r_1 (p_t^i - x_t^i) + c_2 r_2 (p_t^g - x_t^i) \tag{9}$$

$$x_{t+1}^i = x_t^i + v_{t+1}^i \tag{10}$$

where w_t is the inertia weight of the particle, the larger the value, the stronger the particle's exploration ability;

$$w_t = (w_{\max} - w_{\min}) * \frac{(t_{\max} - t)}{t_{\max}} + w_{\min} \tag{11}$$

The pseudo code of the particle swarm algorithm is given as following Algorithm 2:

Algorithm 2. Particle swarm algorithm.

1: **Start**
2: Randomly initialize particle swarm
3: **While** (number of iterations or the stopping iteration on is not met)
4: Evaluate fitness of the particle swarm
5: **for** n = 1 to number of particles
6: Find individual optimal solution p_t^i
7: Find group optimal solution p_t^g
8: **for** d = 1 to number of dimensions of particle
9: update the velocity of particles via $v_{t+1}^i = w_t v_t^i + c_1 r_1 (p_t^i - x_t^i) + c_2 r_2 (p_t^g - x_t^i)$
10: update the position of particles via $x_{t+1}^i = x_t^i + v_{t+1}^i$
11: **end for**
12: **end for**
13: update the inertia weight via $w_t = (w_{\max} - w_{\min}) * \frac{(t_{\max} - t)}{t_{\max}} + w_{\min}$
14: **end While**
15: Output the best solution found

Therefore, we introduce PSO in the early stage of FPA execution to compensate for the randomness generated by the initial solution in FPA. In the IFPASO execution process, it is divided into two stages, the first stage executes PSO and the second stage executes FPA. Through this method, we can make the search range closer to the area where the optimal solution is located and avoid the possibility of invalid value divergence, thereby increasing the algorithm's optimization ability and its convergence speed.

In summary, based on the dynamic conversion probability strategy and the introduction of PSO in the early stage of FPA execution, the algorithm's ability to solve practical problems can be greatly improved. The pseudo code of the IFPASO algorithm is shown as follows Algorithm 3:

3.4. IFPASO Performance Test

In order to verify the effectiveness of the proposed algorithm, we compare IFPASO with traditional FPA and PSO algorithms for verification. We have selected two well-known benchmark function functions for verification here. For the two algorithms, for comparison and verification, we have adopted the most common parameter settings in the literature. For fairness, we use the same fixed individual scale for the above algorithms and all the algorithms are independently run the same number of times, the following is the introduction of the two selected benchmark functions:

Algorithm 3. IFPASO algorithm.

Start
Randomly initialize particle swarm
While (number of iterations or the stopping iteration on is not met)
Evaluate fitness of the particle swarm
for n = 1 to number of particles
Find individual optimal solution p_t^i
Find group optimal solution p_t^g
for d = 1 to number of dimensions of particle
update the velocity of particles via $v_{t+1}^i = w_t v_t^i + c_1 r_1 (p_t^i - x_t^i) + c_2 r_2 (p_t^g - x_t^i)$
update the position of particles via $x_{t+1}^i = x_t^i + v_{t+1}^i$
end for
end for
update the inertia weight via $w_t = (w_{\max} - w_{\min}) * \frac{(t_{\max} - t)}{t_{\max}} + w_{\min}$
end While
Output the best solution found
The best solution found by PSO is regarded as initial points for FPA algorithm g_{best}^*
While $t < Max\_generation$
for i=1:n (each flower in the population)
get dynamic switch probability p via $0.8 - 0.1 * \frac{Max\_T - t}{Max\_T}$
if (rand < p)
Draw a (d-dimensional) step vector L which obeys a Lévy distribution
Global pollination via $x_i^{t+1} = x_i^t + \gamma L(\lambda)(x_i^t - g_{best}^*)$
else
Draw ε from a uniform distribution in [0, 1]
Do local pollination via $x_i^{t+1} = x_i^t + \varepsilon(x_j^t - x_k^t)$
end if
Evaluate each new solution x_i^t
If new solution is better, update it in the population
end for
Find the current best solution g_{best}^*
end While
Output the final best solution found

Test function 1: Ackle() function:

$$f(x) = -20\exp\left(-0.2\sqrt{\frac{1}{n}\sum_{j=1}^{n} x_j^2}\right) - \exp\left(\frac{1}{n}\sum_{j=1}^{n}\cos(2\pi x_j)\right) + 20 + e - 8 \le x \le 8 \quad (12)$$

Test function 2: Schaffer() function:

$$\min f(x_1, x_2) = 0.5 + \frac{\left(\sin\sqrt{x_1^2 + x_2^2}\right)^2 - 0.5}{\left(1 + 0.001(x_1^2 + x_2^2)\right)^2} - 10.0 \le x_1, x_2 \le 10.0 \quad (13)$$

Figure 2 is the test result of the Ackle() function and the Schaffer() function using PSO, FPA and IFPASO respectively.

Table 1 shows the best values of PSO, FPA and IFPASO for the final results of the Ackle() function and Schaffer() function.

It is seen from the iterative curve and convergence optimum results that although the three algorithms converge to the global optimal solution, IFPASO shows faster convergence speed and higher accuracy for both test functions. As a result, it can be concluded that the IFPASO proposed in this paper has excellent optimization ability and overcomes some drawbacks of traditional algorithms to some extent. Therefore, we can use IFPASO for the parameter identification of Bouc–Wen model.

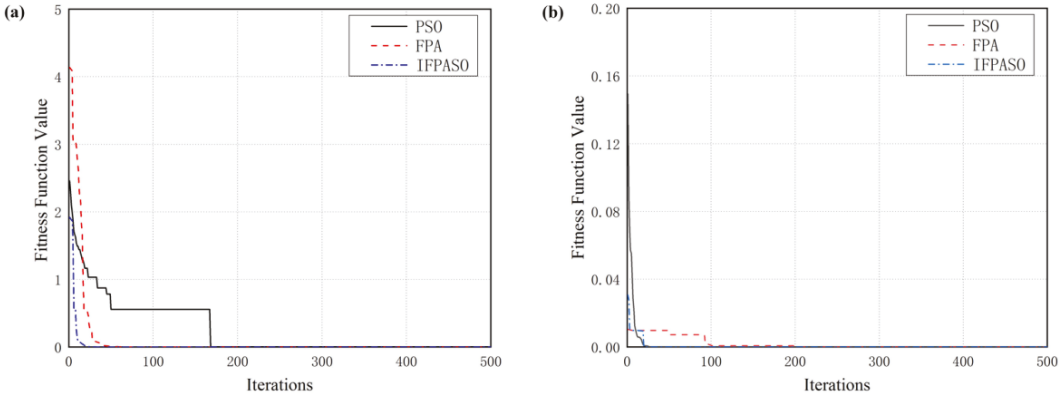

Figure 2. Convergence result (**a**) Ackle() function (**b**) Schaffer() function.

Table 1. Comparison results of the three algorithms.

	PSO	FPA	IFPASO
Ackle () function	0.000780527	5.35228×10^{-5}	1.00×10^{-8}
Schaffer () function	5.39183×10^{-5}	4.13×10^{-9}	1.00×10^{-15}

4. Simulation Experiment and Result Analysis

In this section, the IFPASO algorithm with good optimization performance verified above is applied to the parameter identification of the Bouc–Wen model and, finally, the accuracy of the identification results is verified through the modeling comparison in 3D-EVC.

4.1. Experimental Setup

The experimental setup part is mainly divided into hardware part and software part. Hardware part: 3D-EVC system, PC, signal generator, power amplifier, displacement sensor, Power PMAC; Software part: Matlab2012a.

The Bouc–Wen model parameter identification experiment setting of 3D-EVC system is shown in Figure 3.

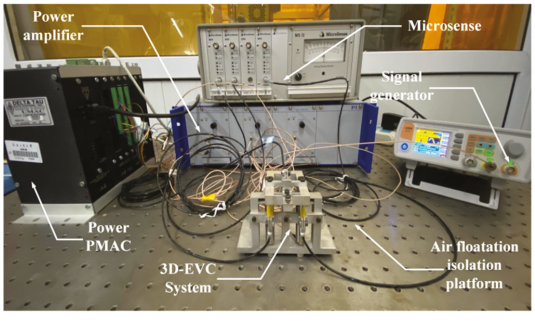

Figure 3. Experimental setup.

4.2. Parameter Identification of Bouc–Wen Model

According to the Bouc–Wen dynamic nonlinear model we established in the previous content, we can see that the parameters we need to identify are $c_0, c_1, c_2, A, \beta, \gamma, n$. Based on the piezoelectric hysteresis characteristics of the 3D-EVC system and the piezoelectric stack, in order to identify the parameters in the Bouc–Wen model, a sinusoidal excitation

signal is given to the 3D-EVC system for parameter identification of the piezoelectric hysteresis model.

In order to identify the parameters in the Bouc–Wen model used to characterize the Y1 axial subsystem, a sinusoidal excitation signal is given to the 3D-EVC system, as shown in Figure 4 and the corresponding displacement excitation curve collected by the displacement sensor.

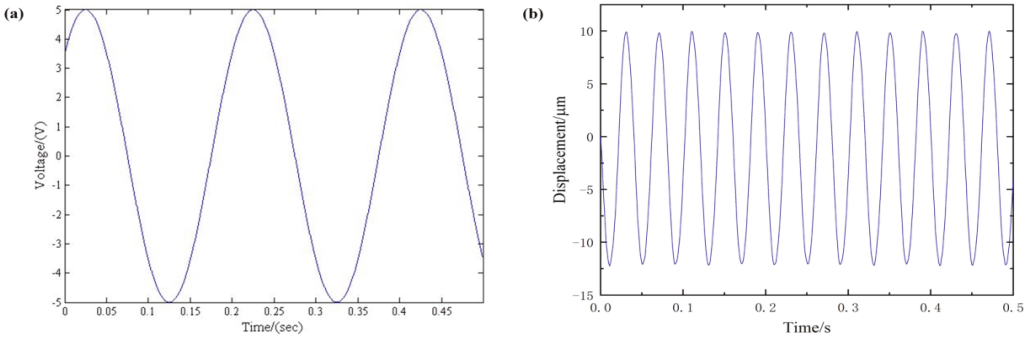

Figure 4. Excitation condition (**a**) sinusoidal excitation signal (**b**) corresponding displacement excitation curve.

The results of the Bouc–Wen model parameter identification of each axial subsystem of the 3D-EVC system are shown in the Table 2:

Table 2. Bouc–Wen model parameters of each axis of 3D-EVC system.

	C_0	C_1	C_2	A	B	fl	n
Y1	−1349.77	1863.74	−1543.57	0.3961	0.5765	0.21	1.2
Y2	−1479.62	1938.74	−1637.54	0.3879	0.6524	0.2483	1
Z	−1551.36	1926.21	−1703.45	0.4215	0.6952	0.2431	1

4.3. Test of Model Identification Effect

In order to verify whether the Bouc–Wen model obtained through parameter identification can accurately describe the hysteresis nonlinearity exhibited by the 3D-EVC system, the hysteresis curve output under the Bouc–Wen model was fitted with the actual hysteresis curve under 50 Hz excitation and the fitting error was calculated. In this paper, the mean square error (MSE) is selected as the target fitness function for model accuracy verification and its expression is shown in Equation (14):

$$OF(r) = \frac{1}{N}\sum_{i=1}^{N}(x_{\exp}(i) - x_{mdl}(i))^2 \tag{14}$$

Figures 5–7 are, respectively, the hysteresis curve fitting diagram and fitting error diagram of the Y1, Y2 and Z-direction subsystems of the 3D-EVC system. The maximum modeling error and modeling accuracy results of each axial subsystem are shown in Table 3.

From the hysteresis curve fitting and fitting error of the three axial subsystems, it can be seen that the Bouc–Wen model obtained by using the IFPASO algorithm proposed in this paper for parameter identification can effectively and accurately describe the hysteresis of the 3D-EVC system. The maximum modeling error is only 0.5332 μm and the maximum modeling accuracy can reach 98.86%, which can satisfy the accuracy requirements of subsequent related work for hysteresis modeling and it has high modeling accuracy.

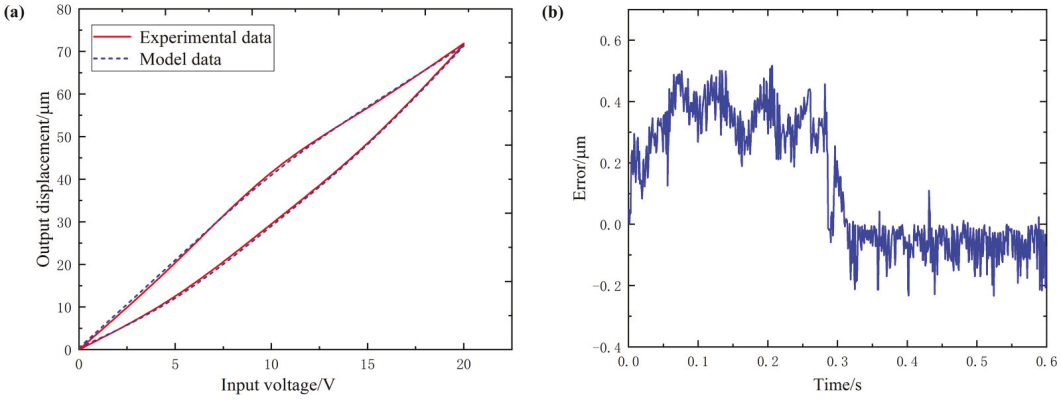

Figure 5. (**a**) hysteresis curve fitting of Y1 (**b**) fitting error of Y1.

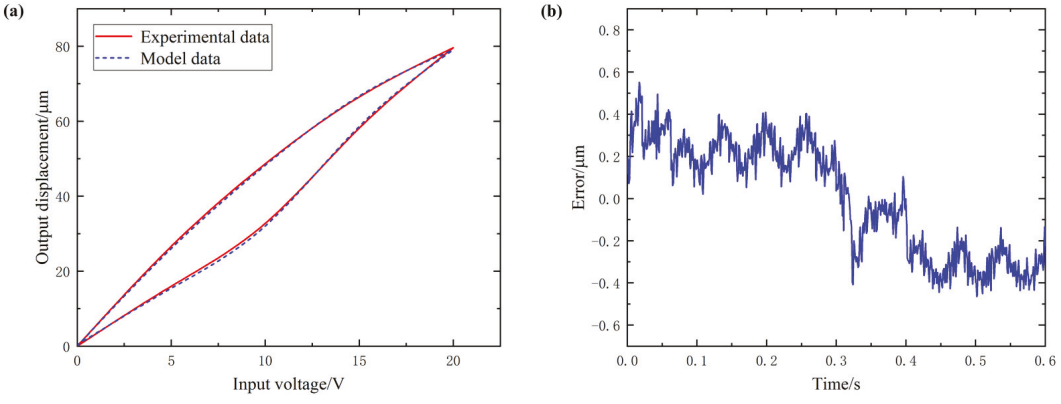

Figure 6. (**a**) hysteresis curve fitting of Y2 (**b**) fitting error of Y2.

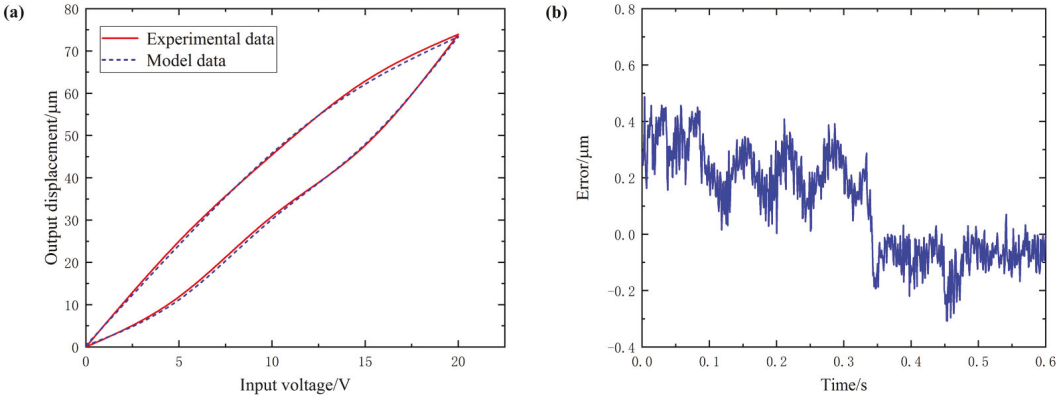

Figure 7. (**a**) hysteresis curve fitting of Z (**b**) fitting error of Z.

Table 3. Modeling error and accuracy of each axis of 3D-EVC system.

	Maximum Modeling Error	Modeling Accuracy
Y1	0.5074 μm	98.24%
Y2	0.5332 μm	98.05%
Z	0.4878 μm	98.86%

5. Conclusions

This paper focuses on the 3D-EVC system due to the piezoelectric hysteresis characteristics that affect the precision machining accuracy and the output of the elliptical trajectory. A Bouc–Wen hysteresis model is used to characterize the relationship between the input voltage and the output displacement of the 3D-EVC system.

1. In order to improve the accuracy of model parameter identification, this paper proposes an improved flower pollination algorithm (IFPASO) based on the original flower pollination algorithm (FPA) algorithm structure, introducing particle swarm optimization (PSO) and dynamic conversion probability strategy. Performance test results show that the new flower pollination algorithm (IFPASO) has better optimization effect and faster convergence speed.
2. The results of the model identification effect test show that the Bouc–Wen model obtained by using the new flower pollination algorithm (IFPASO) identification parameters can completely describe the piezoelectric hysteresis characteristics of the three axial subsystems of the 3D-EVC system and has high Modeling accuracy.
3. The maximum modeling error and modeling accuracy of the three axial subsystems Y1, Y2 and Z are 0.5074 μm, 98.24%; 0.5332 μm, 98.05%; 0.4878 μm, 98.86%, respectively. It can be seen that the Bouc–Wen model obtained by using the improved flower pollination algorithm (IFPASO) for parameter identification can effectively characterize the piezoelectric hysteresis characteristics of the 3D-EVC system and the fitting accuracy is higher. It provides a theoretical model reference and basis for the control system design of the high-performance 3D-EVC system.

Author Contributions: Writing—original, draft preparation, X.F.; Conceptualization, H.G.; Conceptualization, Supervision, M.L.; Methodology, J.Z.; Investigation, Validation, J.L.; Data curation, Formal Analysis, Y.D.; Data curation, Formal analysis, R.Z. All authors have read and agreed to the published version of the manuscript.

Funding: This research was funded by National Natural Science Foundation of China (51905046), Science and Technology Development Projects of Jilin Province (20190201303JC), Micro-Nano and Ultra-Precision Key Laboratory of Jilin Province (20140622008JC).

Institutional Review Board Statement: Not applicable.

Informed Consent Statement: Not applicable.

Data Availability Statement: Not applicable.

Conflicts of Interest: The authors declare that there are no conflict of interest regarding the publication of this paper.

Nomenclature

M	the system's mass	$\Gamma(\lambda)$	standard gamma function
B	damping coefficient	x_j^t, x_k^t	random pollen
K	stiffness	ε	random number in [0, 1]
C	scale factor	p	switching probability
$x(t)$	state variable	v_t^i	particle i speed at iteration t
$h(t)$	output of the hysteresis part	p_t^i	particle i optimal solution

D	ratio coefficient	p_t^g	population optimal solution
A, B	hysteresis parameter	c_1, c_2	learning factor
γ, n	hysteresis parameter	r_1, r_2	random number in [0, 1]
$u(t)$	input signal	w_t	inertia weight
$u'(t)$	first derivative of $u(t)$	$w_{\min}$	minimum value of w_t
c_0, c_1, c_2	coefficient to be identified	$w_{\max}$	maximum value of w_t
$y(t)$	output displacement of the system	$t_{\max}$	maximum number of iterations
x_i^t	solution i at iteration t	Max_T	maximum number of iterations
x_i^{t+1}	solution i at iteration $t+1$	t	current iteration number
g_{best}^*	global optimal solution	r	$r = (c_0, c_1, c_2, A, \beta, \gamma, n)$
γ	scale factor of the control step	N	total number of data
$L(\lambda)$	Lévy flight	$x_{\exp}$	experimental data
S	step length	x_{mdl}	model data

References

1. Shamoto, E.; Moriwaki, T. Study on elliptical vibration cutting. *CIRP Ann. Manuf. Technol.* **1994**, *43*, 35–38. [CrossRef]
2. Kim, G.D.; Loh, B.G. Characteristics of elliptical vibration cutting in micro-V grooving with variations in the elliptical cutting locus and excitation frequency. *J. Micromech. Microeng.* **2008**, *18*, 025002. [CrossRef]
3. Zhang, C.; Ehmann, K.; Li, Y. Analysis of cutting forces in the ultrasonic elliptical vibration-assisted micro-groove turning process. *Int. J. Adv. Manuf. Technol.* **2015**, *78*, 139–152. [CrossRef]
4. Lu, M.; Zhou, J.; Lin, J.; Gu, Y.; Han, J.; Zhao, D. Study on Ti-6Al-4V alloy machining applying the non-resonant three-dimensional elliptical vibration cutting. *Micromachines* **2018**, *8*, 306. [CrossRef]
5. Lu, M.; Wang, H.; Guan, L.; Lin, J.; Gu, Y.; Chen, B.; Zhao, D. Modeling and analysis of surface topography of Ti6Al4V alloy machining by elliptical vibration cutting. *Int. J. Adv. Manuf. Technol.* **2018**, *98*, 2759–2768. [CrossRef]
6. Lu, M.; Zhou, X.; Lin, J. Improved memetic algorithm for nonlinear identification of a three-dimensional elliptical vibration cutting system. *Proc. Inst. Mech. Eng. Part I J. Syst. Control Eng.* **2014**, *228*, 449–460. [CrossRef]
7. Lin, J.; Guan, L.; Lu, M.; Han, J.; Kan, Y. Modeling and analysis of the chip formation and transient cutting force during elliptical vibration cutting process. *AIP Adv.* **2017**, *7*, 125101. [CrossRef]
8. Bhattacharjee, A.; Mohanty, A.K.; Chatterjee, A. Expansion of Preisach density in magnetic hysteresis using general basis functions. *Appl. Math. Comput.* **2019**, *341*, 418–427. [CrossRef]
9. Zhou, M.; He, S.; Hu, B.; Zhang, Q. Modified KP Model for Hysteresis of Magnetic Shape Memory Alloy Actuator. *IETE Tech. Rev.* **2015**, *32*, 29–36. [CrossRef]
10. Kim, S.Y.; Lee, C.H. Description of asymmetric hysteretic behavior based on the Bouc-Wen model and piecewise linear strength-degradation functions. *Eng. Struct.* **2019**, *181*, 181–191. [CrossRef]
11. Mohammad, N.F.; Ikhouane, F. Consistency of the duhem model with hysteresis. *Math. Probl. Eng.* **2013**, *2013*, 586130. [CrossRef]
12. Qin, Y.; Zhao, X.; Zhou, L. Modeling and identification of the rate-dependent hysteresis of piezoelectric actuator using a modified Prandtl-Ishlinskii model. *Micromachines* **2017**, *8*, 114. [CrossRef]
13. Rakotondrabe, M. Bouc-Wen modeling and inverse multiplicative structure to compensate hysteresis nonlinearity in piezoelectric actuators. *IEEE Trans. Autom. Sci. Eng.* **2010**, *8*, 428–431. [CrossRef]
14. Charalampakis, A.E.; Dimou, C.K. Identification of Bouc-Wen hysteretic systems using particle swarm optimization. *Comput. Struct.* **2010**, *88*, 1197–1205. [CrossRef]
15. Fujii, F.; Tatebatake, K.; Morita, K.; Shiinoki, T. A bouc–wen model-based compensation of the frequency-dependent hysteresis of a piezoelectric actuator exhibiting odd harmonic oscillation. *Actuators* **2018**, *7*, 37. [CrossRef]
16. Yang, X.S. *International Conference on Unconventional Computing and Natural Computation*; Flower pollination algorithm for global optimization; Springer: Berlin/Heidelberg, Germany, 2012; pp. 240–249.
17. Nabil, E. A Modified Flower Pollination Algorithm for Global Optimization. *Expert Syst. Appl.* **2016**, *57*, 192–203. [CrossRef]
18. Abdel-Basset, M.; El-Shahat, D.; El-Henawy, I.; Sangaiah, A.K. A modified flower pollination algorithm for the multidimensional knapsack problem: Human-centric decision making. *Soft Comput.* **2018**, *22*, 4221–4239. [CrossRef]
19. Fouad, A.; Gao, X.Z. *A Novel Modified Flower Pollination Algorithm for Global Pptimization*; Springer: London, UK, 2019; Volume 31, pp. 3875–3908.
20. Yang, X.; Shen, Y. An Improved Flower Pollination Algorithm with Three Strategies and Its Applications. *Neural Process. Lett.* **2020**, *51*, 675–695. [CrossRef]
21. Chen, Y.; Pi, D. An innovative flower pollination algorithm for continuous optimization problem. *Appl. Math. Model.* **2020**, *83*, 237–265. [CrossRef]
22. Ismail, M.; Ikhouane, F.; Rodellar, J. The hysteresis Bouc-Wen model, a survey. *Arch. Comput. Methods Eng.* **2009**, *16*, 161–188. [CrossRef]
23. Okwu, M.O.; Tartibu, L.K. Particle Swarm Optimisation. *Stud. Comput. Intell.* **2021**, *927*, 5–13. [CrossRef]
24. Wang, D.; Tan, D.; Liu, L. Particle swarm optimization algorithm: An overview. *Soft Comput.* **2018**, *22*, 387–408. [CrossRef]

micromachines

MDPI

Article

Research on Self-Aligning Flanges Based on Piezoelectric Actuators Applied to Precision Grinding Machines

Xuepeng Huang [1,2], Zhenzhong Wang [1,2,*], Bingyi Shen [1] and Pengli Lei [1]

[1] Department of Mechanical and Electrical Engineering, Xiamen University, Xiamen 361005, China; 19920210156226@stu.xmu.edu.cn (X.H.); 19920191151158@stu.xmu.edu.cn (B.S.); 19920190154065@stu.xmu.edu.cn (P.L.)
[2] Shenzhen Research Institute of Xiamen University, Shenzhen 518057, China
* Correspondence: wangzhenzhong@xmu.edu.cn

Abstract: Laser fusion research requires a large number of high-precision large-diameter aspherical components. To improve the grinding efficiency in the component production process, the manual operation time during the grinding process needs to be reduced. The grinding process requires the installation of the dressed grinding wheel onto the grinding machine spindle, and the off-line dressing results in installation errors during the loading and unloading process, which requires more time for manual alignment. To achieve self-aligning, the circumferential contour of the grinding wheel was first restored by the reversal method, then noise reduction and circle fitting were performed to obtain the eccentricity value and eccentricity position between the flange and the spindle, and finally, the flange was adjusted finely by three piezoelectric actuators installed inside the flange to reduce the eccentricity. Three repetitive experiments were conducted to verify that the self-aligning flange can reduce the eccentricity value by retracting the piezoelectric actuators so that the proper alignment between the flange and the spindle could meet the requirements; the average eccentricity value of the three experiments decreased by 74%, which greatly improved the efficiency of the grinding wheel alignment.

Keywords: reversal method; eccentricity; piezoelectric actuator; flange

Citation: Huang, X.; Wang, Z.; Shen, B.; Lei, P. Research on Self-Aligning Flanges Based on Piezoelectric Actuators Applied to Precision Grinding Machines. *Micromachines* **2021**, *12*, 1393. https://doi.org/10.3390/mi12111393

Academic Editors: Chengwei Kang, Chunjin Wang and Jiang Guo

Received: 14 October 2021
Accepted: 10 November 2021
Published: 13 November 2021

1. Introduction

As the precision manufacturing industry requires higher and higher surface processing accuracy for optical components [1,2], the requirements for the accuracy of the grinding process for optical components are also increasing; however, the grinding wheel mounting error has become an important concern in the high-precision grinding process. In the grinding process, the high hardness and low fracture toughness make the cutting force fluctuate greatly during grinding, which affects the surface quality of the components. Therefore, if there is a large eccentricity error in the grinding wheel installation, it will lead to an increase in the fluctuation of grinding force and affect the machining quality [3,4]. The causes of grinding wheel mounting errors are as follows: roundness error of the grinding wheel and coaxiality error of the grinding machine spindle, both of which are generally small. The important influencing factor is the eccentricity error generated by the mounting eccentricity between the grinding wheel center and the spindle axis. The installation eccentricity of the grinding wheel will directly cause changes in the thickness of the surface of the machined component, due to the unevenness of the thickness of the machined surface. Therefore, it will indirectly lead to uneven changes in the force on the grinding machine spindle, and even produce a certain impact that will shorten the working life of the grinding machine spindle [5]. Therefore, the precision mounting of grinding wheels has become one of the key problems that need to be solved in the field of precision grinding at present [6].

The process of manual precision assembly and calibration of grinding wheels is usually used to detect the circumferential runout of the grinding wheel, roughly determine the location of the eccentricity, fine-tune it by tapping the grinding wheel, and then repeat the detection of circumferential runout—and if it is not satisfied, to repeat the alignment until the circumferential runout is reduced to the qualified standard. The centering process is tedious and inefficient, so it is necessary to propose a self-aligning principle and corresponding instrument to replace manual centering, to improve the accuracy and efficiency of centering.

To achieve automatic centering, it is necessary to obtain the grinding wheel contour first, and there are mainly two methods: the machine vision method [7,8] and the reversal method [9], among which the reduction accuracy of the reversal method is higher than that that of machine vision method, and the accuracy is micron level, so the reversal method based on a laser displacement sensor for grinding wheel contour reduction is the more commonly used method for grinding wheel contour reduction at present.

Chen et al. [10] designed a grinding wheel centering device based on the reversal method to reduce the grinding wheel contour, which can effectively achieve centering by applying micro-displacement on the sidewall of the cup grinding wheel. This is the only study that uses piezoelectric actuators to achieve automatic grinding wheel aligning. However, the disassembly and installation of the centering fixture are tedious, and it can only center small-sized cup grinding wheels, which cannot be applied to most grinding applications. In order to automatically align grinding wheels of different sizes and types, this paper designs a self-aligning flange based on the commonly used flange size for mounting grinding wheels, and realizes grinding wheel alignment through a drive mechanism and a micro-displacement mechanism installed inside the flange. The main research contents of this paper are: (1) Error analysis of the inverse rotation method for reducing the grinding wheel contour. (2) Designing the self-aligning flange mechanism based on the commonly used flange dimensions. (3) The moving average filter is used to reduce the noise of the grinding wheel contour data, and the least squares method is used to fit a circle to the contour data to obtain the grinding wheel eccentricity information.

2. Derivation of the Self-Aligning Principle

The first step to realizing the self-aligning of the grinding wheel is to identify the outer contour of the grinding wheel and fit the optimal circular contour. According to the fitted circle, the diameter of the grinding wheel and the coordinates of the center of the circle can be obtained. At present, the commonly used methods to restore the circle contour include the machine vision contour restoration method and the reversal method based on the laser displacement sensor. Since the grinding wheel of a precision grinder needs high-precision restoration, and the machine vision restoration accuracy is low, the reversal method is adopted.

Firstly, the laser displacement sensor is fixed to the grinding machine table so that the laser beam from the laser displacement sensor passes through the center of the grinding machine spindle. Secondly, the grinding wheel contour data is collected using the laser displacement sensor after starting the grinding machine spindle. Finally, the actual circle contour is reduced by polar coordinates in combination with the angular velocity of spindle rotation. As shown in Figure 1, an arbitrary point P(x_p,y_p) on the actual circle circumference can be expressed by Equation (1):

$$x_p = L * \ cos\beta; y_p = L * \ sin\beta \tag{1}$$

where L denotes the distance of the laser displacement sensor from the center of the spindle, and β denotes the radian between the two sampling points.

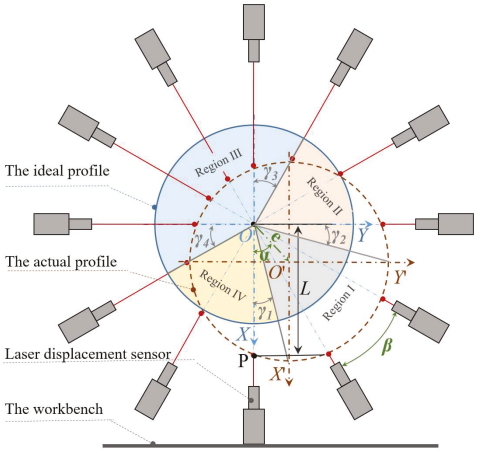

Figure 1. Schematic diagram of the reversal method.

To evaluate the error caused by sampling unevenness, the actual contour is divided into four quadrants according to the coordinate axes, and the total number of samples of the actual contour is defined as N. The number of samples of the arc segments in the four quadrants corresponding to the actual contour is n_1, n_2, n_3, and n_4. Additionally, the maximum of n_1, n_2, n_3, and n_4 is defined as as n_{max}, and the minimum as n_{min}. The ratio ε between n_{max} and n_{min} is the evaluation of sampling uniformity, as shown in Equation (2). If ε is close to 1, it indicates that the sampling uniformity is better.

$$\begin{gathered}
\Delta x = e{\cdot}cos\alpha,\ \Delta y = e{\cdot}sin\alpha; \\
\gamma_1 = arctan\left(\frac{\Delta y}{R+\Delta x}\right),\ \gamma_2 = arctan\left(\frac{\Delta x}{R+\Delta y}\right); \\
\gamma_3 = arctan\left(\frac{\Delta y}{R-\Delta x}\right), \gamma_4 = arctan\left(\frac{\Delta x}{R-\Delta y}\right); \\
n_1 = \frac{\frac{\pi}{2}-\gamma_1-\gamma_2}{2*\pi} * N, n_2 = \frac{\frac{\pi}{2}+\gamma_2-\gamma_3}{2*\pi} * N; \\
n_3 = \frac{\frac{\pi}{2}+\gamma_3+\gamma_4}{2*\pi} * N, n_4 = \frac{\frac{\pi}{2}-\gamma_4+\gamma_1}{2*\pi} * N\ ; \\
\varepsilon = \frac{\max(n_1,n_2,n_3,n_4,)-\min(n_1,n_2,n_3,n_4,)}{\min(n_1,n_2,n_3,n_4,)}
\end{gathered} \tag{2}$$

where e is the eccentricity value; α is the eccentric phase.

The calculation of the above Equation (2) shows that for the eccentricity level within 10 μm, the small displacement eccentricity has less influence on the spindle contour reduction, and the evaluation index ε is 1. The accuracy of the reduction contour can be guaranteed, so the reversal method can be used for the circle contour reduction.

After the reconstruction of the grinding wheel contour by laser displacement sensor is verified to be feasible, a suitable micro-displacement mechanism needs to be used for fine-tuning to achieve centering. It is known from the geometry that at least three directions of micro-displacement are required to achieve in-plane centering, and the relationship between the alignment amount of the micro-displacement mechanism and the eccentricity state needs to be deduced. The *XOY* reference coordinate system is established with the center of the grinding wheel spindle as the origin of the coordinate system, as shown in Figure 2, and the right-angle coordinate system $X'O'Y'$ is established with the center of the actual grinding wheel contour, where a', b' and c' are the displacement states of the micro-displacement mechanism after contacting the grinding machine spindle, and a, b and c are the displacement states of the micro-displacement mechanism after self-aligning. To obtain the required displacement in the three directions, the coordinates of the contact

points need to be found according to the circular contour of the grinding wheel before and after alignment, respectively.

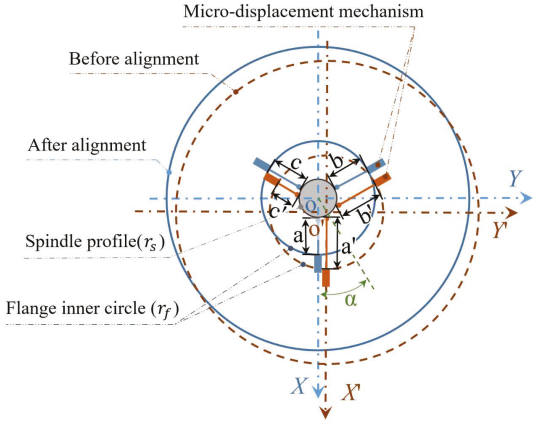

Figure 2. Schematic diagram of three-way alignment.

The circumferential contour before self-aligning is shown as the dashed line, and the circumferential contour after self-aligning is shown as the solid line. Defining r in Equation (3) is equal to the spindle radius r_s and the flange inner circle radius r_f, respectively. The position points of the three micro-displacement mechanisms in contact with the spindle before self-aligning can be obtained as $A'_s(x'_{as}, y'_{as})$, $B'_s(x'_{bs}, y'_{bs})$, $C'_s(x'_{cs}, y'_{cs})$. The position points of the three micro-displacement mechanisms in contact with the inner circle of the flange before self-aligning can be obtained as $A'_f\left(x'_{af}, y'_{af}\right)$, $B'_f\left(x'_{bf}, y'_{bf}\right)$, $C'_f\left(x'_{cf}, y'_{cf}\right)$. The length of the three micro-displacement mechanisms before self-aligning is $a' = \sqrt{\left(x'_{as} - x'_{af}\right)^2 + \left(y'_{as} - y'_{af}\right)^2}$, $b' = \sqrt{\left(x'_{bs} - x'_{bf}\right)^2 + \left(y'_{bs} - y'_{bf}\right)^2}$, $c' = \sqrt{\left(x'_{cs} - x'_{cf}\right)^2 + \left(y'_{cs} - y'_{cf}\right)^2}$.

$$\begin{cases} (x_{a'} - e{\cdot}cos\alpha)^2 + (y_{a'} - e{\cdot}sin\alpha)^2 = r^2 \\ y_{a'g} = e{\cdot}sin\alpha \\ x > 0 \end{cases};$$

$$\begin{cases} (x_{b'} - e{\cdot}cos\alpha)^2 + (y_{b'} - e{\cdot}sin\alpha)^2 = r^2 \\ y_{b'} = -\sqrt{3}x_{b'} + e{\cdot}sin\alpha + \sqrt{3}e{\cdot}cos\alpha \\ x_{b'} < 0 \end{cases};$$

$$\begin{cases} (x_{c'} - e{\cdot}cos\alpha)^2 + (y_{c'} - e{\cdot}sin\alpha)^2 = r^2 \\ y_{c'} = \sqrt{3}x_{c'} + e{\cdot}sin\alpha - \sqrt{3}e{\cdot}cos\alpha \\ x < 0 \end{cases}; \quad (3)$$

Defining r in Equation (4) as equal to the spindle radius r_s and the flange inner circle radius r_f, respectively. The position points of the three micro-displacement mechanisms in contact with the spindle after self-aligning can be obtained as $A_s(x_{as}, y_{as})$, $B_s(x_{bs}, y_{bs})$, $C_s(x_{cs}, y_{cs})$. The position points of the three micro-displacement mechanisms in contact with the inner circle of the flange after self-aligning can be obtained as $A_f(x_{af}, y_{af})$, $B_f(x_{bf}, y_{bf})$, $C_f(x_{cf}, y_{cf})$. The length of the three micro-displacement mechanisms after self-aligning is

$$a = \sqrt{\left(x_{as} - x_{af}\right)^2 + \left(y_{as} - y_{af}\right)^2}, \quad b' = \sqrt{\left(x'_{bs} - x'_{bf}\right)^2 + \left(y'_{bs} - y'_{bf}\right)^2},$$
$$c' = \sqrt{\left(x'_{cs} - x'_{cf}\right)^2 + \left(y'_{cs} - y'_{cf}\right)^2}.$$

$$\begin{cases} {x_a}^2 + {y_a}^2 = r^2 \\ y_a = 0 \\ x_a > 0 \end{cases} ; \begin{cases} {x_b}^2 + {y_b}^2 = r^2 \\ y_b = -\sqrt{3}x_b \\ x_b < 0 \end{cases} ; \begin{cases} {x_c}^2 + {y_c}^2 = r^2 \\ y_c = \sqrt{3}x_c \\ x_c < 0 \end{cases} \quad (4)$$

Therefore, to achieve self-aligning, three micro-displacement mechanisms are needed to move the distances $L_a = a' - a$, $L_b = b' - b$, $L_c = c' - c$, with positive values representing retraction and negative values representing extension.

3. Structural Design of Self-Aligning Flange

Mounting an offline dressed grinding wheel on the grinding machine spindle causes circumferential runout, which requires the use of suitable alignment elements for alignment. From the above self-aligning principle, it is clear that self-aligning requires three micro-displacement output devices

The mechanisms that produce micro-displacement mainly include mechanical drive micro-displacement, linear motor micro-displacement [11], the magnetostrictive micro-displacement mechanism [12,13], and piezoelectric actuated micro-displacement [14,15]. Among them, the mechanical transmission-type displacement mechanism can produce a large stroke, but it is easy to produce backlash and friction wear and crawl phenomenon, so the accuracy is not high. Linear motor-type micro displacement intermediates without a transmission mechanism, and has a high transmission efficiency, but due to its higher cost and it being easy to heat, it is not suitable for application with the self-aligning of grinding wheel in this paper. The magnetostrictive type can produce accurate micro-displacement with better repeatability, but it is easy to heat up under the action of the magnetic field, which has some influence on its accuracy. The piezoelectric actuation type is based on the inverse piezoelectric effect, and the value of displacement is changed by adjusting the input voltage value of the piezoelectric element, which has the advantages of small size, high resolution, and high output force.

Limited by the compact structure of the grinding wheel flange, the piezoelectric actuator was finally selected as the micro-displacement structure. Its piezoelectric characteristic curve is shown in Figure 3. When installing the self-aligning flange, to avoid collision between the grinding wheel spindle and the piezoelectric actuator, the piezoelectric actuator needs to be set back along the axial direction, and after the flange is installed, the piezoelectric actuator installation is moved forward along the respective axial direction until it touches the outer surface of the grinding wheel spindle.

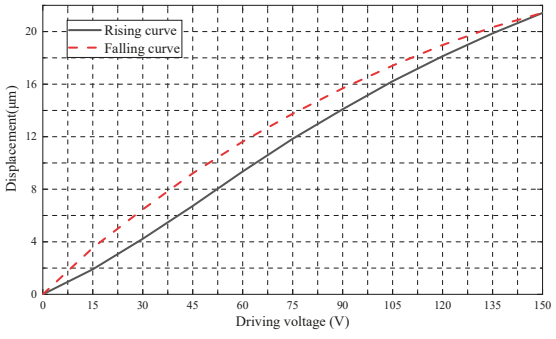

Figure 3. Piezoelectric characteristic curve.

To realize the requirement of three piezoelectric actuators advancing and retreating simultaneously in their respective axial directions, the flange is designed with a three-jaws chuck structure on the lathe. As shown in Figure 4, the internal structure of the self-aligning flange consists of three jaws, three piezoelectric actuators, three bevel gears, three bushings, and a crown gear. In order to make the crown gear and bevel gears and jaws fit at the same time, it is designed to be divided into six equal parts, with the bevel tooth part alternating with the helix curve. When using the flange, a wrench is used to rotate the bevel gear and drive the crown gear to turn, thus driving the jaws to move in the respective axial direction in translation.

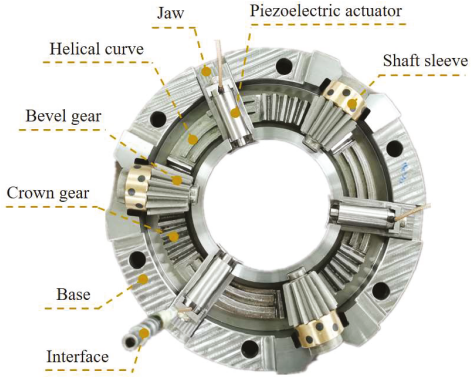

Figure 4. Internal diagram of self-aligning flange.

By attaching the piezoelectric actuator to the jaws, it can be seen that the piezoelectric actuator only touches the grinding machine spindle during alignment. It should be noted that due to the limitation of the machining accuracy of the bevel gear, there will be a backlash in the transmission, but since the self-aligning flange only uses a single reverse rotation to drive the tooth discs during use, the backlash between the bevel gear and the crown gear has no effect on its performance.

4. Results and Discussion

4.1. Processing of Circumferential Data

In sampling the grinding wheel circumference data, the displacement signal from the laser displacement sensor is theoretically started while the grinding wheel is rotating, but there is no trigger to turn on the laser displacement sensor for contour acquisition while the grinding machine spindle is rotating. Therefore, when the circular contour acquisition is performed, the laser displacement sensor is turned on first for data acquisition, and the grinding machine spindle is subsequently rotated. The contour signal is obtained as the initial segment is the same and is programmable for identification and deletion. Since the contour data has different degrees of noise, which affect the reduction of the grinding wheel circumferential contour, the original contour data needs to be noise-reduced to obtain a relatively accurate circumferential contour for the subsequent calculation of the eccentric phase and eccentricity. In this paper, the moving average filter is selected for noise reduction. The algorithm itself is based on the principle of low-pass filtering, and a total of five values are taken before and after each value as well as itself for averaging, which is a simple fast and accurate calculation principle [16–18].

After noise reduction of the circular signal, it is necessary to calculate the discrete points for circle fitting to obtain the eccentricity and eccentric phase. Since there are coordinates for each data point, it is theoretically possible to obtain the circle center coordinates by averaging the x and y values of all coordinates—but due to the noise and uneven distribution of sampling points in the actual sampling process, it is not possible to use

this method to obtain the circle center coordinates. In this paper, the least squares method was used to fit the circle by calculating the difference between the square of the distance from the center of the circle to each data point and the square of the radius, to get the smallest difference and obtain the best-fitting circle. As shown in Figure 5, the solid line is the original data, the dashed line is the data after noise reduction; the dotted line is the fitted circle.

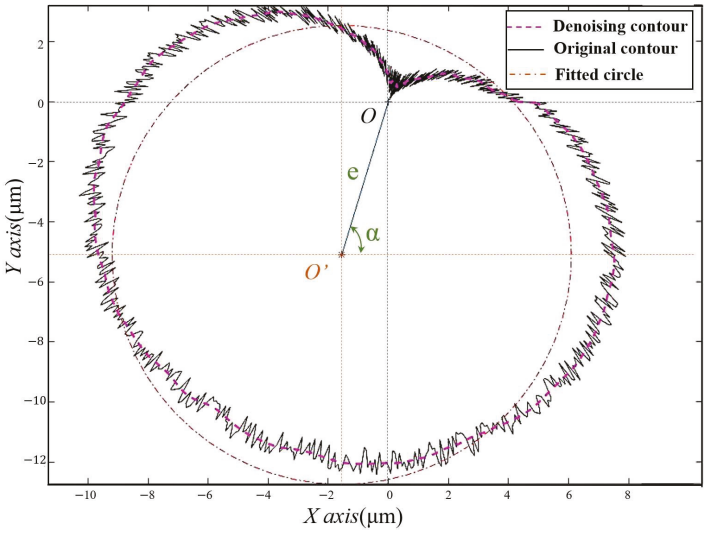

Figure 5. Graph of circumference data after processing.

4.2. The Self-Aligning Validation Experiment

To verify the accuracy of the results of the self-aligning method and data collection and analysis, a verification experiment was conducted. In the experiment, there was no grinding wheel with a well-dressed surface available for the experiment due to the lack of an offline dressing machine for grinding wheels. Since the grinding wheel is always mounted on the self-aligning flange during the dressing and use of the grinding wheel, the eccentric characteristics presented by the grinding wheel contour data were consistent with those presented by the self-aligning flange, so the contour data collected in the verification experiment could be used as the contour data of the mating surface of the flange and the grinding wheel.

During the experiment, the laser displacement sensor was first mounted on the grinding machine table, and the grinding machine spindle was moved to find the lowest point of the spindle so that the laser beam of the laser displacement sensor could pass through the center of the grinding machine spindle circle as close as possible to the theoretical requirements. The self-aligning flange was then mounted to the grinding machine spindle and half-tightened with a nut, i.e., the self-aligning flange was fixed but the relative position could be adjusted. The self-aligning flange was moved to the recognizable range of the laser displacement sensor to start sampling, then the grinding machine spindle was turned on to rotate at low speed, and the secondary development software automatically processed the data and generated the required voltage values for the three piezoelectric actuators when the sampling was completed.

The self-aligning process was then carried out by rotating the bevel gear with a wrench to bring the piezoelectric actuator into contact with the grinding spindle surface. The piezoelectric controller was connected to the computer, and a signal cable was used to connect the piezoelectric actuator to the piezoelectric controller, as shown in Figure 6. After the connection was made, the secondary development software sent the calculated voltage

value to the piezoelectric controller, and the output voltage value from the piezoelectric controller caused the piezoelectric actuator to move accordingly. When the piezoelectric actuator was displaced for self-centering, the nut was fully tightened. The signal line connected to the piezoelectric actuator was then removed, and the centered circumferential contour was collected and compared. Detailed experimental parameters are shown in Table 1.

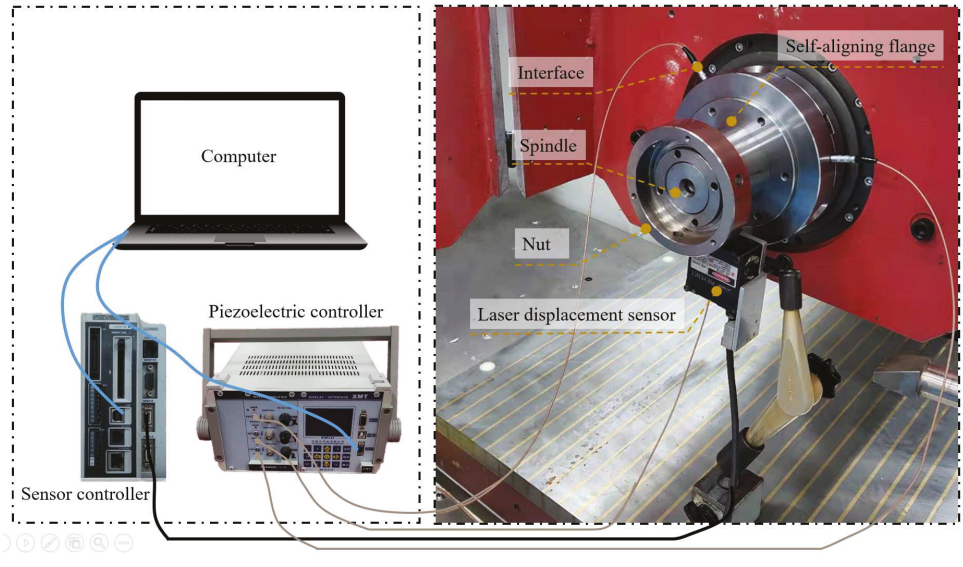

Figure 6. Diagram of the experimental setup.

Table 1. Experimental parameters.

Spindle Speed (rpm)	Sampling Frequency (Hz)	Number of Sampling Laps	Diameter of Flange Mating Surface (mm)
60	1000	5	74

After self-aligning according to the calculated theoretical voltage value, it was found that the circumferential runout value did not change significantly. As the piezoelectric characteristic curve in Figure 3 was obtained under non-stressed conditions, the piezoelectric actuator did not get the ideal displacement under stressed conditions by inputting the theoretical voltage, so the subsequent experiment could be centered according to the theoretical eccentric phase obtained by the algorithm. Through several attempts, self-aligning could be achieved by giving the piezoelectric actuator 0.8 times its maximum voltage input. Accordingly, three repetitive experiments were carried out respectively, and the results of the centering were obtained as shown in Figure 7.

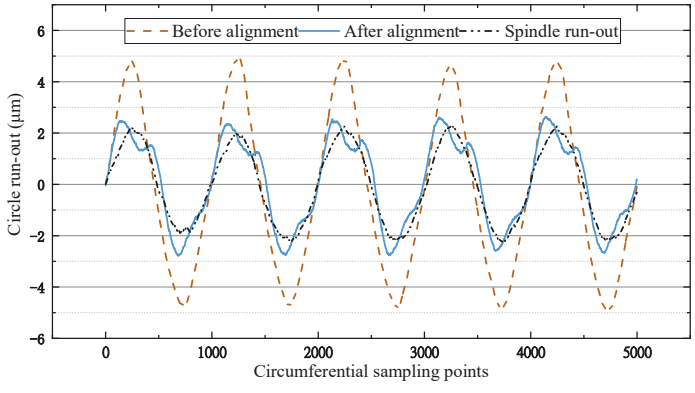

(**a**)

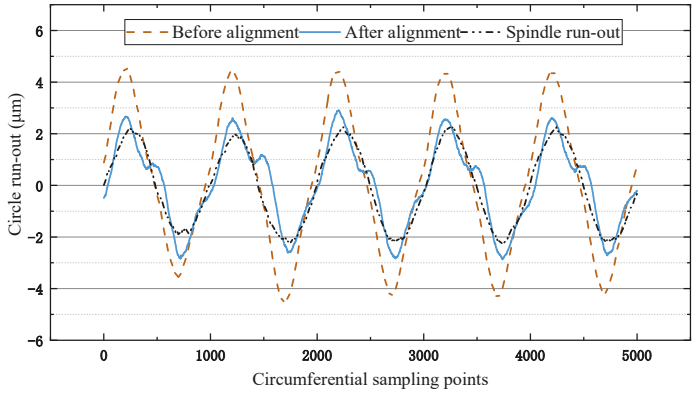

(**b**)

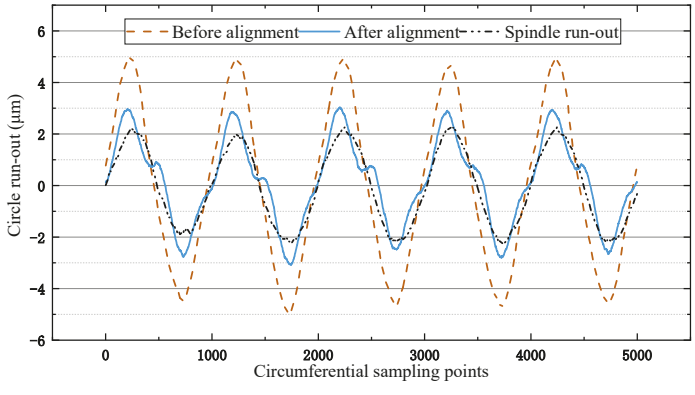

(**c**)

Figure 7. *Cont.*

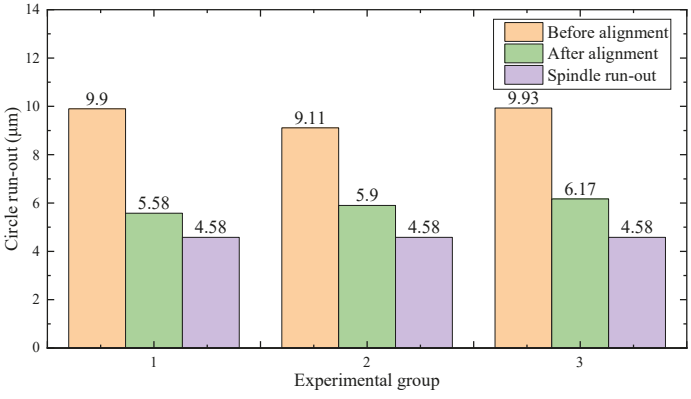

(**d**)

Figure 7. Experimental results. (**a**) Results of the first self-aligning experiment. (**b**) Results of the second self-aligning experiment. (**c**) Results of the third self-aligning experiment. (**d**) Comparison chart of the three experimental results.

From the experimental results in Figure 7, it can be seen that the average eccentricity before the alignment of the three experiments was 9.65 μm, and the average eccentricity after the alignment was 5.88 μm. Since the eccentricity of the spindle itself was 4.58 μm as measured by the laser displacement sensor, it can be calculated that the eccentricity of the flange was reduced by 74% after the self-aligning, which can meet the production requirements of the grinding machine.

During the self-aligning experiment, the grinding machine spindle and flange had a tapered fit, which itself had a good centering effect [19]. Therefore, in the process of half-tightening and full-tightening of the nut, there is a possibility that the full-tightening will lead to a fuller conical fit, resulting in the centering effect. In addition, due to the use of the three-jaws chuck structure for the movement of the piezoelectric actuator, the self-aligning flange may be aligned due to the centering function of the three-jaws chuck [20]. In order to investigate the cause of the self-aligning phenomenon more accurately, the experiment of nut tightness and the single-factor experiment of three-jaws centering were carried out. The experimental parameters are shown in Tables 2 and 3.

Table 2. Single-factor experimental parameters of nut tightness.

Spindle Speed (rpm)	Sampling Frequency (Hz)	Number of Sampling Laps	Diameter of Flange Mating Surface (mm)	Tightness of Nut
60	1000	5	74	Half-tightened/Fully tightened

Table 3. Single-factor experiment of three-jaws aligning.

Spindle Speed (rpm)	Sampling Frequency (Hz)	Number of Sampling Laps	Diameter of Flange Mating Surface (mm)	Experimental Factors
60	1000	5	74	With jaws/Without jaws

From the results of Figure 8, it can be seen that the eccentricity was 10.32 μm at half-tightening and 12.56 μm at full tightening, so the tightening of the nut did not affect the self-aligning of the flange.

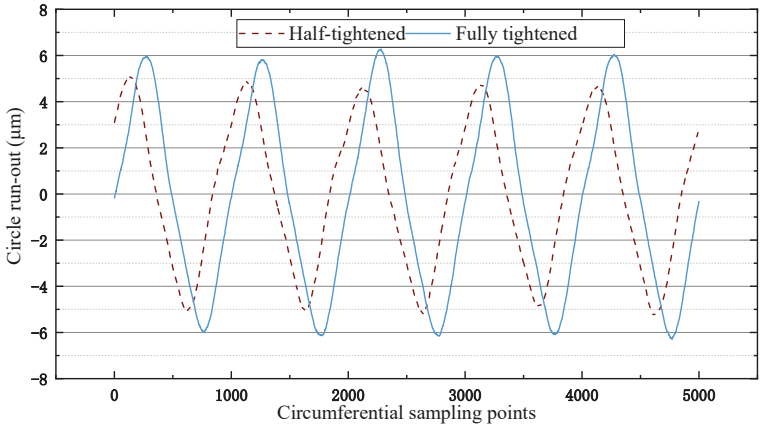

Figure 8. Graph of nut tightness experimental results.

From the results in Figure 9, it can be seen that the eccentricity before the spin jaws was 10.53 μm and the eccentricity after the spin jaws was 11.44 μm, both of which are basically the same. Therefore, using the jaws alone to hold the spindle did not result in self-aligning. In summary, the self-aligning flange designed in this paper can realize the self-aligning function through the expansion and contraction of the piezoelectric actuator and has a higher alignment efficiency than the results of Chen et al.

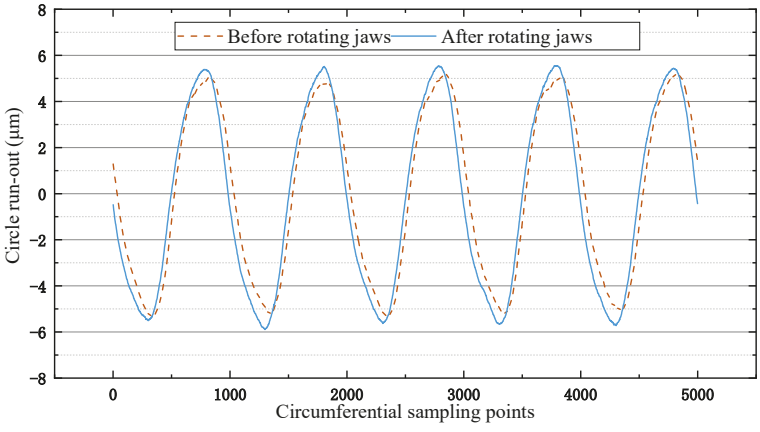

Figure 9. Graph of rotating jaws experimental results.

5. Conclusions

The problem of eccentricity exists when the dressed grinding wheel is mounted to the grinding machine spindle, and the traditional manual alignment requires several alignments, which is less efficient and less accurate. In this paper, a self-aligning flange based on a piezoelectric actuator is proposed to replace the traditional manual alignment of the grinding wheel, and the eccentricity is reduced by 74% after the self-aligning. This greatly ensures the accuracy of the grinding process and reduces the damage to the grinding machine due to grinding wheel vibration. The self-aligning flange significantly reduces the time needed for grinding wheel installation and has a good engineering application prospect. The main innovations of this paper are as follows:

(1) The uneven error in the reduction of the grinding wheel contour using the reversal method was investigated.
(2) Based on the dimensions of the universal flange, bevel gears, jaws, and tooth discs were designed to control the movement of the piezoelectric actuator.
(3) The eccentricity and eccentric phase were obtained by processing the raw data with averaging filters and using the least squares method for circle fitting.
(4) The laser displacement sensor acquisition and the piezoelectric controller were combined by secondary development software to shorten the operation time and improve the efficiency of grinding wheel installation and centering.

Author Contributions: Conceptualization, Z.W.; methodology, P.L.; software, X.H.; validation, P.L., X.H. and B.S.; formal analysis, B.S.; investigation, B.S.; resources, P.L.; data curation, X.H.; writing—original draft preparation, X.H.; writing—review and editing, X.H.; visualization, X.H.; supervision, Z.W.; project administration, Z.W.; funding acquisition, Z.W. All authors have read and agreed to the published version of the manuscript.

Funding: This research was funded by The Science and Technology Projects of Shenzhen, grant number JCYJ20180306172924636.

Conflicts of Interest: The authors declare no conflict of interest.

References

1. Singleton, R.; Marshall, M.B.; Lewis, R.; Evans, G. Rail grinding for the 21st century-taking a lead from the aerospace industry. *Proc. Inst. Mech. Eng. Part F J. Rail Rapid Transit* **2015**, *229*, 457–465. [CrossRef]
2. Tan, N.Y.J.; Zhang, X.; Neo, D.W.K.; Huang, R.; Liu, K.; Kumar, A.S. A review of recent advances in fabrication of optical Fresnel lenses. *J. Manuf. Process.* **2021**, *71*, 113–133. [CrossRef]
3. Manea, H.; Cheng, X.; Ling, S.; Zheng, G.; Li, Y.; Gao, X. Model for Predicting the Micro-Grinding Force of K9 Glass Based on Material Removal Mechanisms. *Micromachines* **2020**, *11*, 969. [CrossRef] [PubMed]
4. Wang, Q.; Lin, S.; Jiang, Z.; Yin, Y.; Zhao, Y. Fewer-axis grinding methodology with simultaneously guaranteeing surface accuracy and grinding force for large optical SiC mirror. *Int. J. Adv. Manuf. Technol.* **2018**, *99*, 1863–1875. [CrossRef]
5. Chen, Y.; Chen, X.; Xu, X.; Yu, G. Quantitative impacts of regenerative vibration and abrasive wheel eccentricity on surface grinding dynamic performance. *Int. J. Adv. Manuf. Technol.* **2018**, *96*, 2271–2283. [CrossRef]
6. Tian, Y.; Wang, Y.; Wang, L.; Zhao, W. The centering and leveling adjustment and control technology for the ultra-precision turntable. In Proceedings of the 2015 International Conference on Optical Instruments and Technology: Optical Systems and Modern Optoelectronic Instruments, Beijing, China, 17–19 May 2015; International Society for Optics and Photonics: Bellingham, WA, USA, 2015; Volume 9618, p. 96181A.
7. Shahabi, H.H.; Ratnam, M.M. Assessment of flank wear and nose radius wear from workpiece roughness profile in turning operation using machine vision. *Int. J. Adv. Manuf. Technol.* **2009**, *43*, 11–21. [CrossRef]
8. Wei-Heng, S.; Syh-Shiuh, Y. Using the Machine Vision Method to Develop an On-machine Insert Condition Monitoring System for Computer Numerical Control Turning Machine Tools. *Materials* **2018**, *11*, 1977.
9. Okuyama, E.; Fukazawa, N.; Muraoka, M.; Nosaka, N. Angular motion and circular profile measurements using the reversal method. *J. Phys. Conf. Ser.* **2005**, *13*, 123–126. [CrossRef]
10. Chen, S.-P.; Wang, Z.-Z.; Yu, H.; Lin, L.-Q. Research on Automatic Compensation Technology for Eccentricity of Grinding Wheel. *Int. J. Precis. Eng. Manuf.* **2018**, *19*, 1201–1209. [CrossRef]
11. Shinno, H.; Yoshioka, H.; Taniguchi, K. A Newly Developed Linear Motor-Driven Aerostatic X-Y Planar Motion Table System for Nano-Machining. *CIRP Ann.* **2007**, *56*, 369–372. [CrossRef]
12. Yang, X.; Jia, Z.; Guo, D. Study on Giant Magnetostrictive Microdisplacement Actuator Having the Function of Sensing its Displacement. In Proceedings of the Fifth World Congress on Intelligent Control and Automation (IEEE Cat. No.04EX788), Hangzhou, China, 15–19 June 2004; IEEE: Piscataway, NJ, USA, 2004.
13. Zhu, Y.; Ji, L. Theoretical and experimental investigations of the temperature and thermal deformation of a giant magnetostrictive actuator. *Sens. Actuators A Phys.* **2014**, *218*, 167–178. [CrossRef]
14. Jie, D.G.; Sun, L.N.; Qu, D.S.; Wang, L.; Cai, H.G. Fuzzy-reasoning based self-tuning PID control for piezoelectric micro-displacement system. *J. Harbin Inst. Technol.* **2005**, *37*, 145–147.
15. Wang, X.; Chu, Y.; Zhai, Z. Research of Micro-Positioning System Based on Piezoelectric Actuator. In Proceedings of the 2009 9th International Conference on Electronic Measurement & Instruments, Beijing, China, 16–19 August 2009; IEEE: Piscataway, NJ, USA, 2009; pp. 1–897.
16. Shestakov, A.L.; Keller, A.V. Optimal Dynamic Measurement Method Using Digital Moving Average Filter. In *Journal of Physics: Conference Series*; IOP Publishing: Bristol, UK, 2021; Volume 1864, p. 012073.

17. Junhong, L.; Feng, D. Filtering-based recursive least-squares identification algorithm for controlled autoregressive moving average systems using the maximum likelihood principle. *J. Vib. Control* **2015**, *21*, 3098–3106.
18. Babu, C.N.; Reddy, B.E. A moving-average filter based hybrid ARIMA–ANN model for forecasting time series data. *Appl. Soft Comput.* **2014**, *23*, 27–38. [CrossRef]
19. Smith, S. Understanding tapered spindle connections. *Cut. Tool Eng.* **2014**, *66*, 20–21.
20. Hans-Otto, H.; Franz, T. Chuck for Work Holding in Lathe Has Radial Clamping Jaws with Sprung Faces to Allow Compensation for Stepped Workpieces. 2004. Available online: https://patents.google.com/patent/DE10322857A1/en (accessed on 21 July 2021).

micromachines

MDPI

Article

Influence of Lubricant Environment on Machined Surface Quality in Single-Point Diamond Turning of Ferrous Metal

Menghua Zhou [1,2,†], Jianpeng Wang [1,†] and Guoqing Zhang [1,3,*]

[1] Shenzhen Key Laboratory of High Performance Nontraditional Manufacturing, College of Mechatronics and Control Engineering, Shenzhen University, Nan-hai Ave 3688, Shenzhen 518060, China; 1810293032@emial.szu.edu.cn (M.Z.); 1900291014@email.szu.edu.cn (J.W.)
[2] Levoit Structure Research and Development Department, Vesync Company Limited, Zhongshanyuan Ave, Shenzhen 518060, China
[3] Guangdong Key Laboratory of Electromagnetic Control and Intelligent Robots, College of Mechatronics and Control Engineering, Shenzhen University, Nan-hai Ave 3688, Shenzhen 518060, China
* Correspondence: zhanggq@szu.edu.cn
† Authors with equal contribution.

Abstract: In the field of single-point diamond turning (SPDT), machining ferrous metal is an important research topic with promising application. For SPDT of ferrous metal, the influence of lubricant on the workpiece surface morphology remains to be studied. In this study, three lubricant machining environments were selected to carry out specific control experiments. The machined surface morphology and cutting force in different lubricant machining environments were analyzed. The experiment results showed that the lubricant environment will have significant impacts on the quality of the machined surface morphology of ferrous metal. In the environment of minimum quantity lubrication machining (MQLM-oil), better machined surface quality can be obtained than that in ordinary dry machining (ODM) and high-pressure gas machining (HGM). Furthermore, the cutting force captured in the ODM and HGM environment increased with the increase of the cutting depth, while the cutting force in the MQLM-oil environment remained almost unchanged. That indicates MQLM-oil can suppress the formation of hard particles to improve the machining quality.

Keywords: diamond tool; single-point diamond turning; lubricant; ferrous metal

Citation: Zhou, M.; Wang, J.; Zhang, G. Influence of Lubricant Environment on Machined Surface Quality in Single-Point Diamond Turning of Ferrous Metal. *Micromachines* **2021**, *12*, 1110. https://doi.org/10.3390/mi12091110

Academic Editors: Jiang Guo, Chunjin Wang and Chengwei Kang

Received: 20 August 2021
Accepted: 13 September 2021
Published: 15 September 2021

1. Introduction

Ferrous metals are widely applied in industrial production due to their excellent mechanical properties, while can cause catastrophic tool wear in single-point diamond turning (SPDT) of ferrous metal. Furthermore, grinding, polishing, etc. applied in ultraprecision machining of ferrous metal have low machining efficiency which is difficult to meet the current manufacturing needs [1,2]. Therefore, researches related to STDP ferrous metal is necessary.

Single-crystal diamonds have extremely high hardness and can be ground to produce extremely sharp cutting edges, which can provide important support for controllability in ultraprecision turning [3]. However, when diamond tools are employed to machine ferrous metal, chemical reactions will lead to catastrophic diamond tool wear to lose the ability to machine steel molds for optical components [4,5]. Catastrophic wear is affected by many factors, including the workpiece material, machining parameters, environment etc. [6] Paul et al. suggested that the unpaired d-electrons induced a chemical reaction between Fe and C [7]. Furthermore, high temperature and high pressure in the machining process increased the chemical reaction speed to increase the wear of diamond tools [8]. Compared with the wear in turning nonferrous metals, mechanical wear of diamond tools accounts for a small part [9,10]. In fact, numerous complex chemical reactions lead to the catastrophic chemical wear of diamond tool, whereas the dominant chemical wear is graphitization [11].

In Komanduri's study, comb-like groove wear was captured, and the groove direction is consistent with the cutting direction [10]. It is hard to have scratch patterns on the diamond surface due to weak hardness of low-carbon steel, therefore they propose a mechanism of graphitization wear of diamond tools which can weaken the diamond hardness [10–12]. Thornton and Wilks further studied the graphitization of diamond, and the experimental results showed that the temperature of diamond graphitization is about 1800 K under static vacuum conditions, while that is between 1000~1100 K in the presence of Fe [13]. However, because the process of SPDT ferrous metals is not static contact, Narulkar et al. further researched the graphitization mechanism of diamond by employing molecular dynamics (MD) and showed that iron catalysis plays an important role leading to the graphitization of diamond tools [14].

To suppress diamond tool wear in SPDT ferrous metals, many assisted methods have been developed and mainly through the way of improved machining technology, modified diamond tools and workpiece material [15]. At present, ultrasonic vibration-assisted cutting (UVC) is the most effective machining technology to suppress diamond graphitization wear in cutting ferrous metals and can achieve the mirror-level machined surface roughness [16,17]. Furthermore, assisted method employing CO_2, CO, CH_4, C_2H_2 etc. are unable to enhance effectively diamond tool life, due to the close contact between workpieces and diamond tools [18,19]. Focusing on the tool properties, nanodiamond coating and diamond tools modified by ion implantation have been developed to suppress graphitization of diamond [20,21]. However, diamond tool wear is still serious. Furthermore, assisted method of workpiece nitriding has also been developed and can achieve mirror-level machined surface roughness, which is nonetheless limited on the nitriding layer [22]. More importantly, these assisted methods are subject to their own limitations and rarely applied in industry production. Therefore, the method of improving machined surface quality, especially in-depth insight into physical or chemical mechanisms in SPDT ferrous metals, is still needed.

Lubricant is wildly applied in machining process as a typically physical cooling and lubrication method [23]. More importantly, lubricant has a significant influence on diamond wear in SPDT ferrous metals [24]. Therefore, researches on the lubricant is one of the most basic topics in SPDT ferrous metals. However, the influence of lubricant on the machined surface quality in SPDT ferrous metals is still unclear. In this study, by single-groove scraping experiments, an in-depth insight into the physical mechanism of the influence of lubricant environments to the machined surface quality is provided, and provides an important reference for the subsequent research on relevant aspects.

2. Experiments

To explore the influence of lubricant on SPDT ferrous metals, this section will focus on the two sets of single-groove scraping experiments, and conduct a detailed and in-depth analysis of the experimental results. Benefitting from high measurement accuracy, white light interferometer is a typical measurement apparatus to capture the surface morphology of workpieces in ultraprecision machining. In this study, the morphology of machined surfaces and grooves was captured by means of the white light interferometer (Contour GT-X, Bruker, Billerica, MA, USA) by vertical scanning interferometry (VSI) mode with no filter. Appling relatively low-hardness die steel AISI 4140 (Shengjili Co., Ltd., Sichuan, China) to carry out specific experiments. The cutting force was captured by an ultra-precision dynamometer (Kistler 9017C, Winterthur, Switzerland). Before the single-groove scraping experiment, the workpieces were rough-machined with a polycrystalline diamond (PCD) tool (Shenzhen Yuhe Diamond Tools Co., Ltd., Shenzhen, China). Three machining environments of minimum-quantity lubrication machining (MQLM-oil), ordinary dry machining (ODM) and high-pressure gas machining (HGM) were selected to rough-machine the workpiece surface. The surface morphology and roughness obtained by the two machining environments of HGM and ODM were similar. The specific rough-machined surface morphology was captured by means of the white light interferometer, as shown in Figure 1.

The value of the surface roughness *Sa* (see Figure 1) indicates that MQLM-oil is beneficial to improving the machined quality compared with ODM and HGM.

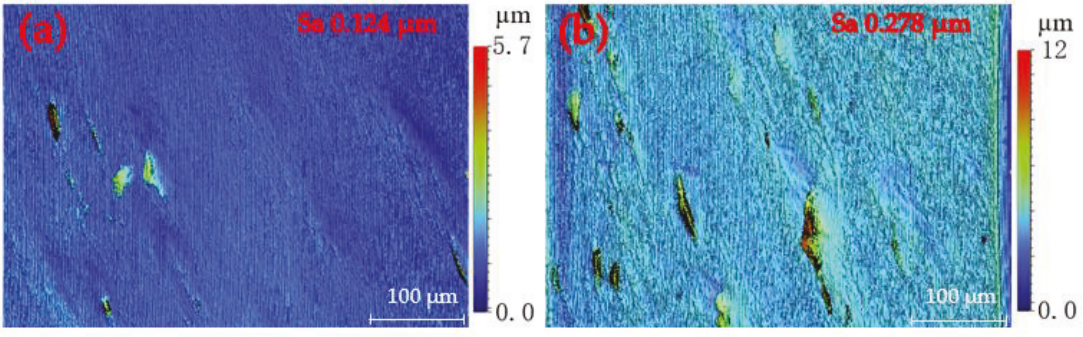

Figure 1. Machined surface morphology captured by means of the white light interferometer in (**a**) minimum quantity lubrication machining (MQLM-oil) and (**b**) high-pressure gas machining (HGM) environments.

The single-groove scraping experiments were divided into two parts, employing four natural single-crystal diamond tools (Shenzhen Yuhe Diamond Tools Co., Ltd., Shenzhen, China) T1 with 496.2 μm radius, T2 with 490.9 μm radius, T3 with 492.6 μm and T4 with 483 μm radius. All of the diamond tools have the rake angle of 0°and the clearance angle of 10°. The first part was the 360° single-groove scraping experiment on the rough-machined surface obtained in three machining environments. The theoretical depth of the single groove is 12 μm. The feed of Z-axis was achieved by 2 μm, and the cutting force was captured by the ultraprecision dynamometer, as shown in E-1 to E-3 in Table 1. The second part was also carried on the rough-machined surface obtained in the three machining environments, as shown in Figure 2. The annular groove was divided into six uniform parts (N1–N6). In the experiments, the feed of Z-axis was 2 μm and the scraping angle of a single-groove was 60°; the cutting force was captured by the ultraprecision dynamometer. After the experiments, the white light interferometer was employed to capture the surface morphology of the workpiece, and the cutting edge of the diamond tool was observed with a metallographic microscope and there was minimal wear of diamond tools in the scratching experiments since the scraping time was very short and the scraping speed was very slow compared to turning. Therefore, the wear status of the employed cutting tool could be negligible.

Table 1. Detailed parameters in the single-groove scraping experiments.

Group Number	Rough-Machining Environment	Tool Number	Turning Environment	Single Scraping Depth ∗ Angle	Total Scraping Depth
E-1	OHGM/ODM/MQLM-oil	T1	MQLM-oil	2 μm ∗ 360°	12 μm
E-2	HGM/ODM/MQLM-oil	T2	HGM	2 μm ∗ 360°	12 μm
E-3	HGM/ODM/MQLM-oil	T3	ODM	2 μm ∗ 360°	12 μm
N-1	HGM/ODM/MQLM-oil	T4	MQLM-oil	2 μm ∗ 360°	2 μm
N-2	HGM/ODM/MQLM-oil	T4	MQLM-oil	2 μm ∗ 300°	4 μm
N-3	HGM/ODM/MQLM-oil	T4	MQLM-oil	2 μm ∗ 240°	6 μm
N-4	HGM/ODM/MQLM-oil	T4	MQLM-oil	2 μm ∗ 180°	8 μm
N-5	HGM/ODM/MQLM-oil	T4	MQLM-oil	2 μm ∗ 120°	10 μm
N-6	HGM/ODM/MQLM-oil	T4	MQLM-oil	2 μm ∗ 60°	12 μm

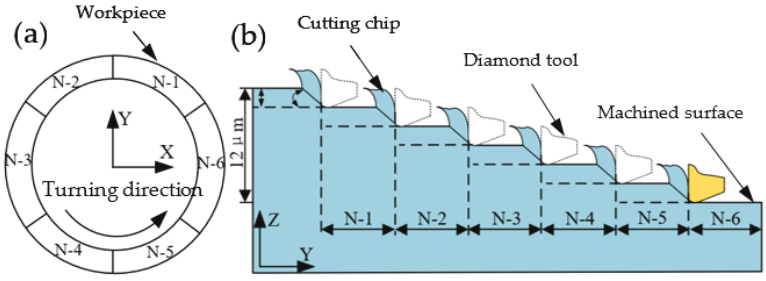

Figure 2. Diagram of (**a**) single-groove scraping experiments on the workpiece and (**b**) cutting depth changed from N-1 to N-6.

3. Results and Discussions

3.1. Surface Morphology of Single-Groove

PCD tools were employed to rough-machine the AISI 4140 workpiece with a diameter of 10 mm in the ODM environment, and the surface morphology with a surface roughness of 0.278 μm is shown in Figure 1b. The scraping depth was 2 μm and the total scraping depth was 12 μm. Figure 3a is part of the surface morphology in the HGM, which is similar to the ODM; Figure 3c is part of the surface morphology in the MQLM-oil. Comparing the experimental results, there were pits on the surface of the groove in HGM and ODM environments, while there were almost no pits on the surface of the groove in the MQLM-oil environment. According to statistics on the occurrence frequency and depth of pits, it was found that pits appeared the most and had the deepest depth in the HGM environment and found that the amount of pits in a single-groove in HGM and ODM was much more than that in the MQLM-oil environment, and the depth of pits in the MQLM environment was also smaller compared with the other two machining environments. The appearance of pits resulted in the terrible morphology of the single-groove, as shown in Figure 3b,d. The details of the depth of the pit in three machining environments are shown in Figure 4.

The experiments of E-1, E-2 and E-3 were repeated on the rough-machined surface, which was machined in the MOLM-oil and ODM environments, respectively. The experimental results of rough-machining in the ODM were almost as the same as the experimental results of the rough-machining in the HGM environment, and the experimental results of rough-machining in the MOLM-oil are shown in Figure 4b. There are numerous pits on the single-groove surface in HGM and ODM environments, and the depth of pits was 12 μm to 16 μm; in MQLM-oil environment, few pits were found on the single-groove surface. Compared the experimental results in the HGM rough-machining environment, it was found that in the single-groove scraping experiment on the surface rough-machined by the HGM environment, there were still a few pits in the MQLM-oil environment.

To explore the influence of the rough-machining environment on the subsequent machining, more detailed scraping experiments were carried out. After rough-machined experiments in the HGM environment, the experiments of N-1 to N-6 were carried out (see Table 1) and the experimental results were shown in Figure 5a. In both HGM and ODM environments, the maximum pit depth will not increase or decrease significantly with the increase of the cumulative cutting depth, while in the MQLM-oil environment, the maximum pit depth will reduce significantly with the increase of the cumulative cutting depth. Repeated experiments are carried out for rough-machining workpieces in HGM and MQLM-oil environments. The rough-machining results in ODM environment are similar to that in HGM environment. Figure 5b shows the details of pits in the MQLM-oil environment. Summarizing the data of the surface pits of the rough-machining in the MQLM-oil environment, it was found that there were no obvious pits on the single-groove surface in this environment, and the results obtained in this rough-machining environment of the other environments were almost the same. The depth increased first and then remained almost unchanged.

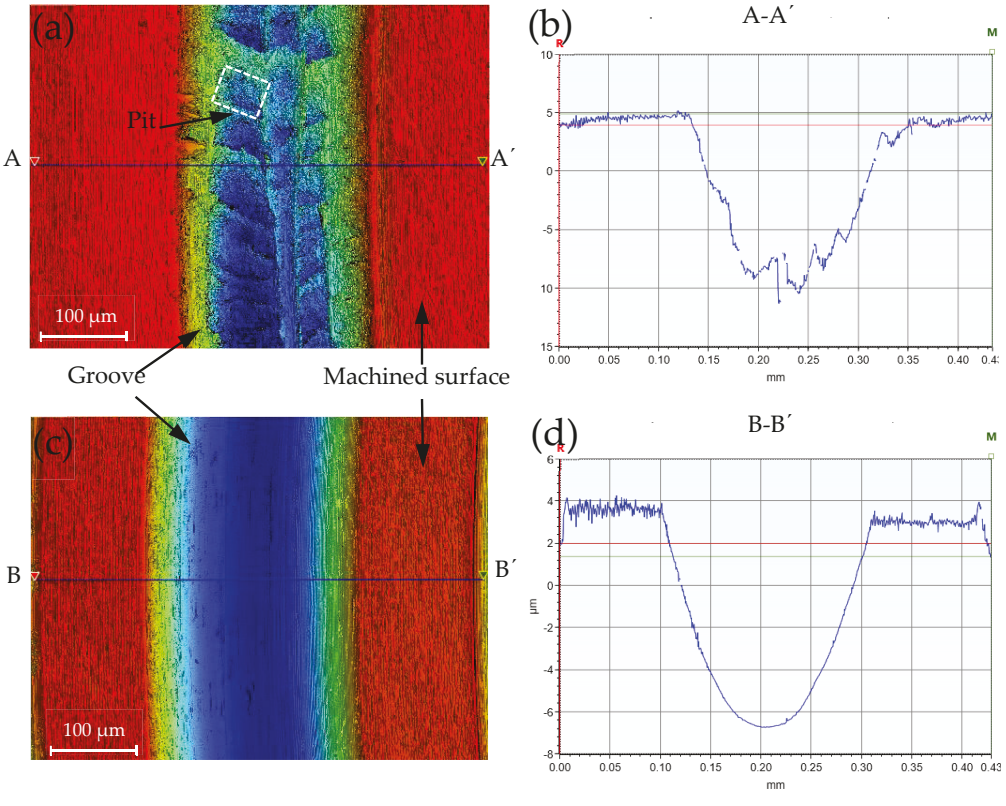

Figure 3. Single-groove scraping morphology captured by means of the white light interferometer in (**a**) HGM environment and (**c**) MQLM-oil environment; (**b**) the cross section curve of A-A′ and (**d**) the cross section curve of B-B′.

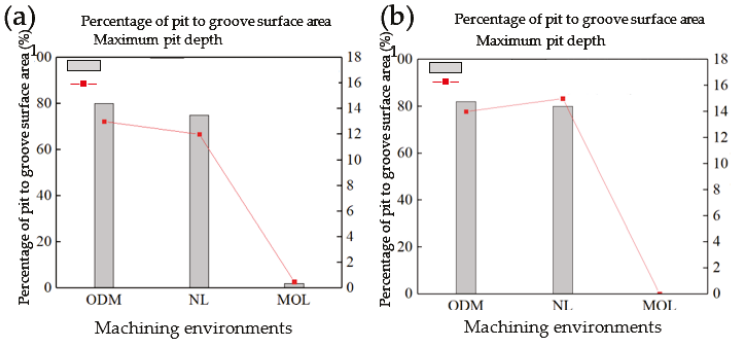

Figure 4. The statistical data of the pits in the groove scraping experiments of E-1, E-2 and E-3 in rough-machined surface machined in (**a**) HGM and (**b**) MQLM-oil environments.

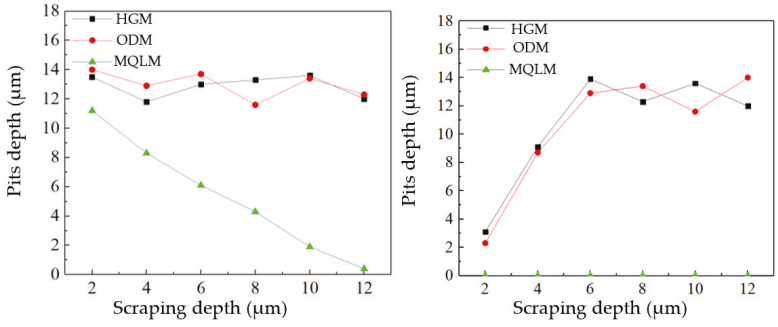

Figure 5. Relation of the scraping depth and the depth of the pits in the rough-machined surface of (**a**) HGM environment and (**b**) MQLM-oil environment.

Therefore, the MQLM-oil environment had a prominent effect on reducing the number of the appearance of pits. It also proved that other environments will cause a significant body of pits in SPDT ferrous metal. The maximum depth of the pits will not increase indefinitely with the increase of the cumulative cutting depth, but will eventually remain between 12 μm and 16 μm.

3.2. Cutting Force Analysis of Single-Groove Scraping Experiments

The cutting force in the above-mentioned experiment was captured and analyzed. The magnitude of force when scraping depth of 2 μm was shown in Figure 6. In Figure 6a are shown the scraping experimental carried out in the three environments when the surface of the workpiece was rough-machined in the MQLM-oil environment. The average cutting forces under the three environments were almost same in the first experiment. The cutting force increased in the three environments with the cutting depth increased. More importantly, the increased force in the HGM environment was the most obvious, whereas that in the MQLM-oil environment was not obvious. Moreover, the average cutting force in the two machining environments of MQLM-oil and HGM was almost equal at a depth of scraping 2–8 μm, while the average cutting force in the HGM environment appeared to significantly increase after scarping depth more than 8 μm.

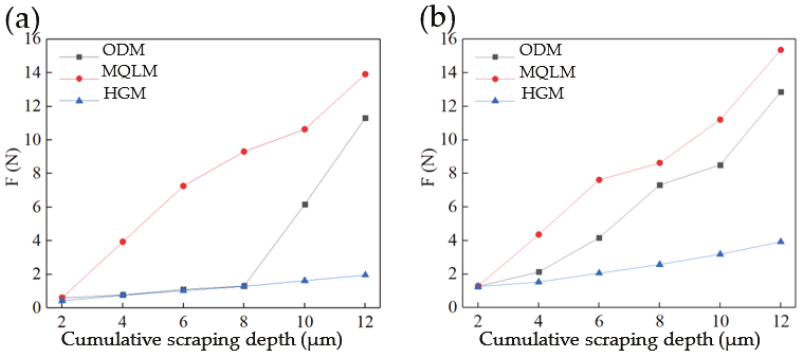

Figure 6. The average force of single-groove scraping experiments of E-1 (MQLM-oil), E-2 (HGM) and E-3 (ordinary dry machining (ODM)) on the rough-machined surface of (**a**) MQLM-oil environment and (**b**) HGM environment.

In Figure 6b are shown the scraping experimental results in the three environments when the surface of the workpiece was rough-machined in the HGM environment. The experimental results of ODM were similar to that of the HGM. The average cutting forces under the three cutting environments were almost same in the first experiment. With the increased depth of cutting, the cutting force was increased in the HGM environment. When the cutting depth was 2 μm, the cutting force captured in MQLM-oil rough-machined was only about 0.6 N, while the surface cutting force obtained by others was about 1.1 N.

Therefore, the surface of rough-machined will affect the results of the initial scraping experiments, whereas the effect will be less as the cumulative cutting depth increases. Furthermore, the surface morphology of the groove captured in different scraping environments is almost the same. Therefore, the rough-machining environment will have a significant influence on the subsequent cutting, whereas it will not continue to affect that and the critical depth is 12 μm.

3.3. Physical Mechanism of the Lubricant Influence on Single-Groove Surface Morphology

The existence of hard carbide particles is the dominant physical mechanism of the lubricant influence on single-groove surface morphology. There are numerous hard carbide particles in AISI 4140. As shown in Figure 7, a trace of hard particles of about 2 μm can be found on the machined surface which are two orders of magnitude harder than the workpiece [1,25].

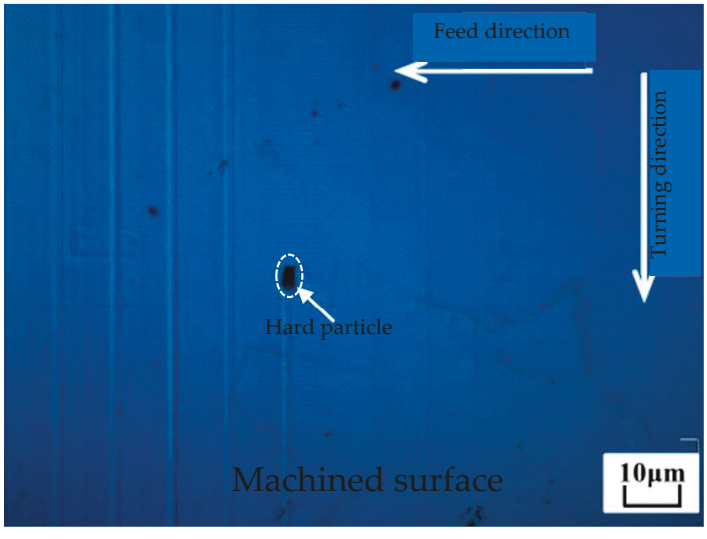

Figure 7. Hard particles on the machined surface in SPDT ferrous metals.

Figure 8a is shown a pit area captured by means of the white light interferometer, and the morphology of the pits are along the cutting direction. The generation mechanism of pits is illustrated in Figure 8b. The pits always present a steep surface on one side and a gentle surface on the other side. Obviously, this is caused by hard particles being pulled out by the diamond tool during the cutting process. In the experiments, the position of the diamond tool installed on the tool holder remains fixed. Therefore, the pit within the material cannot removal by plastic caused by the hardness advantage of diamond tools. The mechanism of pits generation can be clearly expressed in Figure 8b. In the process of single-groove scraping, the speed of the diamond tool is low. When it meets soft ferrous metal, the material can be plastically removed to form a single-groove morphology in low cutting speed. However, the hard particles in the ferrous metal cannot be plastically removed

when the tool interferes with the hard particles during the cutting process, therefore the hard particles will be pulled out to form pits.

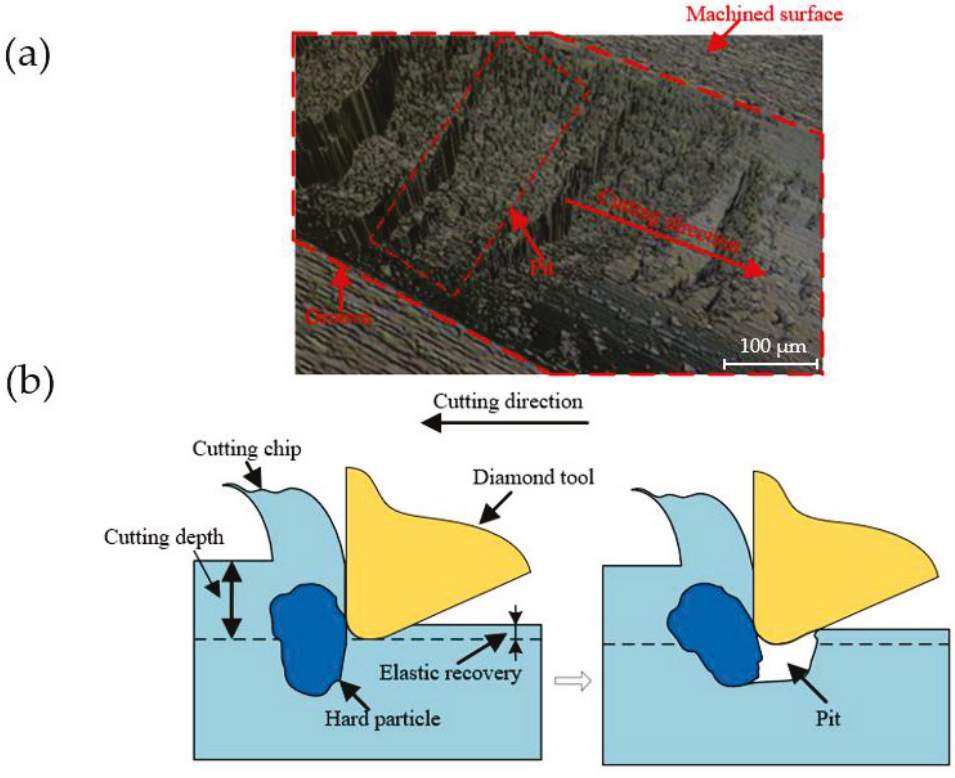

Figure 8. (**a**) Enlarged surface of a pit area on the groove surface and (**b**) the illustration of the pit generation mechanism on the ferrous metal surface in SPDT.

The appearance of hard carbide particles will lead to the fluctuation of cutting force, therefore it is suitable to employ cutting force to characterize the characteristics of pits in the cutting process. Figure 9 shows the corresponding cutting force and the corresponding single-groove morphology in the three environments. In the environment, with the diamond tool cutting the material beginning, there was a sudden change of cutting force. The same phenomenon also appeared in other two machining environments. However, only the cutting force in the MQLM-oil environment remained basically stable during the subsequent processing; while that of HGM and ODM showed large fluctuations. Because the removal of materials in these two types of environments is unstable, the formation process of pits will inevitably lead to continuous fluctuation in the captured cutting force.

Moreover, under the HGM environments, the cutting force fluctuated for a long time corresponding represents the large volume of pits; under the ODM environments, the cutting force fluctuated for a short time corresponding represents the small volume of pits; under the MQIL-oil environments, the cutting force changed smoothly, which means there were no pits. Therefore, cutting forces can be employed to properly characterize the properties of pits during cutting.

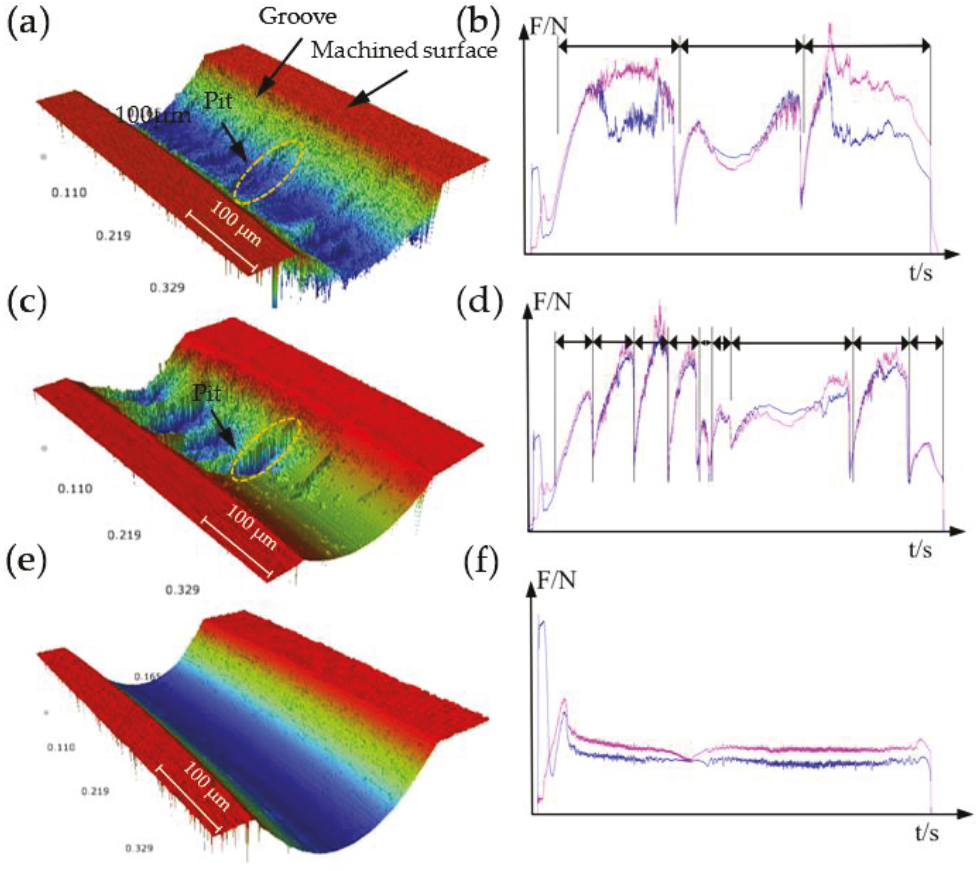

Figure 9. Groove surface morphology and cutting force in (**a**,**b**) HGM environment, (**c**,**d**) ODM environment and (**e**,**f**) MQLM-oil environment.

3.4. Influence of Closed-Loop-Stiffness of the Lathe on Single-Groove Surface Morphology

Another possible reason is that the closed-loop-stiffness of the ultraprecision lathe was not enough caused the spindle crawled during machining. In the experiment, especially the scraping experiment of the single-groove, the diamond tool was stressed by a large force when removing the workpiece material. The force generated in this process will be transmitted to the spindle eventually. As the aerostatic spindle, the stiffness of the spindle is very limited. When the force is large, the spindle is usually prone to crawling and the pulsed force causes an unstable process of material removal.

As shown in Figure 10a, during the working process of the ultra-precision lathe, the interaction force caused by the interference between the tool and the workpiece will be transmitted through the spindle and lathe bed, and finally form a closed-loop force caused the phenomenon of spindle crawling. As shown in Figure 10b, the tool is mainly subjected to two forces in the Z-axis and Y-axis directions during the machining process. The force in the Z-axis direction may cause the crawl of the Z-axis, and the force in the Y-axis direction may cause the crawl of the C-axis. During the relative sliding process between the spindle and the guide rail, when the driving force of the spindle cannot overcome the resistance, the motion will be stopped, and as the driving equipment subjected to the spindle continues to motion, it will eventually overcome the resistance and leap forward. This phenomenon is commonly known as crawling for the spindle.

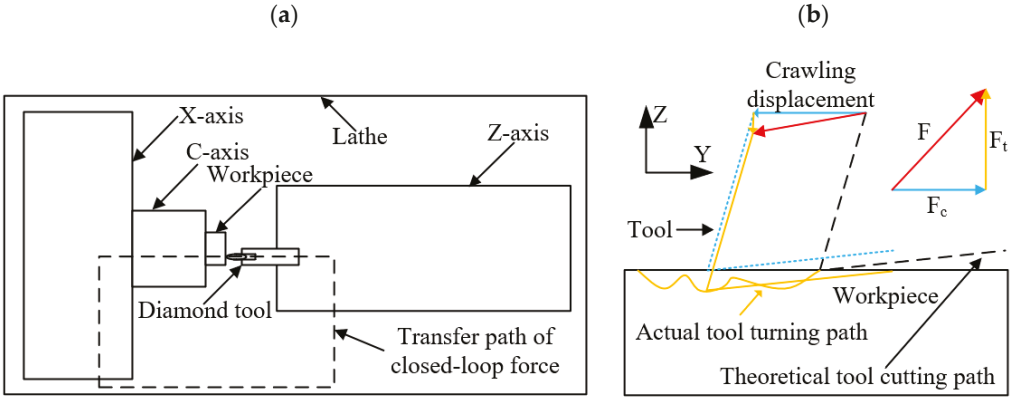

Figure 10. (**a**) Transfer path of closed-loop force on the lathe and (**b**) transfer direction of the force.

Obviously, the lubrication effect produced by different lubricant environments is inconsistent, and the equivalent friction coefficient of MQLM-oil is lower than that of the ODM environment. The equivalent friction coefficient is high, which means that the resistance to overcome increases, and the probability of occurrence of the phenomenon of spindle crawling becomes greater. As shown in Figure 10b, under the action of the resultant force of the tool, if the crawling phenomenon occurs, an irregular tool path will be generated, and the crawling of the tool in the Z-axis direction will cause the single-groove surface to sink downward.

As shown in Figure 11, the pits caused by different factors had different forms in single-groove. The pit morphology caused by the removal of hard particles was limited by the size of the hard particles and could not affect the cross-sectional profile of the entire single-groove, as shown in Figure 11a. The pits caused by the crawling phenomenon were caused by the irregular changes of the tool path. The pits must have affected the cross-sectional of the entire single-groove, as shown in Figure 11b.

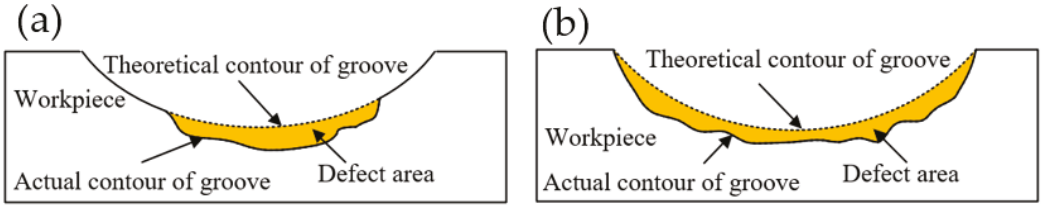

Figure 11. Different types of pit on the groove surface of (**a**) hard particles caused the defect area and (**b**) crawling caused the defect area.

4. Conclusions

In this study, the influence of the lubricant on machined surface morphology was studied. Three experiments of HGM, MQLM-oil, and ODM were carried out and the cutting force was analyzed. To conclude, we found:

(1) The lubrication and cooling method by applying lubricant have an important influence on the surface morphology in SPDT ferrous metals. In the MQLM-oil environment, better surface quality can be obtained than that in the HGM and ODM environments.

(2) The existence of hard carbide particles is the main reason for the physical mechanism of pit generation in scraping ferrous metal.

(3) Cutting force can be employed to characterize the properties of pits during cutting, the frequency and period of large-scale fluctuation of the cutting force represent the number and size of pits respectively.
(4) The closed-loop-stiffness of the ultra-precision lathe is low, resulting in discontinuous and large-area pits on the surface of the ferrous metal.

Author Contributions: Conceptualization, G.Z.; Data curation, M.Z. and J.W.; Formal analysis, M.Z. and J.W.; Investigation, M.Z. and J.W.; Methodology, M.Z. and J.W.; Project administration, G.Z.; Resources, G.Z.; Validation, M.Z.; Writing—original draft, M.Z. and J.W.; Writing—review & editing, J.W. All authors have read and agreed to the published version of the manuscript.

Funding: The work described in this paper was supported by the National Natural Science Foundation of China (Grant No. U2013603, 51827901), the Shenzhen Natural Science Foundation University Stability Support Project (Grant No. 20200826160002001), and the Postgraduate Innovation Development Fund Project of Shenzhen University (Grant No. 315-0000470813).

Conflicts of Interest: The authors declare no conflict of interest.

References

1. Wang, Y.; Suzuki, N.; Shamoto, E.; Zhao, Q. Investigation of tool wear suppression in ultraprecision diamond machining of die steel. *Precis. Eng.* **2011**, *35*, 677–685. [CrossRef]
2. Osmer, J.; Glaebe, R.; Riemer, O.; Brinksmeier, E.; Butepage, S.; Hoffmann, F. Diamond milling of nitrided steels for optical mold making. *J. Vac. Sci. Technol. B Microelectron. Nanometer Struct.* **2009**, *27*, 1238–1240. [CrossRef]
3. Zhang, S.J.; To, S.; Zhang, G.Q. Diamond tool wear in ultra-precision machining. *Int. J. Adv. Manuf. Technol.* **2017**, *88*, 1–29. [CrossRef]
4. Zhang, C.B.; Cheung, C.F.; Bulla, B.; Zhao, C.Y. An investigation of the high-frequency ultrasonic vibration-assisted cutting of steel optical moulds. *Micromachines* **2021**, *12*, 460. [CrossRef]
5. Li, Z.; Gang, J.; Fang, F.; Gong, H.; Jia, H. Ultrasonically assisted single point diamond turning of optical mold of tungsten carbide. *Micromachines* **2018**, *9*, 77. [CrossRef] [PubMed]
6. Zhang, Q.L.; Guo, N.; Chen, Y.; Fu, Y.C.; Zhao, Q.L. Simulation and Experimental Study on the Surface Generation Mechanism of Cu Alloys in Ultra-Precision Diamond Turning. *Micromachines* **2019**, *10*, 573. [CrossRef] [PubMed]
7. Paul, E.; Evans, C.J.; Mangamelli, A.; Mcglauflin, M.L.; Polvani, R.S. Chemical aspects of tool wear in single point diamond turning. *Precis. Eng.* **1996**, *18*, 4–19. [CrossRef]
8. Shimada, S.; Tanaka, H.; Higuchi, M.; Yamaguchi, T.; Obata, K. Thermo-Chemical Wear Mechanism of Diamond Tool in Machining of Ferrous Metals. *CIRP Ann.* **2004**, *53*, 57–60. [CrossRef]
9. Lu, H.Y. Discussion on wear mechanism of diamond tool. *Mach. Manuf.* **2003**, *1*, 38–39.
10. Komanduri, R.; Shaw, M.C. Wear of synthetic diamond when grinding ferrous metals. *Nature* **1975**, *255*, 211–213. [CrossRef]
11. Thornton, A.G.; Wilks, J. The Wear of Diamond Tools Turning Mild-Steel. *Wear* **1980**, *65*, 67–74. [CrossRef]
12. Zou, L.; Yin, J.; Huang, Y.; Zhou, M. Essential causes for tool wear of single crystal diamond in ultra-precision cutting of ferrous metals. *Diam. Relat. Mater.* **2018**, *86*, 29–40. [CrossRef]
13. Zong, W.J.; Li, Z.Q.; Sun, T.; Li, D.; Cheng, K. Analysis for the wear resistance anisotropy of diamond cutting tools in theory and experiment. *J. Mater. Process. Technol.* **2010**, *210*, 858–867. [CrossRef]
14. Narulkar, R.; Bukkapatnam, S.; Raff, L.M.; Komanduri, R. Graphitization as a precursor to wear of diamond in machining pure iron: A molecular dynamics investigation. *Comput. Mater. Sci.* **2009**, *45*, 358–366. [CrossRef]
15. Brinksmeier, E.; Gläbe, R. Diamond Machining of Steel Molds for Optical Applications. *Key Eng. Mater.* **2007**, *364*, 701–706. [CrossRef]
16. Zhang, X.Q.; Liu, K.; Kumar, A.S.; Rahman, M. A study of the diamond tool wear suppression mechanism in vibration-assisted machining of steel. *J. Mater. Process. Technol.* **2014**, *214*, 496–506. [CrossRef]
17. Moriwaki, T. Development of 2DOF Ultrasonic Vibration Cutting Device for Ultraprecision Elliptical Vibration Cutting. *Adv. Precis. Eng.* **2010**, *447–448*, 164–168. [CrossRef]
18. Casstevens, J.M. Diamond Turning of steel in Carbon-saturated Atmospheres. *Precis. Eng.* **1983**, *5*, 9–15. [CrossRef]
19. Zhang, X.Q.; Deng, H.; Liu, K. Oxygen-shielded ultrasonic vibration cutting to suppress the chemical wear of diamond tools. *CIRP Ann.* **2019**, *68*, 69–72. [CrossRef]
20. Yan, J.L.; Li, H.; Lüder, J.; Chaudhari, A.; Hao, W. Micromachining of ferrous metal with an ion implanted diamond cutting tool. *Carbon* **2019**, *152*, 598–608.
21. Ahmad, N.K.; Mursaleen, B.M. Development of a dual-layered diamond-coated WC-Co cutting tool for enhancing tool life in the dry machining of mild-steel alloy. *Proc. Inst. Mech. Eng. Part. B J. Eng. Manuf.* **2019**, *233*, 1515–1528.

22. Saito, H.; Jung, H.J.; Shamoto, E.; Hara, Y.; Hara, T. Suppression of tool damage in ultraprecision diamond machining of stainless steel by applying electron-beam-excited plasma nitriding. *Precis. Eng. J. Int. Soc. Precis. Eng. Nanotechnol.* **2020**, *63*, 126–136. [CrossRef]
23. Huang, P.; Li, H.; Zhu, W.L.; Wang, H.; Zhang, G.; Wu, X.; To, S.; Zhu, Z. Effects of eco-friendly cooling strategy on machining performance in micro-scale diamond turning of Ti–6Al–4V. *J. Clean. Prod.* **2020**, *243*, 118526. [CrossRef]
24. Zhou, M.H.; Zhang, G.Q.; Chen, N. Effects of lubricant on cutting performance in single-point diamond turning of ferrous metal NAK 80. *Inter. J. Adv. Manuf. Technol.* **2020**, *109*, 2549–2558. [CrossRef]
25. Evans, C.; Bryan, J.B. Cryogenic diamond turning of stainless steel. *CIRP Ann.* **1991**, *40*, 571–575. [CrossRef]

micromachines

MDPI

Article

Study on the Electrorheological Ultra-Precision Polishing Process with an Annular Integrated Electrode

Cheng Fan, Yigang Chen, Yucheng Xue and Lei Zhang *

Jiangsu Provincial Key Laboratory of Advanced Robotics, Soochow University, Suzhou 215021, China; chfan@suda.edu.cn (C.F.); ygchenygchen@stu.suda.edu.cn (Y.C.); 20185229045@stu.suda.edu.cn (Y.X.)
* Correspondence: sudazhanglei@suda.edu.cn

Abstract: Electrorheological (ER) polishing, as a new ultra-precision super-effect polishing method, provides little damage to the workpiece surface and is suitable for polishing all kinds of small and complex curved surface workpieces. In this paper, an ER polishing tool with an annular integrated electrode is developed. The orthogonal experiments are carried out on the six influencing factors of ER polishing which include the applied voltage, the abrasive particle size, the abrasive concentration, the polishing gap, the polishing time and the tool spindle speed. The influence order of these six factors on the ER polishing is obtained. On this basis, the effect of a single process parameter of ER polishing on surface roughness is studied experimentally.

Keywords: electrorheological polishing; polishing tool; roughness; integrated electrode

Citation: Fan, C.; Chen, Y.; Xue, Y.; Zhang, L. Study on the Electrorheological Ultra-Precision Polishing Process with an Annular Integrated Electrode. *Micromachines* **2021**, *12*, 1235. https://doi.org/10.3390/mi12101235

Academic Editors: Jiang Guo, Chunjin Wang and Chengwei Kang

Received: 25 September 2021
Accepted: 9 October 2021
Published: 12 October 2021

1. Introduction

With the development of communications technology and the modern medical level, there is an increasing demand for electronic and optical components with complex surfaces and high surface quality, such as the spherical and aspheric lenses [1]. In the traditional process, most aspheric lenses are made by cemented carbide mold. These molds not only need higher geometric accuracy but also require lower surface roughness. Therefore, after the mold is made, the polishing process must be carried out to ensure the surface quality of the mold [2]. As the final step in the manufacturing process, polishing is used for the machining of plane, mirror and free-form surface, which ultimately affect the quality of the workpiece [3–5]. In the traditional polishing methods, the polishing pad and grinding head are mostly used to directly contact with the workpiece surface for polishing, and grinding paste is added between the polishing pad and the workpiece, or abrasive particles such as abrasive belt and grinding wheel are fixed on the grinding head [6,7]. When the polishing head is used to polish the complex and small mold, the traditional processing technology cannot make the polishing head suitable for the small mold due to the limitation of the tool size. On the other hand, the polishing head with fixed abrasive wears easily [8]. With the reduction of the number of effective cutting edges and the decrease of the shear speed, the surface roughness of the workpiece becomes uneven [9,10]. In order to overcome the defects of traditional polishing, it is necessary to seek a flexible and compliant polishing process that can continuously gather the abrasive particles in the polishing area for a long time. People have begun to study and use non-traditional polishing methods to achieve a constant material removal rate, including laser polishing [11,12], ultrasonic polishing [13–15], electrochemical polishing [16–18], solid jet polishing [19–23], liquid suspension polishing [24,25], etc.

ER polishing is a new type of compliant ultra-precision polishing methods. The ER fluid is a kind of suspension composed of solid particles (dispersed phase) with high dielectric constant and liquid (continuous phase) with good insulation performance. The ER effect occurs under the action of an electric field. The apparent viscosity increases with the increase of electric field strength, showing obvious shear yield strength. When the

electric field intensity decreases to zero, the viscosity of ER fluid decreases and returns to the initial value. The ER polishing technology is a compliant polishing method which uses the ER effect under an electric field to process the workpiece surface. It is suitable for both conductive and non-conductive workpieces [26]. The controllable flexible polishing head is generated by the ER effect to realize the adaptive polishing of complex surfaces. The complex surface can be polished by controlling the voltage, tool electrode speed and polishing path, improving the processing quality.

Since the emergence of the ER polishing technology, many researchers have been trying to research and explore it. At present, research on ER polishing mainly focuses on the process method, process law, tool system and corresponding equipment development of polishing micro-aspheric lenses of optical glass and their forming die made of cemented carbide, silicon wafer and other conductive and non-conductive workpieces [27–29]. Zhang et al. [30–32] studied the mechanism and material removal model of ER polishing, regarding tool electrode speed, processing time, applied voltage, abrasive type and concentration. Hui et al. [33] applied torque sensor and speed sensor to study the shear characteristics of ER polishing and greatly reduced the surface roughness of K9 glass by polishing. Luo et al. [34] polished the surface of optical glass with the ER fluid containing ferric oxide abrasive and explained the influence of polishing pressure and slurry shear rate on the final material removal rate. However, due to the poor practicability of ER polishing tool design and low material removal rate, ER polishing is still not widely used in industry. In this paper, a new tool system of ER polishing is designed and developed, which contains an annular integrated electrode. The tool system integrates the cathode and anode that produce the ER effect but insulates them from each other. The proposed ER polishing tool system can be installed on the machine center as a module, and the machining materials are not limited by conductors or non-conductors.

The remainder of the paper is organized as follows. Section 2 introduces a new developed ER tool system. Section 3 shows the experiments and discussion. Conclusions are presented in Section 4.

2. ER Polishing Equipment

Figure 1 shows the structure of the self-made integrated ER polishing tool system. The tool system is composed of the motor, the support plate, the sliding plate, the synchronous pulley, the synchronous belt, the conductive slip ring, the outer sleeve, the deep groove ball bearing, the angular contact bearing, the tool shaft, the tool needle, the lock nut, the connecting flange and the annular electrode. Figure 2 shows the ER polishing equipment and the flexible polishing head due to ER effect.

The motor drives the tool shaft to rotate through the synchronous wheel and synchronous belt. The tool shaft is equipped with conductive slip ring. The outer ring of conductive slip ring is fixed with the support plate by bolts and nuts. The inner ring and tool shaft cooperate to transmit electricity to the tool shaft and the tool pin and rotate with the tool shaft synchronously. The tool pin is connected to the tool shaft by a thread and rotates with the tool shaft. The annular electrode is installed on the connecting flange in a static state. During ER polishing, the positive pole of the power is supplied to the annular electrode, and the negative power is supplied to the terminal of the conductive slip ring. By immersing the tool end into the ER polishing liquid mixed with polishing abrasive particles, the high voltage electric field is formed between the tool needle and the annular electrode, which causes the ER fluid mixed with polishing abrasive particles near the tool end to produce the ER effect. As a result, a soft flexible polishing head is formed at the tip of needle electrode (as shown in Figure 2). The rotation of the needle electrode drives the movement of the polishing abrasive particles to realize the micro removal of the material on the workpiece surface.

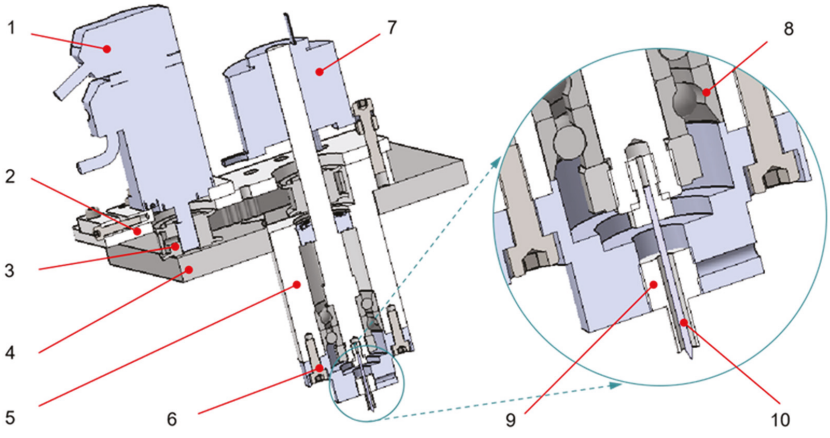

Figure 1. Structure diagram of integrated ER polishing tool system. (1) Driving motor, (2) Moving slide plate, (3) Synchronous pulley, (4) Support plate, (5) Outer sleeve, (6) Connection flange, (7) Conductive slip ring, (8) Deep groove ball bearing, (9) Annular electrode, (10) Tool needle.

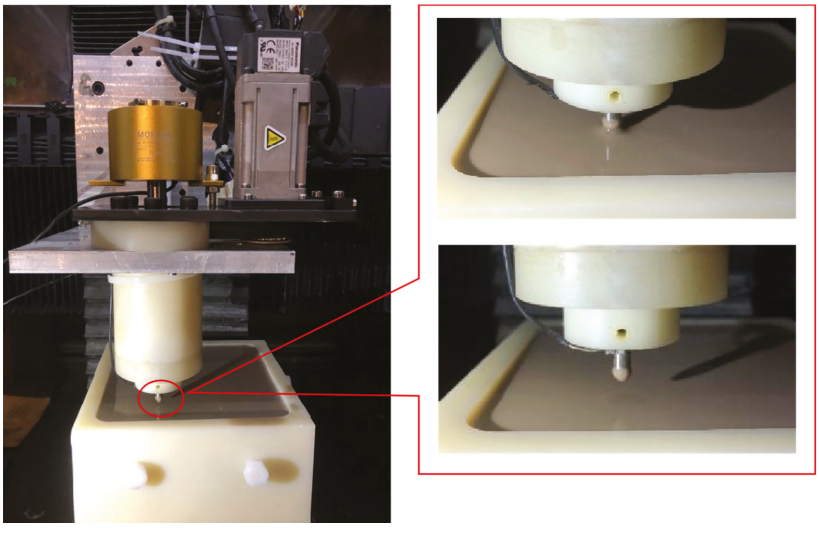

Figure 2. ER polishing equipment and flexible polishing head due to ER effect.

Different from the traditional ER polishing tool which needs auxiliary electrodes to construct electric field, the polishing tool with an annular electrode can construct an electric field by itself. When the polishing tool is working, the annular electrode is connected to the positive pole, and the tool needle is connected to the negative pole. As a result, an electric field is formed between the annular electrode and the tool needle. When people polish different materials, they do not need to redesign the polishing tool or add auxiliary electrodes.

3. Experiments and Discussion

In this paper, the key factors affecting ER polishing are explored by orthogonal experimental method, and then, the influence of a single factor on polishing is studied. The ER fluid used in the experiments is composed of starch particles as disperse phase, silicone

oil as continuous phase and diamonds as abrasive particles. When the composition of ER fluid and abrasive particles are determined, the main factors affecting polishing are applied voltage, abrasive particle size, abrasive concentration, polishing gap, polishing time and tool spindle speed.

In the experiments, aluminum is used as the workpiece. Before ER polishing, hand-held pneumatic polishing machines were used to pre-polish the surface of the workpiece, making the surface roughness reach 0.2μm. In both orthogonal experiments and single factor experiments, the polished area is a circle with a radius of 5 mm, and the recorded data is the average roughness of the six measuring points. The measurement of the roughness is carried out on the WYKO NT1100, as shown in Figure 3a. The distribution of the six-measuring points is shown in Figure 3b.

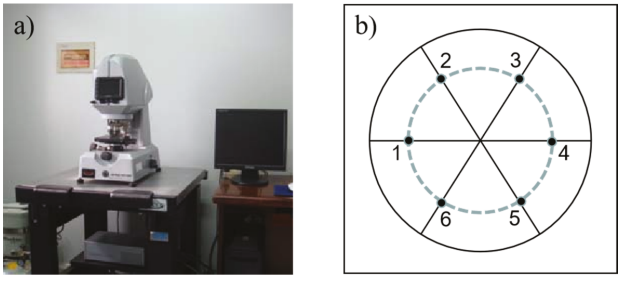

Figure 3. (**a**) The measuring equipment and (**b**) the distribution of the measuring points.

3.1. Orthogonal Experiments of ER Polishing

In the orthogonal experiment, each factor is divided into three levels. The applied voltages are 1000, 2000 and 3000 V. The abrasive particles used for polishing are diamond abrasive particles, and the polishing grinding particle sizes are W1, W5 and W10, respectively. The polishing abrasive particle concentrations are fixed as 5%, 10% and 15%, respectively. The processing gaps are 0.3, 0.5 and 1 mm respectively. The polishing times are set as 10, 20 and 30 min, respectively. The speeds of the polishing spindle are 1000, 2000 and 3000 r/min, respectively. The surface roughness after polishing is the index which is used to describe the polishing effect. In order to verify the influence of the various factors on the surface roughness after polishing, an orthogonal table L_{18} (3^6) with 6 factors and 3 levels is designed for orthogonal experiment. The distribution of the factors and the levels for the ER polishing experiments are shown in Table 1.

Table 1. Distribution of the factors and the levels in the experiments.

	A Applied Voltage (V)	B Abrasive Particle Size (μm)	C Abrasive Concentration (%)	D Polishing Gap (mm)	E Polishing Time (min)	F Spindle Speed (r/min)
1	1000	1	5	0.3	10	1000
2	2000	5	10	0.5	20	2000
3	3000	10	15	1	30	3000

The aforementioned equipment and polishing tools are used to carry out 18 relevant experiments. The experimental scheme, experimental results and SPSS analysis and processing results are shown in Table 2.

Table 2. Experimental scheme and results.

Experiment Number	Applied Voltage (V)	Abrasive Particle Size (μm)	Abrasive Concentration (%)	Polishing Gap (mm)	Polishing Time (min)	Tool Spindle Speed (r/min)	Roughness after Polishing (μm)
1	3000	5	5	0.3	30	3000	0.0325
2	3000	10	10	0.5	20	1000	0.0842
3	1000	5	15	0.5	10	1000	0.1702
4	3000	5	5	1	20	1000	0.1366
5	1000	10	15	1	20	3000	0.1268
6	2000	5	10	1	10	3000	0.0894
7	2000	5	15	0.3	20	2000	0.0823
8	3000	1	15	1	10	2000	0.0743
9	3000	1	15	0.5	30	3000	0.0452
10	3000	10	10	0.3	10	2000	0.0745
11	2000	10	5	0.5	10	3000	0.0882
12	1000	1	10	0.3	20	3000	0.1156
13	1000	5	10	0.5	30	2000	0.0908
14	2000	1	5	0.5	20	2000	0.0894
15	2000	1	10	1	30	1000	0.1263
16	2000	10	15	0.3	30	1000	0.1008
17	1000	1	5	0.3	10	1000	0.1612
18	1000	10	5	1	30	2000	0.1042
k1	0.128	0.102	0.102	0.094	0.11	0.13	
k2	0.096	0.1	0.097	0.095	0.106	0.086	
k3	0.075	0.096	0.1	0.11	0.083	0.083	
Range	0.053	0.006	0.005	0.016	0.027	0.047	

Firstly, the sum and average of the roughness corresponding to the same level of each factor should be calculated. For example, in Table 2, when the applied voltage is 1000 V which is the first level in Table 1, the corresponding roughness values are 0.1702, 0.1268, 0.1156, 0.0908, 0.1612 and 0.1042 μm, respectively, and the average value k_1 is 0.128 μm. When the input voltage is 2000 V, the average roughness k_2 is 0.097; when the input voltage is 3000 V, the average surface roughness k_3 is 0.075. For the factor of input voltage, the range value, which is the difference between the maximum and minimum values of k_1, k_2 and k_3, is 0.128 − 0.075 = 0.053. The ranges of other factors in Table 2 can also be calculated according to this method. The range indicates the influence degree of the factor on the final index. The greater the range of the factor, the greater the influence of the factor on the index. After analyzing the range values of the orthogonal experimental results, it can be seen from Table 2 that the order of influence factors on the surface roughness after ER polishing is as follows: applied voltage, tool spindle speed, polishing time, polishing gap, abrasive particle size and abrasive concentration. The purpose of optimizing parameters in this paper is to reduce the roughness value. Therefore, the smaller the value of k, the better the polishing effect. Therefore, we choose the parameter value according to k. Then the best combination scheme is selected as A3F3E3D1B3C2. In the optimized scheme selected, the applied voltage is set to 3000 V, the tool spindle speed is set to 3000 r/min, the polishing time lasts for 30 min, the polishing gap is 0.3 mm, the abrasive particle size is selected as W10, and the abrasive concentration is 10%.

The ER polishing experiments are carried out in the best experimental combination, and the concentration of dispersed phase remains unchanged. The experimental results are shown in Figure 4. Figure 4a,b is an image enlarged by using tungsten filament scanning electron microscopy after pre-rough polishing, while Figure 4c,d is an image of surface after ER polishing. In Figure 4a,b, it can be found that there are some bumps on the workpiece surface, which are well improved in Figure 4c,d, indicating that the ER polishing has a good effect on removing the scratches and bumps on the workpiece surface. Although some small scratches can be observed on the polished surface, large scratches have been

removed. Small scratches are caused by the abrasive particles that constantly rotate and hit the surface of the workpiece.

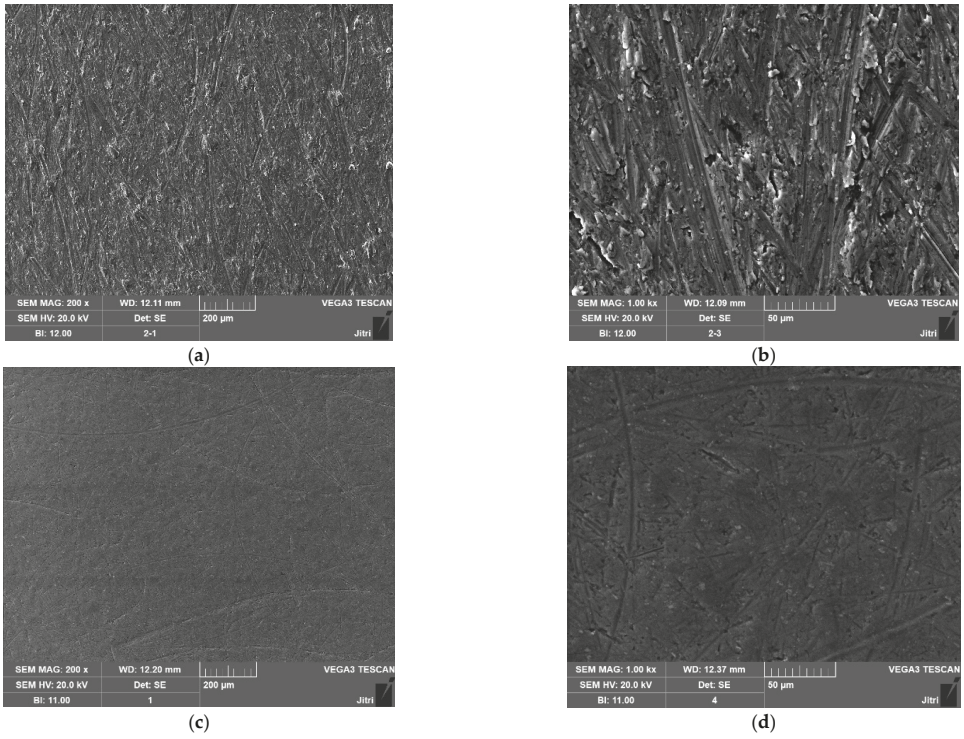

Figure 4. Surface morphology before and after ER polishing. (**a**) The enlarged surface before polishing (Scale: 200 µm). (**b**) The enlarged surface before polishing (Scale: 50 µm). (**c**) The enlarged surface after polishing (Scale: 200 µm). (**d**) The enlarged surface after polishing (Scale: 50 µm).

3.2. Single Factor Experiments of ER Polishing

In order to further explore the effects of the applied voltage, abrasive particle size, polishing abrasive concentration, polishing gap, polishing time and spindle speed on the polished roughness of the workpiece surface, single factor experiments of ER polishing were carried out. The material of the workpiece was aluminum, and the surface roughness was 0.2µm before polishing. In the experiments, we changed the value of a single factor, and the comparative experiments were carried out with three different polishing gaps for each factor to explore the influence law of a single factor.

Firstly, the initial applied voltage was set to 1000 V, the size of the abrasive particle was W1 and the concentration of the polishing slurry was 5%. Additionally, the polishing gap between the tool and surface was kept as 1 mm, the spindle speed was set to 1000 r/min and the polishing lasted for 20 min.

The variation of workpiece surface roughness with voltage under various polishing gaps is shown in Figure 5. As indicated by Figure 5, when the voltage increases two times from 1000 to 3000 V, the roughness decreases by 52.5% when h = 0.3 mm and 48.1% when h = 0.5 mm. When the applied voltage is low, the ER effect is weak, the "hardness" of the flexible polishing head is relatively low, and the polishing pressure on the workpiece is also not high enough. As a result, the phenomenon of material removal is not obvious. With the increase of the applied voltage, the ER effect is enhanced, and the bonding force between particles and the slurry viscosity increases. What is more, the abrasive aggregation effect

is more obvious. That is to say, with the increase of the number of abrasives involved in polishing, the material removal ability of the polishing head is gradually enhanced, and the polishing effect is better.

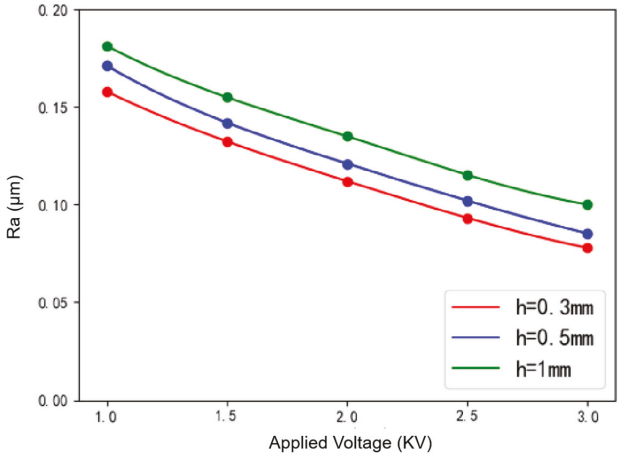

Figure 5. Variation of surface roughness with voltage under various polishing gaps.

The variation trend of surface roughness with abrasive particle size is shown in Figure 6. It can be seen that when the size of the diamond abrasive gets larger, the surface roughness value decreases. When the size of the diamond abrasive increases from 1 to 10 μm, the roughness value decreases by 7.88% when h = 0.3 mm and 5.71% when h = 0.5 mm. The abrasive particles adhere to the chain of particles composed of dispersed particles, and the radius of the abrasive particles is much smaller than that of dispersed particles. Because the polishing tool head used in the experiment is small and the number of abrasive particles gathered at the end of the polishing tool head is limited, the actual effect of the abrasive particle size on the polishing is not obvious; thus, the variation of the surface roughness of the workpiece after polishing with different abrasive particle sizes does not change significantly.

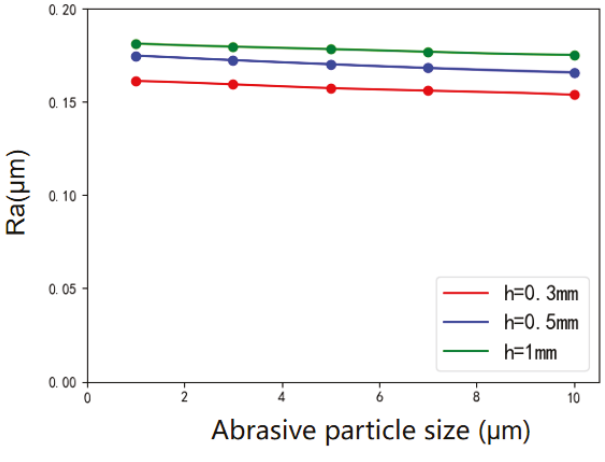

Figure 6. Variation of surface roughness with abrasive particle size under various polishing gaps.

The variation trend of surface roughness with abrasive concentration under various polishing gaps is shown in Figure 7. When the abrasive concentration is about 10%, the surface roughness is the lowest, and the polishing effect is the best. However, the effect of abrasive concentration on surface roughness is not obvious generally. For a similar reason that the abrasive particle size has little effect on surface roughness, the polishing tool head used in the experiment is small, and the number of abrasive particles gathered at the end of the polishing tool head is also limited. Therefore, the improvement effect of abrasive concentration on surface roughness is not obvious.

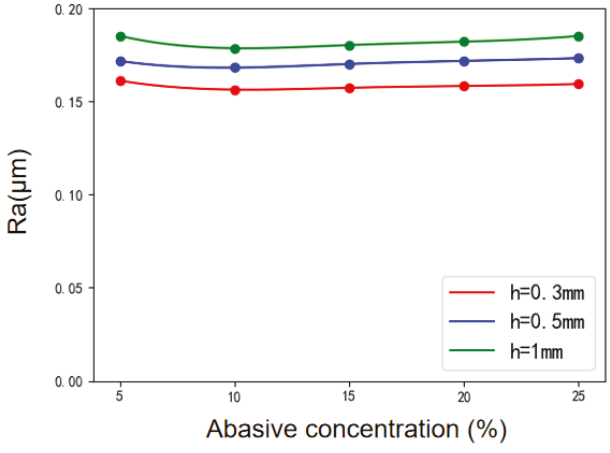

Figure 7. Variation of surface roughness with abrasive concentration under various polishing gaps.

The variation of surface roughness of workpiece with polishing gaps under various applied voltages is shown in Figure 8. The polishing gap affects the electric field intensity in the polishing area, which directly affects the polishing effect of the workpiece surface. It can be seen that the surface roughness of the workpiece increases with the increase of the polishing gap. As the polishing gap increases fourfold from 0.3 to 1.5 mm, the surface roughness increases by 15.3% when the voltage is 1000 V and 42.5% when the voltage is 3000 V. The greater the distance from the end of the tool to the surface, the smaller the electric field intensity. The "hardness" of the polishing head formed by the ER effect is directly related to the electric field intensity. With the increase of the polishing gap, the "hardness" of the polishing head formed by the ER effect decreases gradually, and the material removal ability gets weaker. In addition, the larger the polishing gap is, the longer the chain which formed by the dispersed phase particles under the effect of the electric field is, and the arrangement is not as compact as that of the small gap. The abrasive particles cannot be attached to the chain better. During the process of tool spindle rotation, the abrasive particles may be far away from the polishing area, thus the material removal cannot be completed efficiently, and the surface roughness of the workpiece cannot be reduced.

The variation of surface roughness of workpiece with different polishing times under various polishing gaps is shown in Figure 9. In general, the longer the polishing time, the lower the surface roughness and the better the polishing effect. The decreasing trend of surface roughness is most obvious at 20 min. With the increase of time, the surface roughness no longer decreases significantly, because it reaches the limit polishing effect that the polishing abrasive can complete. In order to reduce the surface roughness continuously and efficiently, we have to change other process parameters.

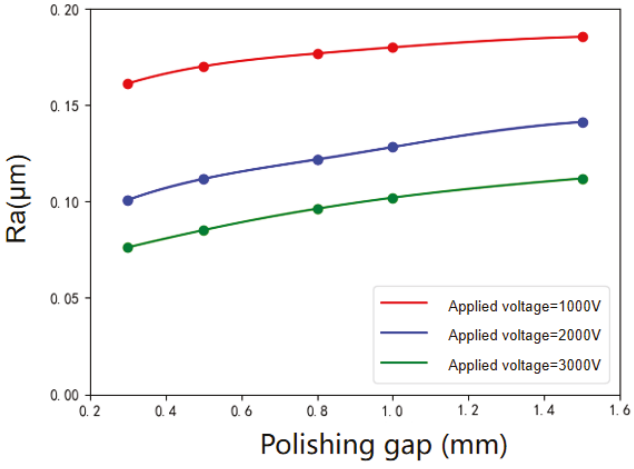

Figure 8. Variation of surface roughness with polishing gap under various applied voltages.

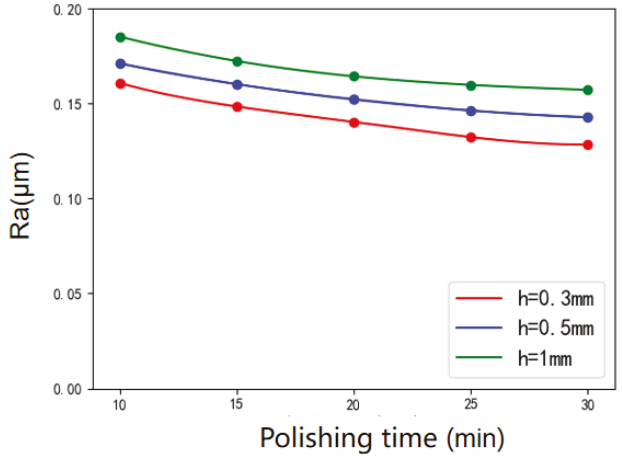

Figure 9. Variation of surface roughness with polishing time under various polishing gaps.

Figure 10 shows the variation of workpiece surface roughness with tool spindle speeds under various polishing gaps. It can be seen that with the increasing of tool spindle speed, the surface roughness value of the workpiece decreases. When the spindle speed increases from 1000 to 3000 rpm, the surface roughness decreases by 34.4% when h = 0.3 mm and 26.5% when h = 0.5 mm. According to the hydrodynamics, the relative velocity between the polishing tool and the workpiece surface will increase with the increase of the polishing tool spindle speed. According to Preston law, the material removal rate will also increase. Therefore, increasing the spindle speed can effectively improve the polishing efficiency.

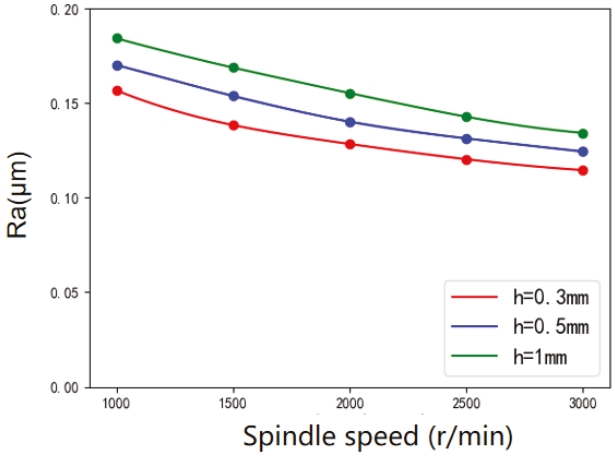

Figure 10. Variation of surface roughness with tool spindle speed under various polishing gaps.

4. Conclusions

In this paper, a new ER polishing tool with an annular integrated electrode is developed. After determining the composition of ER fluid (the concentration of the dispersed phase and the type of the polishing abrasive), six possible factors affecting the ER polishing are determined: the applied voltage, the polishing abrasive particle size, the polishing abrasive concentration, the polishing gap, the polishing time and the tool spindle speed. Then, we get the best combination of parameters. In the optimized scheme selected, the applied voltage is set to 3000 V, the tool spindle speed is set to 3000 r/min, the polishing time lasts for 30 min, polishing gap is 0.3 mm, the abrasive particle size is selected as W10, and the abrasive concentration is 10%. According to the single factor experiments, the value of the surface roughness will decrease significantly with the increase of the applied voltage, the tool spindle speed and the polishing time and increase significantly with the increase of the polishing gap. The effect of the applied voltage, the tool spindle speed, the polishing time and gap on the surface roughness is obvious, but the effect of the polishing abrasive particle size and concentration on the surface roughness is relatively small.

Author Contributions: Investigation, Y.C. and Y.X.; Project administration, C.F. and L.Z.; Validation, C.F.; Writing—original draft, C.F. and Y.C.; Writing—review and editing, L.Z. All authors have read and agreed to the published version of the manuscript.

Funding: This research was funded by the National Natural Science Foundation of China (grant no. 51975392), the Natural Science Foundation of the Jiangsu Higher Education Institutions of China (grant no. 19KJA220001), and the Natural Science Foundation of Jiangsu Province (grant no. BK20201412).

Institutional Review Board Statement: Not applicable.

Informed Consent Statement: Not applicable.

Data Availability Statement: Not applicable.

Conflicts of Interest: The authors declare no conflict of interest.

References

1. Yang, M.Y.; Lee, H.C. Local material removal mechanism considering curvature effect in the polishing process of the small aspherical lens die. *J. Mater. Process. Technol.* **2001**, *116*, 298–304. [CrossRef]
2. Chen, W.; Kuriyagawa, T.; Huang, H.; Yosihara, N. Machining of micro aspherical mould inserts. *Precis. Eng.* **2005**, *29*, 315–323. [CrossRef]

3. Evans, C.; Paul, E.; Dornfeld, D.; Lucca, D.; Byrne, G.; Tricard, M.; Klocke, F.; Dambon, O.; Mullany, B. Material Removal Mechanisms in Lapping and Polishing. *CIRP Ann.* **2003**, *52*, 611–633. [CrossRef]
4. Yan, B.-H.; Tzeng, H.-J.; Huang, F.Y.; Lin, Y.-C.; Chow, H.-M. Finishing effects of spiral polishing method on micro lapping surface. *Int. J. Mach. Tools Manuf.* **2007**, *47*, 920–926. [CrossRef]
5. Tam, H.; Cheng, H. An investigation of the effects of the tool path on the removal of material in polishing. *J. Mater. Process. Technol.* **2010**, *210*, 807–818. [CrossRef]
6. Klocke, F.; Dambon, O.; Zunke, R. Modeling of contact behavior between polishing pad and workpiece surface. *Prod. Eng.* **2007**, *2*, 9–14. [CrossRef]
7. Van Der Velden, P. Chemical mechanical polishing with fixed abrasives using different subpads to optimize wafer uniformity. *Microelectron. Eng.* **2000**, *50*, 41–46. [CrossRef]
8. Li, W.; Wang, Y.; Fan, S.; Xu, J. Wear of diamond grinding wheels and material removal rate of silicon nitrides under different machining conditions. *Mater. Lett.* **2007**, *61*, 54–58. [CrossRef]
9. Webster, J.; Tricard, M. Innovations in Abrasive Products for Precision Grinding. *CIRP Ann.* **2004**, *53*, 597–617. [CrossRef]
10. Xie, Y.; Bhushan, B. Effects of particle size, polishing pad and contact pressure in free abrasive polishing. *Wear* **1996**, *200*, 281–295. [CrossRef]
11. Ukar, E.; Lamikiz, A.; de Lacalle, L.N.L.; del Pozo, D.; Arana, J. Laser polishing of tool steel with CO2 laser and high-power diode laser. *Int. J. Mach. Tools Manuf.* **2010**, *50*, 115–125. [CrossRef]
12. Nüsser, C.; Wehrmann, I.; Willenborg, E. Influence of Intensity Distribution and Pulse Duration on Laser Micro Polishing. *Phys. Procedia* **2011**, *12*, 462–471. [CrossRef]
13. Curodeau, A.; Guay, J.; Rodrigue, D. Ultrasonic abrasive μ-machining with thermoplastic tooling. *Int. J. Mach. Tools Manuf.* **2008**, *48*, 1553–1561. [CrossRef]
14. Kobayashi, N.; Wu, Y.; Nomura, M.; Sato, T. Precision treatment of silicon wafer edge utilizing ultrasonically assisted polishing technique. *J. Mater. Process. Technol.* **2008**, *201*, 531–535. [CrossRef]
15. Suzuki, H.; Hamada, S.; Okino, T.; Kondo, M. Ultraprecision finishing of micro-aspheric surface by ultrasonic two-axis vibration assisted polishing. *CIRP Ann. Manuf. Technol.* **2010**, *59*, 347–350. [CrossRef]
16. Han, S.; Seo, Y. Voltage-induced material removal mechanism of copper for electrochemical-mechanical polishing applications. *Trans. Nonferrous Met. Soc. China* **2009**, *19*, 262–265. [CrossRef]
17. Jang, K.; Seok, J.; Min, B. An electrochemomechanical polishing process using magnetorheological fluid. *Int. J. Mach. Tools Manuf.* **2010**, *50*, 869–881. [CrossRef]
18. Hocheng, H.; Sun, Y.H.; Lin, S.C. A material removal analysis of electrochemical. *J. Mater. Process. Technol.* **2003**, *140*, 264–268. [CrossRef]
19. Ramachandran, N.; Ramakrishnan, N. A review of abrasive jet machining. *J. Mater. Process. Technol.* **1993**, *39*, 21–31. [CrossRef]
20. Park, D.; Cho, M.; Lee, H. Micro-grooving of glass using micro-abrasive jet machining. *J. Mater. Process. Technol.* **2004**, *146*, 234–240. [CrossRef]
21. Tricard, M.; Kordonski, W.; Shorey, A.; Evans, C. Magnetorheological Jet Finishing of Conformal, Freeform and Steep Concave Optics. *CIRP Ann.* **2006**, *55*, 309–312. [CrossRef]
22. Arnold, T.; Böhm, G.; Fechner, R.; Meister, J.; Nickel, A.; Frost, F.; Hänsel, T.; Schindler, A. Ultra-precision surface finishing by ion beam and plasma jet techniques—status and outlook. *Nucl. Instrum. Methods Phys. Res. Sect. A Accel. Spectrometers Detect. Assoc. Equip.* **2010**, *616*, 147–156. [CrossRef]
23. Wakuda, M.; Yamauchi, Y.; Kanzaki, S. Material response to particle impact during abrasive jet machining of alumina ceramics. *J. Mater. Process. Technol.* **2003**, *132*, 177–183. [CrossRef]
24. Gorana, V.; Jain, V.; Lal, G. Forces prediction during material deformation in abrasive flow machining. *Wear* **2006**, *260*, 128–139. [CrossRef]
25. Wang, A.; Tsai, L.; Liang, K. Uniform surface polished method of complex holes in abrasive flow machining. *Trans. Nonferrous Met. Soc. China* **2009**, *19*, 250–257. [CrossRef]
26. Suyoshi, K.T.; Tsunmemoto, K.; Nobuhito, Y. Study on electrorheological fluid assisted micro-aspherical polishing. *Kosaku Kikai Bumon Koenkai Koen Ronbunshu* **2004**, *5*, 197–198.
27. Kuriyagawa, T.; Saeki, M.; Syoji, K. Electrorheological fluid-assisted ultra-precision polishing for small three-dimensional parts. *Precis. Eng.* **2002**, *26*, 370–380. [CrossRef]
28. Kim, W.B.; Min, B.K.; Lee, S.J. Development of a padless ultraprecision polishing method using electrorheological fluid. *J. Mater. Process. Technol.* **2004**, *155–156*, 1293–1299. [CrossRef]
29. Akagami, Y.; Umehara, N. Development of electrically controlled polishing with dispersion type ER fluid under AC electric field. *Wear* **2006**, *260*, 345–350. [CrossRef]
30. Zhang, L.; Kuriyagawa, T.; Kaku, T. Investigation into electrorheological fluid-assisted polishing. *Int. J. Mach. Tools Manuf.* **2005**, *45*, 1461–1467. [CrossRef]
31. Zhang, L.; Zhao, Y. An investigation of effective area in electrorheological fluid-assisted polishing of tungsten carbide. *Int. J. Mach. Tools Manuf.* **2008**, *48*, 295–306. [CrossRef]
32. Zhang, L.; He, X.; Yang, H.; Zhang, Y. An integrated tool for five-axis electrorheological fluid-assisted polishing. *Int. J. Mach. Tools Manuf.* **2010**, *50*, 737–740. [CrossRef]

33. Li, H.; Cheng, H.; Feng, Y. Investigation of electrorheological fluid for optical finishing. *Front. Optoelectron. China* **2011**, *4*, 213–216. [CrossRef]
34. Lu, J.; Yan, Q.; Tian, H.; Gao, W. Polishing properties of the Fe3O4-based electrorheological fluid. *Lubr. Eng.* **2008**, *33*, 27–30.

micromachines

MDPI

Article

Study on the Algorithm of Three-Dimensional Surface Residual Material Height of Nano-ZrO_2 Ceramics under Ultra-Precision Grinding

Yanyan Yan [1], Zhaoqing Zhang [1,2,*], Junli Liu [1], Haozhe Yan [1] and Xiaoxu Wang [1]

[1] School of Mechanical and Power Engineering, Henan Polytechnic University, Jiaozuo 454003, China; yyy@hpu.edu.cn (Y.Y.); ljl@hpu.edu.cn (J.L.); 15038245590@163.com (H.Y.); 15238028789@163.com (X.W.)
[2] School of Mechanical Engineering, Northwestern Polytechnical University, Xi'an 710072, China
* Correspondence: zhang-zhaoqing@foxmail.com

Abstract: A large number of studies have shown that the height of a residual material is the key factor affecting the surface quality of ultra-precision grinding. However, the grinding process contains several random factors, such as the randomness of grinding particle size and the random distribution of grinding particles, which cause the complexity of the material removal process. In this study, taking the Nano-ZrO_2 as an example, the removal process of surface materials in ultra-precision grinding of hard and brittle materials was analyzed by probability. A new calculation method for the height of surface residual materials in ultra-precision grinding of Nano-ZrO_2 was proposed, and the prediction model of the three-dimensional roughness S_a and S_q were established by using this calculation method. The simulation and experimental results show that this calculation method can obtain the more accurate surface residual material height value which accords with the characteristics of three-dimensional roughness sampling, which provides a theoretical reference for the analysis of the material removal process and the surface quality evaluation of ultra-precision grinding of hard and brittle materials.

Keywords: Nano-ZrO_2 ceramics; ultra-precision grinding; surface residual material; surface quality; three-dimensional surface roughness

Citation: Yan, Y.; Zhang, Z.; Liu, J.; Yan, H.; Wang, X. Study on the Algorithm of Three-Dimensional Surface Residual Material Height of Nano-ZrO_2 Ceramics under Ultra-Precision Grinding. *Micromachines* **2021**, *12*, 1363. https://doi.org/10.3390/mi12111363

Academic Editor: Aiqun Liu

Received: 28 September 2021
Accepted: 29 October 2021
Published: 4 November 2021

1. Introduction

With the improvement in material preparation methods and the processing level, hard and brittle materials are widely applied in the industrial field. At present, ultra-precision grinding is usually used for the efficient machining of hard and brittle materials. The height of residual material on the grinding surface is the key factor affecting the quality of the ultra-precision machined surface. However, the grinding particle size and the distribution of the abrasive particles are random, which leads to the complexity of the process of material removal, the removal process of grinding machined surface material needs further study. Most of the previous research on the grinding mechanism was based on assumptions, such as uniformity of the abrasive particle distribution or the same size of the abrasive particles, which deviates from the actual grinding process. There are many factors that affect the surface quality during the actual grinding process, and these factors obey the probability theory, so it is necessary to analyze the grinding process according to the probability theory, which can describe the process of material removal and the surface morphology more realistically [1,2]. Hou and Komanduri [3] made a probabilistic analysis of the interaction between the abrasive particles and the workpiece material, which provided a new idea for analyzing the grinding process. Agarwal et al. [4] propose that, due to the randomness of the grinding process, it was more appropriate to analyze the process of material removal by probability theory, especially, they pointed out that any attempt to analyze the process of material removal of grinding should be probabilistic.

The influence of random factors on the grinding process is reflected in the quality of the machined surface. With the improvement in the measurement precision of ultra-precision machined surface, the three-dimensional roughness has been widely used in the quality evaluation of ultra-precision machined surfaces. Xiao et al. [5] established a two-dimensional surface roughness prediction model based on the random distribution of abrasive particles, which provided a new way for the quality evaluation of ceramic surfaces since the three-dimensional roughness is sampled based on a limited number of points in the surface area, which can reflect the surface characteristics of parts more accurately and comprehensively [6,7]. Additionally, the height of each sampling point is closely related to the height of surface residual materials in the sampling area, which makes the height of surface residual materials in the sampling area become a key index in predicting the three-dimensional roughness. Several researchers have studied the effect of three-dimensional roughness in the evaluation of the machined surface. For example, Zhou et al. [8] proposed a modeling method of the machined surface that considers the effect of abrasive plowing during grinding and studied the effect of plowing and the micro-interaction between the abrasive particle and the workpiece on the three-dimensional surface morphology, and the three-dimensional roughness parameters were simulated. Chen et al. [9] developed a three-dimensional surface prediction model of grinding, but unfortunately, there are no specific three-dimensional surface roughness parameters for modeling and calculation. At present, the application of the height of the residual material on the processed surface to predict the three-dimensional roughness needs to be further explored.

In this context, the material removal process of the ultra-precision grinding surface of Nano-ZrO_2 ceramics was analyzed by probability theory in this study. A new method for calculating the height of residual materials in ultra-precision grinding was proposed, and the height model of residual materials in nano ZrO_2 ultra-precision grinding was established. The application of the calculation method and the height model in surface quality evaluation and three-dimensional roughness prediction of ultra-precision grinding was studied, which is expected to provide a theoretical reference for the removal process and surface quality evaluation of ultra-precision machining of hard and brittle materials.

2. The New Method for Calculating the Height of the Surface Residual Material of Nano-ZrO_2

The surface of ultra-precision grinding is formed by the interaction of a large number of abrasive particles. Figure 1 shows the material removal process of the arbitrary single abrasive particle on the machined surface. The combined action of a large number of arbitrary abrasive particles results in the removal of macroscopic surface material [10]. The formation process of Nano-ZrO_2 ceramic machining surface micromorphology is shown in Figure 2. When a large number of abrasive particles act together on the surface S_A of Nano-ZrO_2 ceramic to be processed, the processed surface $S_A{}^*$ is formed after sliding, plowing, and cutting. In the grinding process, there will be material residue on the grinding surface $S_A{}^*$, and the height of the material residual is the key factor affecting the surface quality of ultra-precision machining. Due to the large number of random factors involved in the process, this study conducted probabilistic analysis on the key factors affecting the height of machined surface residual materials and proposed a new calculation method for the height of machined surface residual materials.

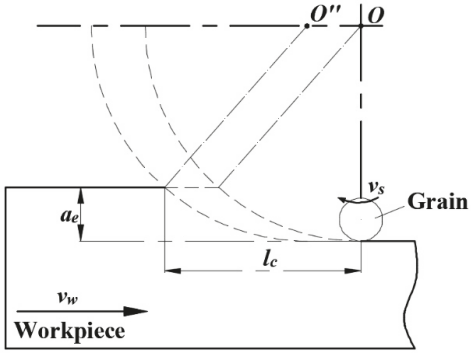

Figure 1. The material removal process of a single abrasive particle.

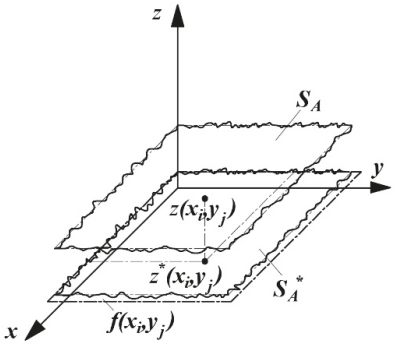

Figure 2. The formation process of the surface morphology of Nano-ZrO_2.

2.1. Probabilistic Analysis of the Grinding Process of Nano-ZrO_2 Ceramics

The grinding process of Nano-ZrO_2 ceramics is shown in Figure 3. As the grinding wheel enters the grinding area, randomly distributed abrasive particles are applied to the machined surface for sliding, plowing, and cutting, resulting in the macroscopic removal of surface materials. Since the protrusion height of the abrasive particles in the radial direction of the grinding wheel is a random value, it is necessary to analyze the micro-cutting depth between the abrasive particles and the workpiece by probability theory. In the probabilistic analysis of the micro-cutting depth, the Rayleigh probability density function is usually used to define the thickness of the undeformed chip. Rayleigh probability density function is shown in Equation (1) [11]:

$$f(h_{m.x}) = \frac{h_{m.x}}{\eta^2} \exp\left[-\frac{1}{2}\left(\frac{h_{m.x}}{\eta}\right)^2\right]; h_{m.x} > 0, \eta > 0 \quad (1)$$

where, $h_{m.x}$ is the undeformed chip thickness; η is the parameter defining the Rayleigh probability density function, which depends on the grinding conditions, the characteristics of the workpiece material and the microstructure of the grinding wheel, etc. [12]. The expected value and standard deviation of the Rayleigh probability density function can be expressed as Equations (2) and (3).

$$E(h_{m.x}) = \eta\sqrt{\pi/2} \quad (2)$$

$$\sigma(h_{m.x}) = \eta\sqrt{(4-\pi)/2} \quad (3)$$

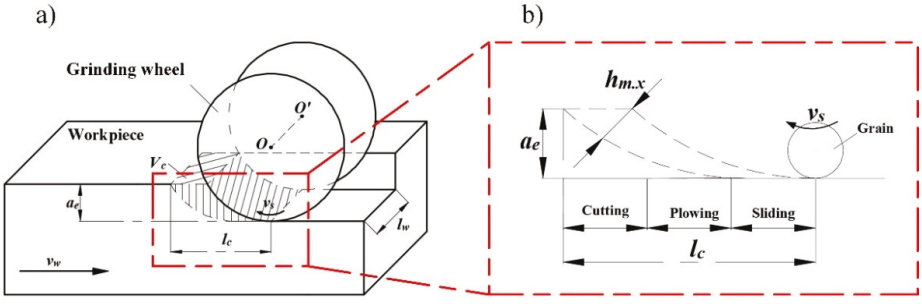

Figure 3. Schematic diagram of the grinding process. (**a**) Grinding motion diagram. (**b**) The division of the instantaneous grinding area.

In addition, the total number of abrasive particles in the instantaneous grinding area is the key factor in determining the proportion of surface residual materials of Nano-ZrO_2 ceramic in ultra-precision machining. The division of the instantaneous grinding area is shown in Figure 3b. According to Figure 3b, when the abrasive particles pass through the grinding zone, the abrasive particles interact with the workpiece through the sliding, plowing, and cutting stages. Combined with Figures 1 and 2, the velocity component of the abrasive particle in the direction opposite to the workpiece feed is moved by the distance l_c relative to the workpiece at a relative speed v_w. After time t_m, the height of a finite number of points on the original surface S_A of the workpiece is descended to form a machined surface $S_A{}^*$, and t_m is given by Equation (4):

$$t_m = l_c \cdot v_w^{-1} \tag{4}$$

where, v_w is the workpiece feed rate, l_c is the length of the grinding contact zone in the direction of the workpiece feed rate.

When the grinding wheel passes the grinding zone with the grinding width l_w at the grinding wheel linear speed v_s in the time t_m, the volume V_c of the removal materials can be approximated as:

$$V_c = l_w v_s t_m h_{m.x} \tag{5}$$

This study gives the total number of abrasive particles of the instantaneous grinding area. It can be expressed as:

$$N_m = V_c N_{EV} = l_w v_s t_m h_{m.x} N_{EV} \tag{6}$$

where, N_{EV} is the number of abrasive particles per unit grinding wheel volume, Jiang et al. [13] proposed a method to calculate the number of abrasive particles per unit grinding wheel volume N_{EV}, it can be expressed as:

$$N_{EV} = \frac{3V_t\delta\sqrt{2\pi}}{4.4\pi\int_{-\delta/2}^{\delta/2} d_{gx}^3 \exp\left[-\frac{1}{2}\left(\frac{4.4}{\delta/2}x\right)^2\right]dx} \tag{7}$$

where, d_{gx} is the diameter of a specific abrasive particle, and the diameter of abrasive particle obeys normal distribution, the normal distribution curve of abrasive particle diameter is shown in Figure 4, and $\delta = d_{g.\max} - d_{g.\min}$. V_t [14] is the percentage of abrasive volume based on the grinding wheel structures number, N, specified by Equation (8).

$$V_t = \frac{3}{2}(37 - N), \% \tag{8}$$

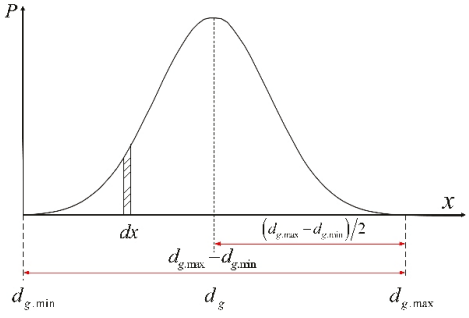

Figure 4. Normal distribution curve of abrasive particle diameter.

2.2. The New Method for Calculating the Height of Residual Materials on the Grinding Surface of Nano-ZrO_2

The original surface of the Nano-ZrO_2 is not an ideal plane. The height of the arbitrary point on the original surface of the Nano-ZrO_2 and the average height of the original surface of the Nano-ZrO_2 are shown in Figure 5. To facilitate the description of the original surface of the Nano-ZrO_2 before grinding, it is necessary to define z_m as the average height of the workpiece surface from the xoy-plane before grinding, define $d_{w.\max}$ as the maximum height of the Nano-ZrO_2 surface from the xoy-plane before grinding, and define $d_{w.\min}$ as the minimum height of the Nano-ZrO_2 surface from the xoy-plane before grinding. $z_b(x_i, y_j)$ may be used to describe the height value of the arbitrary random point (x_i, y_j) on the original surface of the workpiece. According to the probability theory, the value of $z_b(x_i, y_j)$ can be given by Equation (9):

$$z_b(x_i, y_j) = z_m + \varphi, \varphi \in \left[-\frac{d_{w.\max} - d_{w.\min}}{2}, \frac{d_{w.\max} - d_{w.\min}}{2} \right] \tag{9}$$

where, φ is the height deviation of the original surface of the Nano-ZrO_2.

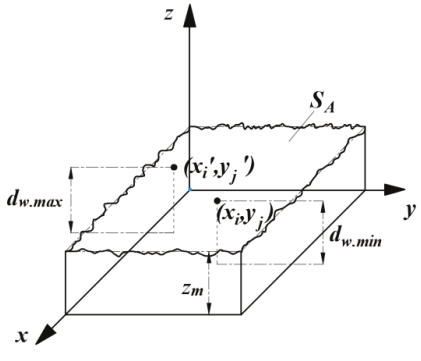

Figure 5. Height of the arbitrary point on the original surface and the average height of the original surface.

After the arbitrary abrasive particle G act on the original surface of the Nano-ZrO_2, the descending depth $z_d(x_i, y_j)$ of arbitrary point (x_i, y_j) on the original surface of the Nano-ZrO_2 along the z-axis can be given by the Equation (10):

$$z_d(x_i, y_j) = a_e \cdot N_m^{-1} \tag{10}$$

where, a_e is grinding depth.

Substituting Equation (6) into Equation (10) yields:

$$z_d(x_i, y_j) = \frac{a_e}{l_w v_s t_m h_{m.x} N_{EV}} \tag{11}$$

The height $z_r(x_i, y_j)$ of the residual material at an arbitrary point (x_i, y_j) on the surface of the Nano-ZrO_2 after grinding in the z-axis direction can be given by Equation (12).

$$z_r(x_i, y_j) = z_b(x_i, y_j) - z_d(x_i, y_j) \tag{12}$$

Combining Equations (4), (9) and (11) into (12), the height value $z_r(x_i, y_j)$ of the surface residual material along the z-axis can be given by Equation (13).

$$z_r(x_i, y_j) = z_m - \frac{a_e v_w}{N_{EV} h_{m.x} l_w l_c v_s} + \varphi \tag{13}$$

Based on the above analysis, the height model of the surface residual material of Nano-ZrO_2 ceramics obeys the probability theory. In order to verify its prominent role in the grinding surface quality evaluation of Nano-ZrO_2 ceramics and its three-dimensional roughness prediction, this study will use the new calculation method and height model of the surface residual material to model the three-dimensional roughness evaluation index of Nano-ZrO_2 ceramic grinding surface.

3. Application of the New Calculating Method in the Prediction of Three-Dimensional Roughness

Since the three-dimensional roughness is sampled based on a limited number of points in the surface area, the height of each sampling point is closely related to the height of the surface residual material in the sampling area, this study will apply the new calculating method for the height of residual material on the grinding surface to predict the three-dimensional roughness of the grinding surface. ISO 25178 divides the three-dimensional surface roughness parameters into six groups. At present, the arithmetic square root deviation S_a of the machined surface and the root mean square deviation S_q of the machined surface are regarded as the most important parameters that characterize three-dimensional roughness [6].

3.1. Establishment of Three-Dimensional Roughness Evaluation Datum Plane

The two-dimensional roughness parameter is established based on the datum line. Similarly, the datum plane needs to be established before the S_a and S_q are deduced. At present, the commonly used methods for establishing datum planes include the wavelet analysis method, least square method, etc. [15]. In this study, the three-dimensional roughness datum plane will be established based on the least-squares method. Firstly, the equation of the actual surface is defined as $z(x, y)$ in the Cartesian coordinate system, and the least-squares datum plane equation can be expressed as:

$$f(x, y) = a + bx + cy \tag{14}$$

where, the coefficients a, b, and c are constants.

According to Equation (14), the least-squares datum plane may be obtained once the value of a, b and c are calculated. Assuming that the deviation square between the actual surface and the datum plane is ξ, then ξ can be expressed as:

$$\xi = \sum_{i=1}^{N} \sum_{j=1}^{M} \left[z(x_i, y_j) - f(x_i, y_j) \right]^2 = \sum_{i=1}^{N} \sum_{j=1}^{M} \left[z(x_i, y_j) - (a + bx_i + cy_j) \right]^2 \tag{15}$$

In order to ensure that the square of the deviation is the smallest, it must simultaneously satisfy the following equations:

$$\begin{cases} \frac{\partial \xi}{\partial a} = \sum_{i=1}^{M}\sum_{j=1}^{N}\left[z(x_i,y_j) - (a + bx_i + cy_j)\right] = 0 \\ \frac{\partial \xi}{\partial b} = \sum_{i=1}^{M}\sum_{j=1}^{N}\left[z(x_i,y_j) - (ax_i + b + cx_iy_j)\right] = 0 \\ \frac{\partial \xi}{\partial c} = \sum_{i=1}^{M}\sum_{j=1}^{N}\left[z(x_i,y_j) - (ay_j + bx_iy_j + cy_j^2)\right] = 0 \end{cases} \tag{16}$$

The terms $\overline{x}$, $\overline{y}$, and $\overline{z}$ are defined as:

$$\overline{x} = \frac{\sum_{i=1}^{M} x_i}{m};\ \overline{y} = \frac{\sum_{j=1}^{N} y_j}{n};\ \overline{z} = \frac{\sum_{i=1}^{M}\sum_{j=1}^{N} z(x_i,y_j)}{mn} \tag{17}$$

Substituting Equation (17) into the first equation of Equation (16), the following equation can be obtained:

$$a = \overline{z} - b\overline{x} - c\overline{y} = \frac{\sum_{i=1}^{M}\sum_{j=1}^{N} z(x_i,y_j)}{mn} - b\frac{\sum_{i=1}^{M} x_i}{m} - c\frac{\sum_{j=1}^{N} y_j}{n} \tag{18}$$

Substituting Equation (18) into the second and third equations of Equation (16), the following equation can be obtained:

$$\begin{cases} \sum_{i=1}^{M}\sum_{j=1}^{N} z(x_i,y_j)x_i - \sum_{i=1}^{M}\sum_{j=1}^{N} ax_i - \sum_{i=1}^{M}\sum_{j=1}^{N} bx_i^2 - \sum_{i=1}^{M}\sum_{j=1}^{N} cx_iy_j = 0 \\ \sum_{i=1}^{M}\sum_{j=1}^{N} z(x_i,y_j)y_j - \sum_{i=1}^{M}\sum_{j=1}^{N} ay_j - \sum_{i=1}^{M}\sum_{j=1}^{N} bx_iy_j - \sum_{i=1}^{M}\sum_{j=1}^{N} cy_j^2 = 0 \end{cases} \tag{19}$$

Equation (20) is obtained through mathematical transformation:

$$\begin{cases} \sum_{i=1}^{M}\sum_{j=1}^{N} x_i = N\sum_{i=1}^{M} x_i \\ \sum_{i=1}^{M}\sum_{j=1}^{N} y_j = M\sum_{j=1}^{N} y_j \\ \sum_{i=1}^{M}\sum_{j=1}^{N} x_iy_j = \sum_{i=1}^{M} x_i\sum_{j=1}^{N} y_j \end{cases} \tag{20}$$

Substituting Equation (20) into Equation (19), the following equation can be obtained:

$$\begin{cases} a = \frac{\sum_{i=1}^{M}\sum_{j=1}^{N} z(x_i,y_j)}{MN} - b\frac{\sum_{i=1}^{M} xi}{M} - c\frac{\sum_{j=1}^{N} y_j}{N} \\ b = \frac{\sum_{i=1}^{M}\sum_{j=1}^{N} z(x_i,y_j)x_i - MN\overline{x}\overline{z}}{N\sum_{i=1}^{M} x_i^2 - MN\overline{x}^2} \\ c = \frac{\sum_{i=1}^{M}\sum_{j=1}^{N} z(x_i,y_j)y_j - MN\overline{y}\overline{z}}{M\sum_{j=1}^{N} y_j^2 - MN\overline{y}^2} \end{cases} \tag{21}$$

Substituting Equation (21) into Equation (17), the least-squares datum plane can be determined, there is a unique least-squares fitting datum in the sampling area, and

the corresponding least-squares datum plane equation can be obtained by providing the coordinate values of arbitrary points.

3.2. The Arithmetic Square Root Deviation S_a of the Machined Surface

The arithmetic square root deviation S_a of the machined surface is the arithmetic mean distance between the measured contour surface and the datum plane along the z-axis in the sampling area. It can be expressed mathematically as [16]:

$$S_a = \frac{1}{MN}\sum_{j=1}^{N}\sum_{i=1}^{M}\left|z_a(x_i, y_j)\right| \tag{22}$$

where, M and N are the number of sampling points in the x-axis and y-axis directions, respectively, in the sampling area.

After the datum plane $f(x_i, y_j)$ was established, the distance $z_a(x_i, y_j)$ between the arbitrary point (x_i, y_j) on the machined surface and the datum plane along the z-axis can be defined as:

$$z_a(x_i, y_j) = f(x_i, y_j) - z_r(x_i, y_j) \tag{23}$$

Substituting Equation (13) into Equation (23), the following equation can be obtained:

$$z_a(x_i, y_j) = f(x_i, y_j) + \frac{a_e v_w}{N_{EV} h_{m.x} l_w l_c v_s} - z_m - \varphi \tag{24}$$

Substituting Equation (24) into Equation (22), the arithmetic square root deviation S_a of the machined surface can be expressed as:

$$S_a = \frac{1}{MN}\sum_{j=1}^{N}\sum_{i=1}^{M}\left|f(x_i, y_j) + \frac{a_e v_w}{N_{EV} h_{m.x} l_w l_c v_s} - z_m - \varphi\right| \tag{25}$$

3.3. The Root Mean Square Deviation S_q of the Machined Surface

The root mean square deviation S_q of the machined surface is the root mean square distance between the measured contour surface and the datum plane along the z-axis in the sampling area, it can be expressed mathematically as [16]:

$$S_q = \sqrt{\frac{1}{MN}\sum_{j=1}^{N}\sum_{i=1}^{M} {z_a}^2(x_i, y_j)} \tag{26}$$

Substituting Equation (24) into Equation (26), the root mean square deviation S_q of the machined surface can be expressed as:

$$S_q = \sqrt{\frac{1}{MN}\sum_{j=1}^{N}\sum_{i=1}^{M}\left[f(x_i, y_j) + \frac{a_e v_w}{N_{EV} h_{m.x} l_w l_c v_s} - z_m - \varphi\right]^2} \tag{27}$$

For different grinding parameters, MATLAB was used to calculate the prediction model of S_a and S_q, and the results are shown in Figure 6. It can be seen that, within a certain range, the arithmetic square root deviation S_a and the root mean square deviation S_q of the machined surface are positively correlated with the grinding depth a_e and the feed speed v_w, and negatively correlated with the grinding wheel linear speed v_s.

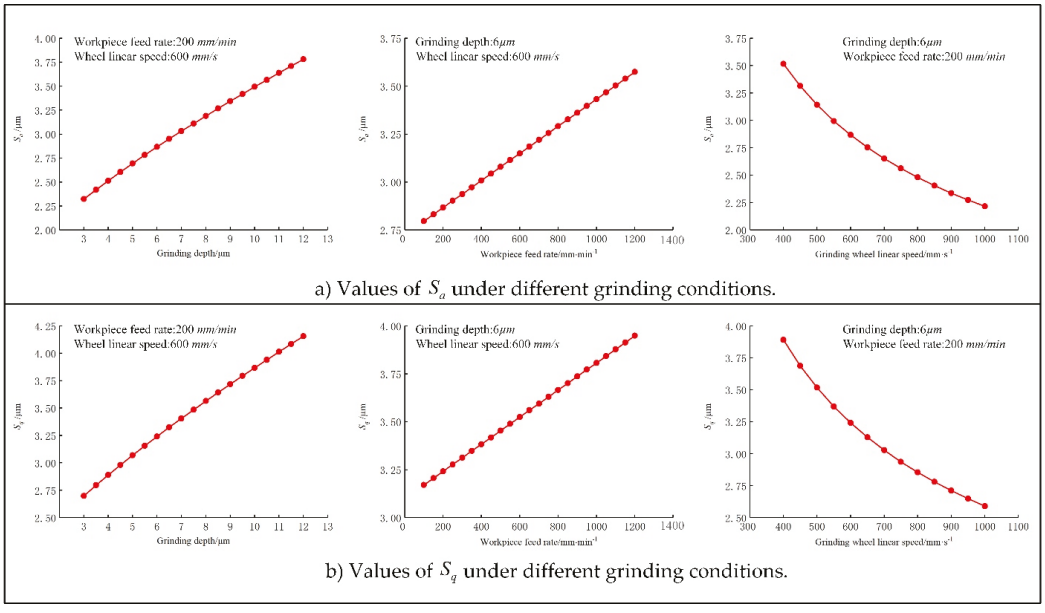

Figure 6. Values of S_a and S_q under different grinding conditions.

4. Experimental Verification

4.1. Experimental Scheme

In order to verify the accuracy of the new method for calculating the height of surface residual materials in ultra-precision grinding and its key role in the surface quality evaluation and three-dimensional roughness prediction of Nano-ZrO_2 ceramic ultra-precision grinding, a single-factor grinding experiment of Nano-ZrO_2 ceramics with the diamond grinding wheel was designed. The grinding experiment was carried out on the vertical machining center (VMC850E), and the experimental platform is shown in Figure 7a. The machining parameters of the single-factor grinding experiment are shown in Table 1, and the specific experimental conditions are shown in Table 2. The performance parameters of Nano-ZrO_2 ceramic are shown in Table 3. In order to prevent the experimental results from being affected by the abrasion of the grinding wheel, the resin-based diamond grinding wheel was dressed by the silicon nitride grinding wheel after each group of experiments. The three-dimensional morphology and microstructure of the machined surface were observed by the white light interferometer (Lecia DCM3D) and the scanning electron microscope (FEI SCIOS), the surface measurement of Nano-ZrO_2 is shown in Figure 7b. In order to make the measurement results more precise, the machined surface was cleaned by the ultrasonic cleaner after the grinding process, and five sampling areas were randomly selected on each sample, and the average value of the measurement results of the five sampling areas was taken as the measured results of the three-dimensional surface roughness of the machined surface.

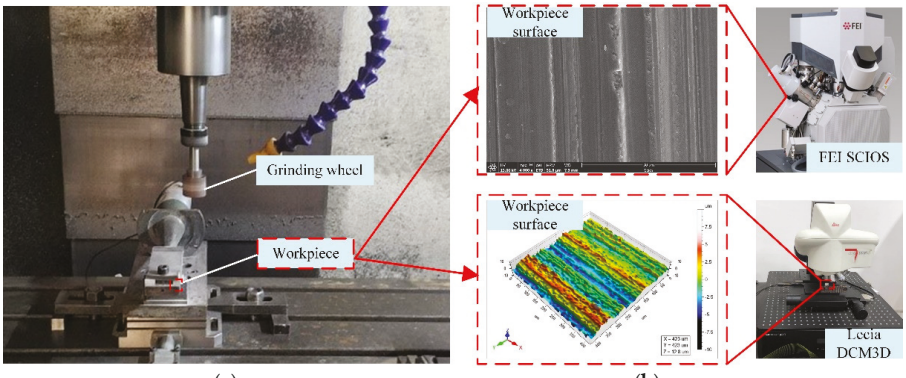

Figure 7. Experimental procedure. (**a**) Experimental platform. (**b**) Surface measurement of Nano-ZrO_2.

Table 1. Single-factor grinding experimental machining parameters.

Exp. Number	Grinding Depth a_e/μm	Workpiece Feed Rate v_w/mm·min^{-1}	Grinding Wheel Linear Speed v_s/mm·s^{-1}
1	3/6/9/12	200	600
2	6	100/400/800/1200	600
3	6	200	400/600/800/1000

Table 2. Experimental conditions.

Condition	Feature
Grinding method	Dry grinding
Workpiece material	Nano-ZrO_2 ceramic
Size of workpiece	15 × 10 × 5 mm
Grinding wheel	Resin-based diamond grinding wheel, 150#, 150%
Diameter of wheel	D = 25 mm

Table 3. Performance parameters of Nano-ZrO_2 ceramic.

Item	Parameters
Density (g/cm^3)	5.5–6.05
Poisson ratio	0.3
Elastic modulus (Gpa)	220
Bending strength (Mpa)	1100
Compressive strength (Mpa)	2500
Fracture toughness *KIC* (Mpa·m$^{1/2}$)	12

4.2. Experimental Results and Discussion

Figure 8 shows the comparison of the predicted and actual values of the three-dimensional surface roughness of the Nano-ZrO_2 ceramic under different grinding depths. It can be seen from Figure 8 that when other processing conditions are the same, the changing trend of S_a and S_q positively correlates with grinding depth a_e, the experiment data and the trend of change are consistent with the calculation results of the prediction model established in this study, which verifies the validity and accuracy of the new method for calculating the height of surface residual materials and the three-dimensional surface roughness prediction model established in this study. Figure 9 shows the comparison of the three-dimensional microstructure of the machined surface of Nano-ZrO_2 ceramics under different grinding depths. Combined with the height model of Nano-ZrO_2 ceramic

ultra-precision grinding surface residual material established in this study, the observation results were analyzed, it can be seen that when the grinding depth is increased from 3 μm to 6 μm, the material removal method of the machined surface is mainly plastic removal, and when the grinding depth is increased to 6 μm or more, the micro-crush damage of the machined surface increases, and the surface quality deteriorates rapidly. This phenomenon may be attributed to the fact that as the grinding depth increases, the increase in the thickness of the undeformed chips of a single abrasive particle causes the residual material on the machined surface to accumulate during processing, which results in a larger residual material height and a larger peak height and valley depth on the machined surface.

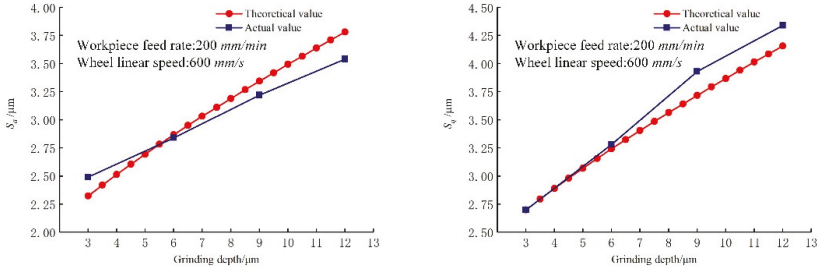

Figure 8. Effect of grinding depth on the three-dimensional surface roughness. (Feed rates: 200 mm/min, Grinding wheel linear speeds: 600 mm/min).

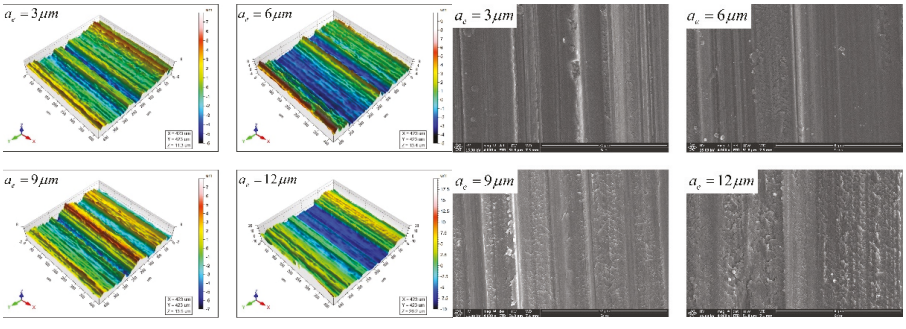

Figure 9. Comparison of three-dimensional surface microstructure under different grinding depths. (Feed rates: 200 mm/min, Grinding wheel linear speeds: 600 mm/min). (**a**) White light interferometer observation results. (**b**) Scanning electron microscope observation results.

The comparison of the predicted and actual values of the three-dimensional surface roughness of the Nano-ZrO_2 ceramic under different workpiece feed rates is shown in Figure 10. It can be seen in Figure 10 that under the same grinding conditions, S_a and S_q gradually increase with the increase in the feed rate, and the values and changing trends of each three-dimensional roughness parameter of the Nano-ZrO_2 ceramic are consistent with the calculation results of the prediction model established in this study. Figure 11 shows the comparison of the three-dimensional microstructure of the machined surface of Nano-ZrO_2 ceramics under different feed rates. Combined with the height model of Nano-ZrO_2 ceramic ultra-precision grinding surface residual material established in this study, the observation results were analyzed, it can be seen that as the feed rate increases, the grinding groove becomes more uneven in depth and width, and the surface quality deteriorates. That is, the deviation of the peak and trough on the machined surface increases, and its

distribution becomes more uneven. It also means that when the feed rate increases, the material removal rate of the machined surface increases, but the overall height deviation of the machined surface gradually increased.

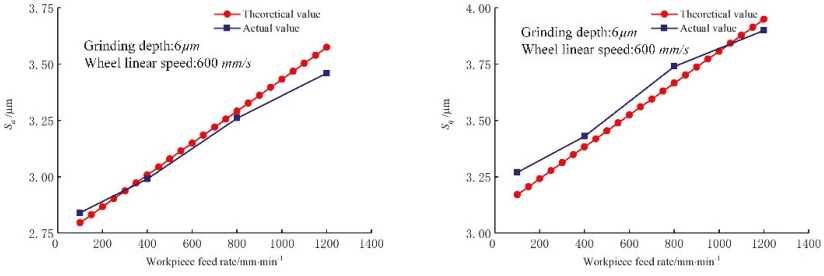

Figure 10. Effect of feed rate on the three-dimensional surface roughness. (Grinding depths: 6 μm, Grinding wheel linear speeds: 600 mm/min).

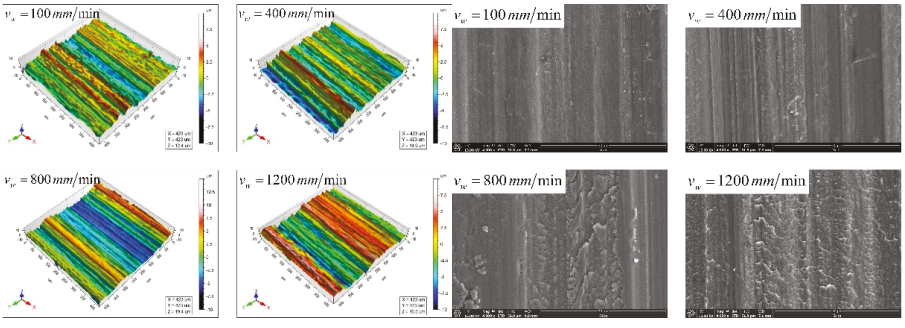

(**a**) (**b**)

Figure 11. Comparison of three-dimensional surface microstructure under different feed rates. (Grinding depths: 6 μm, Grinding wheel linear speeds: 600 mm/min). (**a**) White light interferometer observation results. (**b**) Scanning electron microscope observation results.

The comparison of predicted and actual values of the three-dimensional surface roughness of the Nano-ZrO_2 ceramic of TUAG under different grinding wheel linear speed is shown in Figure 12. It can be seen from Figure 12 that as the grinding wheel linear speed v_s increases, S_a and S_q gradually decreases, the calculated results of the prediction model established in this study are consistent with the actual values obtained from the experiment, which reflects the reliability of the calculation method and related model proposed in this study. Figure 13 shows the comparison of the three-dimensional microstructure of the machined surface of Nano-ZrO_2 ceramics under different grinding wheel linear speeds. Combined with the height model of Nano-ZrO_2 ceramic ultra-precision grinding surface residual material established in this study, the observation results were analyzed, it can be seen that as the grinding wheel linear speed increases, the micro-crush damage of the machined surface is weakened, and the peak height and valley depth of the machined surface decrease, and the overall height deviation of the machined surface decreases gradually. In addition, the accumulation of residual materials on the surface during the grinding process is weakened with the grinding wheel linear speed increases, resulting in a decrease in the height of the residual material, and the surface quality was significantly improved. This phenomenon indicates that the grinding process parameters can affect the surface quality by affecting the formation of residual materials on the machined surface.

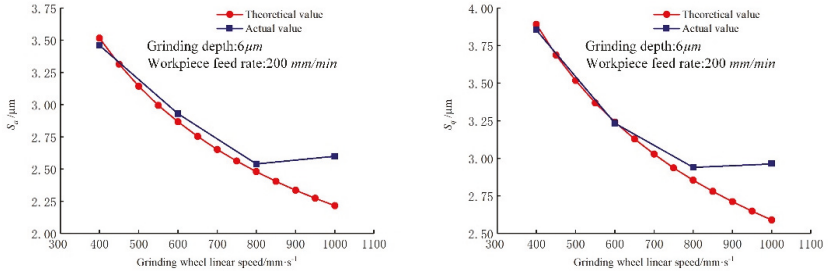

Figure 12. Effect of grinding wheel linear speed on the three-dimensional surface roughness. (Grinding depths: 6 μm, Feed rates: 200 mm/min).

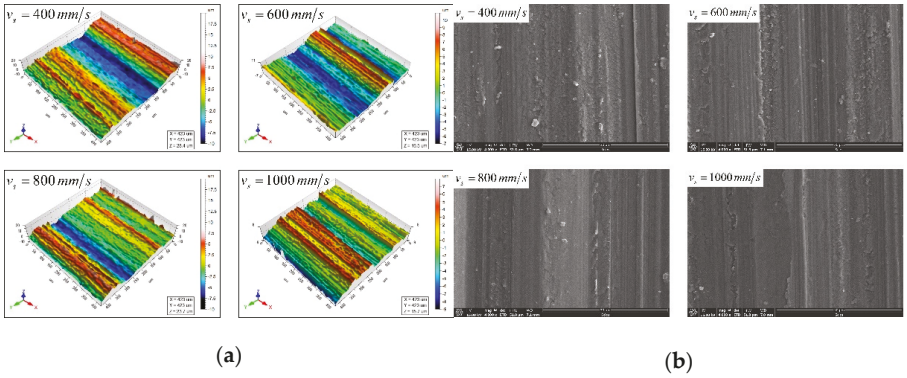

Figure 13. Comparison of three-dimensional surface microstructure under different grinding wheel linear speeds. Grinding depths: 6 μm, Feed rates: 200 mm/min. (**a**) White light interferometer observation results. (**b**) Scanning electron microscope observation results.

5. Conclusions

This study proposes a new method for calculating the height of surface residual materials of Nano-ZrO_2 ceramic under ultra-precision grinding and researches its application in Nano-ZrO_2 ceramic ultra-precision grinding surface quality evaluation and three-dimensional roughness prediction, which provides a theoretical reference for the analysis of the material removal process and the surface quality evaluation of ultra-precision grinding of hard and brittle materials. The main conclusions are as follows:

1. In this study, a new method for calculating the height of surface residual materials of Nano-ZrO_2 ceramic in ultra-precision grinding was proposed, which can obtain the height of surface residual materials that conform to the characteristics of three-dimensional roughness sampling and has more accurate results. It is of great significance for the development of the three-dimensional roughness prediction model for ultra-precision grinding;
2. The numerical value and change trend of S_a and S_q under different grinding conditions measured in the experiment are consistent with the calculation results of the prediction model. The Nano-ZrO_2 ceramic three-dimensional roughness prediction model developed by the new method for calculating the height of surface residual materials of Nano-ZrO_2 ceramic in ultra-precision grinding has better accuracy and reliability;
3. Simulation and experimental results show that grinding with lower feed rate, lower grinding depth, and higher grinding wheel linear speed can reduce the cutting depth of single abrasive particle and micro-crush damage of the machined surface, and the

accumulation of residual material on the machined surface can be weakened, thus making the height of the residual material on the machined surface descent.

Author Contributions: Conceptualization, Z.Z.; methodology, Z.Z.; software, Z.Z.; validation, Z.Z.; formal analysis, Z.Z.; investigation, Z.Z., H.Y. and X.W.; resources, Y.Y. and J.L.; data curation, Z.Z.; writing—original draft preparation, Z.Z.; writing—review and editing, Z.Z.; visualization, Z.Z.; supervision, Z.Z.; project administration, Y.Y. and J.L.; funding acquisition, Y.Y. and J.L. All authors have read and agreed to the published version of the manuscript.

Funding: This research was sponsored by the National Natural Science Foundation of China (51575163).

Conflicts of Interest: The authors declare no conflict of interest.

References

1. Gong, Y.; Wang, B.; Wang, W. The simulation of grinding wheels and ground surface roughness based on virtual reality technology. *J. Mater. Process. Technol.* **2002**, *129*, 123–126. [CrossRef]
2. Zhou, X.; Xi, F. Modeling and predicting surface roughness of the grinding process. *Int. J. Mach. Tools Manuf.* **2002**, *42*, 969–977. [CrossRef]
3. Hou, Z.B.; Komanduri, R. On the mechanics of the grinding process—Part I. Stochastic nature of the grinding process. *Int. J. Mach. Tools Manuf.* **2003**, *43*, 1579–1593. [CrossRef]
4. Agarwal, S.; Rao, P.V. Modeling and prediction of surface roughness in ceramic grinding. *Int. J. Mach. Tools Manuf.* **2010**, *50*, 1065–1076. [CrossRef]
5. Xiao, X.Z.; Li, G.; Li, Z.H. Prediction of the surface roughness in ultrasonic vibration-assisted grinding of dental zirconia ceramics based on a single-diamond grit model. *Micromachines* **2021**, *12*, 543. [CrossRef] [PubMed]
6. He, B.F.; Wei, C.E.; Liu, B.X.; Ding, S.Y.; Shi, Z.Y. Three-dimensional surface roughness characterization and application. *Opt. Precis. Eng.* **2018**, *26*, 1994–2011.
7. Li, C.G.; Dong, S. The current situation and development of surface roughness. *Aviat. Precis. Manuf. Technol.* **1999**, *5*, 1–4.
8. Zhou, W.; Tang, J.; Chen, H.; Zhu, C.; Shao, W. A comprehensive investigation of plowing and grain-workpiece micro interactions on 3D ground surface topography. *Int. J. Mech. Sci.* **2018**, *144*, 639–653. [CrossRef]
9. Chen, H.; Tang, J. A model for prediction of surface roughness in ultrasonic-assisted grinding. *Int. J. Adv. Manuf. Technol.* **2015**, *77*, 643–651. [CrossRef]
10. Setti, D.; Ghosh, S.; Rao, P.V. A method for prediction of active grits count in surface grinding. *Wear* **2017**, *382–383*, 71–77. [CrossRef]
11. Younis, M.; Alawi, H. Probabilistic Analysis of the Surface Grinding Process. *Trans. Can. Soc. Mech. Eng.* **1984**, *8*, 208–213. [CrossRef]
12. Agarwal, S.; Rao, P.V. A probabilistic approach to predict surface roughness in ceramic grinding. *Int. J. Mach. Tools Manuf.* **2005**, *45*, 609–616. [CrossRef]
13. Jiang, J.L.; Ge, P.Q.; Hong, J. Study on micro-interacting mechanism modeling in grinding process and ground surface roughness prediction. *Int. J. Adv. Manuf. Technol.* **2013**, *67*, 1035–1052. [CrossRef]
14. Company, N. *Standard Stock and Specifications Manual*; Municode library: Tallahassee, FL, USA, 1978.
15. Zhang, Z.; Cui, H.; Ding, H.; Guo, L. The reference plane by wavelets for 3D roughness evaluation of micro wire electrical discharge machining (MWEDM). *J. Harbin Eng. Univ.* **2011**, *32*, 1185–1189.
16. Qiao, G.C. *Research on Machined Surface Integrity in Ultrasonic Vibration Mill-Grinding of Silicon Nitride Ceramics*; Doctor, Harbin Institute of Technology: Harbin, China, 2013.

micromachines

MDPI

Article

Influence of Different Tool Electrode Materials on Electrochemical Discharge Machining Performances

Islam Md. Rashedul [1], Yan Zhang [1,*], Kebing Zhou [2], Guoqian Wang [1], Tianpeng Xi [1] and Lei Ji [1]

[1] School of Mechanical and Power Engineering, Nanjing Tech University, Nanjing 211800, China; rashed.eee38@gmail.com (I.M.R.); wangy_cgte@163.com (G.W.); xtp63@163.com (T.X.); jilei.1993@163.com (L.J.)

[2] National Key Laboratory for Remanufacturing, Beijing 100072, China; zhoukb99@sina.com

* Correspondence: zhangyanzy@njtech.edu.cn; Tel.: +86-25-5813-9346

Abstract: Electrochemical discharge machining (ECDM) is an emerging method for developing micro-channels in conductive or non-conductive materials. In order to machine the materials, it uses a combination of chemical and thermal energy. The tool electrode's arrangement is crucial for channeling these energies from the tool electrode to the work material. As a consequence, tool electrode optimization and analysis are crucial for efficiently utilizing energies during ECDM and ensuring machining accuracy. The main motive of this study is to experimentally investigate the influence of different electrode materials, namely titanium alloy (TC4), stainless steel (SS304), brass, and copper–tungsten (CuW) alloys (W70Cu30, W80Cu20, W90Cu10), on electrodes' electrical properties, and to select an appropriate electrode in the ECDM process. The material removal rate (MRR), electrode wear ratio (EWR), overcut (OC), and surface defects are the measurements considered. The electrical conductivity and thermal conductivity of electrodes have been identified as analytical issues for optimal machining efficiency. Moreover, electrical conductivity has been shown to influence the MRR, whereas thermal conductivity has a greater impact on the EWR, as characterized by TC4, SS304, brass, and W80Cu20 electrodes. After that, comparison experiments with three CuW electrodes (W70Cu30, W80Cu20, and W90Cu10) are carried out, with the W70Cu30 electrode appearing to be the best in terms of the ECDM process. After reviewing the research outcomes, it was determined that the W70Cu30 electrode fits best in the ECDM process, with a 70 μg/s MRR, 8.1% EWR, and 0.05 mm OC. Therefore, the W70Cu30 electrode is discovered to have the best operational efficiency and productivity with performance measures in ECDM out of the six electrodes.

Keywords: electrochemical discharge machining (ECDM); material removal rate (MRR); electrode wear ratio (EWR); overcut (OC); electrical properties; tool material

Citation: Rashedul, I.M.; Zhang, Y.; Zhou, K.; Wang, G.; Xi, T.; Ji, L. Influence of Different Tool Electrode Materials on Electrochemical Discharge Machining Performances. *Micromachines* **2021**, *12*, 1077. https://doi.org/10.3390/mi12091077

Academic Editors: Jiang Guo, Chunjin Wang and Chengwei Kang

Received: 24 August 2021
Accepted: 5 September 2021
Published: 7 September 2021

1. Introduction

The manufacturing industry faces a challenge in creating holes or cuts in rigid materials with high geometrical precision. The process of electrochemical discharge machining (ECDM) is a combination of electrochemical and electro-discharge machining, with applications in aerospace, electronics, and miniaturized medical equipment, especially for drilling holes with complex shapes and geometries. However, due to the uncertain nature of the ECDM mechanism, electrode material selection is made on an empirical basis based on experimental results. As a result, it is critical to select an effective tool electrode to improve performances, such as the material removal rate (MRR), electrode wear ratio (EWR), overcut (OC), and surface defects on difficult-to-machine alloys.

According to the literature, the electrode content, electrode shape, and machining parameters all have a significant impact on electrical discharge machining (EDM) and ECDM efficiency. It can be inferred that there is a requirement for a comparative investigation about the effects of the tool material. In the hybrid EDM process, brass, copper

(Cu), and copper–tungsten (CuW) are used [1]. For all current settings, the Cu electrode gave the highest MRR, followed by the brass and CuW electrodes, and CuW also had the lowest rate of EWR. The MRR and tools wear rate (TWR) was greatly influenced by the material properties of the electrode [2]. An inappropriate combination of the workpiece and the electrode leads to a reduced productivity in EDM sinking dies and excessive TWR. When executing the EDM operation with Ti-6Al-4V, using a cryogenically treated copper electrode produced an optimized MRR, improved surface quality, and reduced the EWR [3]. In the EDM performance of titanium grade six alloy, Cu anodes displayed a more moderate tool wear than brass and zinc anodes [4]. For both brass and zinc cathodes, a higher TWR was observed at a lower peak current (10 A). The magnitude of the TWR and overcut was of the order Cu > CuW > W, according to the experimental inquiry [5]. This occurred as a result of deviations in the thermal properties of the electrode materials. When drilling stainless steel with μ-EDM, the impact of the anode material and power discharge on the drilling time and TWR was investigated [6]. When a tungsten carbide electrode was used, the increased power discharge resulted in a significant reduction in drilling time, causing the TWR to be degraded and overlapped. The EDM of AISI 1040 stainless steel used an AlSiMg electrode prepared through the selective laser sintering (SLS) process, as well as a Cu and brass electrode [7]. The electrode that was the best EDM parameter setting found for the maximization of the MRR and minimization of the TWR, ROC, and Ra was a novel type of tool electrode in a rod made of carbon fibers [8]. The MRR shows that the investigated electrodes are comparable to tungsten (W), silver tungsten (AgW), and CuW electrodes in terms of process efficiency, and can be considered a possible complementary electrode material for EDM. An experiment in EDM was conducted in which a Nimonic C263 superalloy was machined with Cu, W, and CuW electrodes [9]. As a result of the electrode material and discharge current, the Cu electrode exhibited a higher MRR and a lower EWR. The effects of input variables, such as DC supply voltage, electrolyte concentration, pulse-on-time, pulse-off-time, and the inter-electrode gap using three different tool electrode (Cu, brass, W) materials, on developing the ECDM setup on the MRR were investigated, where the optimum MRR is depicted by a brass electrode through the KOH electrolyte and the proper set-up combination of voltage and pulse-on-time [10].

Regarding the machining of the Ti-6Al-4V titanium alloy, the optimal technological parameter combination in EDM with the AlCrNi-coated electrode was found to be the peak current (40 A), voltage (55 V), and pulse-on-time (1000 s). As a result of the electrical conductivity of the tool coating, the current was discovered to be the most important element in the EDM process with the coated tool [11]. A Taguchi L_{18} experimental design was used to compare the process performances of the EDM of HcHcr D2 steel (DIN EN ISO 4957) using different electrode materials (copper, graphite, and brass), dielectric fluids (distilled water and kerosene), peak current, and pulse-on-time, and the process performances were analyzed with respect to MRR, SR, and TWR. Graphite electrodes using distilled water as a dielectric fluid had a higher MRR of 0.0632 g/min and a lower SR of 1.68 μm and TWR of 0.012 g/min than brass and copper electrodes [12]. An investigation of the characterization of ternary metals (Cu–Ni–TiN) for EDM electrodes using powder metallurgy for the formation of Cu in Ni-TiN electrodes was conducted using a cold press at pressures of 18, 20, and 22 MPa, which led to the enhancement of mechanical properties, such as hardness, electrical properties, and other properties. The result show that the 80% Cu–3% Ni–17% TiN electrode at 18 MPa had the highest hardness (124.38 HV) and lowest electric resistivity (0.39188 cm), whereas the specimen with an increased Cu, with a ratio of 85% Cu–3% Ni–12% TiN at 20 MPa, had the highest density (8.5472 g/cm^3) and lowest porosity (6.2922%) [13]. While the Nb powder was mixed in dielectric fluid, a composite layer of TiO_2-TiC-NbO-NbC was coated on the Ti-64 alloy using two separate methods (electric discharge coating (EDC) and EDM processes). It has been discovered that, in the EDC process, the high peak current and high Nb powder concentration increase the material migration, resulting in the deposition of a crack-free thick layer (215 m) on the workpiece surface [14].

Because of the combined effects of the chemical and thermal energies of ECDM, its machining performance is faster and it has a lower processing cost, a simpler setup, and a higher MRR with low EWR than other methods, such as EDM and ECM, irrespective of the typical properties of newer materials. As a result, researchers have always been interested in the ECDM efficiency upgrade. Regarding the combined process of EDM ablation and ECM in an aerosol dielectric, the MRR was 3.7 times higher than that of EDM or ECM, the TWR was reduced by 53.3%, and the value of the corner arc radius decreased by 44.3% [15]. An experimental study comparing the effects of molybdenum and high carbon steel (HCS) electrode materials on the creation of micro-holes in glass by pulse ECDM was conducted, where molybdenum electrodes had minor tool corrosion compared to HCS electrodes, due to their higher melting point [16]. Four tool materials, namely copper, tungsten, stainless steel, and high carbon steel, were used to build a >300-µm-deep micro-hole in glass using gravity feed ECDM, where the tungsten and copper tools achieved the highest and lowest machining speeds of 95 µm/s and 20 µm/s [17]. Regarding the efficiency of gravity feed ECDM with three different tool materials, tungsten, tungsten carbide, and stainless steel, the tungsten carbide tool had the fastest machining speed because of its highest average current, and the stainless steel tool had the highest tool wear because of both its lowest melting point and its thermal conductivity [18]. Using a $NaNO_3$ working fluid and an electrochemical discharge drilling system with a conductivity of about 4.0 mS/cm resulted in optimum quality holes in the nickel-based superalloy, with a low TWR of the brass electrode [19]. The effects of tool electrode electrochemical discharge machining process parameters, where the machining is performed through a chemical etching effect, were investigated, and it was discovered that the melting of the workpiece material due to electrical discharges and the influence of the ECDM process parameters are associated with the tool electrode [20]. For sound hole making and an improved electro-discharge machining efficiency, an optimal parameter setting has been established [21], and the impact of process parameters on various process performance characteristics, such as the material removal rate, surface roughness, surface crack density, white layer thickness, radial overcut, and hole taper, has been investigated.

According to published research, several attempts have been made to optimize EDM results by using different tool electrodes. In order to observe EDM results, the majority of researchers concentrate on machining parameter variation. Parameter variation is not the only crucial aspect for analyzing the machining performance; a proper electrode selection for different machining is also important. In this study, different material electrodes are proposed in the ECDM process, whereby the effects of the electrodes on the machining performance parameters, including the machining efficiency, machining accuracy, MRR, EWR, OC and surface behavior, are investigated. First, four different electrodes are compared on the command variable. However, it has been found that two of the very-low-conductive electrodes' performances are very poor compared to other two. Secondly, an electrode that performs well is taken from the first step of the experiment and compared to the other two electrodes, where these three electrodes are made of the same alloy but have a different chemical composition.

The present article focuses on the experimental study: stainless steel, titanium, brass, and copper–tungsten alloy-made electrodes are used to confirm the electrical conductivity and thermal conductivity effect on the ECDM performance. Machining parameters, normal flushing pressure, dielectric fluid, and rotational speed have been kept at constant in order to analysis the ECDM performances. If the tool electrodes' electrical conductivity is high, the local temperature rise would owe less to the faster heat dissipation to the workpiece. As a result, the MRR gain is higher with a lower EWR. On the other hand, if the thermal conductivity is low, the electrode's body temperature would be raised rapidly due to the reduction in heat transfer to the workpiece. As a result, a lower MRR is associated with a higher EWR, resulting in an irregular surface with more cavities and cracks. Furthermore, a scanning electron microscopy (SEM) analysis of the drilled holes and electrodes is performed to determine micro-voids, cracks, and craters on the surface,

as well as material migration on the tip of the electrodes. After analyzing the experimental findings, it was discovered that the W70Cu30 electrode performs the best, with a 70 μg/s MRR, 8.1% EWR, and 0.05 mm OC in the ECDM machining process.

2. Mechanism of Electrochemical Discharge Machining (ECDM)

ECDM is a combined process of EDM and ECM, in which electrochemical dissolution and electrical discharge erosion occur simultaneously in ECDM in the lateral machining gap and frontal gap, respectively. The mechanism of ECDM is depicted in Figure 1. In this hybrid machining, sodium nitrate ($NaNO_3$) has been used. $NaNO_3$ is used for machining stainless steel when close replication of the tool is of utmost importance, as it prevents stray corrosion, ensuring precise tool replication. Lower concentration electrolytes are used to improve the machining resolution. The resolution is improved due to the increased electrolyte resistance, which requires shorter current paths for a given pulse length.

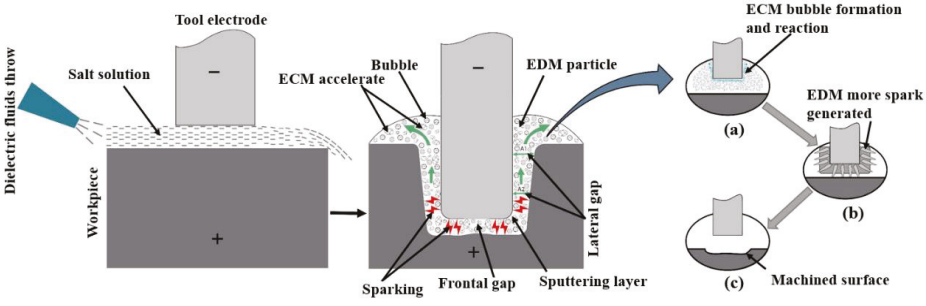

Figure 1. Schematic diagram of tool electrode high-speed electrochemical discharge machining mechanism. (**a**) ECM bubble formation and reaction, (**b**) EDM spark generating (**c**) Machined surface.

Both EDM and ECM are used to increase the lateral gap distance at the start of the drilling process. The lateral gap distance increases steadily with an increasing drilling depth due to the removal of materials from the electrochemical dissolution. When the lateral gap distance exceeds the theoretical maximum value, EDM becomes slow and eventually stops. Electrochemical dissolution will be the only process left in the side gap, and will start to remove the side wall material and expand the gap width. As a result, the conductivity of the solution, which affects electrochemical dissolution, is critical for minimizing electrode erosion and maintaining a good surface quality.

Since the electrode tip feeds towards the workpiece during the operation, the gap between the tool and workpiece is always kept at a gap distance smaller than the theoretical maximum value. This causes a spark discharge that is concentrated in the front gap. Electrolytic corrosion predominates in material removal, whereas the effects of electrochemical dissolution are relatively minor. In this process, bubbles are created by hydrogen evolution from an electrochemical reaction. The working fluid is constantly washed off from the process products, ensuring continuous spark discharge. Thus, the predominant material removal effect of electrostatic discharge erosion leads to a high drilling speed of the ECDM process.

In this ECDM process, the below electrochemical reaction equations are as follows:

At the anode:

The metal material can be dissolved as

$$Fe \rightarrow Fe^{2+} + 2e^{-}$$

Subsequently, the metal ions combine with the hydroxyl ions to precipitate as iron hydroxide,

$$Fe^{2+} + 2OH^{-} \rightarrow Fe(OH)_2\downarrow$$

Hydroxyl ions evolve oxygen at the anode as

$$4OH^- \rightarrow O_2\uparrow + 2H_2O + e^-$$

At the cathode:
The reaction is likely to be the generation of hydrogen gas and hydroxyl ions.

$$2H_2O + 2e^- \rightarrow 2OH^- + H_2\uparrow$$

Following that, an electrochemical reaction could produce many bubbles, such as H_2 and O_2, surrounding the end tool electrode (anode). In the left part of Figure 1a, the formation of the bubble by the chemical reaction is depicted schematically where formation process of discharge channel are completed in the gas medium. The electrochemical discharges start small on the active electrode zone, and then more of the spark spreads out to a wide area of the workpiece (Figure 1b). This is due to the electrolyte's lower electrical conductivity and material is removed from these discharges through melting, vaporization, and high-temperature chemical etching.

3. Experimental Setup

3.1. Machine Tool

A machine tool has been shown in Figure 2, which includes an XYZ motion table, a working fluid recycling system, tool electrode clamp, high-pressure flushing unit, a power supply cell, voltage and current measuring unit, a pressure pump with pressure regulating valve, and a self-designed fixture. Tool electrode can be fixed into the machine head and can be carried in the feed rate guidance via a servomotor in the direction perpendicular to the XY plane. A motor is mounted on the *Z*-axis and rotates the tool electrodes. The control box contains the pulse generator, which provides the pulse voltage and the process control system. Due to the salt solution, all of the equipment's exterior enclosures, especially the parts in contact with the solution, are constructed with a stainless steel portion.

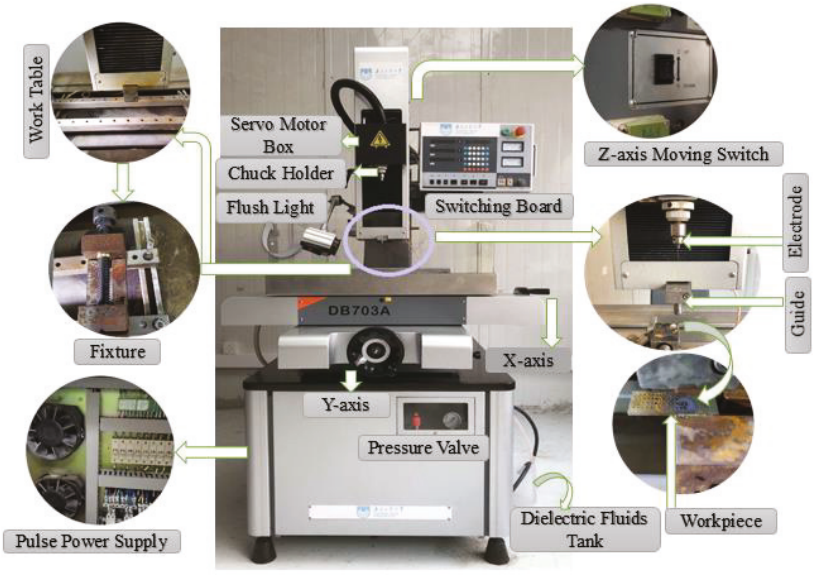

Figure 2. Photograph of the electrochemical discharge machining (ECDM) machine tool.

3.2. Materials and Properties

All experiments were carried out on stainless steel (SS304) workpiece with the size of 43 mm (length) × 15 mm (width) × 2 mm (thickness), and all cylindrical electrodes were 1.0 mm in diameter and 200 mm in length. Figure 3 represents the six different tool electrodes before machining. SS304 has a high initial melting temperature, heat corrosion resistance, and strong properties, such as creep resistance and fatigue resistance (Figure 3a). The TC4 has excellent corrosion resistance, and can withstand high temperature (Figure 3b). Brass is copper alloyed with high Zinc content, which is most widely regarded for non-traditional machining with various electrodes (Figure 3c). Compared with copper and other traditional electrode materials, CuW alloy has a maximum melting point, and is a relatively cost-effective and efficient choice as electrode material (Figure 3d–f). As shown in Figure 4, EDX analysis of six types of electrodes was performed to investigate the accurate mass percentage of element contents before ECDM. Moreover, from the EDX spectrum, how much the other particle added to the tip part of the electrode after machining was confirmed. Electrode materials' properties have been given in Table 1.

Table 1. Properties of the electrode materials.

Properties	TC4	SS304	Brass	W70Cu30	W80Cu20	W90Cu10
Density (g/cm^3)	4.43	8	8.73	13.80	15.15	16.75
Melting point (°C)	1660	1455	904	3420	3420	3420
Thermal conductivity (W/m K)	7	16.2	159	200	180	170
Specific heat capacity (J/kg K)	553	500	920	232	190	155
Tensile strength (Mpa)	862	515	360	516	620	700

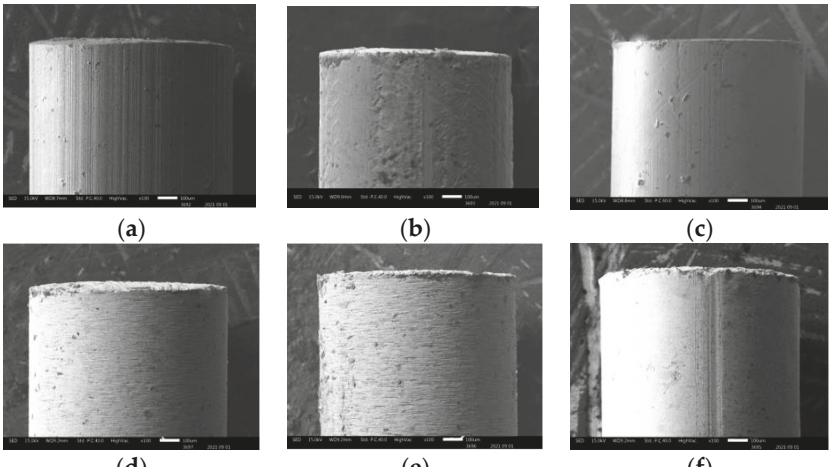

Figure 3. Scanning electron microscopy (SEM) picture of six different electrodes before machining: (**a**) SS304; (**b**) TC4; (**c**) brass; (**d**) W90Cu10; (**e**) W80Cu20; (**f**) W70Cu30.

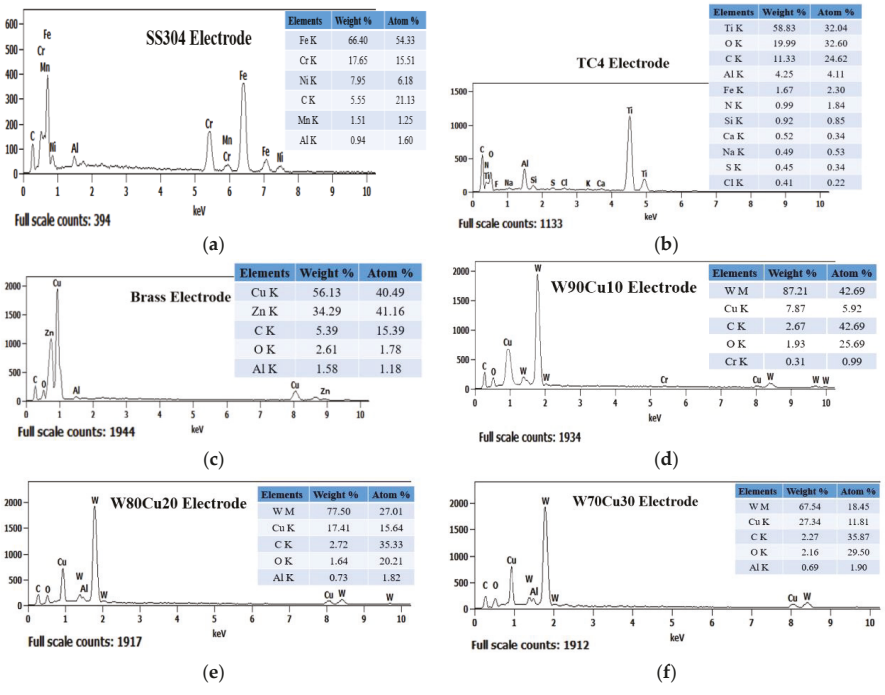

Figure 4. Energy-dispersive X-ray spectroscopy (EDX) spectrum analysis of six electrodes before ECDM: (**a**) SS304; (**b**) TC4; (**c**) brass; (**d**) W90Cu10; (**e**) W80Cu20; (**f**) W70Cu30.

3.3. Measurements and Acquisitions

The main machining performance of the ECDM process was assessed by the MRR, EWR, overcut, surface defects, and machining quality of holes. The assessment of MRR and EWR was conducted on weight basis using high precision weight balance. Every electrode and workpiece was measured before and after machining carefully. After one single drilling, it is difficult to obtain weight of electrode and workpiece, which is why four repetitions were carried out by one electrode every time. Then, the electrode and workpiece weights were measured. However, the machining time was counted with every single drilling finish and calculated by mean statistical method. After that, the following equations were used to find out MRR, EWR, and OC.

The following equation gives the material removal rate of the workpiece:

$$MRR = (W_i - W_f) \div T \quad (1)$$

Here, W_i is the initial weight of the workpiece, W_f is the final weight of the workpiece after machining, and T is machining time.

Electrode wear ratio is given by the following equation:

$$EWR = \{(E_{wb} - E_{wa}) \div (W_i - W_f)\} \times 100 \quad (2)$$

Here, E_{wb} is the electrode weight before machining and E_{wa} is electrode weight after machining.

Overcut (OC) is calculated using the following equation:

$$OC = (D_w - D_t) \div 2 \quad (3)$$

Here, D_w is the frontal hole diameter of the workpiece and D_t is the tool electrode diameter. Overcut per side has been specified.

The tool electrode material electrical conductivity value is calculated using the below equation:

$$S = L \div (R \times A) \quad (4)$$

Here, L and A are the length and diameter of tool electrode, S is the electrical conductivity, and R is the electrical resistance.

3.4. Machining Procedure and Condition

The material removal mechanism of ECDM, surface defects in workpiece and tools, and machining efficiency were investigated. The machining process is carried out in two stages. First of all, copper, titanium, stainless steel, and tungsten alloys were commonly used as electrode materials; thus, the brass, TC4, SS304, and W80Cu20 are compared in order to obtain the better electrode material choice. Further, for the tungsten alloys, the W70Cu30, W80Cu20, and W90Cu10 are investigated as the electrode materials, according to the MRR, EWR, and OC, whereby the optimal electrode is identified. The workpiece and electrodes were observed by a scanning electron microscope (SEM), model JSM-IT300, JEOL, Japan and the material composition of the tool tips after machining was analyzed by energy-dispersive X-ray spectroscopy (EDX) system integrated with this SEM. The conductivities of salt solution were measured using the conductivity test instrument SevenCompact S230, produced by Mettler Toledo Company. A series of experiments were carried out to evaluate the performance of different electrode materials using the machining conditions listed in Table 2.

Table 2. Machining parameters for electrochemical discharge machining (ECDM) experiments for brass, TC4, SS304, W70Cu30, W80Cu20, and W90Cu10 electrodes.

Machining Parameters	Fixed Parameters
Pulse width, T_{on} (μs)	12
Pulse interval, T_{off} (μs)	12
Peak current, I_p(Amp.)	14.17
Open circuit voltage, V_{OC}(V)	85
Electrolyte, $NaNO_3$ (g/L)	4
Regulation per minute(RPM)	300

4. Result and Discussion

4.1. Comparison of MRR, EWR, and OC by W80Cu20, Brass, TC4, and SS304 Electrodes

In the ECDM process, the effect of the tool materials' electrical conductivity and thermal conductivity on the MRR and EWR for W80Cu20, brass, TC4, and SS304 are shown in Figure 5. In Figure 5a, the MRR decreases as conductivity decreases, recording at 59.3, 57.4, and 12.1 μg/s for W80Cu20, brass, and TC4 electrodes, respectively. Following this, the MRR increases up to about 26.35 μg/s due to the higher conductivity of the SS304 electrode over the TC4 electrode. The higher the electrical conductivity of the electrode material, the faster the thermal energy is dissipated to the machining zone. This thermal energy evaporates the water from the electrolyte at the machining zone. Thus, only molten salt (sludge) is left at the tool–work material interface. The accumulation of this sludge ceases bubble formation beneath the tool electrode. Hereafter, bubbles evolve only from the edges and side walls of the tool electrode. These bubble coalesce and form thicker films and initiate more discharges at the tool edges. Hence, the amount of thermal energy reaching the workpiece material is cut down, and the majority of this energy is dissipated in the electrolyte by convection. W80Cu20 transfers more heat energy to the workpiece during the machining process. As a result, W80Cu20 generates a higher MRR by melting the workpiece.

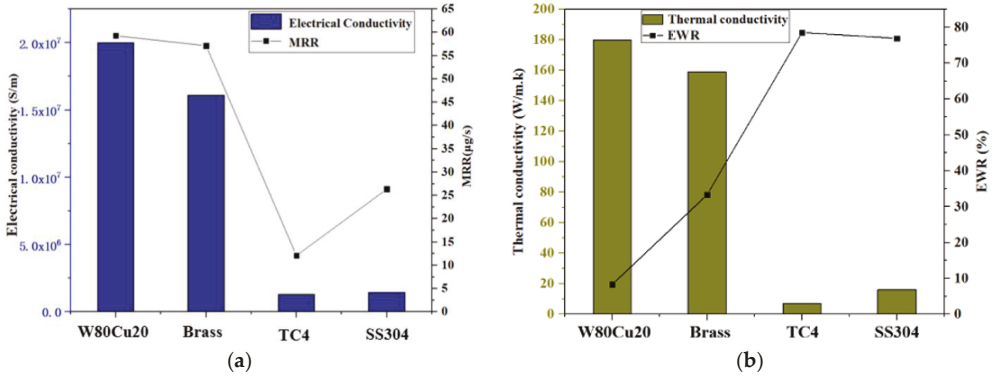

Figure 5. Influence of electrical conductivity and thermal conductivity of different electrodes under machining conditions Ton = 12 μs, Toff = 12 μs, Ip = 14.17 A; (**a**) MRR and (**b**) EWR.

The high thermal conductivity of the electrode materials is crucial in determining the EWR. The TC4 electrode has the highest EWR (78.54%), followed by SS304 (76.92%), brass (33.33%), and W80Cu20 (8.33%), as shown in Figure 5b. The tool electrode's thermal conductivity determines the electron's drifting ability in any substance. Due to the tool electrodes' low thermal conductivity, TC4 and SS304 electrodes represent the highest EWR. These two electrodes' drifting electrons are very low in bulk material for discharging, and the temperature increases towards the electrode's own body. Following that, the TC4 and SS304 electrodes burn during the machining mode with a lower MRR and a higher electrode wear ratio. The brass electrodes' high thermal conductivity allows for more heat to be applied to the workpiece, resulting in faster machining and a far lower EWR. However, W80Cu20 has the highest thermal conductivity (180 $Wm^{-1}k^{-1}$) compared to the other three electrodes, followed by brass (159 $Wm^{-1}k^{-1}$), SS304 (16.2 $Wm^{-1}k^{-1}$), and TC4 (7 $Wm^{-1}k^{-1}$), respectively. Heat cannot pass through a material with a low thermal conductivity without damaging the electrode. The low EWR is due to the higher thermal conductivity of W80Cu20.

In the ECDM process, the overcut is an essential factor that affects geometrical accuracy. By comparing the overcut caused by the four electrodes, it can be seen in Figure 6 that the SS304, TC4, and brass electrodes have created relatively larger overcuts (0.240, 0.195, 0.115 mm), whereas the W80Cu20 electrode produces a lower overcut (0.100 mm). Figure 7c,e,g show that the brass, TC4, and SS304 electrodes have made large diameters of 1.23, 1.39, and 1.48 mm, respectively, whereas the W80Cu20 (Figure 7a) electrode has created a 1.20 mm diameter on the workpiece. For W80Cu20, the heat from the electrochemical discharges is quickly removed from the machining zone, but for the other three electrodes, the electrochemical discharges are slowly removed. As a result, electrode and hole wall side sparking of the workpiece occurs more often for the SS304, TC4 and brass electrodes than the W80Cu20 (Figure 7a) electrode. The hole wall surface roughness, side gap spark, and electrode erosion are higher for brass, TC4 and SS304 electrode as shown in Figure 7c,e,g. The thermal conductivity of the SS304, TC4, and brass electrode materials are low, as well as the number of the drifting electrons, resulting in a lower discharging in the tip than in the W80Cu20 electrode. The corner of the electrode end has the highest current density and suffers the maximum wear. From the observations in Figure 7d,f,h, the brass, TC4, and SS304 electrodes' tip part eroded with more roughness than that of the W80Cu20 (Figure 7b) electrode. W80Cu20 has the largest thermal conductivity and its melting point is higher than the other three electrodes.

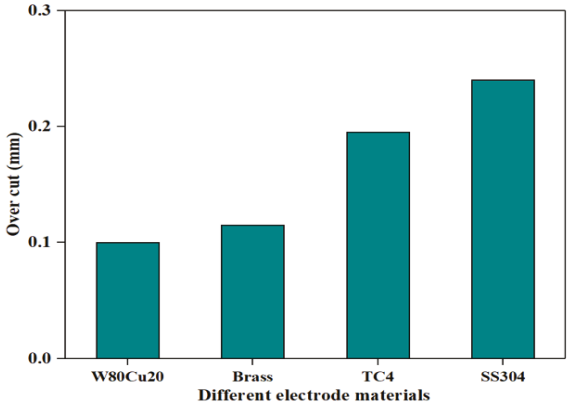

Figure 6. Different tool electrodes' effects on side overcut under machining conditions T_{on} = 12 µs, T_{off} = 12 µs, I_p = 14.17 A.

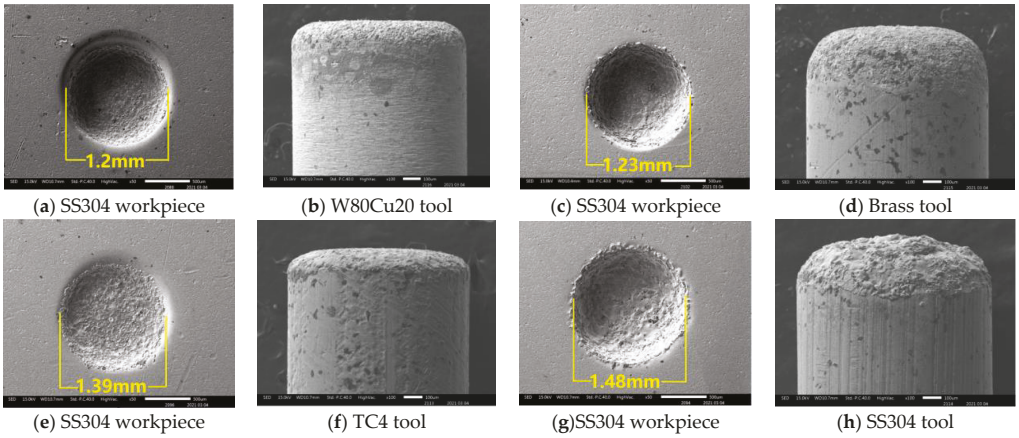

(**a**) SS304 workpiece (**b**) W80Cu20 tool (**c**) SS304 workpiece (**d**) Brass tool

(**e**) SS304 workpiece (**f**) TC4 tool (**g**)SS304 workpiece (**h**) SS304 tool

Figure 7. SEM picture of different electrodes and discharging phenomena of the holes on SS304 workpiece under machining conditions Ton = 12 µs, Toff = 12 µs, Ip = 14.17 A.

It is concluded that it is essential for the material that acquires good electrode wear properties in a machine with a high electrical conductivity to be complex. The W80Cu20 acquires a higher electrical conductivity (2.0×10^7 S/m) than the brass (1.61×10^7 S/m), SS304 (1.45×10^6 S/m), and TC4 (1.28×10^6 S/m) electrodes. A higher electrical conductivity enables a quick heat transfer through all of the workpiece. Subsequently, the lowest EWR with a higher MRR and minimum overcut are obtained by the W80Cu20 electrode.

4.2. Surface Defects on Workpiece and Material Transfer on Electrodes

In Figure 8, SEM images are used to study the surface topography of the machined SS304 alloy. The electrode material properties have an impact on the surface roughness. If the electrode material's electrical conductivity is higher, it allows for effective discharges while lowering ineffective pulses, resulting in an improved workpiece surface quality. The electrodes with the most cracks and pinholes on the machined surface are SS304 (Figure 8a) and TC4 (Figure 8b), followed by brass and W80Cu20 electrodes. The hydrodynamic regime is vigorously non-desirable. On the one hand, it increases the drilling time, and on the other hand, it is responsible for lowering the micro-aperture quality, as structural damage

(micro-cracks and pinholes) of the drilled micro-apertures transpires in this regime. This phenomenon is caused by the formation of distinct thermally impaired areas. The erosion of the TC4 and SS304 electrodes is high with a lower MRR because the discharging effect is very weak with higher surface defects. However, machining with brass (Figure 8c) and W80Cu20 (Figure 8d) electrodes creates fewer craters and a smaller pinhole. The W80Cu20 electrode has a better surface than the other three electrodes. The W80Cu20 electrode provides the best surface with the least amount of erosion and the highest MRR.

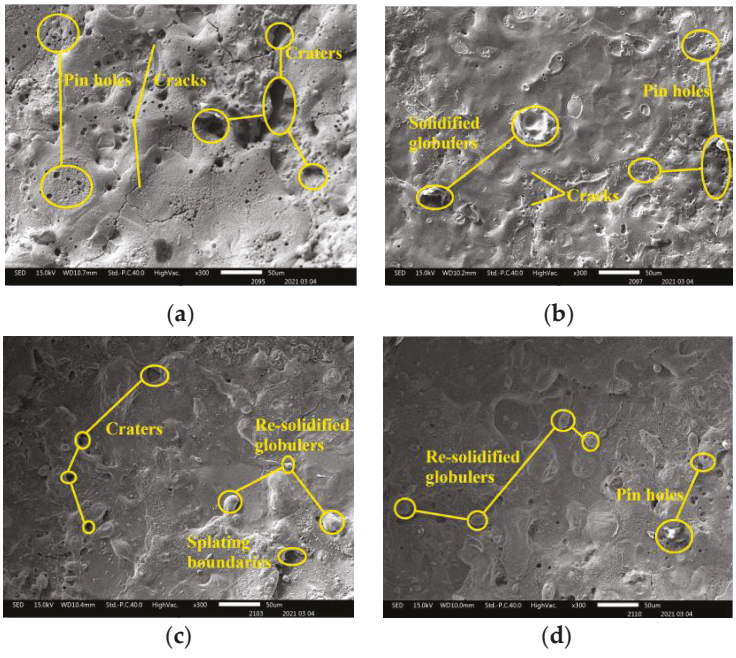

Figure 8. The surface of SS304 machined by different electrodes: (**a**) SS304; (**b**) TC4; (**c**) brass; (**d**) W80Cu20.

In terms of surface composition, Figure 9 shows the EDX spectrum analysis results for four different electrodes used in the ECDM process. The unexpected oxygen accumulation on the electrode surface can be explained by the reformulation layer formation mechanism. During an electrical discharge, high temperatures in the discharge channel induce the melting and evaporation of the metal from the surface; at the same time, the electrolyte decomposes into oxygen and hydrogen at these high temperatures. The TC4 electrode produced the highest oxygen layer (42.69%) among the four electrodes, whereas SS304 produced the second highest oxygen layer (29.84%). The lowest oxygen element composition was achieved using brass and W80Cu20 electrodes (27.56 and 25.58%). Due to their low conductivity and worse machining instability, the tip part of the SS304 and TC4 electrodes over-melted, and other particles attached more. Comparing the brass and W80Cu20 electrode, the brass electrode has the lowest melting point and thermal conductivity; as a result, there are a large amount of other substances associated with the brass electrode.

The excellent electrical conductivity and thermal conductivity of the electrode materials facilitate uniform and effective discharges, minimizing short pulses and enhancing the workpiece surface nature. As a result, choosing a tool electrode that is close to the manufacturing or machining process is needed.

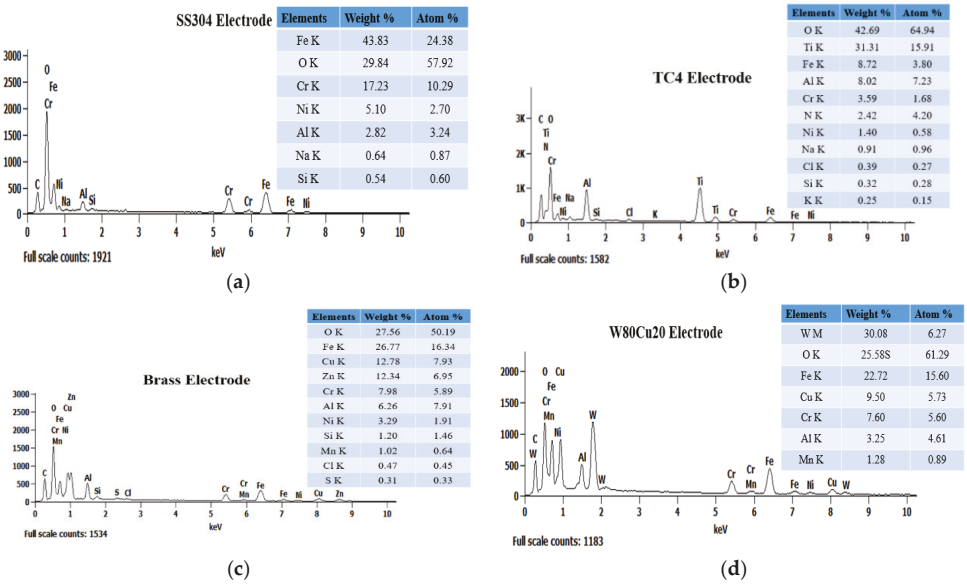

Figure 9. EDX spectrum analysis of four electrodes after ECDM: (**a**) SS304; (**b**) TC4; (**c**) brass; (**d**) W80Cu20.

4.3. MRR, EWR, and OC Machining with W70Cu30, W80Cu20, and W90Cu10 Electrodes

Since tungsten alloy is better than other alloys, W70Cu30, W80Cu20, and W90Cu10 made up of the same elements with different tungsten and copper contents were further investigated. Figure 10 shows the experimental results in order to explain the effects of electrode materials on the MRR and EWR. W70Cu30 has been found to be the most superior among the three electrodes, due to its high electrical conductivity (Figure 10a), and the material removal rate by the W70Cu30 electrode is about 70 μg/s, which is higher than that of the W80Cu20 (59.3 μg/s) and W90Cu10 (45 μg/s). W70Cu30's high conductivity allows for rapid electron flow and heat dissipation on the workpiece. The amount of electric energy lost as electrothermal energy at the tool electrode (W70Cu30) is lower; thus, most of the energy is dissipated on the bulk of the workpiece for eroding the material.

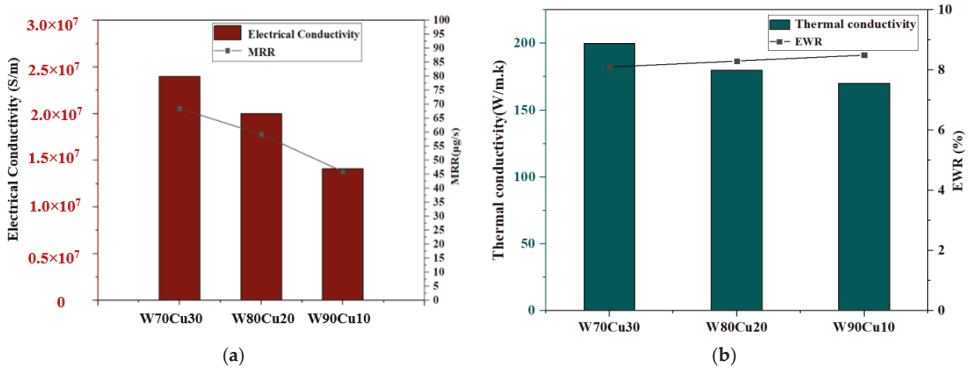

Figure 10. Influence of electrical conductivity and thermal conductivity under machining conditions T_{on} = 12 μs, T_{off} = 12 μs, I_p = 14.17 A; (**a**) MRR and (**b**) EWR for W70Cu30, W80Cu20, and W90Cu10 electrodes.

The W90Cu10 and W80Cu20 electrodes' EWR is higher than W70Cu30, as shown in Figure 10b, with 8.5, 8.3, and 8.1%, respectively. Thermal conductivity is inversely proportional with electrical resistivity, but proportional with electrical conductivity. W70Cu30's low resistivity allows for rapid heat dissipation to the workpiece material, lowering the EWR and improving the tool shape retention. When the tool electrode material's thermal conductivity is high, the electron flow through the material is high; thus, the majority of the heat has dissipated by an electron hitting the workpiece, which is used to melt the particle.

Concerning the geometrical characteristics of holes, the manufacturing process is more accurate when the CuW electrode is used for the overcut (Figure 11), and diameters are lower (Figure 12). From the SEM images (Figure 12) of three CuW electrodes and the machining workpiece hole, the W70Cu30 electrode machining hole diameter (Figure 12a) is 1.1mm, which is lower than the other two holes' diameter, i.e., 1.2 and 1.32 mm (Figure 12b,c), respectively. This occurs on the machining instant, because the edge sparking for W80Cu20 and W90Cu10 appeared more than W70Cu30. The machining time for W80Cu20 and W90Cu10 is also more than W70Cu30. It can be seen from the SEM images of the three-electrode tip and upper body part that the W90Cu10 and W80Cu20 electrodes' surfaces are rougher than that of W70Cu30. Due to large diameter holes processing by W90Cu10 and W80Cu20, the overcut is also higher for these two electrodes (0.1 and 0.16 mm) than W70Cu30 (0.05 mm), as shown in Figure 11. A high thermal diffusivity means that heat moves rapidly through the electrode without damaging it. A lower thermal diffusivity of W80Cu90 and W80Cu20 results in the two electrodes' side sparking between the hole wall and electrode happening more frequently than the tip part, when compared to W70Cu30. Hence, the OC is lower for W70Cu30 than the other two electrodes. When concerning machining complex geometrical materials, choosing suitable electrodes is extremely important. The main reason is that, due to the higher conductivity of W70Cu30, the corner end of the electrode is not more eroded.

It is concluded that the tool's thermal conductivity regulates the amounts of thermal energy extracted from the electrochemical discharge, as well as the temperature variations in the workpiece in front of it, resulting in viscosity changes. As a result, it is likely that the tool's heat conductivity will influence how the drilling progresses. The W70Cu30 acquires a higher thermal conductivity (200 W/m·k.) than the W80Cu20 (180 W/m·k.) and W90Cu10 (170 W/m·k.) electrodes. Subsequently, the lowest EWR is obtained by the W70Cu30 electrode.

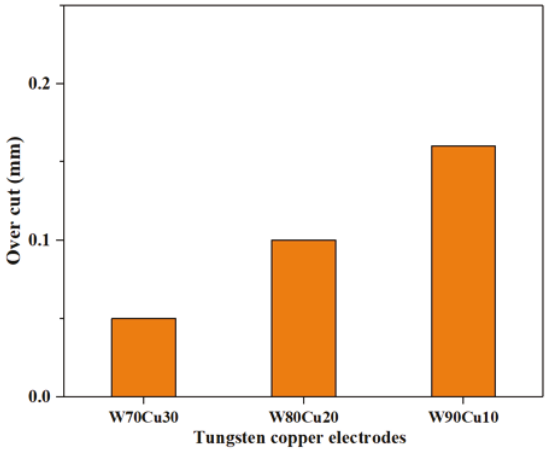

Figure 11. Tungsten–copper tool electrodes' effect on side overcut under machining conditions T_{on} = 12 µs, T_{off} = 12 µs, I_p = 14.17 A.

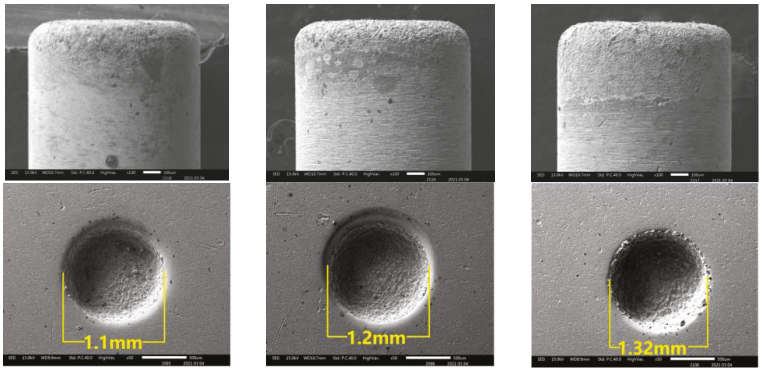

(**a**) W70Cu30 tool (**b**) W80Cu20 tool (**c**)W90Cu10 tool

Figure 12. SEM images of three types of CuW electrodes and discharging phenomena of the hole on SS304 workpiece under machining conditions T_{on} = 12 µs, T_{off} = 12 µs, I_p = 14.17 A.

4.4. Surface Defects on Workpiece and Material Transfer on W90Cu10, W80Cu20, and W70Cu30 Electrodes

SEM and EDX are used to examine the surface topography of machined SS304 alloy workpiece, as seen in Figure 13. The surface produced by various electrode machining on the workpiece with the static fluid machining was covered by pinholes, craters, and a re-solidified layer containing oxidized and hydroxides generated by the ECDM process. W90Cu10 (Figure 13a) and W80Cu20 (Figure 13b) electrodes have contributed to generate more craters and pinholes on the machined surface. As a result of improper thermal energy distribution and the shortage of electrolytes inside the micro-hole during drilling, a limited amount of materials were removed by chemical etching and a generous amount of surface deformities occurred. Furthermore, under the high temperature and rapid cooling process, the unsatisfactory flushing condition affects the removal of the machining by-products, and sections of the machining by-products cohere on the surface. The discharging effect is very poor with higher surface defects, and the W90Cu10 and W80Cu20 electrodes' erosion is high with a lower MRR. The W70Cu30 electrode produces the optimal surface, with the most negligible erosion and the maximum MRR.

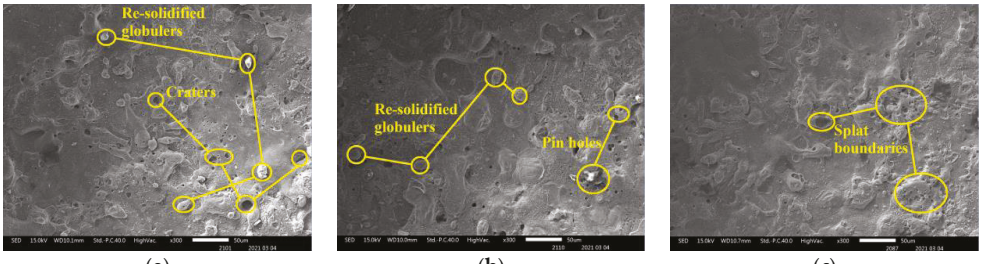

(**a**) (**b**) (**c**)

Figure 13. The surface of SS304 alloy machined by different electrodes: (**a**) W90Cu10; (**b**) W80Cu20; (**c**) W70Cu30.

Figure 14 shows the EDX spectrum analysis results for three different electrodes. The reformulation layer formation mechanism can explain the unexpected oxygen deposition on the electrode surface. High temperatures in the discharge channel cause the melting and evaporation of the metal from the surface during electrical discharge; simultaneously, the electrolyte liquid decomposes into oxygen and hydrogen at these elevated temperatures. Between all of the tungsten–copper electrodes, the W70Cu30 electrode generates the lowest

oxygen layer (24.67%), followed by W80Cu20 (25.58%) and W90Cu10 (26.90%). On the other hand, the W90Cu10, W80Cu20, and W70Cu30 electrodes have the most significant effect on the manganese metal, with W70Cu30 having the least (0.81%) connection. The W70Cu10 electrode has a lower (1.36%) aluminum attachment than the other two electrodes. There was also a lower chromium migration to W70Cu30. Among the three materials studied, W80Cu20 and W90Cu10 have the lowest thermal conductivity and machining instability, and also a higher EWR than W70Cu30. During the ECDM process, the tip part of the two electrodes (W80Cu20 and W90Cu10) had melted more, and other machining zone's particles attached more easily than W70Cu30. As a result, W70Cu30 is the most effective electrode for ECDM.

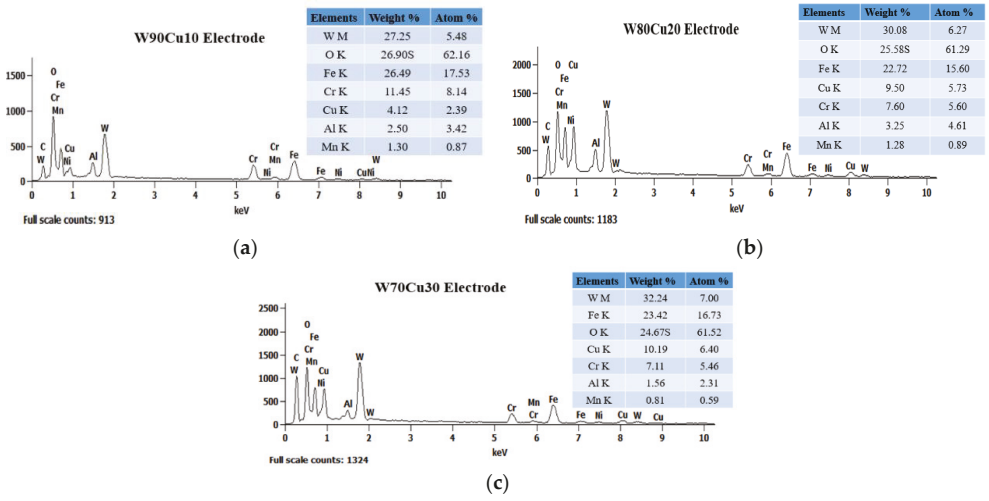

Figure 14. EDX spectrum and material deposition analysis of three electrodes after ECDM process: (**a**) W90Cu10; (**b**) W80Cu20; (**c**) W70Cu30.

It is concluded that the excellent electrical and thermal conductivity of the electrode material promote uniform and effective discharges, enhancing the machined surfaces' nature. Therefore, selecting a tool electrode that is close to the manufacturing or machining process is needed. W70Cu30 is the best electrode, and represents the optimal result in ECDM performances.

5. Conclusions

The selection of the appropriate electrode material is crucial in determining the ECDM performance. In this study, selecting a suitable electrode for the ECDM process has been proposed. Several experimental investigations have been conducted on the corresponding workpiece by the influencing of six different electrode materials, namely TC4, SS304, brass, W80Cu20, W70Cu30, and W90Cu10. Finally, W70Cu30 seems to be well-suited for ECDM, in that it not only achieves a good MRR and suffers the lowest EWR, but also shows the best machining stability. The experimental analysis supports the following inference:

(1) As a result of higher conductivity, the discharge channel forms quickly as the electrical conductivity increases, the discharge delay time decreases, and the discharge energy emitted to the workpiece at the same time increases, resulting in an increase in the MRR. Here, the highest MRR of about 70 μg/s is obtained when using the W70Cu30 electrode over using the other five electrodes;

(2) All CuW electrodes exhibit the lowest EWR, followed by the brass, TC4, and SS304 electrodes. However, among all CuW electrodes, W70Cu30 has shown a lower EWR (8.1%) than the other two electrodes because this electrode has a very high

thermal conductivity. Due to its high thermal conductivity, the heat produced during machining diffuses into the space, decomposing the electrolyte fluids' oxygen at a very high temperature, with some accumulating around the electrode, preventing further electrode erosion;

(3) All CuW electrodes represent the lowest side overcut, followed by the other three electrodes (brass, TC4, and SS304). Among all CuW, W70Cu30 exhibits the least overcut (0.05 mm). W70Cu30 has miniature craters with no cracks and a less rough surface. The unexpected oxygen deposition is the lowest for W70Cu30, followed by the other electrodes. Other material compositions to this electrode are in minimal percentages.

Author Contributions: Conceptualization, I.M.R.; data curation, L.J.; funding acquisition, Y.Z.; investigation, I.M.R. and G.W.; methodology, I.M.R. and T.X.; project administration, Y.Z.; software, K.Z. and L.J.; supervision, Y.Z. and T.X.; writing—original draft, I.M.R.; writing—reviewing and editing, K.Z. and G.W. All authors have read and agreed to the published version of the manuscript.

Funding: This project is supported by the National Natural Science Foundation of China (Grant No. 51705239), Project of Jiangsu Provincial Six Talent Peaks (Grant No. JXQC-009) and the Basic Research Programs of Jiangsu (Grant No. BK20190669).

Data Availability Statement: The data presented in this study are available in this published article.

Conflicts of Interest: The authors declare that the composition has no irreconcilable circumstances. No human members or creatures are engaged with the research. The manuscript has not been submitted to more than one journal for concurrent thought.

References

1. Afzaal, A.; Tanjilul, M.; Rahman, M.; Kumar, A.S. Ultrafast drilling of Inconel 718 using hybrid EDM with different electrode materials. *Int. J. Adv. Manuf. Technol.* **2020**, *106*, 2281–2294.
2. L'uboslav, S.; Slavomíra, H. Optimization of material removal rate and tool wear rate of Cu electrode in die-sinking EDM of tool steel. *Int. J. Adv. Manuf. Technol.* **2018**, *97*, 2647–2654.
3. Rahul; Dileep, K.M.; Saurav, D.; Manjol, M. Effects of Tool Electrode on EDM Performance of Ti-6Al-4V. *Silicon* **2018**, *10*, 2263–2277. [CrossRef]
4. Munmun, B.; Kalipada, M. Effect of different tool materials during EDM performance of titanium grade 6 alloy. *Int. J. Eng. Sci. Technol.* **2018**, *21*, 507–516.
5. Pilligrin, J.C.; Asokan, P.; Jerald, J.; Kanagaraj, G. Effects of electrode materials on performance measures of electrical discharge micro-machining. *Mater. Manuf. Process.* **2017**, *33*, 606–615. [CrossRef]
6. D'Urso, G.; Maccarini, G.; Quarto, M.; Ravasio, C. Investigation on power discharge in micro-EDM stainless steel drilling using different electrodes. *J. Mech. Sci. Technol.* **2015**, *29*, 4341–4349. [CrossRef]
7. Sahu, A.K.; Mahapatra, S.S. Comparison of performance of different tool electrodes during electrical discharge machining. *Int. J. Eng. Mater. Sci.* **2019**, *26*, 186–199.
8. Anna, T.W.; Krzysztof, W. Multifilament carbon fibre tool electrodes in micro EDM-evaluation of process performance based on influence of input parameters. *Int. J. Adv. Manuf. Technol.* **2017**, *91*, 3737–3747.
9. Renu, K.S.; Chinmaya, P.M. Sustainable Electrical Discharge Machining of Nimonic C263 Superalloy. *Arab. J. Sci. Eng.* **2021**. [CrossRef]
10. Saini, G.; Manna, A.; Singh Sethi, A. Investigations on performance of ECDM process using different tool electrode while machining e-glass fibre reinforced polymer composite. *Mater. Today Proc.* **2020**, *28*, 1622–1628. [CrossRef]
11. Phan, N.H.; Dong, P.V.; Dung, H.T.; Thien, N.V.; Muthuramalingam, T.; Shirguppikar, S.; Tam, N.C.; Ly, N.T. Multi-object optimization of EDM by Taguchi-DEAR method using AlCrNi coated electrode. *Int. J. Adv. Manuf. Technol.* **2021**, *116*, 1429–1435. [CrossRef]
12. Chandrashekarappa, M.P.G.; Kumar, S.; Jagadish; Pimenov, D.Y.; Giasin, K. Experimental Analysis and Optimization of EDM Parameters on HcHcr Steel in Context with Different Electrodes and Dielectric Fluids Using Hybrid Taguchi-Based PCA-Utility and CRITIC-Utility Approaches. *Metals* **2021**, *11*, 419. [CrossRef]
13. Saodaen, R.; Janmanee, P.; Rodchanarowan, A. Characteristics of Ternary Metal (Cu-Ni-TiN) Electrodes Used in an Electrical Discharge Machining Process. *Metals* **2021**, *11*, 694. [CrossRef]
14. Prakash, C.; Singh, S.; Pruncu, C.I.; Mishra, V.; Królczyk, G.; Pimenov, D.Y.; Pramanik, A. Surface Modifification of Ti-6Al-4V Alloy by Electrical Discharge Coating Process Using Partially Sintered Ti-Nb Electrode. *Materials* **2019**, *12*, 1006. [CrossRef]
15. Han, Y.; Liu, Z.; Cao, Z.; Kong, L.; Qiu, M. Mechanism study of the combined process of electrical discharge machining ablation and electrochemical machining in aerosol dielectric. *J. Mater. Process. Technol.* **2018**, *254*, 221–228. [CrossRef]

16. Julfekar, A.; Karan, P.; Pradeep, D. Effect of tool-electrode material in through-hole formation using ECDM process. *Mater. Manuf. Process.* **2021**, *36*, 1019–1027. [CrossRef]
17. Mousa, M.; Allagui, A.; Ng, H.D.; Wuthrich, R. The Effect of Thermal Conductivity of the Tool Electrode in Spark-Assisted Chemical Engraving Gravity-Feed Micro-Drilling. *J. Micromech. Microeng.* **2009**, *19*, 015010. [CrossRef]
18. Yang, C.K.; Cheng, C.P.; Mai, C.C.; Wang, A.C.; Hung, J.C.; Yan, B.H. Effect of Surface Roughness of Tool Electrode Materials in ECDM Performance. *Int. J. Mach. Tools Manuf.* **2010**, *50*, 1088–1096. [CrossRef]
19. Zhang, C.; Xu, Z.; Hang, Y.; Xing, J. Effect of solution conductivity on tool electrode wear in electrochemical discharge drilling of nickel-based alloy. *Int. J. Adv. Manuf. Technol.* **2019**, *103*, 743–756. [CrossRef]
20. Gupta, P.K.; Dvivedi, A.; Kumar, P. Developments on electrochemical discharge machining: A review of experimental investigations on tool electrode process parameters. *Proceed. Inst. Mech. Eng. Part B J. Eng. Manuf.* **2014**, *229*, 910–920. [CrossRef]
21. Dileep, K.M.; Rahul; Saurav, D.; Manoj, M.; Siba, S.M. Through hole making by electro-discharge machining on Inconel 625 super alloy using hollow copper tool electrode. *Proceed. Inst. Mech. Eng. Part E J. Process. Mech. Eng.* **2019**, *233*, 348–370.

micromachines

MDPI

Article

Simulation Analysis of Cluster Effect of High-Shear Low-Pressure Grinding with Flexible Abrasive Tools

Chengjin Tian [1], Jinguo Han [1,2], Yebing Tian [1,2,*], Bing Liu [1], Zhiqiang Gu [1] and Xintao Hu [1]

[1] School of Mechanical Engineering, Shandong University of Technology, Zibo 255049, China; zbtiancj@163.com (C.T.); hankeyee@163.com (J.H.); liub384444503@163.com (B.L.); dezay520@163.com (Z.G.); 17853311158@163.com (X.H.)
[2] Institute for Advanced Manufacturing, Shandong University of Technology, Zibo 255049, China
* Correspondence: tianyb@sdut.edu.cn

Abstract: Based on the clustering effect of shear-thickening fluids (STFs), a high-shear low-pressure flexible grinding wheel has been developed. In order to explore the material removal mechanism, the coupled Eulerian—Lagrangian (CEL) method is adopted to simulate the novel grinding process. The simulation results show that particle clustering effects do occur at the tangential and bottom positions of the micro-convex peak when it instantaneously strikes the workpiece surface. The particle clusters drive the harder abrasive particles to resist the strong interactions of micro-convex peaks. The micro-convex peaks are removed due to the cutting effect of the harder abrasive particles. Compared with traditional grinding, the ratio of tangential force to normal force for the high-shear low-pressure flexible grinding wheel is improved. The various trends in force ratio are consistent with the experimental results, which verifies the effectiveness of high-shear low-pressure grinding.

Keywords: flexible grinding; shear thickening fluid; cluster effect; high-shear low-pressure

Citation: Tian, C.; Han, J.; Tian, Y.; Liu, B.; Gu, Z.; Hu, X. Simulation Analysis of Cluster Effect of High-Shear Low-Pressure Grinding with Flexible Abrasive Tools. *Micromachines* **2021**, *12*, 827. https://doi.org/10.3390/mi12070827

Academic Editors: Jiang Guo, Chunjin Wang and Chengwei Kang

Received: 8 June 2021
Accepted: 11 July 2021
Published: 15 July 2021

Publisher's Note: MDPI stays neutral with regard to jurisdictional claims in published maps and institutional affiliations.

1. Introduction

With the continuous development of science and technology, an increasing number of difficult-to-process materials with excellent performance have appeared in the aerospace industry, medical equipment manufacturing, automobile manufacturing, precision manufacturing and other industries [1–4]. Due to the improvement in requirements for material quality and surface accuracy within these industries, some difficult-to-process materials require further processing before they can be used. Grinding is the most widely used precision and ultra-precision processing technology, and is commonly employed in the aerospace industry, precision manufacturing and other fields [5–8]. Grinding is a multi-edge composite cutting technology. The large negative rake angle and the arc radius of the cutting edge drive elastic deformation of the surface of the workpiece [9]. As the cutting depth continues to increase, the surface of the workpiece will form abrasive debris along the cutting direction, which will fall away from the surface of the workpiece. A grain interacts with the workpiece in three stages of material deformation, i.e., sliding, ploughing, and cutting [10]. It is well known that the grinding force plays an important role in the grinding process, and can be divided into the tangential grinding force, normal grinding force and axial grinding force. Generally, the normal grinding force is 2–3 times larger than the tangential grinding force in the traditional grinding process [11]. For aerospace parts and hard-brittle composite materials, this ratio can increase to hundreds of times, which makes the process prone to a series of grinding problems such as grinding cracks, grinding burns, surface and subsurface defects, etc. [12].

In response to the aforementioned problems, many scholars have developed various new grinding wheels, such as the ordered abrasive grain grinding wheel [13], the grooved grinding wheel [14] and the single-layer brazing grinding wheel [15]. Both the grooved

grinding wheel and the ordered grinding wheel can improve processing quality and reduce the normal grinding force. However, the grooved grinding wheel will affect the smoothness of its processing due to its non-continuous surface characteristics. Additionally, the ordered abrasive grain grinding wheel is still in the early stage of research, which means that the abrasive grain arrangement efficiency is relatively low. Compared with traditional grinding wheels, single-layer brazing grinding wheels have many advantages. Nevertheless, the grinding working layer is relatively thin, which means that the service life is relatively short. Zhang et al. [16] developed a diamond grinding wheel with a structured surface. Through the grinding of zirconia ceramic parts, it was found that the new surface-textured diamond grinding wheel forms a coolant film during the grinding movement to improve the quality of the processed table and reduce the grinding force. Wu et al. [17] developed a combined brazed diamond sheets and original resin grinding wheel. The experimental results showed that with increasing working load, the wear rate of the brazing sheet increased and the grinding ratio decreased. In addition, the temperature rose faster. Teicher et al. [18] used a single-layer fiber-welded grinding wheel to perform grinding experiments on titanium alloys. The grinding quality improved when the alkaline grinding fluid was added. Tian et al. [19] used selective laser melting to design metal-bonded diamond grinding wheels, where both improved surface roughness and reduced work hardening were achieved in comparison to electroplated wheels. Tour et al. [20] investigated a grinding wheel made of carbon-fiber-reinforced plastic (CFRP). In comparison with traditional steel wheels with different fiber directions, CFRP wheels have higher anti-vibration stability. Although the grinding wheel made of CFRP can reduce the centrifugal force and thermal stress deformation, the production cost of the CFRP grinding wheel is relatively high. The aforementioned grinding tools are characterized as consolidated abrasive grinding wheels. They have been verified as insufficiently processing some complex profiles. Therefore, great efforts are underway to develop compliant abrasive technologies with enhanced self-adaptability of grinding tools. Islam [21] and Becaucamp [22] developed a bonnet-polishing method based on an elastic tool, which can adapt to the flat surface and freeform better. With further development of compliant abrasive technologies, Walker et al. [23] proposed a shape adaptive grinding (SAG) method using a fabric sheet deposited with diamond grains. The surface roughness was reduced to less than 2 nm. At present, compliant abrasive technologies have become one of the most promising methods for complex profile finishing.

In previous work [5,7], we used STF-Kevlar composite materials with abrasive grains to make a flexible grinding wheel. However, it was difficult to verify the grinding mechanism of the developed high-shear low-pressure flexible grinding wheel in experiments. Thus, the simulation method was adopted to explore the grinding mechanism of the high-shear low-pressure flexible grinding with the flexible STF-Kevlar composited wheel. The processing model of the high-shear low-pressure flexible grinding was simplified as micro-convex peaks impacting the surface of the flexible grinding wheel. Many researchers have already explored the STF-Kevlar composite materials through simulation. Sen et al. [24] used CEL to explore the impact resistance of Kevlar-STF composites. The simulation results showed that the lateral deformation, energy distribution, etc., of the Kevlar-STF composite materials were significantly improved compared with the current multi-layer pure Kevlar. The viscosity of the STF consumed approximately 75% of the energy. Mahdi et al. [25] used LS-DYNA to simulate the impact of Kevlar impregnated with STF. The effect of STF on Kevlar fiber was simulated by changing the friction coefficient of Kevlar warp and weft yarn. Moreover, the friction coefficient of Kevlar fiber and impact body was also changed. The simulation results showed that the Kevlar impregnated with STF improved the friction coefficient between the yarns, thereby improving the impact resistance of the Kevlar fiber. Lu et al. [26] explored the impact properties of warp knitted spacer fabrics (WKSFs) impregnated with STF by simulation. The simulation results showed that the energy absorption of WKSF/STF composite materials occurred in the thickening stage of STF and the friction between yarns. In this paper, the CEL method was

adopted to simulate the grinding process and explore the cluster effect of STF. The simulation results showed that, due to the instantaneous impact of the micro-convex peaks on the surface of the workpiece, particle cluster effects are likely to occur at the tangential and bottom positions of the micro-convex peaks. Compared with traditional grinding, the ratio of tangential force to normal force of the high-shear low-pressure grinding is improved.

2. Principle of High-Shear and Low-Pressure Grinding

To address the problem that the ratio of tangential grinding force to normal force is too large, this paper developed a high-shear low-pressure flexible grinding wheel. The high-shear low-pressure flexible grinding wheel was made by adding shear thickening fluid to Kevlar fiber. Some dispersed phase nanoparticles were also mixed. The mechanism of the shear thickening cluster effect is shown in Figure 1. Generally, shear-thickening fluids are liquid when in a balanced state. However, when suffering an instantaneous impact, the shear rate increases rapidly. The dispersed phase particles will undergo localized thinning. As the shear rate increases, dispersed phase nanoparticles will quickly aggregate to produce a cluster effect and further form a particle cluster effect. The instantaneous impact makes the shear thickening flow fluid instantaneously turn into a solid-like state to absorb the impact kinetic energy. A new type of flexible grinding wheel was fabricated in this research by employing the cluster effect of the shear thickening fluid. Figure 2 illustrates the composition of flexible grinding where dispersed medium, dispersed phase, Kevlar fiber, abrasive particles, and additives are included.

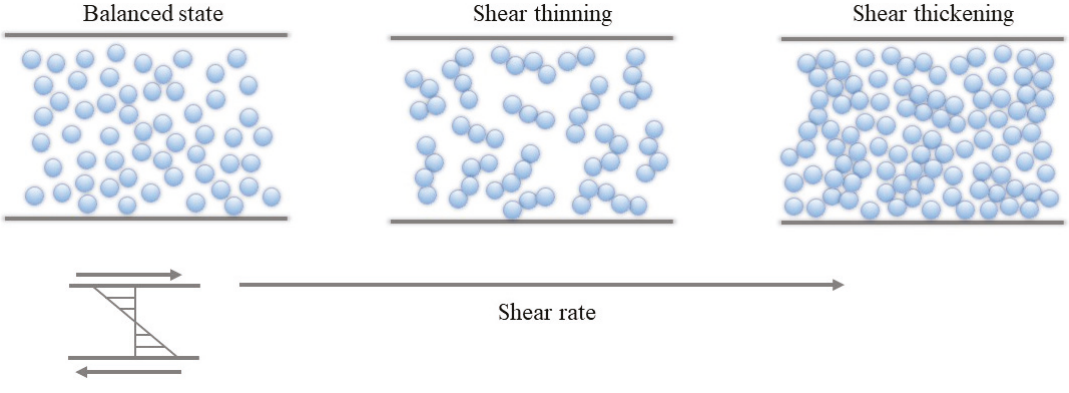

Figure 1. The mechanism of shear-thickening cluster effect.

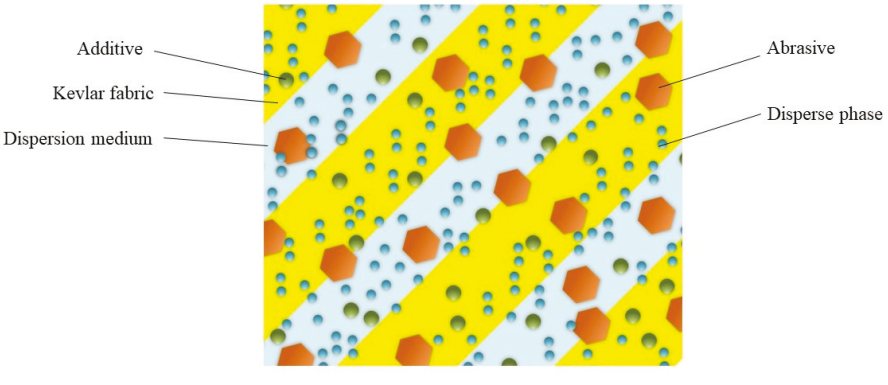

Figure 2. Composition of the high-shear low-pressure grinding wheel.

The processing principle of the high-shear low-pressure flexible grinding wheel is shown in Figure 3. The experimental setup is introduced by Figure 3a. The high-shear low-pressure flexible grinding wheel is loaded on the fixture. the workpiece is fixed and impacts the high-shear low-pressure flexible grinding wheel. The dynamometer is used to monitor the grinding force and indicate the force ratio. In the initial stage of processing, as shown in Figure 3b, the dispersed phase and abrasive particles are uniformly dispersed in the shear-thickening liquid. In Figure 3c, when the grinding wheel touches the micro-convex peaks, the micro-convex peaks produce an instantaneous impact on the grinding wheel and break the balance state. Subsequently, the shear rate increases and the dispersed phase nanoparticles quickly aggregate to form a cluster. The viscosity of the fluid continues to increase, showing a solid-like state. At the same time, the abrasive particles are quickly gathered by the dispersed phase nanoparticles, so that a large number of abrasive particles collide with the micro-convex peaks to achieve the purpose of material removal. In the recovery stage of Figure 3d, the micro-convex peaks are removed. The impact load on the surface of the flexible abrasive grinding wheel disappears. At this time, the dispersed phase nanoparticles are rapidly dispersed into the dispersion medium. The cluster effect is continuously weakened and the viscosity continues to decrease. The abrasive particles are also uniformly dispersed in the dispersion medium along with the dispersed phase nanoparticles. As the grinding process continues, this process proceeds cyclically to achieve material removal.

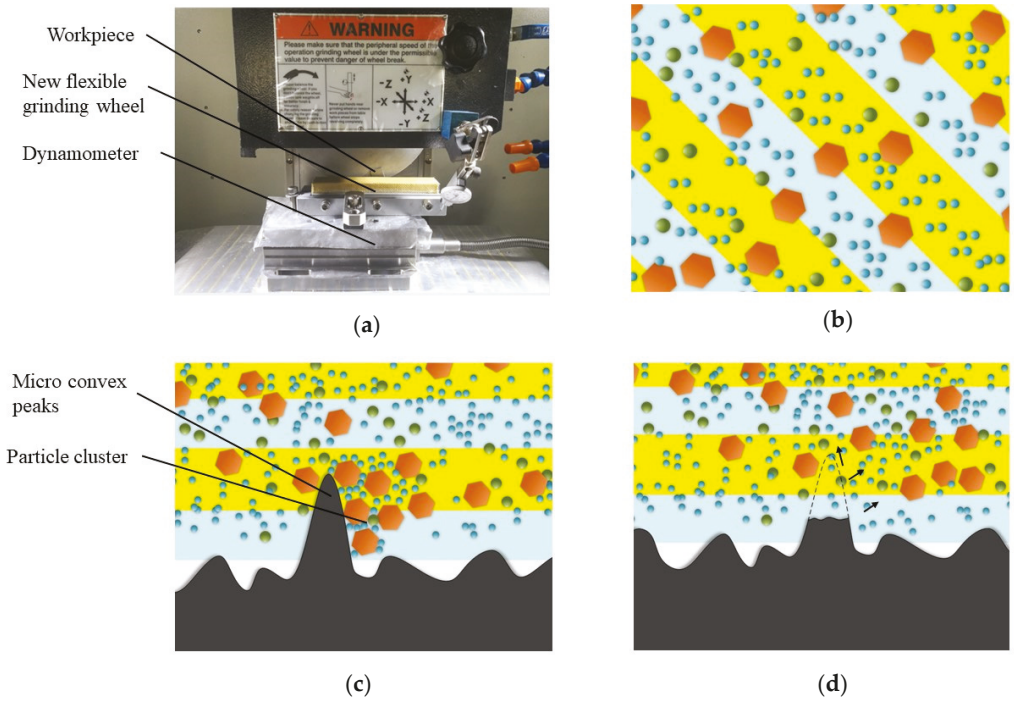

Figure 3. The processing principle of the high-shear low-pressure flexible grinding wheel. (**a**) Experimental setup. (**b**) High-shear low-pressure flexible abrasive grinding wheel in balanced state. (**c**) High-shear low- pressure flexible grinding wheel contact the workpiece and cluster effect occurs. (**d**) The micro-convex peaks are removed and return to the initial state.

3. Numerical Simulation Model

3.1. STF Model Establishment and Material Parameter Definition

The processing model of the high-shear low-pressure flexible grinding is simplified, as micro-convex peaks impact the surface of the flexible grinding wheel. Due to the short impact time of the model, it can be regarded as a transient explicit dynamic simulation and must be adapted to the large deformation of the STF. The CEL technology combining Lagrangian and Eulerian grids is mostly used for fluid–structure coupling analysis. The model of STF grinding is regarded as a fluid–solid coupling model. STF usually exhibits large motion deformation under low viscosity. Therefore, CEL technology is used to simulate the high-shear low-pressure flexible grinding wheel. The Mie-Grüneisen equation of state (EOS) is used to define its viscosity state. Abrasive particles are added to the STF to study the cluster effect of STF and the influence of grinding force. The Mie–Grüneisen equation of state (EOS) describing the behavior of STF fluid is shown below:

$$p = \frac{\rho_0 C_0^2 x}{(1-sx)^2}\left(1 - \frac{\Gamma_0 x}{2}\right) + \Gamma_0 E \tag{1}$$

where p is the pressure, C_0 is the speed of sound through the medium, ρ_0 is the initial density, ρ is the current density, $x = \left(1 - \frac{\rho_0}{\rho}\right)$, $s = dU_s\ /dU_p$ is a linear Hugoniot slope coefficient, Γ_0 is material constant, U_s is the shock wave transmission speed and U_p is the particle speed. In ABAQUS, the fluid behavior of STF can be defined by the U_s-U_P state equation. Table 1 shows the material parameters of STF [24].

Table 1. Material parameters for STF.

Density (kg/m^3)	C_0(m/s)	s	Γ_0
2722	2100	3.75	0.8

Due to the fluid characteristics of STF itself, it cannot be analyzed in a traditional way. This simulation adopts the method of CEL analysis. Eulerian analysis is used to fix the Eulerian grid so the material can flow freely within it. In each time increment, the proportion of the grid occupied by the material is calculated as shown in Figure 4. If the material completely occupies the grid, EVF = 1, and if the material does not occupy the grid, it is 0.

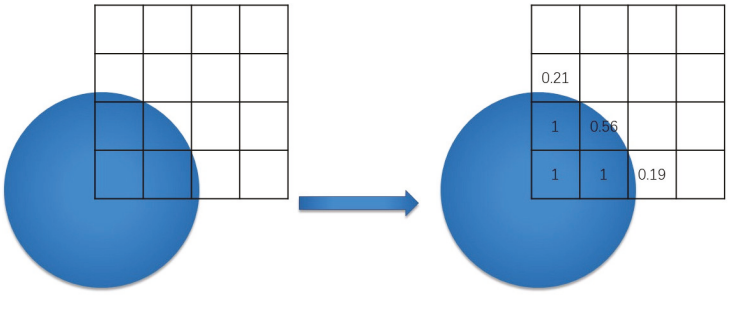

Figure 4. Principle of Eulerian Analysis.

In our experiments, a non-Newtonian fluid was prepared by PEG200 and SiO_2. PEG200 and 15% mass fraction of SiO_2 were mixed in a 60 °C oil bath and abrasive grains were added. The rheological performance of PEG200/SiO_2 non-Newtonian fluid was tested and the result was shown in Figure 5.

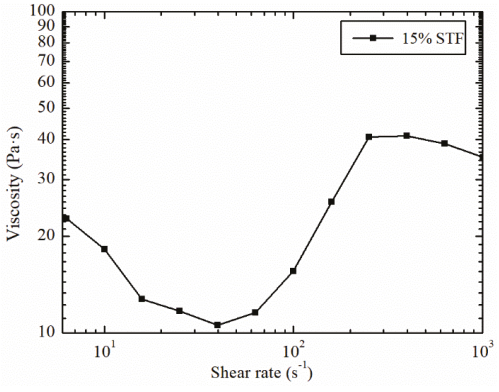

Figure 5. Rheological performance of 15% mass fraction STF.

It can be seen from Figure 5 that as the shear rate continues to increase, the shear-thickening effect is gradually strengthened, reaching a peak viscosity of 41.1 Pa·s. According to the literature [24], the impact velocity can be divided by the diameter of the micro-convex peak. Therefore, the shear rate of the micro-convex peaks to the composite model can be roughly measured. It is estimated that the lowest shear rate (5000 s^{-1}) is much higher than the shear rate (400 s^{-1}) of the peak viscosity in Figure 5, so the viscosity of STF is set at 40 Pa·s. At the same time, different viscosity gradients (10 Pa·s, 20 Pa·s, 30 Pa·s) are used for comparison. These assumed constant viscosity values at higher strain rates are considered independent of impact velocity.

3.2. High-Shear Low-Pressure Flexible Grinding Wheel Composite Model

In finite-element simulation, a good model can not only ensure the accuracy of the simulation, but also save time. Different from traditional impact simulation [24–26], small balls of different sizes are used to simulate the micro-convex peaks and abrasive particles. Compared with the abrasive grains, the hardness of the micro-convex peaks is relatively soft. The abrasive particles and the micro-convex peaks continuously interact to achieve the purpose of material removal. The micro-convex peaks and abrasive grains are modeled by Lagrangian. The element types of the micro-convex peaks and abrasive grains are both C3D8R. In order to accurately and quickly explore the clusters effect on the high-shear low-pressure flexible grinding wheel, the micro-convex peak is set as a rigid body. In addition, the material of abrasive and micro-convex peak are white corundum and steel. The STF is simplified to a rectangular model by Eulerian, and the element type is EC3D8R. At the same time, the overall model is enlarged in order to avoid the problem of the simulation not being easy to converge due to its small scale. Figure 6 is the high-shear low-pressure flexible grinding wheel composite model. The outermost layer is the established Eulerian body. The established Eulerian body is defined in two layers, and the uppermost layer does not specify any material (equivalent to an air layer). The established micro-convex peak model is embedded into it, the lower layer is defined as STF, and abrasive particles are added to the STF. In the actual processing process, abrasive particles are randomly added to the STF, so the established model also adopts a random distribution of abrasive particles. The impact angle and speed are 45 degrees and 100 m/s, respectively.

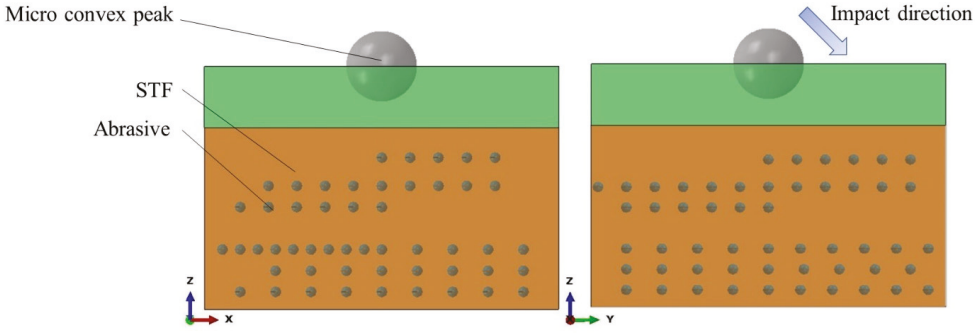

Figure 6. High-shear low-pressure flexible grinding wheel composite model.

4. Results and Discussion

4.1. Simulation Analysis of Cluster Effect

Figure 7 shows a cross-sectional view of particle clustering under 40 Pa·s viscosity. It can be seen that when the micro-convex peak made contact with the STF, the surface of the STF fluctuated due to the impact. However, due to its high viscosity, the splashed STF jet did not disperse. As the impact of the micro-convex peak continued to deepen, an air cavity was formed in the path of the impact of the micro-convex peaks. The abrasive particles began to make contact with the micro-convex peak, and gradually created a particle clustering effect. The particle clusters drove the abrasive particles to accumulate in the tangential direction and bottom of the micro-convex peak, so that the micro-convex peak and the aggregated abrasive particles were continuously in contact. Eventually, this achieved the purpose of removing the micro-convex peak.

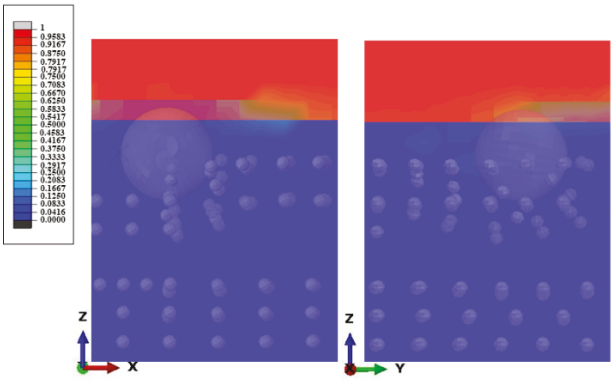

Figure 7. The sectional view of particle clustering under 40 Pa·s viscosity.

Figure 8 shows the results of particle clusters at 40 Pa·s, 30 Pa·s, 20 Pa·s, 10 Pa·s viscosities. It can be seen from the figure that the surface of the STF also fluctuated due to the impact after the micro-convex peak made contact with the STF. However, the fluctuation height was different under different viscosities. The highest jet of STF occurred at a viscosity of 10 Pa·s, and the lowest at 40 Pa·s. The particles under different viscosities had a clustering effect, which made the abrasive particles agglomerate. However, the particle clustering at the impact of 40 Pa·s viscosity was more concentrated. This shows that the higher the viscosity, the more obvious the clustering effect of particles, which can achieve a good material removal effect. In the existing literature, the theories explaining the shear thickening behavior of STF mainly include order–disorder theory [27] and particle cluster theory [28]. Both theories discuss the shear-thickening behavior from the microscopic

particle scale. According to the theory of fluid mechanics, the shear-thickening behavior is due to the mutual dynamic lubrication between particles [29]. When the STF is instantaneously impacted, the shear force in the STF increases instantaneously, causing the dispersed particles to collide with each other. The dynamic pressure in the fluid increases instantaneously, which manifests as an instantaneous increase in the macroscopic viscosity of the STF.

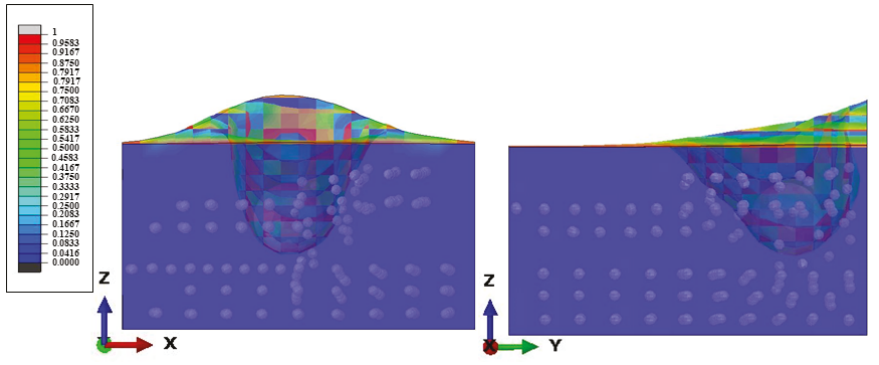

(**a**)

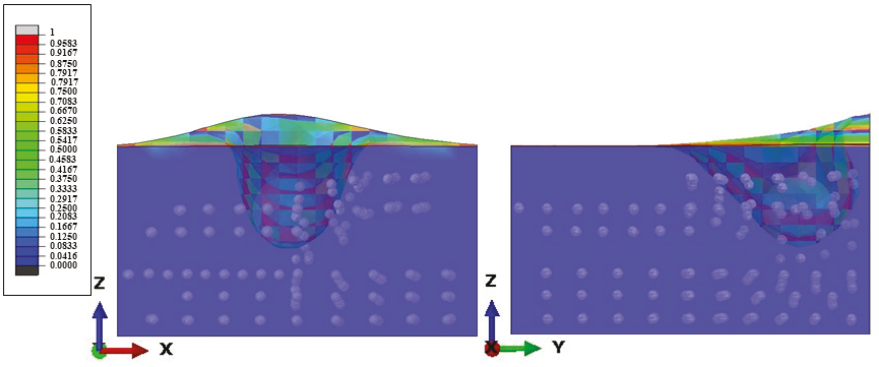

(**b**)

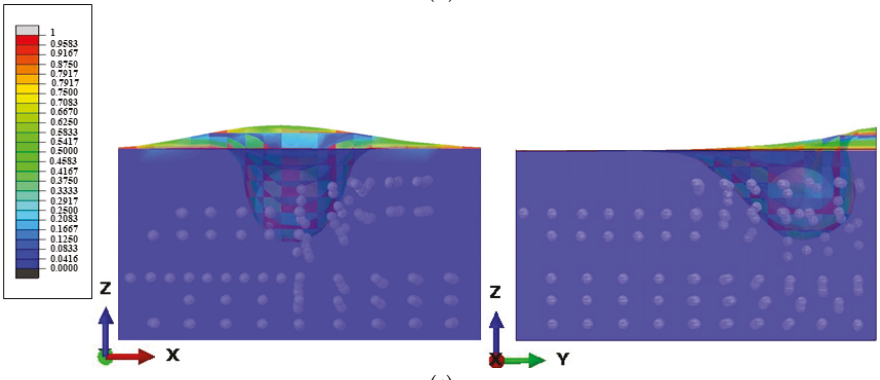

(**c**)

Figure 8. *Cont.*

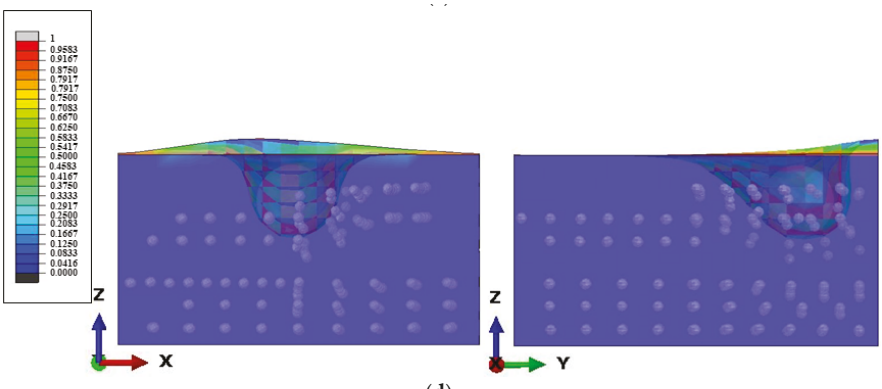

(**d**)

Figure 8. Particle clustering effect under (**a**) 10 Pa·s viscosity, (**b**) 20 Pa·s viscosity, (**c**) 30 Pa·s viscosity, (**d**) 40 Pa·s viscosity.

4.2. Analysis of Tangential Grinding Force and Normal Grinding Force

In the grinding process, the grinding force has a vital influence on the grinding quality and grinding efficiency. In traditional grinding, the normal force is usually 2–3 times larger than the tangential force [11,30,31]. The clustering effect of STF can cause abrasive particles to gather at the tangential position under the tangential impact. Compared with the normal force, the tangential force has a more obvious increase, which improves the force ratio of tangential force to normal force to achieve the effect of high-shear low-pressure. Figure 9 is the numerical values of normal force and tangential force under different viscosities. It can be seen from Figure 9 that the tangential force and the normal force reach their peak values at 0.0003–0.00035 s. Moreover, the peak values of the tangential force and the normal force are not very different under each viscosity. As time goes by, the tangential force and the normal force gradually decrease. However, a convex peak appeared at a viscosity of 20 Pa·s, which is caused by the extrusion and collision of some abrasive grains on the micro-convex peak. The average value of the tangential force and the normal force under each viscosity was stable at 2000–3000 N. In addition, the tangential force and the normal force show a periodic upward and downward trend. In the early stage of impact, the peak values of the tangential force and the normal force at each viscosity are relatively small and stable at 3800 N. As the impact continues to deepen, abrasive particles increasingly gather at the tangential and bottom positions of the micro-convex peak. The abrasive particles continuously collide with the micro-convex peak, resulting in an increase in the peak values of tangential force and normal force. At the end of the impact, due to the continuous action of the clustering effect, the kinetic energy of the micro-convex peaks is continuously reduced. Finally, the degree of collision and extrusion with the abrasive particles is reduced.

In order to analyze the effect of the high-shear low-pressure flexible grinding wheel more intuitively and accurately, the ratio of the tangential force to the normal force at each time point is plotted, as shown in Figure 10. The ratio of the tangential force to the normal force at each viscosity is mostly greater than 0.33 (the position of the red dotted line in the Figure 10). The peak force ratio of some viscosities reach 2.5–3.2. Moreover, the average value of the force ratio reaches the maximum value of 0.82 at 40 Pa·s. The simulation results were compared with the experimental results of Tian and Li [32]. Under the experimental conditions, the ratio of the tangential force to the normal force under the pure Kevlar fiber grinding condition is 0.357, and the ratio of the tangential force to the normal force is increased to 1.055 by adopting the high-shear low-pressure flexible grinding wheel. The tangential force and the normal force ratio trend are consistent with the experimental results, which verifies the effectiveness of high-shear low-pressure grinding. The results show that STF can produce a clustering effect when subjected to a high-speed impact,

which make the dispersed phase particles agglomerate in large numbers from a micro perspective. From a macro perspective, the high-shear low-pressure flexible grinding wheel can effectively increase the force ratio between the tangential force and the normal force.

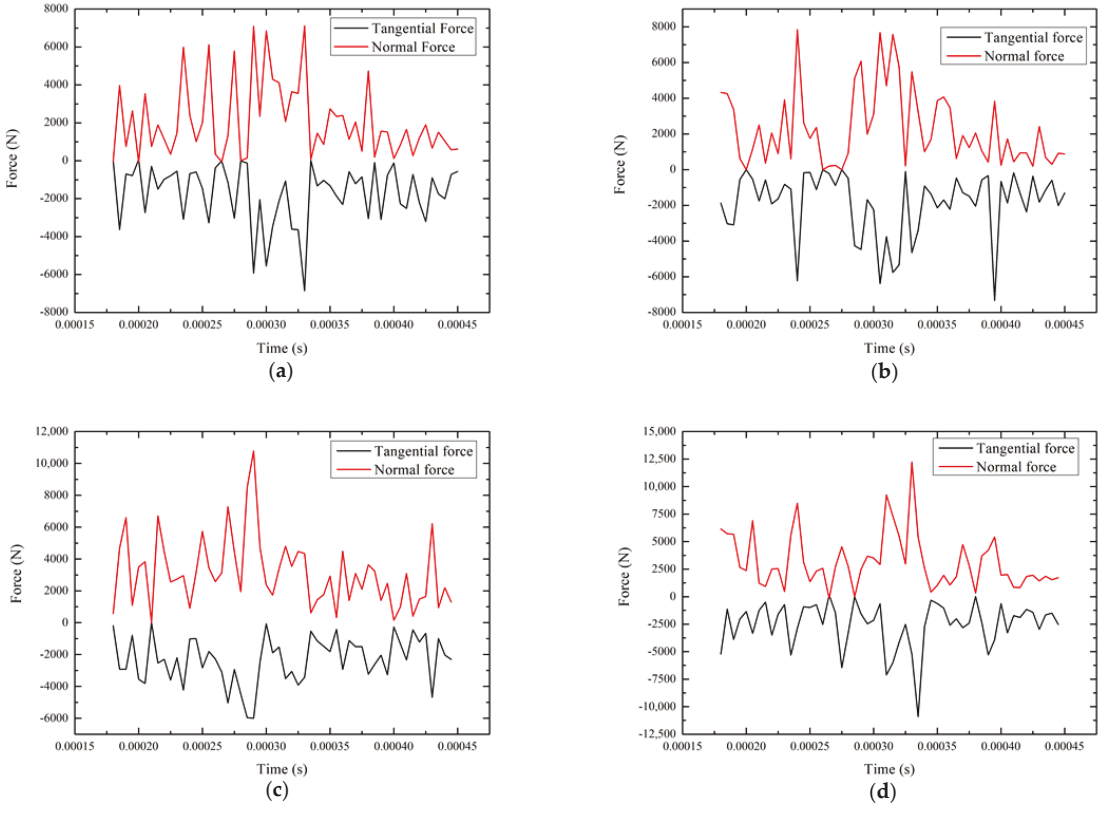

Figure 9. Normal force and tangential force values under different viscosities (**a**) 10 Pa·s viscosity, (**b**) 20 Pa·s viscosity, (**c**) 30 Pa·s viscosity, (**d**) 40 Pa·s viscosity.

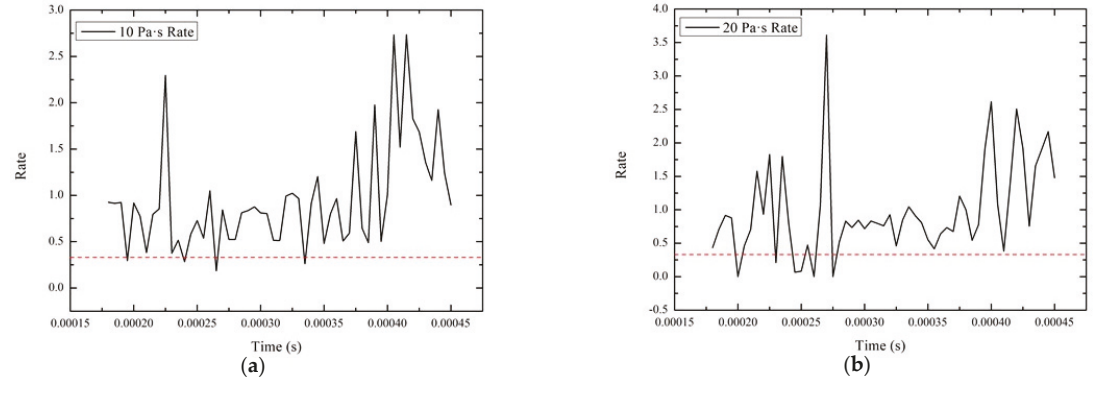

Figure 10. *Cont.*

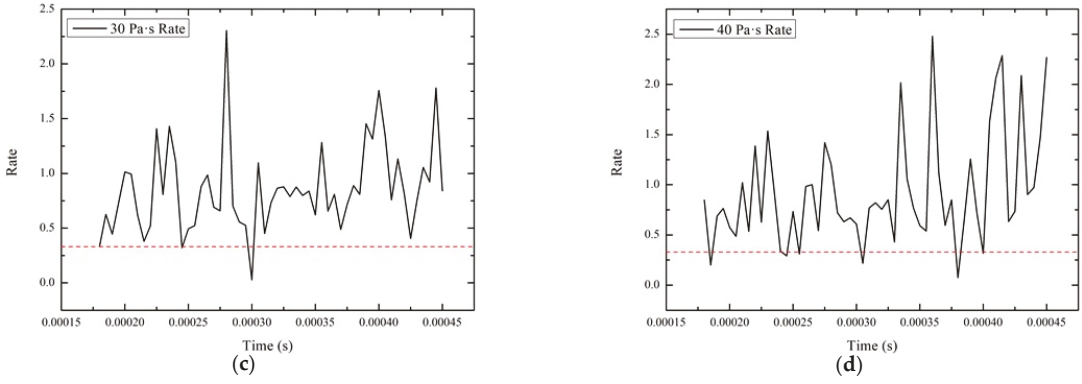

Figure 10. Force ratio of the tangential force to the normal force under different viscosities (**a**) 10 Pa·s viscosity, (**b**) 20 Pa·s viscosity, (**c**) 30 Pa·s viscosity, (**d**) 40 Pa·s viscosity.

4.3. Speed Analysis

The clustering effect of STF can not only bring about the high-shear low-pressure grinding effect, but can also absorb the impact kinetic energy of the micro-peaks and reduce the impact speed of the micro-convex peak. The speed changes at different viscosities are shown in Figure 11. Due to the clustering effect of STF, the speed of the micro-convex peak decreases significantly, which indicates that the kinetic energy absorption effect of STF is more significant. The speed changes rate between the viscosities of 10 Pa·s and 20 Pa·s is large. However, the rate between the viscosities of 20 Pa·s and 30 Pa·s is relatively small. As the viscosity increases, the rate of speed change gradually increases. The biggest rate is between the viscosities of 30 Pa·s and 40 Pa·s. When the viscosity is 40 Pa·s, the rate of speed change reaches the maximum. As the impact energy of the micro-convex peak on the STF gradually fades, the cluster effect gradually disappears, and the aggregation effect of the abrasive particles also slowly dissipates. Therefore, the decrease in the speed of the micro-convex peak starts to slow down after 0.00035 s.

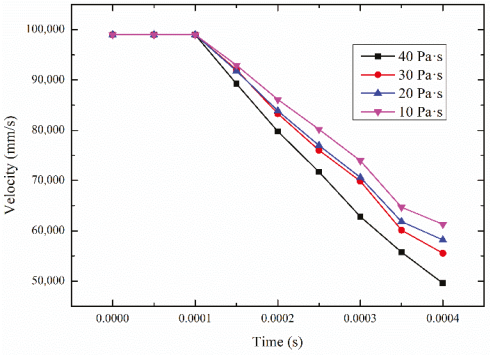

Figure 11. Speed changes rate in different viscosities.

5. Conclusions

In order to explore the grinding mechanism of the high-shear low-pressure flexible grinding wheel developed here, the processing model of the high-shear low-pressure flexible grinding wheel was simplified as micro-convex peaks impacting the surface of the flexible grinding wheel. The CEL method was adopted for modeling and analysis. The STF was modeled by Eulerian, and the abrasive particles was modeled by Lagrangian. The abrasive grains were embedded in the STF.

Simulation results showed that when the STF is impacted by the micro-convex peak, a cluster effect occurs in the tangential direction and at the bottom. Abrasive particles then quickly gather. The ratio of the tangential force to the normal force during the grinding process was approximately 0.82, which is much higher than the ratio in the traditional grinding process. These results show that the flexible grinding wheel has a good high-shear low-pressure grinding effect.

Author Contributions: Conceptualization, C.T. and J.H.; methodology, C.T. and J.H.; software, C.T.; validation, C.T., J.H. and B.L.; formal analysis, C.T.; investigation, C.T.; resources, Y.T.; data curation, C.T. and Z.G.; writing—original draft preparation, C.T.; writing—review and editing, C.T., J.H., Y.T.; visualization, C.T. and X.H.; supervision, Y.T.; project administration, Y.T.; funding acquisition, Y.T. All authors have read and agreed to the published version of the manuscript.

Funding: This research was funded by National Natural Science Foundation of China, grant number 51875329 and 51905322; Taishan Scholar Special Foundation of Shandong Province, grant number tsqn201812064; Shandong Provincial Natural Science Foundation, P.R. China, grant number ZR2017MEE050; Shandong Provincial Key Research and Development Project, P.R. China, grant number 2018GGX103008; Scientific Innovation Project for Young Scientists in Shandong Provincial Universities, grant number 2019KJB030; Project funded by China postdoctoral Science Foundation, grant number 2021T140420; Key Research and Development Project of Zibo City, China, grant number. 2019ZBXC070.

Institutional Review Board Statement: Not applicable.

Informed Consent Statement: Not applicable.

Conflicts of Interest: The authors declare no conflict of interest.

References

1. Wu, C.J.; Li, B.Z.; Liu, Y.; Liang, S.Y. Surface roughness modeling for grinding of silicon carbide ceramics considering co-existence of brittleness and ductility. *Int. J. Mech. Sci.* **2017**, *133*, 167–177. [CrossRef]
2. Godino, L.; Pombo, I.; Sanchez, J.A.; Alvarez, J. On the development and evolution of wear flats in microcrystalline sintered alumina grinding wheels. *J. Manuf. Process.* **2018**, *32*, 494–505. [CrossRef]
3. Tian, Y.B.; Zhong, Z.W.; Rawat, R. Comparative study on grinding of thin-walled and honeycomb-structured components with two CBN wheels. *Int. J. Adv. Manuf. Technol.* **2015**, *81*, 1097–1108. [CrossRef]
4. Agarwal, S.; Rao, P.V. Grinding characteristics, material removal and damage formation mechanisms in high removal rate grinding of silicon carbide. *Int. J. Mach. Tools Manuf.* **2010**, *50*, 1077–1087. [CrossRef]
5. Tian, Y.B.; Li, L.G.; Han, J.G.; Fan, Z.H.; Liu, K. Development of novel high-shear and low-pressure grinding tool with flexible composite. *Mater. Manuf. Process.* **2021**, *36*, 479–487. [CrossRef]
6. Mukhopadhyay, M.; Kundu, P.K.; Das, S. Experimental investigation on enhancing grindability using alkaline-based fluid for grinding Ti-6Al-4V. *Mater. Manuf. Process.* **2018**, *33*, 1775–1781. [CrossRef]
7. Tian, Y.B.; Li, L.G.; Liu, B.; Han, J.G.; Fan, Z.H. Experimental investigation on high-shear and low-pressure grinding process for Inconel718 superalloy. *Int. J. Adv. Manuf. Technol.* **2020**, *102*, 3425–3435. [CrossRef]
8. Dong, G.J.; Wang, X.; Gao, S.D. Molecular dynamics simulation and experiment research of cutting-tool wear mechanism for cutting aluminum alloy. *Int. J. Adv. Manuf. Technol.* **2018**, *96*, 1123–1137. [CrossRef]
9. Li, B.K.; Dai, C.W.; Ding, W.F.; Yang, C.Y.; Li, C.H.; Kulik, O.; Shumyacher, V. Prediction on grinding force during grinding powder metallurgy nickel-based superalloy FGH96 with electroplated CBN abrasive wheel. *Chin. J. Aeronaut.* **2021**, *34*, 65–74. [CrossRef]
10. Cheng, J.; Yin, G.; Wen, Q.; Song, H.; Gong, Y. Study on grinding force modelling and ductile regime propelling technology in micro drill-grinding of hard-brittle materials. *J. Mater. Process. Technol.* **2015**, *223*, 150–163. [CrossRef]
11. Zhang, Y.; Li, C.; Ji, H.; Yang, X.; Yang, M.; Jia, D.; Zhang, X.; Li, R.; Wang, J. Analysis of grinding mechanics and improved predictive force model based on material-removal and plastic-stacking mechanisms. *Int. J. Mach. Tools Manuf.* **2017**, *122*, 81–97. [CrossRef]
12. Tian, Y.; Liu, F.; Wang, Y.; Wu, H. Development of portable power monitoring system and grinding analytical tool. *J. Manuf. Process.* **2017**, *27*, 188–197. [CrossRef]
13. Aurich, J.C.; Braun, O.; Warnecke, G.; Cronjäger, L. Development of a superabrasive grinding wheel with defined grain structure using kinematic simulation. *CIRP Ann. Manuf. Technol.* **2003**, *52*, 275–280. [CrossRef]
14. Zhang, X.H.; Kang, Z.X.; Li, S.; Wu, Q.P.; Zhang, Z.C. Experimental investigations on the impact of different laser macro-structured diamond grinding wheels on alumina ceramic. *Int. J. Adv. Manuf. Technol.* **2018**, *96*, 1959–1969. [CrossRef]

15. Li, Q.L.; Xu, J.H.; Su, H.H.; Lei, W.N. Fabrication and performance of monolayer brazed CBN wheel for high-speed grinding of superalloy. *Int. J. Adv. Manuf. Technol.* **2015**, *80*, 1173–1180. [CrossRef]
16. Zhang, X.; Wang, Z.; Shi, Z.; Shi, Z.; Jiang, R.; Kang, Z. Improved grinding performance of zirconia ceramic using an innovative biomimetic fractal-branched grinding wheel inspired by leaf vein. *Ceram. Int.* **2020**, *46*, 22954–22963. [CrossRef]
17. Wu, H.H.; Xiao, B.; Xiao, H.Z.; Zhang, Y.Q.; Dou, L.Y. Study on wear characteristics of brazed diamond sheet for rail's composite grinding wheel under different pressures. *Wear* **2019**, *424–425*, 183–192. [CrossRef]
18. Teicher, U.; Ghosh, A.; Chattopadhyay, A.B.; Künanz, K. On the grindability of Titanium alloy by brazed type monolayered superabrasive grinding wheels. *Int. J. Mach. Tools Manuf.* **2006**, *46*, 620–622. [CrossRef]
19. Tian, C.; Li, X.; Zhang, S.; Guo, G.; Wang, L.; Rong, Y. Study on design and performance of metal-bonded diamond grinding wheels fabricated by selective laser melting (SLM). *Mater. Des.* **2018**, *156*, 52–61. [CrossRef]
20. Kizaki, T.; Hao, Y.; Ohashi, T.; Kokubo, T.; Nishijima, T. Capability of a grinding wheel reinforced in hoop direction with carbon fiber. *CIRP. Ann. Manuf. Technol.* **2020**, *69*, 285–288. [CrossRef]
21. Islam, M.; Kumar, A.S.; Balakumar, S.; Lim, H.; Rahman, M. Characterization of ELID grinding process for machining silicon wafers. *J. Mater. Process. Technol.* **2008**, *198*, 281–290. [CrossRef]
22. Beaucamp, A.; Namba, Y.; Charlton, P. Corrective finishing of extreme ultraviolet photomask blanks by precessed bonnet polisher. *Appl. Opt.* **2014**, *53*, 3075–3080. [CrossRef]
23. Walker, D.D.; Beaucamp, A.; Bingham, R.G.; Brooks, D.; Freeman, R.; Kim, S.; King, A.; McCavana, G.; Morton, R.; Riley, D. The precessions process for efficient production of aspheric optics for large telescopes and their instrumentation. *Spec. Opt. Dev. Astron.* **2003**, *4842*, 73–85.
24. Sen, S.; Shaw, A.; Deb, A. Numerical investigation of ballistic performance of shear thickening fluid (STF)-Kevlar composite. *Int. J. Mech. Sci.* **2019**, *164*, 105–174. [CrossRef]
25. Hasanzadeha, M.; Mottaghitalaba, V.; Rezaeib, M.; Babaeic, H. Numerical and experimental investigations into the response of STF-treated fabric composites undergoing ballistic impact. *Thin. Wall Struct.* **2017**, *119*, 700–706. [CrossRef]
26. Lu, Z.Q.; Wu, L.W.; Gu, B.H.; Sun, B.Z. Numerical simulation of the impact behaviors of shear thickening fluid impregnated warp-knitted spacer fabric. *Compos. Part B Eng.* **2015**, *69*, 191–200. [CrossRef]
27. Hoffman, R.L. Discontinuous and dilatant viscosity behavior in concentrated suspensions. I. Observations of a flow instability. *Trans. Soc. Rheol.* **1972**, *16*, 155–173. [CrossRef]
28. Bossis, G.; Brady, J.F. The rheology of Brownian suspensions. *J. Chem. Phys.* **1989**, *91*, 1866–1874. [CrossRef]
29. Brady, J.F.; Bossis, G. Stokesian dynamics. *Ann. Rev. Fl. Mech.* **1988**, *20*, 111–157. [CrossRef]
30. Dong, G.J.; Zhang, L.M. Investigation on grinding force and machining quality during rotary ultrasonic grinding deep-small hole of fluorophlogopite ceramics. *Int. J. Adv. Manuf. Technol.* **2019**, *104*, 2815–2825. [CrossRef]
31. Cai, S.J.; Yao, B.; Zheng, Q.; Cai, Z.Q.; Feng, W.; Chen, B.Q.; He, Z. Dynamic grinding force model for carbide insert peripheral grinding based on grain element method. *J. Manuf. Process.* **2020**, *58*, 1200–1210. [CrossRef]
32. Tian, Y.B.; Li, L.G.; Fan, S.; Guo, Q.J.; Cheng, X. A novel high-shear and low-pressure grinding method using specially developed abrasive tools. *Proc. IMechE. Part B J. Eng. Manuf.* **2020**, *235*, 166–172. [CrossRef]

micromachines

MDPI

Article

An Investigation of the Cutting Strategy for the Machining of Polar Microstructures Used in Ultra-Precision Machining Optical Precision Measurement

Chen-Yang Zhao [1,2], Chi Fai Cheung [2,*] and Wen-Peng Fu [1]

[1] School of Mechanical Engineering and Automation, Harbin Institute of Technology, Shenzhen 518055, China; zhaochenyang@hit.edu.cn (C.-Y.Z.); 20s153227@stu.hit.edu.cn (W.-P.F.)
[2] State Key Laboratory of Ultra-Precision Machining Technology, Department of Industrial and Systems Engineering, The Hong Kong Polytechnic University, Hong Kong, China
* Correspondence: Benny.Cheung@polyu.edu.hk

Abstract: In this paper, an investigation of cutting strategy is presented for the optimization of machining parameters in the ultra-precision machining of polar microstructures, which are used for optical precision measurement. The critical machining parameters affecting the surface generation and surface quality in the machining of polar microstructures are studied. Hence, the critical ranges of machining parameters have been determined through a series of cutting simulations, as well as cutting experiments. First of all, the influence of field of view (FOV) is investigated. After that, theoretical modeling of polar microstructures is built to generate the simulated surface topography of polar microstructures. A feature point detection algorithm is built for image processing of polar microstructures. Hence, an experimental investigation of the influence of cutting tool geometry, depth of cut, and groove spacing of polar microstructures was conducted. There are transition points from which the patterns of surface generation of polar microstructures vary with the machining parameters. The optimization of machining parameters and determination of the optimized cutting strategy are undertaken in the ultra-precision machining of polar microstructures.

Keywords: polar microstructures; optimization; machining parameters; ultra-precision machining; cutting strategy

Citation: Zhao, C.-Y.; Cheung, C.F.; Fu, W.-P. An Investigation of the Cutting Strategy for the Machining of Polar Microstructures Used in Ultra-Precision Machining Optical Precision Measurement. *Micromachines* **2021**, *12*, 755. https://doi.org/10.3390/mi12070755

Academic Editor: Martin Byung-Guk Jun

Received: 2 June 2021
Accepted: 25 June 2021
Published: 27 June 2021

1. Introduction

In precision measurement, many basic applications with optical sensing technologies are applied, such as the laser interferometer principle, piezoelectric actuator principle, and micro-encoding principle [1–4]. One of their common characteristics is that they have exacting requirements on the environment, such as vacuum and equipment components, so it is necessary to control the correlative uncertainty sources [5]. For example, errors of air wavelengths and refractive index are the essential uncertainty sources [6] and would lead to Abbe and accumulation errors for multiple degree-of-freedom (DOF) tasks, due to such principles only enabling the measurement of a single DOF [7]. To avoid these limitations, vision-based techniques are used for precision measurement [8–11]. Currently, the vision-based technique is an appealing method for precision measurement because of its technological advantages, including the visualization result, multiple DOF measurement, easy operation and installation, etc. A novel method that attempts to integrate computer vision and ultra-precision machining technologies [11–13] has been presented, which is feasible and promising for precision measurement due to its simplicity, space-saving, low-cost, and high-robust features, etc. The template matching algorithm has been employed for image processing and determined the absolute position of the selected image in the global map [11]. Moreover, a unique surface topography named polar microstructure has been developed for the abovementioned measurement method [12,13]. Polar microstructures aim to serve as a unique global map used for the subsequent matching measurement.

Inspired by the polar coordinate system, a polar microstructure is presented [11], as shown in Figure 1. To generate the polar microstructure surface topography with straight lines and concentric circle trails, a process chain introduced in the literature [14] is designed and fabricated by a combination of single-point diamond turning (SPDT) and single-point diamond grooving (SPDG) processes. It is worth noting that the polar microstructure with form accuracy within the micrometer range still possesses a high discrimination rate. Taking into account the specific characteristics on the surface of the polar microstructure, both the geometric pattern and the arrangement of pixel intensity values are unique. This is due to the unique gray-scale intensity distribution of the polar microstructure that ensures the high reliability and robustness for the optical precision measurement with this polar microstructure.

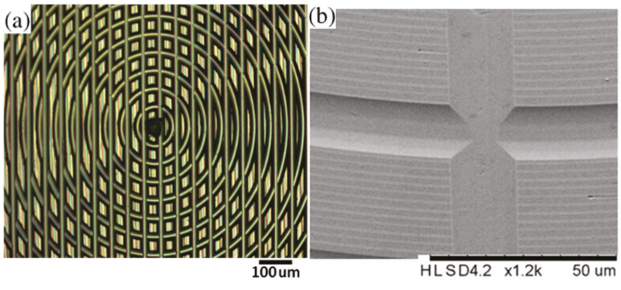

Figure 1. Polar microstructure observed with (**a**) Olympus BX 53M light microscope and (**b**) HITACHI TM3000 Scanning Electron Microscope.

However, the determination of machining parameters is necessary to fabricate polar microstructures. There are many factors to consider in order to meet the functional performance requirements, which include the parameters for microscopic observation, etc. Currently, there are only a few examples of research concerning the optical resolution of micro-structured surface influenced by cutting strategy [15–18]. In this paper, an investigation into the influence of machining parameters of polar microstructures to satisfy the extraction of the feature point matching is presented. First, the chosen field of view was investigated. After that, the modeling of polar microstructures is described, and the algorithm for detecting the feature points is explained. In the results and discussion section, three important parameters for the cutting strategy for polar microstructures are identified, which are tool geometry, depth of cut, and groove spacing. The optimized parameters were obtained according to the simulation and experimental results.

2. Feature Point Distribution Analysis in the Field of View (FOV)

2.1. Determination of the FOV

The choice of machining parameters takes into account various aspects, such as the field of view (FOV) of the microscope. There are many definitions of FOV, such as the vertical angle or horizontal angle of perspective [19–21]. In this paper, FOV refers to the actual size of the area observed by the microscope or camera. The determination of machining parameters of polar microstructure ensures the functional reliability under extreme conditions. Since the FOV of different microscopes or cameras are different, Figure 2 shows a microscope with its FOV matched with the machine tool. This microscope is used to capture the special pattern of polar microstructures for optical position measurement based on the integration of computer vision and ultra-precision machining technologies [11–13]. As shown in Figure 2, it is found that its FOV is a rectangular area 350 μm long and 220 μm wide. One design principle is that there are a number of uniform, sufficient, and accurate feature points, which can be detected by feature point detection algorithms.

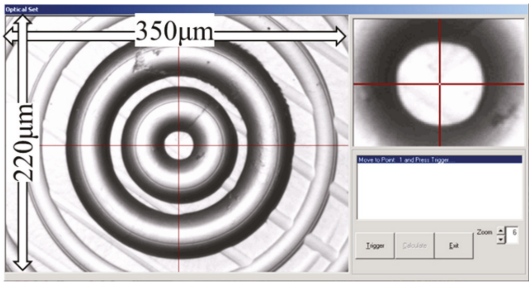

Figure 2. This is a microscope FOV.

2.2. The Vital Parameters Influencing Feature Point Distribution in the FOV

Figure 3 shows the relationship between machining parameters and the FOV. The highlighted intersection points refer to the possible detected designed feature points. Here, it needs to be emphasized that their actual localizations may not be completely consistent with the designed locations for detected feature points (DFP). This is due to the fact that the actual intensity gradient of pixels is not necessarily consistent with the design points due to the machining errors. As a result, the pixels in this area also have differences. However, this does not influence the subsequent matching accuracy since the captured images are from one polar microstructure surface. On the other hand, the measurement algorithms [11] ensure the robustness of the measurement method in response to the pixel intensity changes.

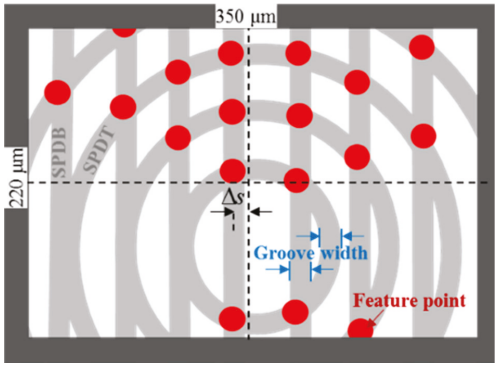

Figure 3. Geometrical relationship between feature point distribution in a microscope's field of view.

According to the analysis of the designed feature point distribution in the FOV, a polar microstructure was fabricated by SPDT and SPDG, as shown in Figure 3, where the intersection points of the two above machining processes constitute the designed feature points. The distribution of feature points is mainly determined by two aspects, i.e., one is the groove spacing, including both SPDT with SPDG, while the other is the groove width. Furthermore, the generation of the groove width is influenced by the machining parameters, including tool nose radius and depth of cut. Hence, three groups of machining parameters are determined, which are investigated to study their influence on the feature point distribution.

Another necessary parameter not mentioned before is the offset of straight grooves, which is denoted by the symbol Δs. Its existence ensures the distinction of a 360-degree displacement angle on a polar microstructure surface. For example, Figure 4 shows the polar microstructure without Δs, and the measurable angle range is only 180 degrees. Theoretically, the measurement algorithms cannot distinguish the central symmetrical

pattern when it rotates 180 degrees with exactly the same distribution of feature points. However, when there is an offset, the measurable angle range is improved, as shown in Figure 5, which realizes a 360-degree detection range.

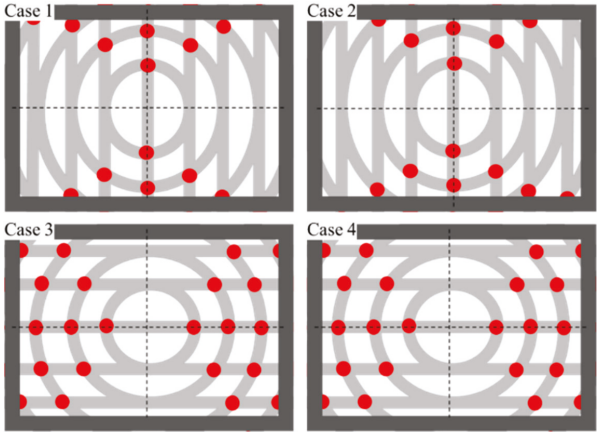

Figure 4. There are four angle detection results without offset ($\Delta s = 0$) Case1: 0°; Case2: 180°; Case3: 90°; Case4: 270°.

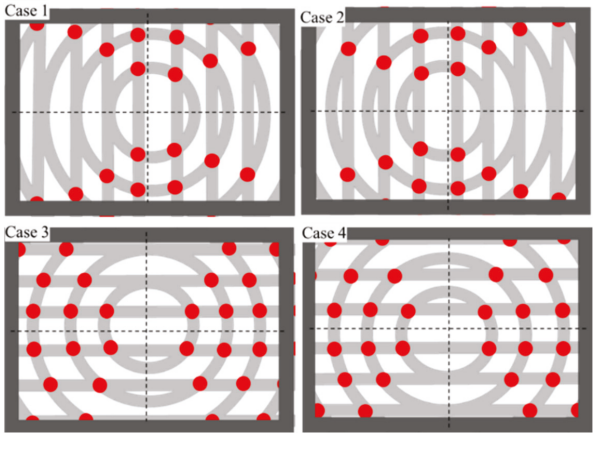

Figure 5. There are four angle detection results with offset ($\Delta s \neq 0$) Case1: 0°; Case2: 180°; Case3: 90°; Case4: 270°.

3. Modeling of Surface Generation for Polar Microstructures

According to the process chain combining SPDG and SPDT, a polar microstructure is a workpiece with a specific surface microstructure. Figure 6 shows the processing principle of SPDT and SPDG. The workpiece is mounted and rotates on the spindle, and the diamond tool mounted on the machine slides on the machine tool.

SPDT(Pre) is an end processing operation that generates the initial workpiece surface, so the initial surface topography model (STM) of the workpiece needs to be firstly established. In this processing operation, the spindle rotational speed for the SPDT is 2000 r/min and the feed rate is 2 mm/min. The geometrical relationship of the initial STM between the tool nose (arc tip) and the initial ST is shown in Figure 7.

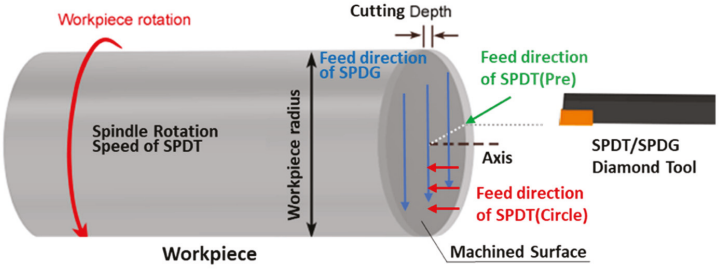

Figure 6. Processing principle of SPDT and SPDG. In the preliminary process of SPDT(Pre), the workpiece turns at a high cutting speed, and the diamond tool feeds in the radial direction until the machined surface becomes smooth. For the concentric circle groove processing in SPDT(Circle), the workpiece keeps spinning, and the diamond tool remains stationary after every certain position of feed direction of SPDT(Circle). For the parallel straight groove processing in SPDG, the workpiece remains stationary and the diamond tool feeds in a series of parallel and equally spaced radial directions.

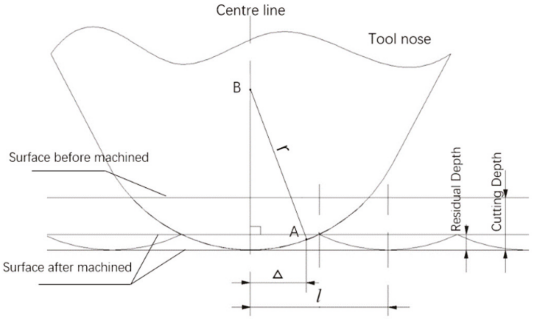

Figure 7. The surface topography geometrical model in SPDT(Pre). l is the length of feed per turn of workpiece; r is the arc tip radius; point $A(x_A, y_A, z_A)$ is an arbitrary position on the end surface of the workpiece; $B(x_B, y_B, z_B)$ is the center of the tool nose arc; Δ is the distance between the center line of the tool nose and point A.

Theoretically, the formation of the initial surface topography is related to the tool and cutting parameters, including the arc tip radius, spindle rotational speed, and feed rate. As shown in Figure 7, l can be represented by Equation (1):

$$l = \frac{f}{\omega} \tag{1}$$

where f is the tool feed rate, ω is the spindle rotational speed of the workpiece, and Δ is deduced as Equation (2):

$$\Delta = \left| \sqrt{{x_A}^2 + {y_A}^2} - k \cdot l \right| \tag{2}$$

where k is the period number from point O to point A. The position relationship between point O and point A is more clearly referred to in Figure 8b. x_A and y_A are the projecting position coordinates of point A on the diamond tool path plane.

According to the movement of the turning face in SPDT(Pre), the cutting tool path formed is a spiral of Archimedes or uniform speed spiral. The cutting tool path of SPDT(Pre) relative to the surface of the workpiece is shown as Figure 8a. As shown in Figure 8a, point O is the center point of the uniform speed spiral; the five-x magnification views of the red circle in Figure 8a is shown in Figure 8b, which depicts the position relationship between

the projecting position of point A and point B; the projecting position of point A is a point on the line OB.

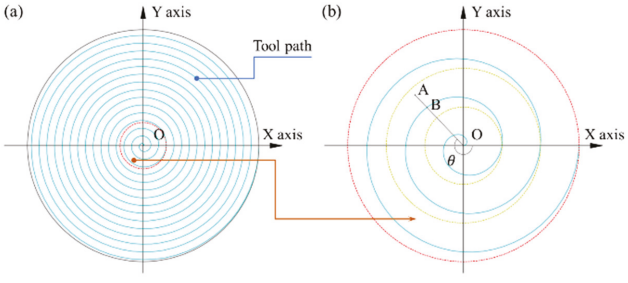

Figure 8. (**a**) Diamond tool path of SPDT(Pre) relative to the surface of the workpiece; (**b**) five-x local magnification view.

Based on the geometrical relationship, Equations (3)–(5) can be derived as follows:

$$\theta = \arctan\left(\frac{y_B}{x_B}\right) \tag{3}$$

$$t_B = \frac{\theta}{2\pi\left(\frac{\omega}{60}\right)} = \frac{30\theta}{\pi\omega} \tag{4}$$

$$r_{OB} = \frac{f\Delta t_B}{60} = k\Delta l \tag{5}$$

where t_B is the feeding time of the tool nose between point B and point O and r_{OB} is the polar radius of B. x_B and y_B are the projecting position coordinates of point B on the diamond tool path plane. θ is the counterclockwise angle from line OX to line OB.

According to the Pythagorean theorem, it is easy to obtain the height z_{pre} of point A, which is derived by Equation (6):

$$z_{pre} = (r - d_1) - \sqrt{r^2 - \Delta^2} \tag{6}$$

where d_1 is the cutting depth.

The initial STM establishing the workpiece in SPDT(Pre) is accomplished, and the derivation is similar to the STM established in SPDT(Circle) and SPDG(Line). The difference between the model established in SPDT and SPDG is the cutting tool path of the tool nose relative to the workpiece. The tool path of the SPDT(Circle) model is a group of concentric circles. For the SPDG model, the tool path is a series of parallel grooves. To distinguish the parameters, z_{pre}, z_{con}, and z_{str} represent the workpiece surface height in the SPDT(Pre) model, the SPDT(Circle) model, and the SPDG model, respectively.

Combining the process chain model, the surface topography of the polar microstructure is generated as a consequence of the processing models of SPDT and SPDG. For an arbitrary point on the surface of the workpiece, the surface height z_{chain} results from the minimum height between z_{pre}, z_{con}, and z_{str}, which can be defined as Equation (7):

$$z_{chain} = \arg\min_{(x,y)\in W}\{z_{pre}, z_{con}, z_{str}\} \tag{7}$$

where W is the workpiece machined area. Hence, the process chain model has been established.

According to the models of SPDT and SPDG, simulation experiments under different machining parameters were conducted. Figure 9 shows one of the comparison groups between simulated and experimental results; a high degree of similarity between the two surface texture images is found. The result demonstrates that the proposed model

is capable of representing the actual machining conditions of the polar microstructure surface. In other words, the simulated surface topography is able to be used in the further image processing as a substitute of the measured surface images. Furthermore, additional attention should be paid to the simulation model, which is able to reduce the cost and improve the efficiency.

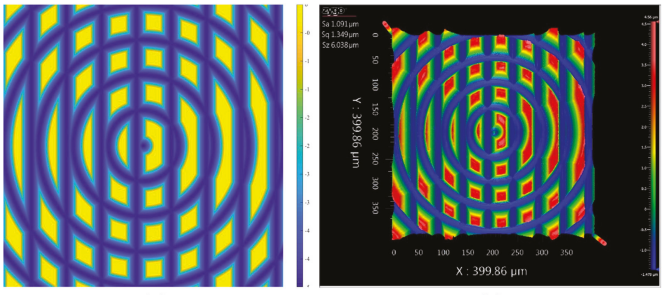

Figure 9. Comparison between modeling and experimental results: (**a**) Simulated surface texture, (**b**) measured surface texture. Machining conditions: Material: Nickel-Copper; Tool radius: 43 µm; Groove spacing: 50 µm; Depth of cut: 5 µm.

4. Feature Point Detection

The modeling of polar microstructures aims to provide their surface topography, which can be shown in the form of images for the feature point detection, which is very significant for the further computer vision-based measurements. The measurement is realized by image matching, and the matching is accomplished by a series of corresponding feature points distributed in different images. As a result, it is necessary to develop the algorithm for feature point detection. There have been many studies providing feature point detection methods, such as canny edge [22], Difference of Gaussians (DoG) [23], and the principal curvature-based region (PCBR) [24]. In this paper, a method named fast and robust feature-based positioning (FRFP) [13] is presented for feature point detection.

Feature point extraction aims to construct a Hessian Matrix (HM) to generate points of interest for feature extraction, named 'Feature point.' Constructing the HM aims to find image stable edge points and blob points and provides a basis for the next step of feature extraction. The HM of an image expressed as $g(x, y)$ is given in Equation (8):

$$H(g(x,y)) = \begin{pmatrix} \frac{\partial^2 g}{\partial x^2} & \frac{\partial^2 g}{\partial x \partial y} \\ \frac{\partial^2 g}{\partial x \partial y} & \frac{\partial^2 g}{\partial y^2} \end{pmatrix} \tag{8}$$

The filtered HM by Gaussian filtering is expressed in Equation (9):

$$H(g,\sigma) = \begin{pmatrix} L_{xx}(g,\sigma) & L_{xy}(g,\sigma) \\ L_{xy}(g,\sigma) & L_{yy}(g,\sigma) \end{pmatrix} \tag{9}$$

To increase the speed of the algorithm, this comes up with one box filter (BF) to replace the Gaussian filter (GF). A schematic diagram of a GF and a BF is shown in Figure 10. D_{xx}, D_{yy}, and D_{xy} are used as the approximation for L_{xx}, L_{yy}, and L_{xy}. The upper two figures, as shown in Figure 10, are the values of the second derivative of the 9×9 GB template in the vertical direction on the image, which are L_{yy} and L_{xy}, and the lower two images are approximated by using a BF, which are D_{yy} and D_{xy}. As shown in Figure 10, the pixel values of the white, black, and gray parts are 1, -2, and 0.

Since the integral image method is used for image convolution, BF increases the computational speed of the algorithm. The integral image method is a fast algorithm that only needs to traverse an image to get the sum of all the pixels in the image, which

improves the efficiency of image eigenvalue calculation. The concept of the integral image is shown in Figure 11. For any point (i, j) in an integral image, its value is the sum of the gray values of the rectangular region from the upper-left point of the original image to the point (i, j), which can be expressed as Equation (10):

$$ii(i, j) = \sum_{i' \le i,\ j' \le i} p(i', j') \tag{10}$$

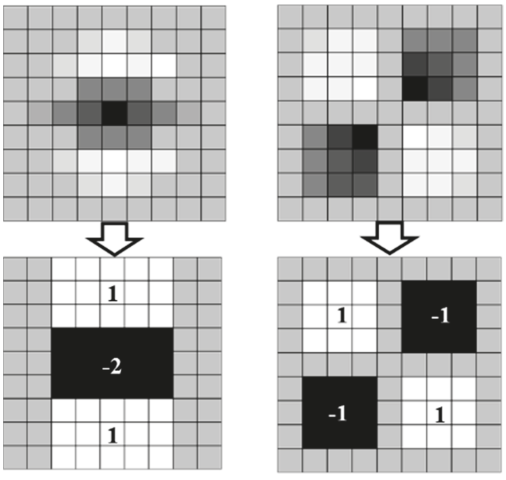

Figure 10. Gaussian filter to box filter.

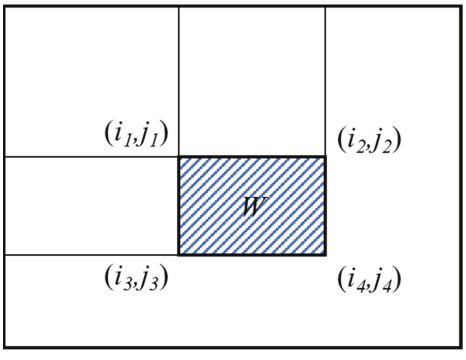

Figure 11. Concept of integral images.

The filtering calculated by BF of an image is equal to calculating the pixel sums among the regions of the image, that is, the strength of the integral graph, and can be simply realized by inquiring an integral graph. Since the integral of a region is determined for a given image, the only work that needs to be done is to calculate the values of the four vertices of this region in the integral image, which can be obtained by two-step addition and two-step subtraction. The mathematical formula is expressed in Equation (11):

$$\sum\nolimits_W = ii(i_4, j_4) - ii(i_2, j_2) - ii(i_3, j_3) + ii(i_1, j_1) \tag{11}$$

When a point is brighter or dimmer than other points surrounding it, the discriminant of the HM yields a local extremum, which determines the position of such a key point. The discriminant of the HM can be derived by Equation (12):

$$\begin{aligned}\mathrm{Det}(H) &= L_{xx}L_{yy} - L_{xy}L_{xy}\\ &= D_{xx}\tfrac{L_{xx}}{D_{xx}}D_{yy}\tfrac{L_{yy}}{D_{yy}} - D_{xy}\tfrac{L_{xy}}{D_{xy}}D_{xy}\tfrac{L_{xy}}{D_{xy}}\\ &= D_{xx}D_{yy}\left(\tfrac{L_{xx}}{D_{xx}}\tfrac{L_{yy}}{D_{yy}}\right) - D_{xy}D_{xy}\left(\tfrac{L_{xy}}{D_{xy}}\tfrac{L_{xy}}{D_{xy}}\right)\\ &= \left(D_{xx}D_{yy} - D_{xy}D_{xy}\left(\tfrac{L_{xy}}{D_{xy}}\tfrac{L_{xy}}{D_{xy}}\right)\left(\tfrac{D_{xx}}{L_{xx}}\tfrac{D_{yy}}{L_{yy}}\right)\right)\left(\tfrac{L_{xx}}{D_{xx}}\tfrac{L_{yy}}{D_{yy}}\right)\\ &= \left(D_{xx}D_{yy} - \left(\omega D_{xy}\right)^2\right)C\end{aligned} \tag{12}$$

In Equation (12), constant C has no effect on the comparison of key points. In this way, when Gaussian second-order differential filtering is used with $\sigma = 1.2$ and the template size is 9×9 as the smallest scale space value to filter the image, ω in Equation (12) can be expressed in Equation (13):

$$\omega = \frac{\left|L_{xy}(1.2)\right|_F\left|D_{xy}(9)\right|_F}{\left|L_{xx}(1.2)\right|_F\left|D_{xy}(9)\right|_F} = 0.912 \tag{13}$$

Equation (12) is then simplified to Equation (14):

$$\mathrm{Det}(H) = \left(D_{xx}D_{yy} - \left(0.192D_{xy}\right)^2\right) \tag{14}$$

where a weighting factor $\omega = 0.912$ is used to remedy the error caused by BF approximation. Additionally, a response value is standardized based on the filter size to ensure that the Frobenius norm of the filter of any size is uniform. At a certain image point, its blob response value is represented by the approximate Hessian matrix determinant. A response image of all detected points on a certain scale is formed after all pixel points are traversed. Moreover, taking diverse template sizes obtains a multi-scale blob response map, which is applied to feature point localization.

Figure 12 shows a sample of detection results by using FRFP algorithms. It is shown that the main DFP are usually distributed around the designed intersection points, as shown in Figure 3. This demonstrates that the detection algorithm is suitable for accurate detection of the feature points of polar microstructures. However, in order to reduce the localization errors of feature points, the algorithm increases the threshold of detection to ensure that the DFP are accurate and stable enough. On the basis of the above principles, the greater the number of feature points to be detected, the greater the number of subsequent matching points, and the more accurate the final measurement result.

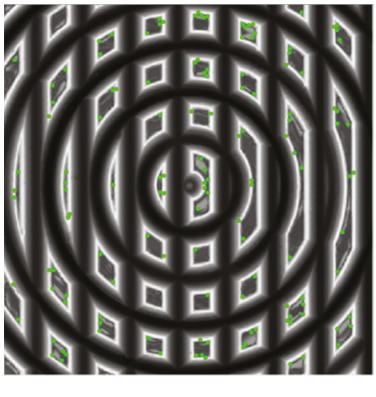

Figure 12. Feature point detection results marked with bright points.

The following section presents an investigation of three machining factors, which are tool nose radius, depth of cut, and groove spacing. For each factor, different machining val-

ues of the parameters were simulated to output the surface image of polar microstructures. Feature point detection was then conducted, and the number of detected points was found as the most important criterion for performance evaluation of polar microstructures.

5. Results and Discussion

5.1. Effect of Tool Geometry

The reason for firstly studying the influence of tool geometry lies in the actual condition. There are two types of diamond tools; one is the sharp tip and the other is the arc tip. The sharp tip is able to machine a fairly narrow groove width, but the tool wear is the biggest constraint for utilization. Figure 13 shows a case of machining grooves with 10-μm spacing with a sharp tip and a contrasting case with an arc tip, and the workpiece was measured with a scanning electron microscope (SEM). Figure 13a is the initial machining stage, and the machining quality was found to be satisfactory, but the sharp tip was worn out at the end stage, as shown in Figure 13b. Comparatively, the arc tip of the diamond cutting tool was not easily worn out and more suitable for prolonging the tool life for the SPDT and SPDG machining processes, as shown in Figure 13c,d. Hence, the cutting tool type was chosen to be the arc tip.

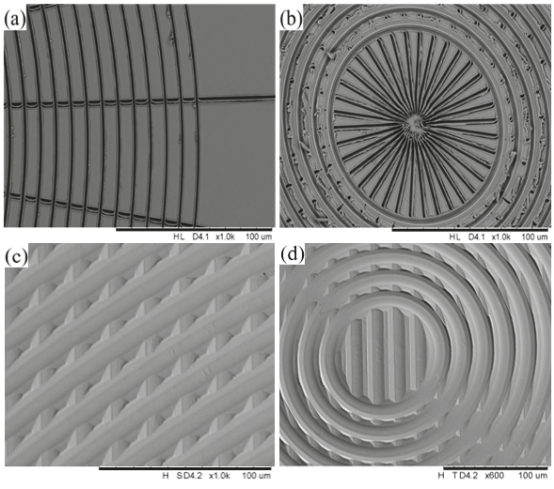

Figure 13. Comparing workpiece machined surfaces by using the sharp tip type and the arc tip type of the diamond tool. Tool wear evolution of the sharp tip type of diamond tool: (**a**) initial machining quality of the workpiece surface by the sharp tip; (**b**) workpiece surface machining quality after tool wear of the sharp tip. Machining quality of the workpiece surface by the arc tip; (**c**) workpiece surface machining quality in the adjacent area; and (**d**) workpiece surface machining quality in the central area.

Considering the extreme conditions, polar microstructures should have distinctive patterns and enough accurate feature points in the FOV area of the 200-μm square. As a result, the simulations should be conducted in a 200-μm square area. According to the previous modeling, tool nose radius is one of the parameters for the generation of the polar microstructure surface. In this section, a series of simulations conducted with the different tool nose radius (TNR), ranging from 43 to 200 μm, is presented, and the smallest TNR was set to 43 μm, limited to the experimental conditions. The simulation results are shown in Figure 14.

With the TNR increasing, the amount of material removal grew, and the groove width became broader. Meanwhile, the intensity change rate of the image weakened, which may reduce the number of DFP. It is worth noting that the number of DFP reduced when the TNR increased, as shown in Figure 15. The number of reduced DFP adversely

affected the process of subsequent matching. Hence, it is concluded that smaller TNR is helpful to improve the feature point detection of polar microstructure surface. Considering the current experimental conditions, the smallest TNR (43 μm) can be chosen in future experiments.

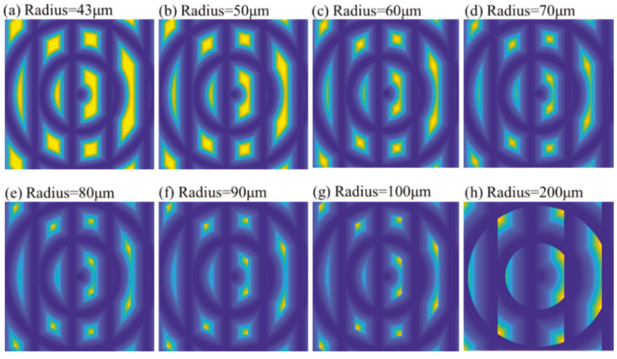

Figure 14. Comparison of simulated surface topography of a polar microstructure with different tool nose radii. Other important machining parameters: groove spacing: 50 μm, depth of cut: 5 μm.

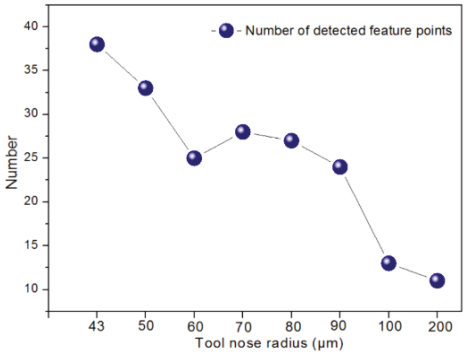

Figure 15. Trend of number of detected feature points (DFP) with different tool nose radii.

5.2. Effect of Depth of Cut

Besides the TNR, the depth of cut (DOC) also influenced the groove width. Figure 16 shows the simulated results when the DOC was varied. A feature point detection process was also conducted, as shown in Figure 17. Similar to the results for TNR, a smaller DOC was helpful in improving the feature point detection of the polar microstructure surface. However, it is worth noting that there is an increasing number of detected points when the DOC increased from 1 to 2 μm. After comparing the distribution of DFP among these conditions, it was found that the DFP were mainly concentrated in the surrounding area of the highlighted intersection points, as shown in Figure 3. When the DOC was too small, the area of the highlighted intersection points was smaller, and hence the total possible DFP reduced in number.

Moreover, it can be observed in Figure 17 that there was an increase in the number of DFP when the DOC was 8 μm. One of the reasons for this is an algorithm error and uncertainty; the simple central moment is only an algorithm to test the feature point detection ability of polar microstructures; advanced algorithms should be investigated and applied in precision measurement. The other important reason for this is that not all of the DFP could be matched well when the noises of the images were large, such as the scale or angle change, etc., and lead to the number of detected and matched points reducing

further; this is also why the number of designed feature points should not be too small. From the view of machining ability, the DOC is usually set manually, and it is difficult to control it accurately when the DOC is too small. To prevent some areas from not perhaps being machined due to the small given DOC, the depth of cut was determined to be 5 μm.

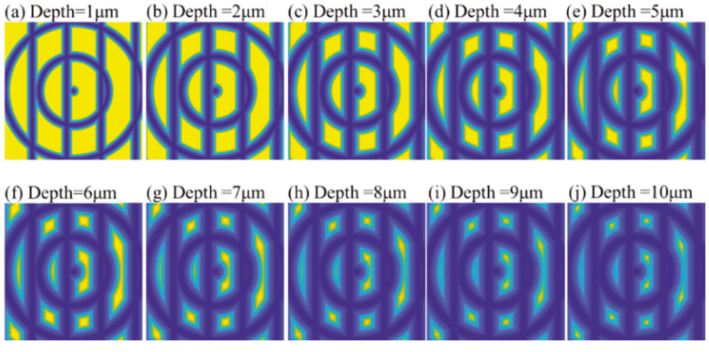

Figure 16. Comparison of the simulated surface topography of a polar microstructure with different depths of cut. Other important machining parameters: groove spacing: 50 μm, tool nose radius: 50 μm.

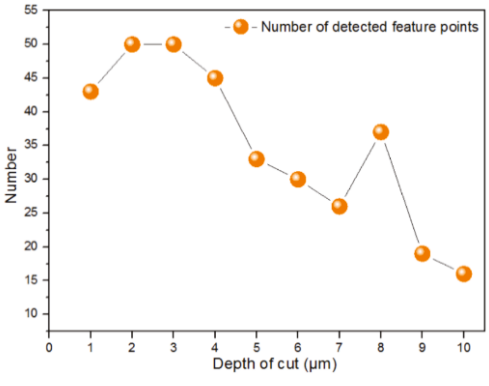

Figure 17. Trend of number of detected feature points (DFP) with different depths of cut.

5.3. Groove Spacing

In addition to groove width, groove spacing (GS) is an important parameter affecting the performance of polar microstructures. The determination of GS should take into account both functional requirements and actual machining ability. For functional requirements, polar microstructures should have distinctive patterns and enough accurate feature points in the FOV area.

Firstly, a series of simulations was carried out whose GS ranged from 150 μm to 50 μm, with six groups in total. The simulated results are shown in Figure 18. In order to ensure enough feature points against various noises, the number of designed feature points should be large enough. From Figure 18a–e, the number of designed feature points was too small, making it hard to ensure the stability of matching accuracy. Moreover, it cannot be neglected that the simulated area is focused on the central area of polar microstructures, but the designed points for the other areas should also be sufficient and distinctive. Shown by the simulation results analysis, as shown in Figure 18, the GS should not be larger than 50 μm.

When decreasing GS, the simulation results show that there are more designed feature points in the FOV. However, the model does not consider the material properties

of the workpiece. To clearly show the cusp caused by SPDT and SPDG, another series of simulations was conducted, whose spacings varied from 50 to 10 μm, as shown in Figure 19.

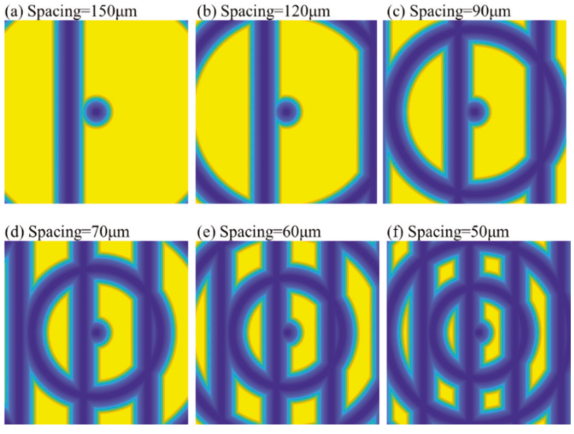

Figure 18. Comparison of simulated surface topography of a polar microstructure with different groove spacing. Other important machining parameters: depth of cut: 5 μm, tool nose radius: 50 μm.

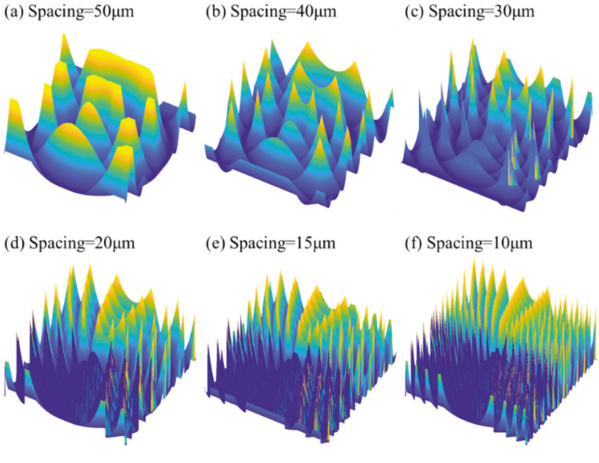

Figure 19. Comparison of simulated 3D surface topography of a polar microstructure with different groove spacing. Other important machining parameters: depth of cut: 5 μm: tool nose radius: 43 μm.

It was found that, when GS was 50 μm, the cusp was smooth, indicating that the material properties do not significantly influence the generation of polar microstructure. However, the cusp in the polar microstructure became large and more intensive when the GS decreased. From the view of the model simulation, they are cusps, but in real conditions, there are many more machining errors due to elastic deformation in ductile materials. In this study, three groups of polar microstructures were machined, as shown in Figure 20. The kinds of GS were 10 μm, 20 μm, and 50 μm. It is interesting to note from Figure 20a,b that the machining quality of polar microstructures was far from that of the simulation due to material properties, but when the GS increased to 50 μm, the machining quality was relatively consistent with the geometrical model. It can also be concluded that the range of GS should be around 50 μm after considering both function performance and machining quality.

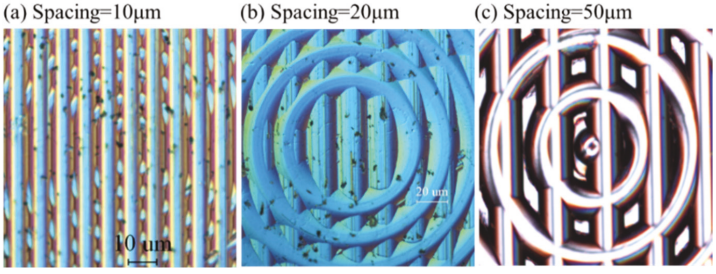

Figure 20. Experimental results of machining a polar microstructure with different groove spacing.

On the whole, the machining parameters of polar microstructures were investigated in order to optimize their performance in feature point detection. The final machining parameters were chosen as referred to in this investigation and they are summarized in Table 1. This paper not only provides a turn-key solution for determining the optimal parameters but also presents a systematic way of studying the cutting strategy in ultra-precision machining of polar microstructures for optical precision measurement.

Table 1. Machining parameters for polar microstructures.

Machining straight grooves (SPDG)	Feed rate of grooving straight grooves (mm/min)	800
	DOC: um	5
	Δs (μm)	10
	p_S (μm)	50
	Number of straight grooves:	250
Machining round grooves (SPDT)	DOC: um	5
	p_T (μm)	50
	Number of round grooves:	250
	The radius of the smallest round groove	100

6. Conclusions

In this study, the influence of the cutting strategy on polar microstructures was investigated. Considering the FOV, the rough size range of grooving spacing was determined. The offset spacing was also designed for a 360-degree measurement. After that, the modeling results of the surface topography were compared with the measured result, which indicated that it is capable of using the simulated surface images for further processing, which greatly reduces the cost. A FRFP-based algorithm was introduced to detect the feature points, and the results show that the polar microstructure was well designed and the algorithm is suitable for detection. Lastly, a series of simulations and experiments was conducted to investigate the influence of machining parameters on the performance of polar microstructures. The three main parameters focused on were tool geometry, depth of cut, and groove spacing. Some experiments were also conducted to demonstrate the accuracy of the simulated results. The optimized parameters were finally chosen for further machining. Other machining parameters, such as cutting speed effect, should be further investigated in future work. This work contributes to the parameter optimization of optic-functional microstructure surface through both theoretical and experimental study.

Author Contributions: C.-Y.Z.: conceptualization, methodology, investigation, validation, data curation, writing—original draft; C.-F.C.: funding acquisition, visualization; resources, supervision, project administration, writing—review and editing; W.-P.F.: investigation, sampling, writing—review and editing, visualization. All authors have read and agreed to the published version of the manuscript.

Funding: This work was supported by the Youth Program of the National Natural Science Foundation of China (Grant No. 52005135), Basic research projects of Shenzhen research and development fund

No. JCYJ20200109112808109. The authors would also like to express their thanks to the Research Office of The Hong Kong Polytechnic University (Project code: BBX7).

Conflicts of Interest: The authors declare no conflict of interest.

References

1. Gao, W.; Kim, S.W.; Bosse, H.; Haitjema, H.; Chen, Y.L.; Lu, X.D.; Knapp, W.; Weckenmann, A.; Estler, W.T.; Kunzmann, H. Measurement technologies for precision positioning. *CIRP Ann.* **2015**, *64*, 773–796. [CrossRef]
2. Sun, B.; Zheng, G.; Zhang, X. Application of contact laser interferometry in precise displacement measurement. *Measurement* **2021**, *174*, 108959. [CrossRef]
3. Mohith, S.; Upadhya, A.R.; Navin, K.P.; Kul Ka Rni, S.M.; Rao, M. Recent trends in piezoelectric actuators for precision motion and their applications: A review. *Smart Mater. Struct.* **2020**, *30*, 013002. [CrossRef]
4. Andre, A.N.; Sandoz, P.; Mauze, B.; Jacquot, M.; Laurent, G.J. Sensing One Nanometer over Ten Centimeters: A Micro-Encoded Target for Visual In-Plane Position Measurement. *IEEE/ASME Trans Mechatron.* **2020**, *25*, 1193–1201. [CrossRef]
5. Coddington, I.; Swann, W.C.; Nenadovic, L.; Newbury, N.R. Rapid and precise absolute distance measurements at long range. *Nat. Photonics* **2009**, *3*, 351–356. [CrossRef]
6. Zahedpour, S.; Wahlstrand, J.; Milchberg, H. Measurement of the nonlinear refractive index of air constituents at mid-infrared wavelengths. *Opt. Lett.* **2015**, *40*, 5794–5797. [CrossRef]
7. Yao, S.; Li, H.; Pang, S.; Zhu, B.; Fatikow, S. A Review of Computer Microvision-Based Precision Motion Measurement: Principles, Characteristics, and Applications. *IEEE Trans. Instrum. Meas.* **2021**, *70*. [CrossRef]
8. Gonzalez-Galvan, E.J.; Skaar, S.B.; Korde, U.A.; Chen, W. Application of a precision-enhancing measure in 3D rigid-body positioning using camera-space manipulation. *Int. J. Robot. Res.* **1997**, *16*, 240–257. [CrossRef]
9. Wu, B.; Zhang, F.; Xue, T. Monocular-vision-based method for online measurement of pose parameters of weld stud. *Measurement* **2015**, *61*, 263–269. [CrossRef]
10. Li, H.; Zhang, X.; Wu, H.; Gan, J. Line-based calibration of a micro-vision motion measurement system. *Opt. Lasers Eng.* **2017**, *93*, 40–46. [CrossRef]
11. Zhao, C.Y.; Cheung, C.F.; Liu, M.Y. Integrated polar microstructure and template-matching method for optical position measurement. *Opt. Express* **2018**, *26*, 4330–4345. [CrossRef]
12. Zhao, C.Y.; Cheung, C.F.; Liu, M.Y. Nanoscale measurement with pattern recognition of an ultra-precision diamond machined polar microstructure. *Precis. Eng.* **2019**, *56*, 156–163. [CrossRef]
13. Zhao, C.Y.; Cheung, C.F.; Xu, P. Optical nanoscale positioning measurement with a feature-based method. *Opt. Lasers Eng.* **2020**, *134*, 106225. [CrossRef]
14. Zhao, C.Y.; Cheung, C.F.; Liu, M.Y. Modeling and simulation of a machining process chain for the precision manufacture of polar microstructure. *Micromachines* **2017**, *8*, 345. [CrossRef]
15. Kong, L.B.; Cheung, C.F. Design, fabrication and measurement of ultra-precision micro-structured freeform surfaces. *Comput. Ind. Eng.* **2011**, *61*, 216–225. [CrossRef]
16. Zhang, H.; Chen, S.; Zhou, M.; Yang, Y. Fast tool servo control for diamond-cutting microstructured optical components. *J. Vac. Sci. Technol. B Microelectron. Nanometer Struct. Process. Meas. Phenom.* **2009**, *27*, 1226–1229. [CrossRef]
17. Neo, D.W.K.; Kumar, A.S.; Rahman, M. A novel surface analytical model for cutting linearization error in fast tool/slow slide servo diamond turning. *Precis. Eng.* **2014**, *38*, 849–860. [CrossRef]
18. Wang, J.; Du, H.; Gao, S.; Yang, Y.; Guo, P. An ultrafast 2-D non-resonant cutting tool for texturing micro-structured surfaces. *J. Manuf. Process.* **2019**, *48*, 97. [CrossRef]
19. Strasburger, H.; Rentschler, I.; Jüttner, M. Peripheral vision and pattern recognition: A review. *J. Vis.* **2011**, *11*, 13. [CrossRef] [PubMed]
20. Martins, A.; Li, K.; Li, J.; Liang, H.; Conteduca, D.; Borges, B.-H.V.; Krauss, T.F.; Martins, E.R. On metalenses with arbitrarily wide field of view. *ACS Photonics* **2020**, *7*, 2073–2079. [CrossRef]
21. Panescu, D.; Jones, D.H.; Allenby, C. Quantitative Three-Dimensional Visualization of Instruments in a Field of View. U.S. Patent Application US 15/300,258, 22 June 2017.
22. Perona, P.; Malik, J. Scale-space and edge detection using anisotropic diffusion. *IEEE Trans. Pattern Anal. Mach. Intell.* **1990**, *12*, 629–639. [CrossRef]
23. Polakowski, W.E.; Cournoyer, D.A.; Rogers, S.K.; DeSimio, M.P.; Ruck, D.W.; Hoffmeister, J.W.; Raines, R.A. Computer-aided breast cancer detection and diagnosis of masses using difference of Gaussians and derivative-based feature saliency. *IEEE Trans. Med. Imaging* **1997**, *16*, 811–819. [CrossRef] [PubMed]
24. Deng, H.; Zhang, W.; Mortensen, E.; Dietterich, T.; Shapiro, L. Principal curvature-based region detector for object recognition. In Proceedings of the 2007 IEEE Conference on Computer Vision and Pattern Recognition, Minneapolis, MN, USA, 17–22 June 2007; pp. 1–8.

micromachines

MDPI

Article

An Elementary Approximation of Dwell Time Algorithm for Ultra-Precision Computer-Controlled Optical Surfacing

Yajun Wang [1,2], Yunfei Zhang [2,*], Renke Kang [1] and Fang Ji [2]

[1] School of Mechanical Engineering, Dalian University of Technology, Dalian 116023, China; jjswang@xjtu.edu.cn (Y.W.); kangrk@dlut.edu.cn (R.K.)
[2] Institute of Machinery Manufacturing Technology, China Academy of Engineering Physics, Mianyang 621900, China; jfang2013@caep.cn
* Correspondence: zhangyf306@yeah.net; Tel.: +86-0286-5726-617

Abstract: The dwell time algorithm is one of the key technologies that determines the accuracy of a workpiece in the field of ultra-precision computer-controlled optical surfacing. Existing algorithms mainly consider meticulous mathematics theory and high convergence rates, making the computation process more uneven, and the flatness cannot be further improved. In this paper, a reasonable elementary approximation algorithm of dwell time is proposed on the basis of the theoretical requirement of a removal function in the subaperture polishing and single-peak rotational symmetry character of its practical distribution. Then, the algorithm is well discussed with theoretical analysis and numerical simulation in cases of one-dimension and two-dimensions. In contrast to conventional dwell time algorithms, this proposed algorithm transforms superposition and coupling features of the deconvolution problem into an elementary approximation issue of function value. Compared with the conventional methods, it has obvious advantages for improving calculation efficiency and flatness, and is of great significance for the efficient computation of large-aperture optical polishing. The flatness of φ150 mm and φ100 mm workpieces have achieved PVr_{150} = 0.028 λ and $PVcr_{100}$ = 0.014 λ respectively.

Keywords: ultra-precision machining; computer-controlled optical surfacing; dwell time algorithm; removal function; elementary approximation

Citation: Wang, Y.; Zhang, Y.; Kang, R.; Ji, F. An Elementary Approximation of Dwell Time Algorithm for Ultra-Precision Computer-Controlled Optical Surfacing. *Micromachines* **2021**, *12*, 471. https://doi.org/10.3390/mi12050471

Academic Editor: Xichun Luo

Received: 23 March 2021
Accepted: 16 April 2021
Published: 21 April 2021

1. Introduction

With the rapid increasing requirements for the fabrication of high-precision optical elements in modern optical systems, several advanced deterministic optical surfacing technologies have been developed over the past decades, such as ultra-precision computer controlled optical surfacing (CCOS), magnetorheological finishing (MRF), ion-beam figuring (IBF), bonnet polishing (BP) [1,2]. These achieve precision material removal on certain workpiece areas by accurately controlling the dwell time on the elaborately predesigned polishing path. Therefore, the dwell time algorithm is one of the key elements in modern advanced deterministic optical surfacing technologies. Among them, most of the removal functions have the characteristics of rotational symmetry, but how to use this feature to develop a high-efficiency, high-precision dwell time algorithm is the current research focus.

In deterministic optical finishing technologies, the amount of material removal can be expressed as discrete two-dimensional convolution operations of the dwell time and removal functions. The dwell time algorithm is used to solve the deconvolution process and to ensure that the calculated dwell time not only meets the performance of machine tools, but also has a high surface error convergence efficiency. Various dwell time algorithms have earlier been proposed, including the Fourier transform method, the numerical iteration method, the matrix equation method. Ronald Aspden et al. [3] studied the polar and rectangular coordinates of the process in CCOS, and discussed the variation of the removal function with the radius of the workpiece in the gyrosymmetric correction process.

Jones et al. [4] proposed an iterative method for solving the dwell time function, studied the relationship between the flatness convergence efficiency and the removal function, and pointed out that only the symmetric central single-peak removal function could converge. The convergence accuracy of these methods is not high enough, and now they are seldom applied. Carnal et al. [5] introduced the linear equation method and solved the dwell time by adopting the LSQR method. Drueding et al. [6] proposed a series expansion solution. Waluschka et al. [7] presented a one-dimensional dwell time function algorithm for cylindrical workpieces based on a graphic method, and Shanbhag et al. [8] proposed an algorithm based on wavelet analysis. Zheng et al. [9] proposed a damped iterative method for solving the CCOS dwell time function. Zhou et al. [10] used the TSVD method to solve the linear equation model, which entailed further research. Wu et al. [11] proposed a solution based on discretized matrix equations using LSQR. Jiao et al. [12] and Jiang et al. [13] improved the traditional L–R algorithm. Taking into account the scanning path of the polishing tool and the tilt angle of the workpiece, Guo [14] proposed a dwell time algorithm to achieve rapid convergence of the accuracy of the optical mold. Pan et al. [15] proposed an improved dwell time calculation algorithm to optimize tool path planning in optical figuring. Li et al. [16] developed a positive dwell time algorithm with minimum equal extra material removal to consider the machine dynamics limitations. Li and Zhou [17] gave a solution algorithm of dwell time in a slope-based figuring model. Wang et al. [18] provided a quantitative study on the performances of dwell time algorithms in ion-beam figuring. Han et al. [19,20] proposed a Gaussian mixture model to model experimental removal functions and provided the dwell time algorithm according to the dynamic characteristics of the machine tool. These methods are mainly based on matrix equations, and the computational efficiency might be much lower especially for large-aperture optical elements, so the solution might not be smooth enough.

The existing dwell time algorithms are conducted mainly based on a meticulous mathematical theory and designed to pursue high convergence rate. Nonetheless, those methods do not adequately consider the distribution characteristics of the removal function and rarely incorporate the speed-smoothing issues that are closely related to convergence efficiency and machine tool motion implementation. Actually, the convergence rate of flatness is only between 1.1X and 1.3X [21] for most CNC machines; hence, it is unnecessary to pursue high convergence rates excessively.

In this paper, an elementary approximation method for solving the dwell time algorithm based on the symmetrical distribution of single-peak rotation of removal function is proposed. The proposed method has the characteristics of clear physical meaning and was verified by simulation and experiments. By using triangular approximation of the removal function, the initial surface shape is discretized reasonably and the approximate solution of dwell time is obtained. In this paper, the performance of the algorithm is verified through residence-time mathematical modeling, accuracy analysis, simulation and experimental research. The results showed that it performs well in the profile for smoothness and convergence efficiency.

2. Dwell Time Algorithm Model

2.1. Approximation Treatment of Removal Function

According to the measured residual error, the surface is polished to achieve a theoretical profile. To eliminate the residual error, the material removal function, generated by the polishing tool in a constant time (also called the removal function) [22–24], and the dwell time of the polishing tool should be known first. It is generally assumed that deterministic optical surfacing technology is a linear shift-invariant system, and the mathematical model of the convolution of the dwell time and removal functions being equal to the distribution of the removal amount is generally adopted, and this is given in Equation (1) [6]:

$$\Delta h(x, y) = R(x, y) * * D(x, y) \tag{1}$$

where $\Delta h(x, y)$ is the distribution function of removal amount, $R(x, y)$ is the removal function (also called influence function), and $D(x, y)$ is the dwell time function.

In some deterministic optical surfacing technologies, the removal function is distributed by rotational symmetry. Suppose an ideal removal function is a two-dimensional Gaussian distribution, as shown in Figure 1.

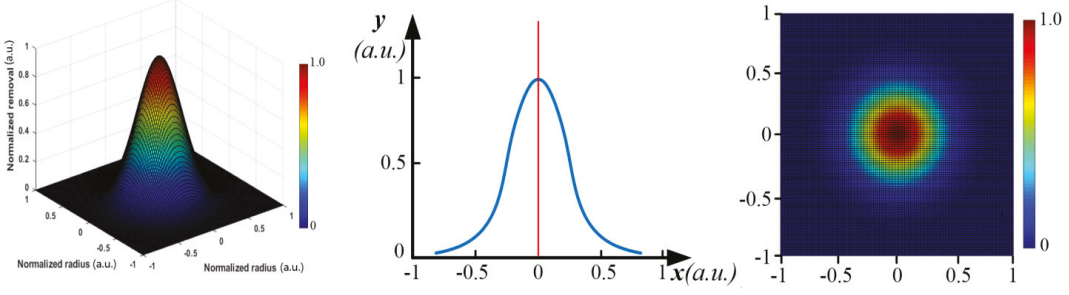

(**a**) (**b**) (**c**)

Figure 1. The basic distribution of removal function in some deterministic optical surfacing technologies: (**a**) Two-dimensional distribution of ideal Gaussian removal function, (**b**) One-dimensional distribution of CCOS removal function, (**c**) Kernel function distribution of ion beam figuring (IBF).

According to the actual characteristics of its distribution [25], the removal function is approximated as shown in Figure 2.

(**a**) (**b**)

Figure 2. Approximate distribution of the removal function: (**a**) One-dimensional approximation, (**b**) Two-dimensional approximation.

In the one-dimensional case, the removal function can be represented by an isosceles triangle distribution with height A and bottom $2R$, similar to the roof function in the one-dimensional finite element method. In the two-dimensional case, it is assumed that the kernel function can be represented by a conic distribution with a height of A and a bottom radius of R. This kind of approximation reflects the main distribution characteristics of the removal function and concentrates more than 80% of volume removal, which is completely acceptable in engineering.

2.2. Dwell Time Algorithm Model

2.2.1. One-Dimensional Analysis

The principle of an elementary approximation for a one-dimensional deconvolution is shown in Figure 3. The blue curve represents the target removal amount distribution curve $H(x)$, and the red curve is the actual removal amount distribution curve $h(x)$. The standard removal function has a maximum width of $2R$ and a height of A. The discretization

distance of the nodes is $L = R$. For each dwell node X_i, the dwell time function is set to $D_i = H(X_i)/A$, which eliminates superposition coupling and is only a simple elementary algebraic operation. It shows that the algorithm has the same accuracy as the trapezoidal method of the one-dimensional definite integral problem, and its approximation residual is a second-order small quantity.

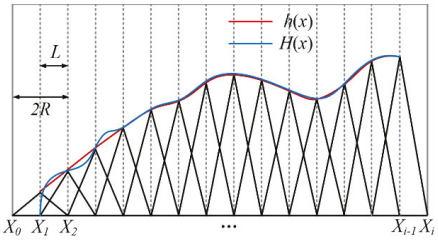

Figure 3. Elementary approximation solution for one dimension.

When $L = R$, the calculated residual error is already a second-order small quantity, but it can still be seen that the actual removal curve is not very smooth, which means that the smoothness of the optical processing surface is poor. When the discretization node is doubled and the spacing $L = R/2$, then $D_i = H(X_i)/2A$. The calculation principle of elementary geometric approximation for one-dimensional mesh refinement is shown in Figure 4.

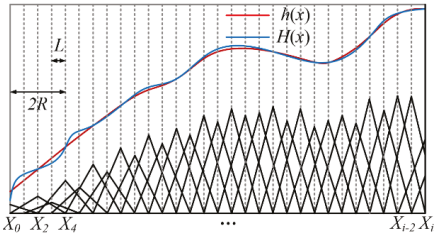

Figure 4. Mesh refinement principle for one dimension.

Generally, let $L = R/2^n$, and the distribution function of target removal amount is $H(x) = 2^n \cdot H(x)/2^n$. The discretized node set $\{X_i\}$ is divided into 2^n groups. The node spacing in each group is $L = R$, and the phase difference between each group of nodes is an integer multiple of $R/2^n$ in turn. Each set of nodes after partition is decoupled according to Figure 3, and then $D_i = H(X_i)/2^n/A$. In this way, the actual processing curve gradually becomes smooth.

According to the above analysis, the basic criteria for the elementary approximation of one-dimensional deconvolution are as follows:

1. It is acceptable to use an isosceles triangle as an approximate expression of the removal function in engineering;
2. The discretization distance of the nodes should not be more than half of the width of the removal function; otherwise, the deconvolution calculation will lose the ability to approximate;
3. When the node spacing is doubled, the time weight of each node is reduced by half, so the total time remains basically unchanged. The dwell time of the subdivided nodes is not the interpolation between the original discrete nodes, but the redistribution of the dwell time. The physical meaning is that the total removal amount is constant, and the removal function is constant, so the total time is basically conserved;

4. The approximation residual of approximate solution is the same as that of definite integral trapezoid method, which is a second-order small quantity.

2.2.2. Two-Dimensional Analysis

The orthogonal grid M is divided according to the spacing R. The coordinates of each grid node are (x_i, y_j), and the target removal amount on the node is H (x_i, y_j). The plane distribution is discussed first, as shown in Figure 5.

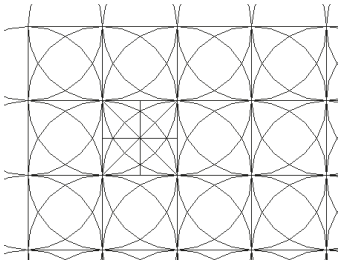

Figure 5. Mesh generation.

Let the removal function be a conic distribution and the center of the conic be the origin. The expression under the rectangular coordinate system is shown as follows:

$$\begin{cases} \varphi_{ij}(x,y) = \frac{A}{R}\left(R - \sqrt{(x-x_i)^2 + (y-y_j)^2}\right), (x-x_i)^2 + (y-y_j)^2 \le R^2 \\ \varphi_{ij}(x,y) = 0, (x-x_i)^2 + (y-y_j)^2 > R^2 \end{cases} \quad (2)$$

Where R is the radius of the circular support region of the removal function, and A is the peak value of the removal function center. The expression in polar coordinate form is shown as follows:

$$\begin{cases} \varphi_{ij}(\rho,\theta) = \frac{A}{R}\left(R - \sqrt{(\rho\cos\theta - \rho_{ij}\cos\theta_{ij})^2 + (\rho\sin\theta - \rho_{ij}\sin\theta_{ij})^2}\right), \\ \qquad \sqrt{(\rho\cos\theta - \rho_{ij}\cos\theta_{ij})^2 + (\rho\sin\theta - \rho_{ij}\sin\theta_{ij})^2} \le R \\ \varphi_{ij}(\rho,\theta) = 0, \sqrt{(\rho\cos\theta - \rho_{ij}\cos\theta_{ij})^2 + (\rho\sin\theta - \rho_{ij}\sin\theta_{ij})^2} > R \end{cases} \quad (3)$$

On the mesh, the removal function is simplified as follows:

$$\begin{cases} \varphi_i(x) = \frac{A}{R}(R - fabs(x - x_i)), (x-x_i)^2 \le R^2 \\ \varphi_i(x) = 0, (x-x_i)^2 > R^2 \end{cases} \quad (4)$$

Or the following polar form:

$$\begin{cases} \varphi_j(y) = \frac{A}{R}(R - fabs(y - y_j)), (y-y_j)^2 \le R^2 \\ \varphi_j(y) = 0, (y-y_j)^2 > R^2 \end{cases} \quad (5)$$

Where *fabs* represents the function of taking absolute value.

Suppose that each node (x_i, y_j) of the grid is superimposed with a removal function φ_{ij} of Equation (2) above, which has the same weight. Then, for the interior of the region M, according to the symmetry, only the case of the middle region $R \times R$ needs to be considered. The edge of the whole grid area is special and will not be discussed here.

For the grid area, it is customary to take the lower left corner of the grid as the origin O, so the center of the removal function is respectively located at the four corners of the

grid, as shown in Figure 6. The green lines are auxiliary lines, the red lines are distances from each corner nodes, and P is an arbitrary point in the polishing area. Set the node number of O as (i, j), OP = r_1, ∠POC = θ_1, CP = r_2, ∠PCB = θ_2, BP = r_3, ∠PBA = θ_3, AP = r_4, and ∠PAO = θ_4 to give the following:

$$\begin{cases} r_{ij} = 0, \theta_{ij} = 0 \\ r_{ij+1} = R, \theta_{ij+1} = 0 \\ r_{i+1j+1} = \sqrt{2}R, \theta_{i+1j+1} = \frac{\pi}{4} \\ r_{i+1j} = R, \theta_{i+1j} = \frac{\pi}{2} \end{cases} \tag{6}$$

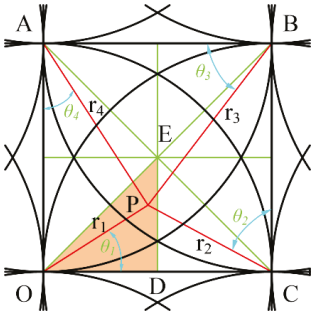

Figure 6. Superposition distribution map in grids.

According to Equation (3), there are the following:

$$\begin{cases} \varphi_{ij}(r_1, \theta_1) = \frac{A}{R}(R - r_1) \\ \varphi_{ij+1}(r_2, \theta_2) = \frac{A}{R}(R - r_2) \\ \varphi_{i+1j+1}(r_3, \theta_3) = \frac{A}{R}(R - r_3) \\ \varphi_{i+1j}(r_4, \theta_4) = \frac{A}{R}(R - r_4) \end{cases} \tag{7}$$

For a discrete mesh, due to the symmetry, only one-eighth of the triangular EOD area in the grid needs to be considered. This area can be further divided into four subareas: boundary line, M1, M2, and M3. For each subregion, only the value range of any point in the region under the function of each removal function (the maximum and minimum values) can be considered for evaluating the approximation ability of the approximate solution. The points where the maximum and minimum are located are the feature points in each square. According to the symmetry, these feature points must be obtained on the symmetry axis or the boundary of the square.

Similar to the one-dimensional case, let $L = R/2^n$, and the distribution function of target removal amount is $H(x) = 2^n \cdot H(x)/2^n$. The discretized node set (x_i, y_j) is divided into 2^n groups. The node spacing in each group is $L = R$, and the phase difference between each group of nodes is an integer multiple of $R/2^n$ in turn. Each set of nodes after partition is decoupled as above, and then there is $D_i = H(x_i, y_j)/(2^n A)$. The basic criteria for the primary approximation of two-dimensional deconvolution are as follows:

(1) It is acceptable to use cone as an approximate expression of the removal function in engineering.
(2) The distance of node discretization should not be larger than the radius of the removal function support domain; otherwise, the deconvolution calculation based on this method will lose the ability to approximate.

(3) When the node spacing is doubled, the time weight of each node is reduced by half, so the total time remains basically unchanged.
(4) The approximation residual of the elementary geometric approximation method for two-dimensional deconvolution is completely acceptable compared with the actual polishing convergence rate.

2.3. Dwell Time Algorithm Analysis

2.3.1. Split Line Value Analysis

In the real polishing case, the workpiece surface is a two-dimensional planar. For each meridian segment or latitude segment, there are only two kernel functions. At this time, the superposition value of the removal function is always A, as shown in Figure 7.

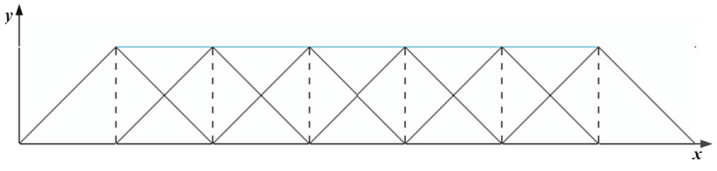

Figure 7. Schematic diagram of value taken on longitude and latitude line.

For example, let $x_i + 1 > x > x_i$, $x_{i+1} = x_i + R$, then the value on the grid is determined by Equation (8).

$$f = \varphi_i(x) + \varphi_{i+1}(x) = \frac{A}{R}(R - (x - x_i)) + \frac{A}{R}(R - (x_{i+1} - x)) = A \tag{8}$$

2.3.2. Area M1 Value Analysis

The point P is located in the region M1 and is acted on by four removal functions as shown in Figure 8.

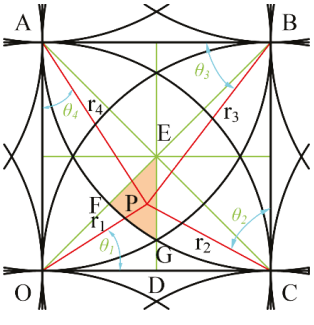

Figure 8. Four kernel function scopes.

According to Equations (3), (6) and (7), at this time the value of any point in M1 is determined by Equation (9).

$$f = \varphi_{ij}(r_1, \theta_1) + \varphi_{ij+1}(r_2, \theta_2) + \varphi_{i+1j+1}(r_3, \theta_3) + \varphi_{i+1j}(r_4, \theta_4) = \frac{A}{R}(4R - (r_1 + r_2 + r_3 + r_4)) \tag{9}$$

The relationships of each parameter are as follows:

$$\begin{aligned} r_2 &= \sqrt{(r_1\cos\theta_1)^2 + (R - r_1\cos\theta_1)^2}, \theta_2 = Arcctg(\tfrac{r_1\sin\theta_1}{R - r_1\cos\theta_1}) \\ r_3 &= \sqrt{(r_2\cos\theta_2)^2 + (R - r_2\cos\theta_2)^2}, \theta_3 = Arcctg(\tfrac{r_2\sin\theta_2}{R - r_2\cos\theta_2}) \\ r_4 &= \sqrt{(r_3\cos\theta_3)^2 + (R - r_3\cos\theta_3)^2}, \theta_4 = Arcctg(\tfrac{r_3\sin\theta_3}{R - r_3\cos\theta_3}) \\ &\left(\sqrt{2} - 1\right)\mathrm{R} \le r_1 \le \tfrac{\sqrt{2}}{2}R, \tfrac{5\pi}{36} \le \theta_1 \le \tfrac{\pi}{4} \end{aligned} \tag{10}$$

According to the symmetry, when point P is located at the vertex G of EFG, that is, $r_3 = r_4 = R$, $r_1 = r_2 = \sqrt{2 - \sqrt{3}}R$, making the sum of r_1+r_2+r_3+r_4 the maximum, then the minimum value of the function in this area is:

$$f_{\min} = 2(1 - \sqrt{2 - \sqrt{3}})A \approx 0.9647A \tag{11}$$

Since the sum of any two sides of a triangle is greater than the third side, it can be known that when P is located at the center of the square; that is, $r_1 = r_2 = r_3 = r_4 = \sqrt{2}R/2$, the sum of r_1+r_2+r_3+r_4, is a minimum, so the maximum value in this area is

$$f_{\max} = 4\frac{A}{R}(R - \frac{\sqrt{2}}{2}R) \approx 1.172A \tag{12}$$

2.3.3. Area M2 Value Analysis

The point P is located in the region M2 and is acted on by three removal functions as shown in Figure 9.

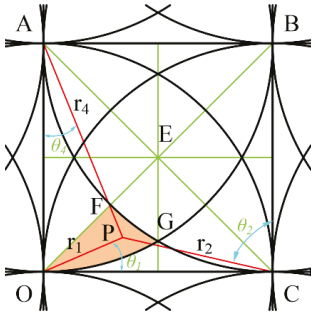

Figure 9. Three removal function scopes.

According to Equation (3), (6) and (7), at this time, the value of any point in M2 is determined by Equation (13).

$$f = \varphi_{ij}(r_1, \theta_1) + \varphi_{ij+1}(r_2, \theta_2) + \varphi_{i+1j}(r_4, \theta_4) = \frac{A}{R}(3R - (r_1 + r_2 + r_4)) \tag{13}$$

The relationships of each parameter are as follows:

$$\begin{aligned} r_2 &= \sqrt{(r_1\cos\theta_1)^2 + (R - r_1\cos\theta_1)^2}, \theta_2 = Arcctg(\tfrac{r_1\sin\theta_1}{R - r_1\cos\theta_1}) \\ r_3 &= \sqrt{(r_2\cos\theta_2)^2 + (R - r_2\cos\theta_2)^2}, \theta_3 = Arcctg(\tfrac{r_2\sin\theta_2}{R - r_2\cos\theta_2}) \\ r_4 &= \sqrt{(r_3\cos\theta_3)^2 + (R - r_3\cos\theta_3)^2}, \theta_4 = Arcctg(\tfrac{r_3\sin\theta_3}{R - r_3\cos\theta_3}) \\ 0 &\le r_1 \le \sqrt{2-\sqrt{3}}R, 0 \le \theta_1 \le \tfrac{\pi}{4} \end{aligned} \tag{14}$$

According to the symmetry, when point P is located at the vertex G of EFG, that is, $r_4 = R$, $r_1 = r_2 = \sqrt{2-\sqrt{3}}R$, making the sum of r_1+r_2+r_4 the maximum, then the minimum value of the function in this area is:

$$f_{\min} = 2\left(1 - \sqrt{2-\sqrt{3}}\right)A \approx 0.9647A \tag{15}$$

According to the symmetry, when point P is located at the vertex G of EFG, that is, $r_1 = 0$, $r_2 = r_4 = R$, making the sum of $r_1 + r_2 + r_4$ the minimum, then the maximum value in this area is:

$$f_{\max} = A \tag{16}$$

2.3.4. Area M3 Value Analysis

The point P is located in the region M2 and is acted by two removal functions as shown in Figure 10.

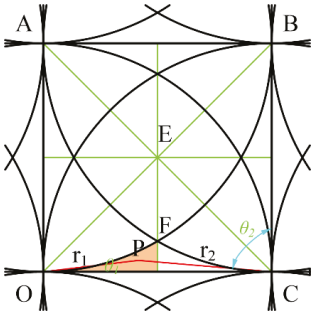

Figure 10. Two removal function scopes.

According to Equation (3), (6) and (7), at this time, the value of any point in M3 is determined by Equation (17).

$$f = \varphi_{ij}(r_1, \theta_1) + \varphi_{ij+1}(r_2, \theta_2) = \frac{A}{R}(2R - (r_1 + r_2)) \tag{17}$$

The relationships of each parameter are as follows:

$$\begin{aligned} r_2 &= \sqrt{(r_1\cos\theta_1)^2 + (R - r_1\cos\theta_1)^2}, \theta_2 = Arcctg(\tfrac{r_1\sin\theta_1}{R - r_1\cos\theta_1}) \\ 0 &\le r_1 \le \sqrt{2-\sqrt{3}}R, 0 \le \theta_1 \le \tfrac{5\pi}{36} \end{aligned} \tag{18}$$

According to the geometric relationship and symmetry, when point P is located at the vertex G of a curved triangle, that is, $r_1 = r_2 = \sqrt{2-\sqrt{3}}R$, the sum of $r_1 + r_2$ is the maximum, then the following function obtains the minimum value:

$$f_{\min} = 2(1 - \sqrt{2-\sqrt{3}})\mathrm{A} \approx 0.9647A \tag{19}$$

When point P is located on the side of the curved triangle OD, that is, $r_1 + r_2 = R$, the sum of $r_1 + r_2$ is the smallest, and the function obtains the maximum value:

$$f_{\max} = A \tag{20}$$

2.3.5. Numerical analysis

Figure 11 is a cloud picture of simulation calculation of an equal weight superposition distribution of removal function in the middle area. The distribution characteristics are consistent with the theoretical analysis.

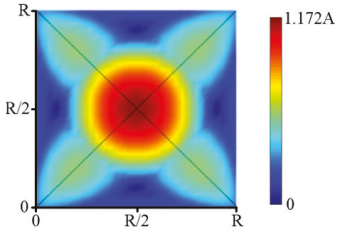

Figure 11. Simulation results of removal function superposition.

According to the results of the above analysis, on the whole grid the maximum and minimum values of the weight superposition distribution of the removal function are as follows:

$$\begin{aligned} f_{\min} &= 2\left(1 - \sqrt{2-\sqrt{3}}\right)A \approx 0.9647A \\ f_{\max} &= 4(1 - \tfrac{\sqrt{2}}{2})A \approx 1.172A \end{aligned} \tag{21}$$

This reflects the approximation ability of the conic distribution removal function to the plane, that is, the error level based on the elementary approximation method. The convergence accuracy of the calculation is much higher than the actual polishing convergence rate.

More generally, if each removal function is weighted according to the value of the surface distribution at the center, the conical distribution removal function can approximate the general surface better. That is to say, for any initial error distribution, the dwell time function the kernel of which is a cone distribution can be approximately determined by the weight of the kernel's center. At this time, the higher deconvolution problem can be simplified to a basic function-value calculation problem.

3. Simulations

The example of a two-dimensional deconvolution based on an elementary approximation is shown below. Three sets of simulations use the cone distribution removal function, and the removal amount distribution is a plane, sphere and arbitrary surface, respectively. The dwell time function is solved by the elementary approximation method proposed in this paper. The results are shown in Figures 12–14.

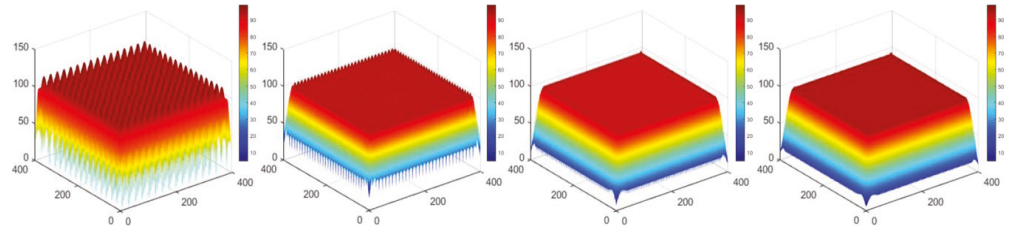

(**a**) (**b**) (**c**) (**d**)

Figure 12. Approximation results for the distribution of plane removal amount (**a**) Grid spacing L = R, (**b**) Grid spacing L = R/2, (**c**) Grid spacing L = R/4, (**d**) Ideal plan distribution.

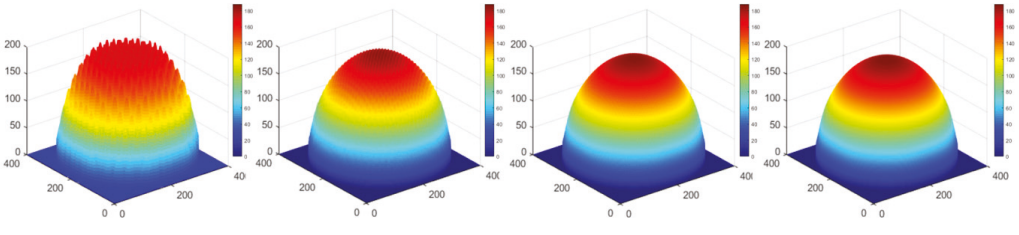

(**a**) (**b**) (**c**) (**d**)

Figure 13. Approximation results for the distribution of spherical removal (**a**) Grid spacing $L = R$, (**b**) Grid spacing $L = R/2$, (**c**) Grid spacing $L = R/4$, (**d**) Ideal hemispheric distribution.

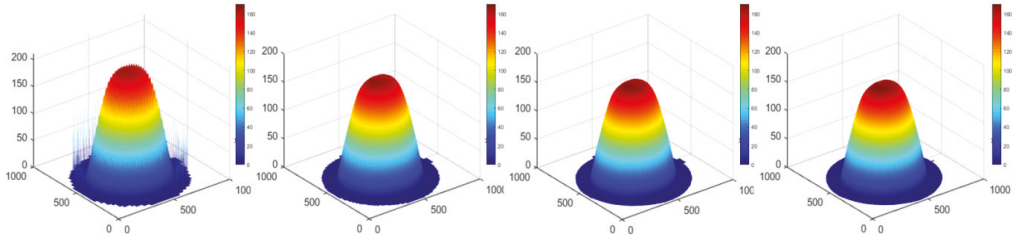

(**a**) (**b**) (**c**) (**d**)

Figure 14. Approximation results for the distribution of arbitrary removal (**a**) Grid spacing $L = R$, (**b**) Grid spacing $L = R/2$, (**c**) Grid spacing $L = R/4$, (**d**) Original surface distribution.

Apparently, the numerical simulation results of a deconvolution calculation based on an elementary approximation are satisfactory.

4. Results and Discussion

4.1. Experiment Setup and the Parameters

To validate the effectiveness of the proposed algorithm, repetitious experimental studies on flatness figuring was carried out based on the self-developed ion-beam figuring (IBF) machine. The experiment setup is shown in Figure 15. It can process planar, spherical and aspheric parts with a maximum size of 300 mm × 300 mm, and the positioning accuracy of the linear axis is below 0.005 mm. This machine can be used for the corresponding

experimental verification of the dwell time solving algorithm. The specific parameters of the polishing processing are shown in Table 1.

Figure 15. The self-developed IBF machine.

Table 1. Parameters of the polishing process.

Parameter	Value
Ion beam voltage	800 V
Ion beam current	60 mA
Ion beam Angle	0°
Processing distance	150 mm
Grating spacing	2 mm

IBF spots were taken on the IBF machine, and the results are shown in Figure 16. The polishing result was detected by the INF300H-LP-WM interferometer made in China, with RMS repeatability of less than 0.3 nm. The removal function result of IBF, shown in Figure 16, was tested on a fixed point, and polishing time was 60 s. The peak removal rate (PRR) of influence function was 0.30614 λ/min, where λ was 658 nm, and the volume removal rate (VRR) was 0.056474 mm^3/min.

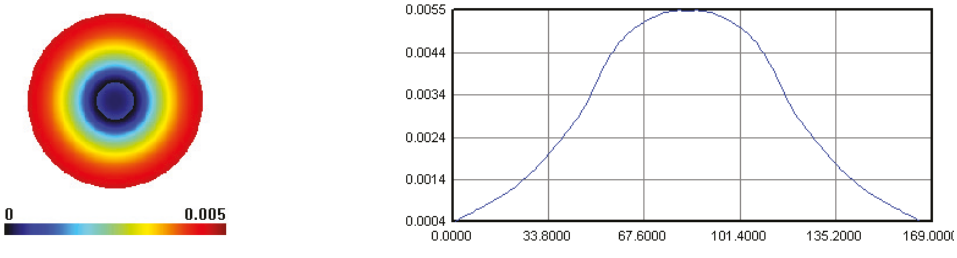

(**a**) (**b**)

Figure 16. Removal function in case 1: (**a**) surface map, (**b**) surface profile.

4.2. Results and Discussion

4.2.1. Experiment Case 1

The workpiece used for figuring is silica flat and the diameter is φ120 mm. The scanning path is in raster with a step of 1.5 mm and spacing of 3.0 mm. Initial flatness was PV 0.259 λ, RMS 0.050 λ; Predicted flatness was PV 0.051 λ and RMS 0.004 λ, with a convergence rate of 80.0% and 92%, respectively.

Experimental result indicated that full-aperture machined flatness was PV 0.077 λ and RMS 0.013 λ with a convergence rate of 70.3% and 74.5% respectively, where the missing

data in the periphery was caused by the fixture. The aperture machined flatness of 90% was PV 0.063 λ and RMS 0.012 λ with a convergence rate of 64% and 70% respectively, as shown in Figures 17 and 18.

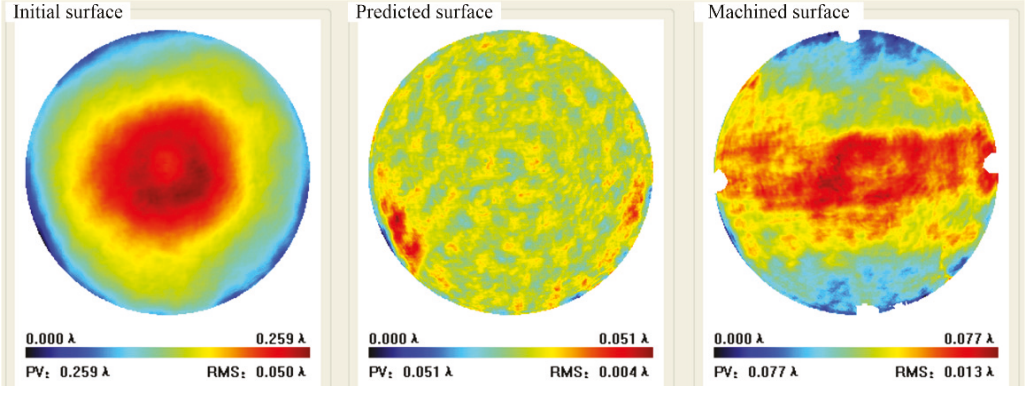

Figure 17. Full aperture data in case 1: (**a**) Initial surface, (**b**) Predicted surface, (**c**) Machined surface.

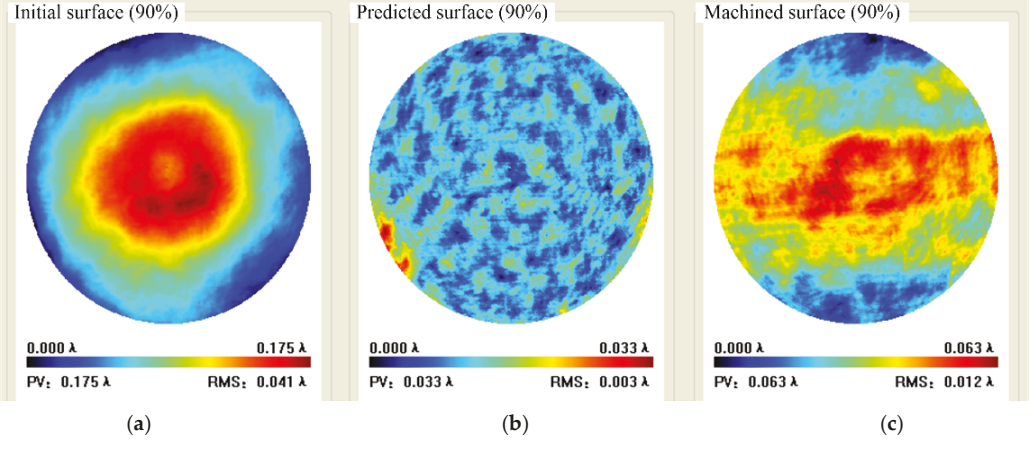

Figure 18. Case 1 90% aperture data: (**a**) Initial surface, (**b**) Predicted surface, (**c**) Machined surface.

4.2.2. Experiment Case 2

The universal measuring software was employed. The PRR of influence function was 0.244 λ/min, and the VRR was 0.0098 mm^3/min as shown in Figure 19.

The workpiece is fused silica with diameter of φ170 mm. Surface map is measured using the relative accuracy method. Initial flatness of φ150 mm aperture is $PV_{\varphi 150}$ = 0.048 λ, $RMS_{\varphi 150}$ = 0.008 λ, and those of φ100 mm aperture are $PV_{\varphi 100}$ = 0.030 λ, $RMS_{\varphi 100}$ = 0.007 λ respectively, as shown in Figure 20.

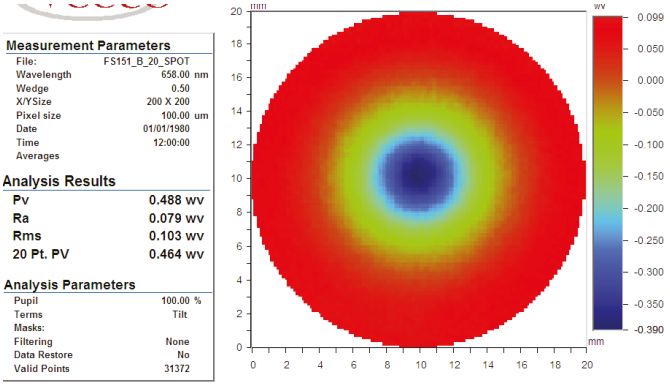

Figure 19. Removal function in case 2.

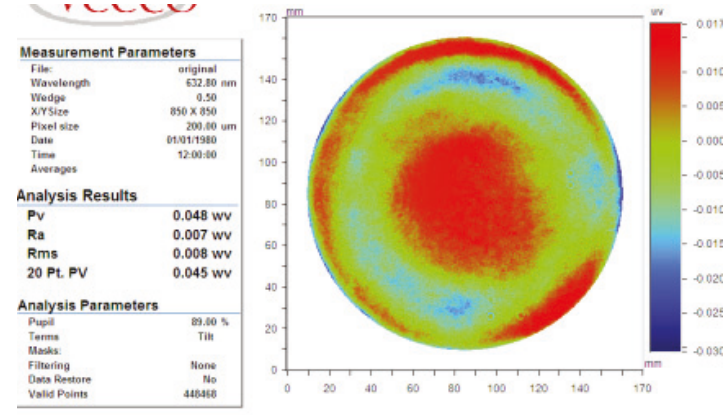

(**a**)

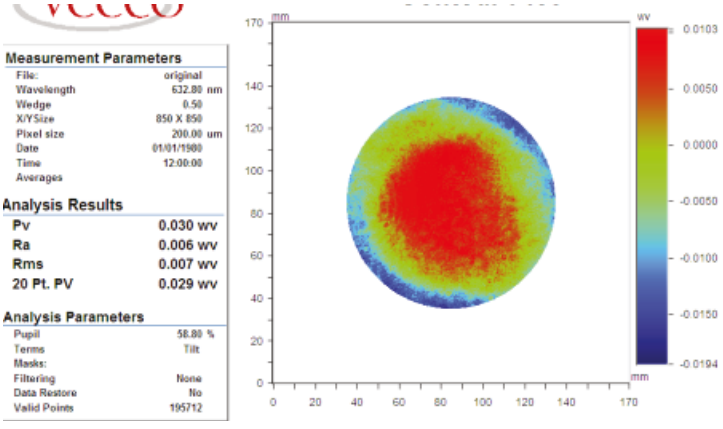

(**b**)

Figure 20. Initial surface in case 2: (**a**) φ150 mm aperture, (**b**) φ100 mm aperture.

The scanning path was rasterized with 2 mm spacing, and the predicted machine time was 83.8 min; the predicted flatness of φ150 mm aperture was PV_{c150} = 0.025 λ, RMS_{c150} = 0.003 λ; and those of φ100 mm were PV_{c100} = 0.014 λ; RMS_{c100} = 0.002 λ, as illustrated in Figure 21.

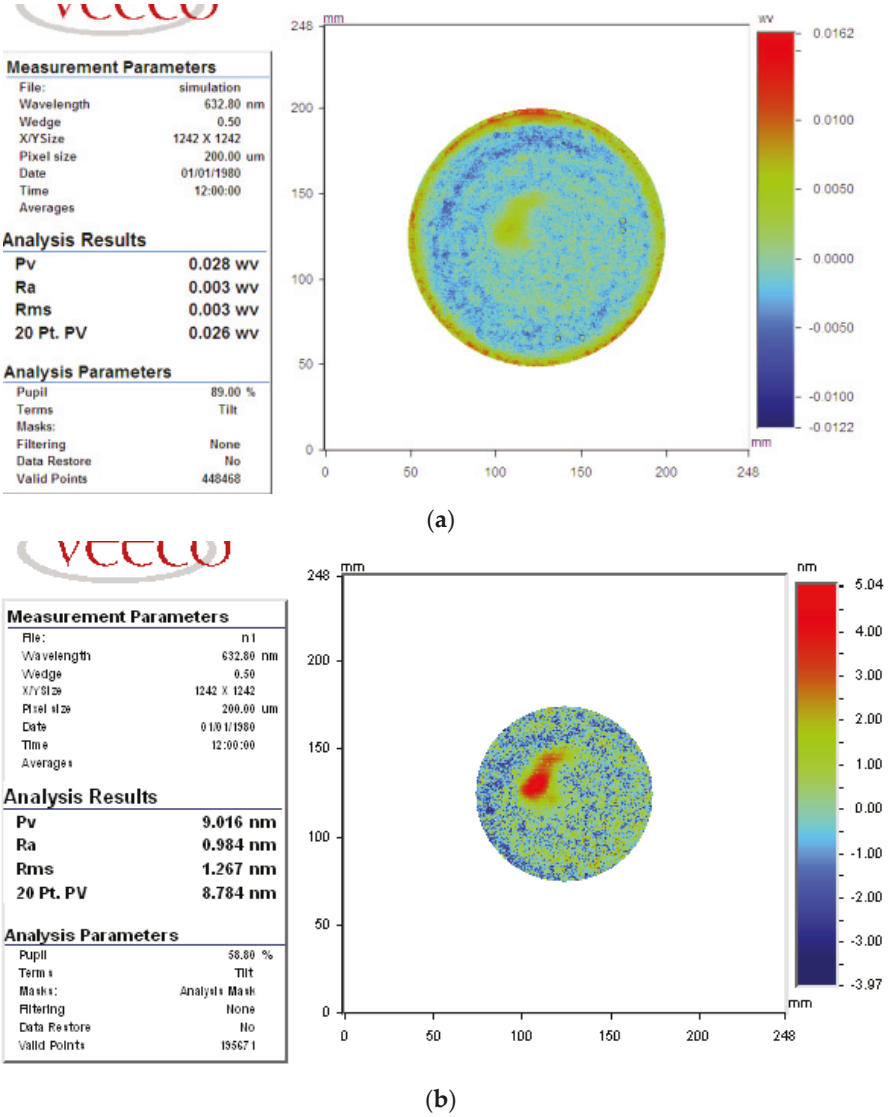

Figure 21. Predicted surface in case 2 (**a**) φ150 mm aperture (**b**) φ100 mm aperture.

The practical polishing time was 84 min. The surface map was also measured using the relative accuracy method. The polished flatness of the φ150 mm aperture was PV_{r150} = 0.028 λ, and RMS_{r150} = 0.005 λ, and those of φ100 mm were PV_{cr100} = 0.014 λ, and RMS_{c100} = 0.002 λ, as shown in Figure 22.

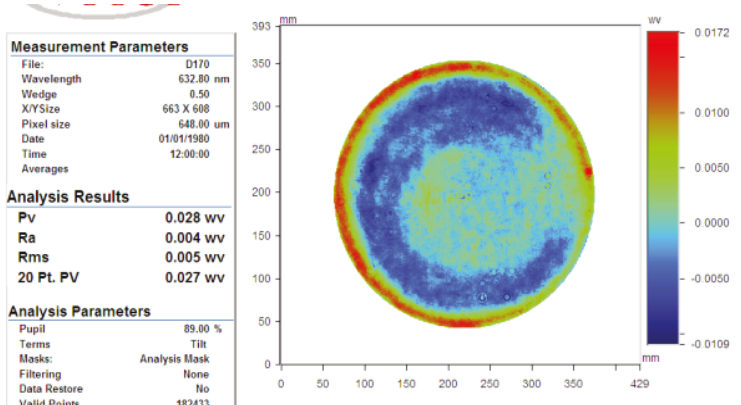

(**a**)

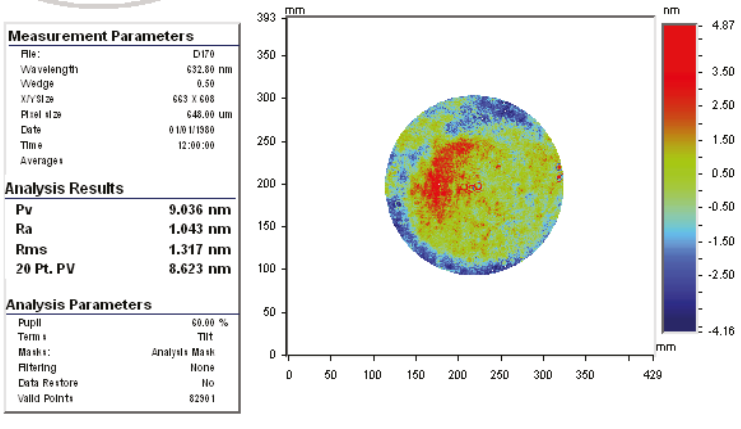

(**b**)

Figure 22. Polished surface in case 2: (**a**) φ150 mm aperture, (**b**) φ100 mm aperture.

Simulated convergence rate was

$$\eta_{c150} = \frac{pv_{o150} - pv_{c150}}{pv_{o150}} \times 100\% = 47.9\% \tag{22}$$

And the practical convergence rate was

$$\eta_{r150} = \frac{pv_{r150} - pv_{r150}}{pv_{r150}} \times 100\% = 41.7\% \tag{23}$$

Taking the surface PV value of φ100 mm aperture as the evaluation index, the predicted convergence rate was 52.0%, and the practical convergence rate was 51.9%.

5. Conclusions

In this paper, an elementary approximation of the dwell time algorithm for single-peak rotational symmetry removal function was presented. The work showed that it is engineeringly acceptable to use the cone distribution as the removal function to approximate expressions of all the subaperture polishing with a single-peak rotational symmetry removal function, such as CCOS, IBF, or BP. The dwell time algorithm model and compu-

tation method were given. When the distance of node discretization was not more than the radius of the support domain of removal function, the coupling characteristic of the deconvolution problem could be eliminated by using the elementary approximation solution proposed in this paper. Theoretical analysis, numerical simulation and experimental results show that the proposed method had a lower calculated residual error than the initial value by one order of magnitude, and had a higher approximation ability. The flatness of φ150 mm and φ100 mm workpieces achieved PVr_{150} = 0.028 λ and $PVcr_{100}$ = 0.014 λ, respectively.

In contrast to conventional dwell time algorithms, this work transformed the superposition and coupling features of the deconvolution problem into a simple calculation of the discretization function value. When the discrete nodes were doubled, the time weight of each node was then halved; consequently, the total time remained unchanged. The approximation ability or smoothness of the deconvolution result was greatly increased, which agreed with the engineering reality that total polishing time remains unchanged if the total removal amount and removal function are unchanged. Compared with conventional methods, the proposed algorithm has obvious advantages for improving calculation efficiency and smoothness, which is of great significance for the efficient computation of large-aperture optical polishing.

Nevertheless, the calculation accuracy of the proposed dwell time algorithm is related to the symmetry of the removal function and its approximation error. Meanwhile, the dwell time algorithm has a limited ability to correct mid-to-high frequency errors determined by the sampling characteristics of the discretization nodes and the scale of the removal function. The approximation error in the edge area of the workpiece needs further analysis.

Author Contributions: All authors have contributed to the study conception and design. Y.W. designed the experiments and wrote the paper. Y.Z. performed the experiments and analyzed the data. R.K. and F.J. supervised the whole project and gave advices on manuscript editing. All authors read and approved the final manuscript.

Funding: This research was funded by the National Natural Science Foundation of China (No. 52005463); the Science Challenge Project (No.TZ2016006-0504-01); High-end CNC Machine Tools and Basic Manufacturing Equipment Major National Science and Technology Project (2017ZX04022001); Laboratory of Precision Manufacturing Technology, CAEP.

Data Availability Statement: NOMENCLATURE is contained within the main text.

Acknowledgments: The authors thank the technical support from peer fellows.

Conflicts of Interest: The authors declare no conflict of interest.

Nomenclature

R(x, y)	Removal function
D(x, y)	Dwell time function
H (Xi, Yj)	Target removal amount
A	Peak value of the removal function center
fabs	Function of taking absolute value
t(xi, yi)	Dwell time at the i th path node
h(xk, yk)	Desired amount of removed material at the k th figure-control node
Nt	Total number of the path nodes
Nh	Total number of the figure-control nodes
r(xk-xi, yk-yi)	Amount of removed material at the k th figure-control node
L	Discretization distance of nodes
CCOS	Computer controlled optical surfacing
MRF	Magnetorheological finishing
IBF	Ion beam figuring
BP	Bonnet polishing

References

1. Zhao, Q.Z.; Zhang, L.; Han, Y.J.; Fan, C. Polishing path generation for physical uniform coverage of the aspheric surface based on the Archimedes spiral in bonnet polishing. *Proc. Inst. Mech. Eng. B J. Eng. Manuf.* **2019**, *233*, 2251–2263. [CrossRef]
2. Zhao, Q.Z.; Zhang, L.; Fan, C. Six-directional pseudorandom consecutive unicursal polishing path for suppressing mid-spatial frequency error and realizing consecutive uniform coverage. *Appl. Opt.* **2019**, *58*, 8529–8541. [CrossRef] [PubMed]
3. Aspden, R.; Mcdonough, R.; Nitchie, F.R. Computer assisted optical surfacing. *Appl. Opt.* **1972**, *11*, 2739–2747. [CrossRef] [PubMed]
4. Jones, R.A. Optimization of computer controlled polishing. *Appl. Opt.* **1977**, *16*, 218–224. [CrossRef] [PubMed]
5. Carnal, C.L.; Egert, C.M.; Hylton, K.W. Advanced matrix-based algorithm for ion-beam milling of optical components. In Proceedings of the Current Developments in Optical Design and Optical Engineering II, SPIE, San Diego, CA, USA, 20–21 July 1992; Volume 1752, pp. 54–62.
6. Drueding, T.W.; Fawcett, S.C.; Wilson, S.R.; Bifano, T.G. Ion beam figuring of small optical components. *Opt. Eng.* **1995**, *34*, 3565.
7. Waluschka, E. Cylindrical optic figuring dwell time optimization. In Proceedings of the International Symposium on Optical Science and Technology, SPIE, San Diego, CA, USA, 30–31 July 2000; Volume 4138, pp. 25–32.
8. Shanbhag, P.M.; Feinberg, M.R.; Sandri, G.; Horenstein, M.N.; Bifana, T.G. Ion-beam machining of millimeter scale optics. *Appl. Opt.* **2000**, *39*, 599–611. [CrossRef] [PubMed]
9. Zheng, L.G.; Zhang, X.J. A novel resistance iterative algorithm for CCOS. In Proceedings of the SPIE—The International Society for Optical Engineering, San Diego, CA, USA, 14 August 2006; Volume 6288, p. 62880N-1-9.
10. Zhou, L.; Dai, Y.F.; Xie, X.H.; Jiao, C.J.; Li, S.Y. Model and method to determine dwell time in ion beam figuring. *Nanotechnol. Precis. Eng.* **2007**, *5*, 107–112.
11. Wu, J.F.; Lu, Z.W.; Zhang, H.X.; Wang, T.S. Dwell time algorithm in ion beam figuring. *Appl. Opt.* **2009**, *48*, 3930–3937. [CrossRef] [PubMed]
12. Jiao, C.J.; Li, S.Y.; Xie, X. Algorithm for ion beam figuring of low-gradient mirrors. *Appl. Opt.* **2009**, *48*, 4090–4096. [CrossRef] [PubMed]
13. Bo, J.; Zhen, M. Dwell time method based on richardson-lucy algorithm. In Proceedings of the Space Optics and Earth Imaging and Space Navigation, SPIE, Beijing, China, 4–6 June 2017; Volume 10463.
14. Guo, J. Corrective finishing of a micro-aspheric mold made of tungsten carbide to 50 nm accuracy. *Appl. Opt.* **2015**, *54*, 5764–5770. [CrossRef] [PubMed]
15. Pan, R.; Zhang, Y.J.; Ding, J.B.; Cao, C.; Wang, Z.Z.; Jiang, T.; Peng, Y.F. Rationality optimization of tool path spacing based on dwell time calculation algorithm. *Int. J. Adv. Manuf. Technol.* **2016**, *84*, 2055–2065. [CrossRef]
16. Li, L.X.; Xue, D.L.; Deng, W.J.; Wang, X.; Bai, Y.; Zhang, F.; Zhang, X.J. Positive dwell time algorithm with minimum equal extra material removal in deterministic optical surfacing technology. *Appl. Opt.* **2017**, *56*, 9098–9104. [CrossRef] [PubMed]
17. Li, Y.; Zhou, L. Solution algorithm of dwell time in slope-based figuring model. In Proceedings of the AOPC 2017: Optoelectronics and Micro/Nano-Optics, SPIE, Beijing, China, 4–6 June 2017; Volume 10460.
18. Wang, Q.H.; Liang, Y.J.; Xu, C.Y.; Li, J.R.; Zhou, X.F. Generation of material removal map for freeform surface polishing with tilted polishing disk. *Int. J. Adv. Manuf. Technol.* **2019**, *102*, 4213–4226. [CrossRef]
19. Wan, S.L.; Zhang, X.C.; Wang, W.; Xu, M. Effect of pad wear on tool influence function in robotic polishing of large optics. *Int. J. Adv. Manuf. Technol.* **2019**, *102*, 2521–2530. [CrossRef]
20. Cao, Z.C.; Cheung, C.F.; Ho, L.T.; Liu, M.Y. Theoretical and experimental investigation of surface generation in swing process bonnet polishing of complex three-dimensional structured surfaces. *Precis. Eng.* **2017**, *50*, 361–371. [CrossRef]
21. Li, L.X.; Zheng, W.J.; Deng, L.G.; Wang, X.; Wang, X.K.; Zhang, B.Z.; Bai, Y.; Hu, H.X.; Zhang, X.J. Optimized dwell time algorithm in magnetorheological finishing. *Int. J. Adv. Manuf. Technol.* **2015**, *81*, 833–841. [CrossRef]
22. Han, Y.J.; Zhu, W.L.; Zhang, L.; Beaucamp, A. Region adaptive scheduling for time-dependent processes with optimal use of machine dynamics. *Int. J. Mach. Tools Manuf.* **2020**, *156*, 103589. [CrossRef]
23. Han, Y.J.; Duan, F.; Zhu, W.L.; Zhang, L.; Beaucamp, A. Analytical and stochastic modeling of surface topography in time-dependent sub-aperture processing. *Int. J. Mech. Sci.* **2020**, *175*, 105575. [CrossRef]
24. Zheng, W.M.; Cao, T.N.; Zhang, X.Z. Applications of a novel general removal function model in the CCOS. *Proc. Soc. Photo Opt. Instrum. Eng.* **2000**, *4231*, 51–58.
25. Ghigo, M.; Canestrari, R.; Spigal, D.; Novi, A. Correction of high spatial frequency errors on optical surfaces by means of ion beam figuring. *Proc. Soc. Photo Opt. Instrum. Eng. Conf. Ser.* **2007**, *6671*, 667114.

micromachines

MDPI

Article

The Influence of Crystal Orientation on Subsurface Damage of Mono-Crystalline Silicon by Bound-Abrasive Grinding

Wei Yang [1] and Yaguo Li [2,*]

[1] School of Aerospace Engineering, Xiamen University, Xiamen 361005, China; yangwei@xmu.edu.cn
[2] Fine Optical Engineering Research Center, Chengdu 610041, China
* Correspondence: yargolee@163.com

Abstract: Subsurface damage (SSD) produced in a grinding process will affect the performance and operational duration of single-crystal silicon. In order to reduce the subsurface damage depth generated during the grinding process by adjusting the process parameters (added), experiments were designed to investigate the influence of machining factors on SSD. This included crystal orientation, diamond grit size in the grinding wheel, peripheral speed of the grinding wheel, and feeding with the intention to optimize the parameters affecting SSD. Compared with isotropic materials such as glass, we considered the impact of grinding along different crystal directions <100> and <110> on subsurface damage depth (added). The Magnetorheological Finishing (MRF) spot technique was used to detect the depth of SSD. The results showed that the depth of SSD in silicon increased with the size of diamond grit. SSD can be reduced by either increasing the peripheral speed of the grinding wheel or decreasing the feeding rate of the grinding wheel in the <100> crystal orientation, if the same size of diamond grit was employed. In addition, we proposed a modified model around surface roughness and subsurface crack depth, which considered plastic and brittle deformation mechanisms and material properties of different crystal orientations. When the surface roughness (R_Z) exceeded the brittle-plastic transition's critical value R_{ZC} ($R_{ZC<100>} > 1.5$ μm, $R_{ZC<110>} > 0.8$ μm), cracks appeared on the subsurface. The experimental results were consistent with the predicted model, which could be used to predict the subsurface cracks by measuring the surface roughness. However, the model only gives the approximate range of subsurface defects, such as dislocations. The morphology and precise depth of plastic deformation subsurface defects, such as dislocations generated in the fine grinding stage, needed to be inspected by transmission electron microscopy (TEM), which were further studied.

Keywords: diamond grinding; single crystal silicon; subsurface damage; crystal orientation

Citation: Yang, W.; Li, Y. The Influence of Crystal Orientation on Subsurface Damage of Mono-Crystalline Silicon by Bound-Abrasive Grinding. *Micromachines* **2021**, *12*, 365. https://doi.org/10.3390/mi12040365

Academic Editor: Jiang Guo

Received: 7 March 2021
Accepted: 25 March 2021
Published: 28 March 2021

1. Introduction

Single-crystal silicon is widely used as a base material in solar cells, integrated circuits, and infrared optical systems. Silicon substrates are generally processed through cutting, grinding, thinning, and finally polishing. In the grinding process, bound-abrasive grinding has increasingly broad applications in the manufacturing of hard and brittle materials due to high efficiency in material removal and comparatively easy control of the surface figure [1]. Subsurface damage (SSD), which is mainly produced following the grinding process, must be removed in the subsequent processes such as Chemo-Mechanical Polishing (CMP). In silicon processing, SSD renders itself as amorphous layers, dislocations, subsurface cracks, etc. [2]. When cracks occur, the machining regime is referred to as "brittle mode machining"; if no crack appears, the machining mode will be in "ductile mode" [3]. Compared to the polishing process, grinding is more prone to brittle fracture and will induce cracks at the bottom of the subsurface. SSD will degrade the strength and reduce the lifetime of silicon substrate. Efforts have been made to suppress SSD induced from grinding, and to obtain a perfect surface.

Yan et al. [4] conducted diamond machining experiments on silicon specimens by using cutting tools with different rake angles and revealed that the SSD depths were increased with the increasing depths of the cut in grinding. Liu et al. [5] found that the change in regulation of the grinding-induced SSD was the same as the change in tendencies of the grinding force, and surface roughness. A number of SSD measurement techniques, such as the angled polishing method [6], ball dimpling [7], scanning infrared depolarization [8], cross-sectional transmission electron microscopy (TEM) [9], energy dispersive spectroscopy (EDS) [10], laser Raman spectroscopy technique [11], and the X-ray diffraction [12] method have been proposed.

The SSD should be removed in the subsequent processes. For these, SSD measurement techniques unavoidably changed or even destroyed the ground silicon surface, while nondestructive methods required high-performance measurement systems and could not be used in-situ. It is necessary to establish a mathematical model for measurement without destroying the sample. Many models have been proposed to evaluate the depth of subsurface cracks of brittle material caused by grinding in brittle mode. Lambropoulos et al. [13] established the relationship between the median crack depth and normal force of the optical glass based on the theory of fracture mechanics. Li et al. [14] established a relationship between surface roughness (SR) and SSD depth for optical materials based on the model established by Lambropoulos et al. Shen et al. [15] presented the relationship between the median crack depth and cutting depth for optical glass during the scratching process. Unlike isotropic materials like glass, single crystal silicon has anisotropy in the surface and exists through the process of brittle-ductile transition [16,17]. Zhang [18] developed an analytical model in the rotation grinding process to predict the SSD depth in the silicon wafer, which considered the effect of anisotropy in the grinding process. Li et al. [19] extended the model to the silicon obtained through the relationship between surface roughness and SSD depth by a CBN (Cubic Boron Nitride) grinding wheel. The SSD depth can be predicted by measuring surface roughness.

In this research, we carried out orthogonal experiments to investigate the SSD in the diamond wheel grinding of silicon. We detected the SSD through the Magnetorheological Finishing (MRF) spot technique, which measured the depth of SSD that was ground along <100> and <110> orientations. The experimental results indicated that the influence of process parameters, including crystal orientation, diamond grit size of the grinding wheels, and feeding rate on subsurface defects during the bound-grinding process, which could be used to reduce the SSD depth and improve the processing efficiency. Then, we proposed a modified model of the relationship between surface roughness (R_Z) and SSD by extending Li's model [14], which considered plastic and brittle deformation mechanism and material properties of different crystal orientations. The proposed model is expected to assess the subsurface damage depth by measuring the roughness of the surface (R_Z) during grinding.

2. Experiments

2.1. Grinding Samples

Single-crystal silicon samples (n-type, (100) plane) with a diameter of 50 mm and 5 mm thick were employed in the experiments. All the samples fixed to a platform with a magnetic clapping device were ground on an ultra-precision grinding machine (Magerle, Switzerland), as shown in Figure 1. To reduce the number of trials, and by extension the experimental costs, the orthogonal experiments that had taken the effects of grain size, wheel feed rate, and wheel rotation speed into consideration were carried out as shown in Table 1 [20]. Two sets of the grinding trials' feed directions were separately parallel to the surface crystallographic orientations of <100> and <110>, and the <110> orientations are at 45° angles to the <100> direction. To preclude possible subsurface damage induced before the trials, the grinding removal depth of all samples were both greater than 12 μm. The particular grinding conditions are listed in Table 2.

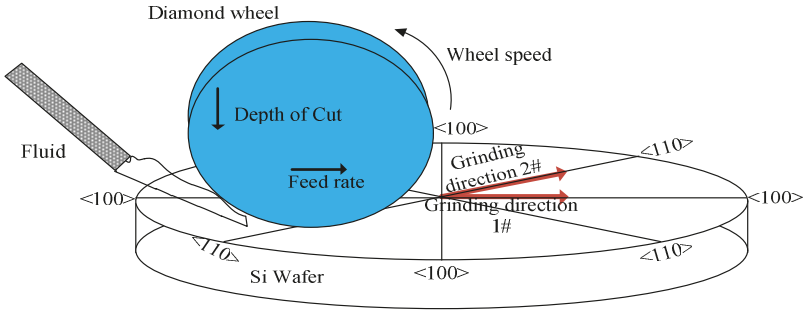

Figure 1. Schematic of trials of grinding along <100> and <110> orientation.

Table 1. Experimental parameters and levels.

Factors	Parameters	Levels		
		1	2	3
A	Grain model [10] (μm)	D15A (10–15)	D91 (75–90)	80# (180–212)
B	Wheel speed (m/s)	10	20	40
C	Feed rate (mm/min)	300	1000	3000
D	Depth of cut (μm)	5	10	15

Table 2. The experiment parameters and results (A, B represent the specimen along the <100> and <110> directions grinding).

NO.	Grain Model	Wheel Speed (m/s)	Feed Rate (mm/min)	Depth of Cut (μm)	<100> R_Z (μm)	<110> R_Z (μm)
A1 B1	D15A	10	300	5	0.4071	0.3914
A2 B2	D15A	20	1000	10	0.3061	0.3037
A3 B3	D15A	40	3000	15	0.2933	0.4486
A4 B4	D91	10	1000	15	5.4685	6.9261
A5 B5	D91	20	3000	5	6.043	6.9867
A6 B6	D91	40	300	10	3.2484	3.675
A7 B7	80#	10	3000	10	11.6924	12.9087
A8 B8	80#	20	300	15	6.3651	6.6319
A9 B9	80#	40	1000	5	7.9160	6.7404

2.2. The Surface Roughness Measurement of the Ground Specimens

To get the relationship between SSD and roughness quantitatively, we examined the surface roughness along the <100> and <110> orientations using a contact profilometer Taylor Hobson 1250XL (Taylor Hobson, Leicester, UK), which were perpendicular to the grinding direction as shown Figure 2. The length of measurement and cut-off were according to ISO 4288–1996. Each sample was examined for three randomly selected positions, raw data of which are shown in Figure 3.

2.3. The Sub-Surface Damage Measurement of the Ground Specimens

SSD is rather difficult to directly observe and detect since it often exists beneath the ground surface at a certain depth. Many methods of detection have been developed, both destructive [2,21–24] and non-destructive [25,26], for the damage, such as the dislocation, amorphous and poly-crystalline layers, and other nano defects, which are often observed through the transmission electron microscopy (TEM) at a high resolution [27].

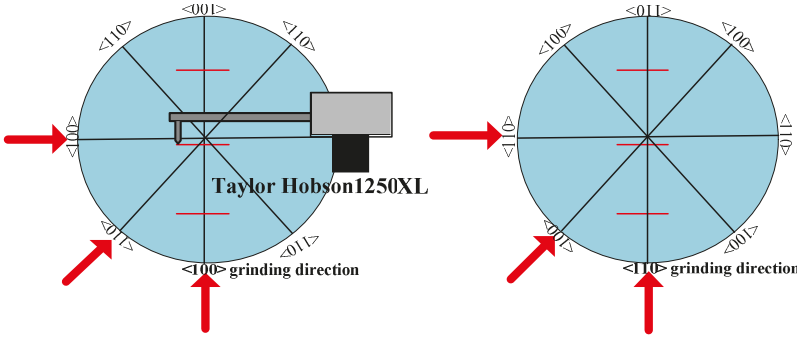

Figure 2. Measurement of the surface roughness of ground samples.

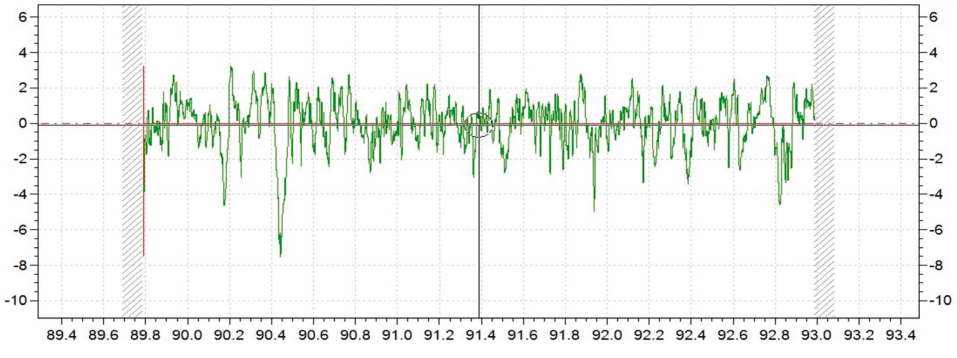

Figure 3. Surface roughness (R_Z) of the grinding surface.

Angle polishing [28] and cross-sectional microscopy [2] are commonly used to detect micro subsurface damage like subsurface cracks (SSC), which initiate from the brittle removal mode. The MRF spot technique is used to measure SSCs in this paper, which will not introduce the additional damage [29], and is more efficient compared with angle polishing and cross-sectional microscopy. The silicon samples were spotted at three random positions along the radial direction with a commercial MRF machine (QED Technologies, Q22-400X, Rochester, NY, USA) and etching with "HNA" solution (HF (49%):HNO_3 (70%):CH_3COOH = 1:3:10) for 15 minutes at room temperature to make the subsurface cracks observable, as shown in Figure 4a. After that, the samples were flushed immediately with water, the ground surface and polished surface at MRF was imaged with an optical microscope (Leica-Camera, Leica DM4000M, Wetzlar, Hesse-Darmstadt, Germany), the grinding-induced SSCs were observed, and the horizontal distance between the last crack and the polished boundary at both edges were recorded, as shown in Figure 4b. Finally, using a profilometer (VEECO, VEECO Dektak 150, Plainview, NY, USA), the spot-depth profiles were measured across the centerline of a MRF spot, as shown in Figure 4c, and the SSCs depth was measured by applying the horizontal distance of the last cracks obtained from the microscope to the depth profile that yielded the SSD depth. The presented SSD has an average of three spot measurements.

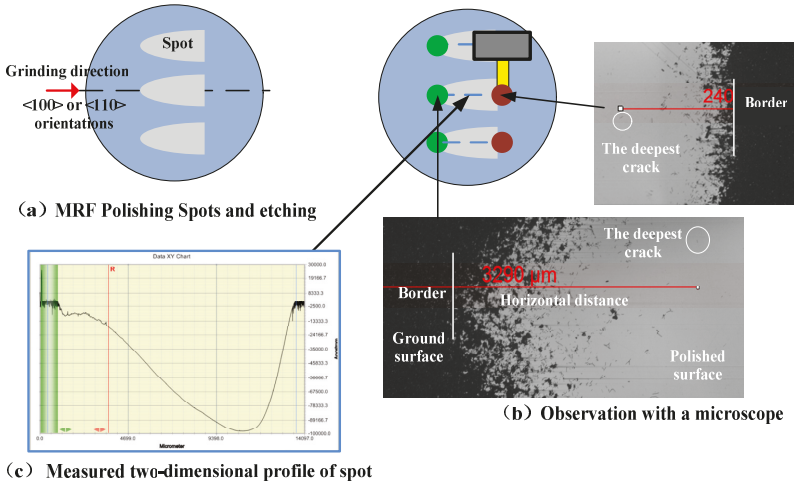

Figure 4. The sub-surface damage (SSD) measurement by spot magnetorheological finishing technique. (**a**) MRF Polishing spots and etching. (**b**) Observation with a microscope. (**c**) Measured two-dimensional profile of spot.

3. The Modeling of Predicting SSD

Based on the previous experimental observations [30–32], the SSD system will be induced during an indenter loaded in silicon, as shown in Figure 5. When the normal indentation is small, the plastic deformed region accompanying the lateral cracks will be formed beneath the indenter. The median microcracks will emanate from the boundary plastic deformation zone, if the threshold for normal indentation for brittle-ductile transition is approached.

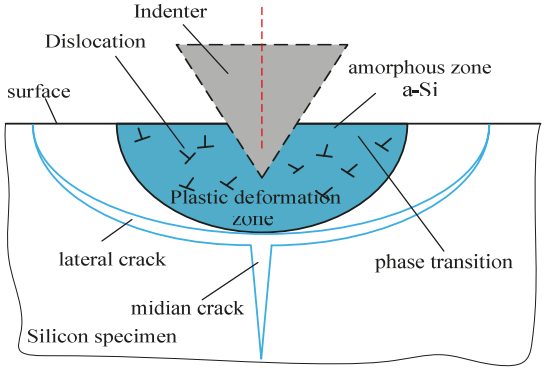

Figure 5. Schematic of damage by a sharp indenter.

Lambropoulos derived an analytical model for median and lateral cracks depths based on micro indentation mechanics and a hill model for indentation of a sharp indenter [33]. Li imposed a correction factor on median crack depth, considering the effect of elastic stress field [14]. The following represents the depth of lateral and median cracks:

$$C_{li} = 0.43(\sin\psi)^{\frac{1}{2}}(\cot\psi)^{\frac{1}{3}}\left(\frac{E}{H}\right)^{m}\left(\frac{P}{H}\right)^{\frac{1}{2}} \quad (1)$$

$$C_{mi} = (k\alpha)^{\frac{2}{3}} \left(\frac{E}{H}\right)^{\frac{2(1-m)}{3}} (\cot\psi)^{\frac{4}{9}} \left(\frac{P}{K_C}\right)^{\frac{2}{3}} \tag{2}$$

where ψ is the sharpness tip angle of the indenter, K_C represents the fracture toughness of the workpiece, E is the elastic modulus, m is a dimensionless quantity ranging between 1/3 and 1/2, and

$$\alpha = 0.027 + 0.09\left(m - \frac{1}{3}\right) \tag{3}$$

Gu calculated the area of contact projected in the normal direction and substituted the definition of hardness, the relationship between the median crack depth and penetration depth was expressed during the process of scratching [32]:

$$C_{mi} = (k\alpha)^{\frac{2}{3}} \frac{\left(E^{1-m} \bullet H^m\right)^{\frac{2}{3}}}{(K_C \bullet \beta)^{\frac{2}{3}}} \tan^{\frac{8}{9}} h_i^{\frac{4}{3}} = m_1 h_i^{\frac{4}{3}} \tag{4}$$

The hardness was substituted into the lateral crack depth Equation (1):

$$C_{li} = 0.43(\sin\psi)^{\frac{1}{2}} \frac{E^m}{H^m \beta^{\frac{1}{2}}} (\tan\psi)^{\frac{2}{3}} h_i = m_0 h_i \tag{5}$$

where h_i is the grain penetration depth, μ is the depth ratio of removal depth to cutting depth, β represents the elastic recovery coefficient of the material.

$$\beta = \frac{1}{4 - 3\mu + \mu^2} \tag{6}$$

The grinding process is similar to the process of a sharp indenter scratch test due to the same material removal mechanism as shown Figure 6. The size of plastic zone bi is equal to the depth of the lateral crack, which nucleate at the bottom of the ductile zone. Therefore,

$$b_i \approx C_{li} - h_r = C_{li} - (1 - \mu)h_i \tag{7}$$

the maximum peak height and valley depth of the ground surface roughness are between the ground surface and the bottom bi of the plastic zone [19].

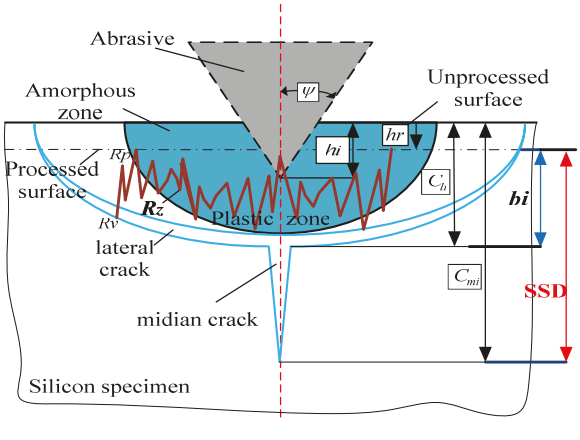

Figure 6. Schematic of subsurface-damage by an abrasive.

$$R_Z = \frac{\sum_{i=1}^{5} y_{pi} + \sum_{i=1}^{5} y_{vi}}{5} \approx C_{li} - (1-\mu)h_i \approx b_i \tag{8}$$

As shown in Figure 6, the depth of median cracks (SSCs) can be expressed:

$$SSD = C_{mi} - h_r = C_{mi} - (1-\mu)h_i \tag{9}$$

The relationship between SSD and (R_Z) could be expressed by eliminating the penetration depth:

$$SSD = \frac{m_1 {R_z}^{\frac{4}{3}}}{(m_0 - (1-\mu))^{\frac{4}{3}}} - \frac{(1-\mu)R_z}{m_0 - (1-u)} \tag{10}$$

In the process of grinding, the influence of the anisotropy of mono-crystalline silicon (Table 3) and different types of ductile- and brittle-regimes on subsurface damage should be considered, the critical ground surface roughness (R_Z) value for the ductile-brittle-transition to be expressed in Li's model [19]:

$$SSD_{<100>} \begin{cases} \approx b_i \approx R_Z & R_Z \le R_{ZC<100>} \\ = SSC_{<100>} = \frac{m_{1<100>} {R_z}^{\frac{4}{3}}}{(m_{0<100>} - (1-\mu)_{<100>})^{\frac{4}{3}}} - \frac{(1-\mu)_{<100>} R_z}{m_{0<100>} - (1-u)_{<100>}} & R_Z \succ R_{ZC<100>} \end{cases} \tag{11}$$

$$SSD_{<100>} \begin{cases} \approx b_i \approx R_Z & R_Z \le R_{ZC<110>} \\ = SSC_{<100>} = \frac{m_{1<110>} {R_z}^{\frac{4}{3}}}{(m_{0<110>} - (1-\mu)_{<110>})^{\frac{4}{3}}} - \frac{(1-\mu)_{<110>} R_z}{m_{0<110>} - (1-u)_{<110>}} & R_Z \succ R_{ZC<110>} \end{cases} \tag{12}$$

Therefore, the depth of SSD can be estimated by Equations (11) and (12).

Table 3. The properties of the mono-crystalline silicon (N type, top surface is oriented in the (100) plane).

Crystalline Orientation	Hardness H (GPa) [33]	Elasticity Modulus E (GPa)	Fracture Toughness K_C (MPa·m$^{1/2}$)	1-μ [8]	β
<100>	10	131	0.95	0.45	0.38
<110>		169	0.72	0.29	0.43

4. The Results and Discussion

4.1. Morphology of Subsurface Damage

As presented in Section 2.3, the processed ground sample that was placed on the stage of an optical microscope (Leica-Camera, Leica DM4000M, Wetzlar, Hesse-Darmstadt, Germany), we moved the stage along the center line of the "D-shaped" spot. The morphology and distribution of subsurface damage induced by three different grinding wheels in some samples is arrayed as below (Figure 7). No cracks are observed in the subsurface ground by the D15A wheel, which is mainly removed by plasticity. The defects are regular grinding marks. Therefore, the position where the last wear scar disappears is defined during the ductile-regime mode of grinding. Obvious cracks appear on the subsurface of D91 and 80# grinding wheels, which are removed in brittle mode. The size of the cracks induced by the 80# wheel is larger than the D91 wheel. The subsurface defects are regular grinding marks by the D15A grinding wheel. For the coarse grinding, like the D91 and 80# wheels, the subsurface damage are obvious cracks.

(**a**) D15A diamond wheel (B2 Sample 100× objective lens).

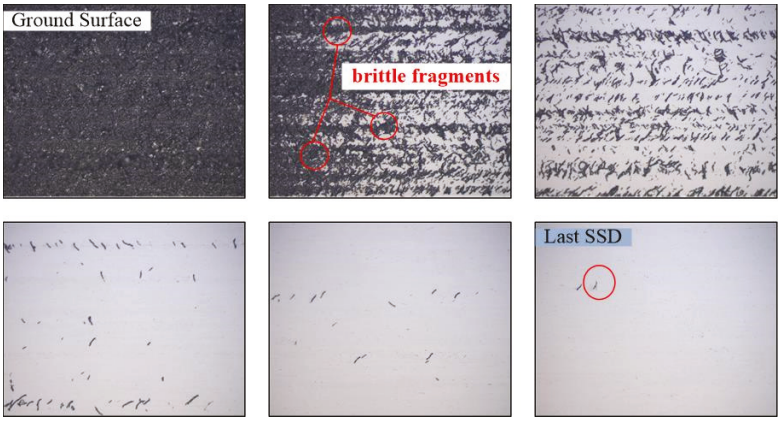

(**b**) D91 diamond wheel (A5 Sample 20× objective lens).

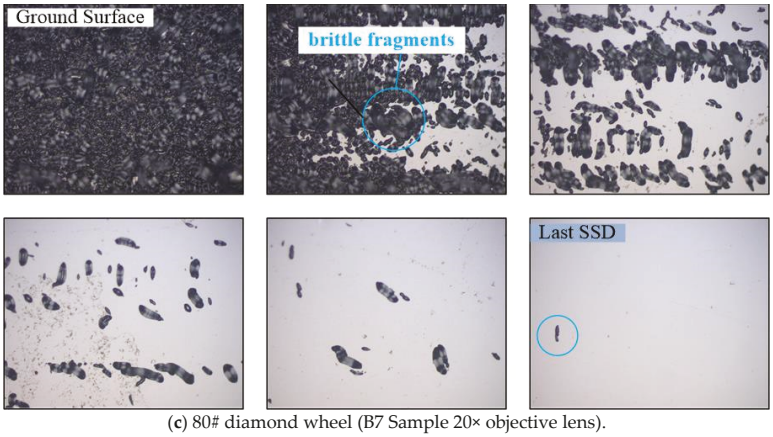

(**c**) 80# diamond wheel (B7 Sample 20× objective lens).

Figure 7. The morphology of subsurface in ground optical samples.

4.2. Depth of Subsurface Damage

The R_Z values under different processing parameters were summarized in Table 2. Based on the model presented in Section 3, the sharpness angle of diamond grits varied in the range of 46°~71° [5]. The experimental and predicted SSD of all grinding samples is shown in Figure 8. Li [19] expressed the critical surface roughness R_Z value for the ductile-brittle-transition:

$$R_{ZC} = 0.37 \bullet \frac{E}{H} \bullet \left(\frac{K_C}{H}\right)^2 \quad (13)$$

The (R_Z) values of A1~A3 and B1~B3 were smaller than the R_{ZC}, and no cracks occurred in the subsurface by the D15A wheel grinding along the <100> and <110> crystal orientations. Therefore, we used the grooves of grinding to represent the subsurface crack value, resulting in the experimental value being slightly larger than the theoretical value. Except for the D15A wheel, other experimental results were within the predicted range.

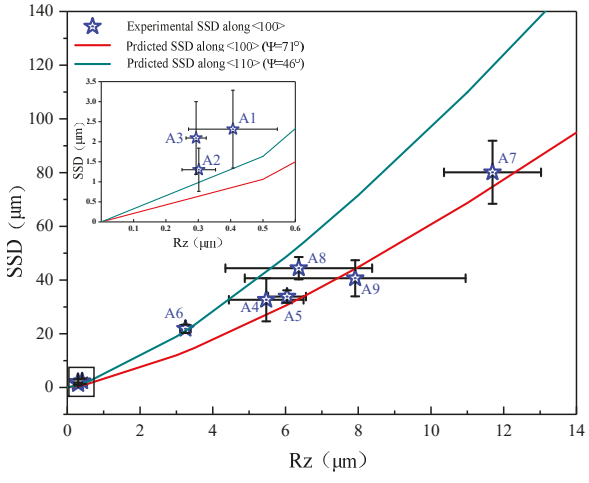

(**a**) The grinding direction along the <100> crystal orientation.

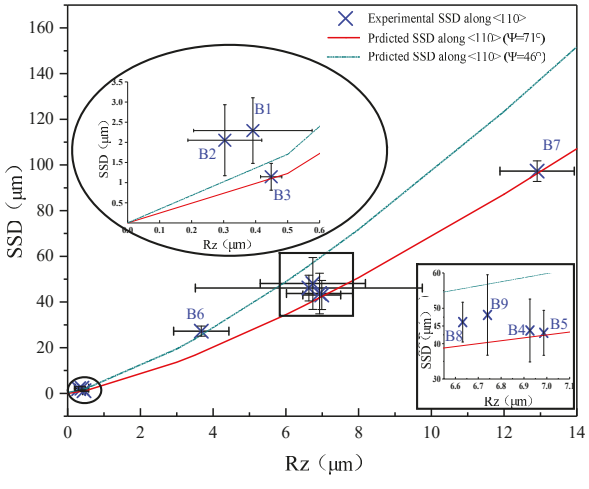

(**b**) The grinding direction along the <110> crystal orientation.

Figure 8. Comparison of experimental and predicted results.

4.3. Effects of Crystal Orientation and Processing Parameters on SSD

When the abrasive grains are ground along the <100> and <110> directions, the subsurface cracks will extend downwards along the (100) and (110) planes and perpendicular to the subsurface, as shown in Figure 9. The Si–Si covalent bond density on the (100) plane is greater than the (110) plane. Therefore, the depth of SSC along the <110> orientation grinding is deeper than along the <100> orientation (see Figure 10), which agrees well with Gao's findings.

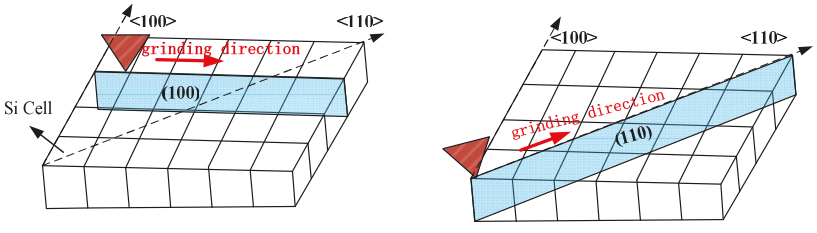

Figure 9. Schematic diagram of grinding direction and crystal orientation.

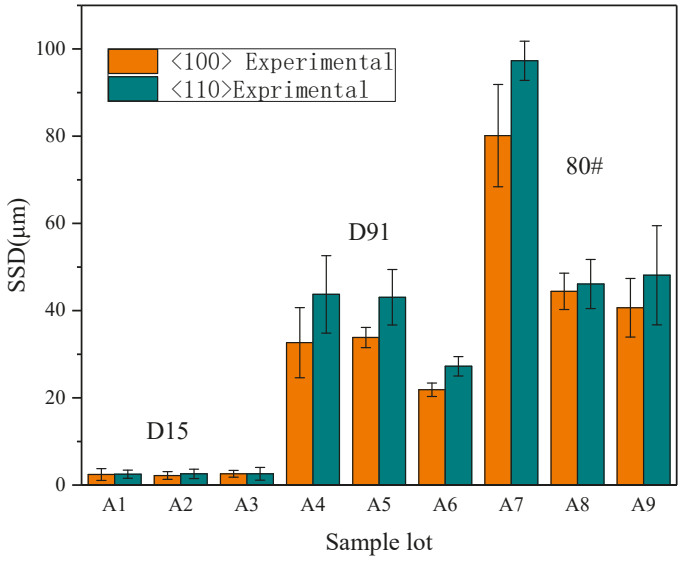

Figure 10. Comparison of the subsurface damage (SSD) along the <100> and <110> direction grinding.

In order to reveal the effects of the grinding parameters on the subsurface damage of mono-crystalline silicon grinding to guide processing for improving the processing productivity, a range of results of orthogonal experiments were analyzed. The influences of the grinding parameters, such as the grain size, wheel speed, and feed rate, were plotted in Figure 11. As can be seen from Figure 11, the depth of SSD for diamond grinding wheels deepens with the increase of grit size and feed rate. However, when the wheel speed is increased, SSD decreases.

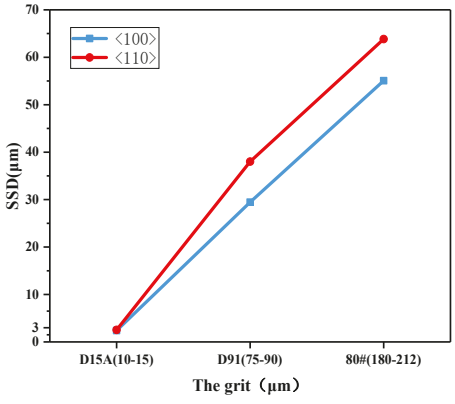

(**a**) The depth of SSD vs. particle size.

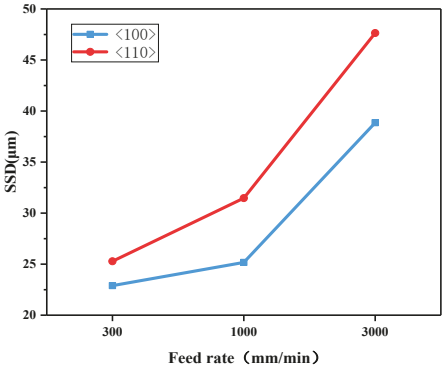

(**b**) The depth of SSD vs. feed rate.

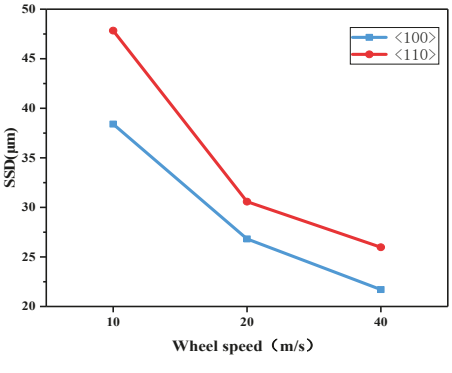

(**c**) The depth of SSD vs. wheel speed.

Figure 11. Sub-surface damage (SSD) vs. grinding parameters by range analysis: error bars represent standard deviations.

5. Conclusions

In order to reduce the subsurface damage depth generated during the grinding process, by adjusting the process parameters, we carried out the orthogonal experiments including grinding wheel particle size, grinding wheel linear speed, and feed rate. Compared with isotropic materials such as glass, we considered the impact of grinding along different crystal directions <100> and <110> on sub-surface damage depth. The MRF spot technique for concurrently determining the depth of sub-surface damage and observing the morphology of subsurface damage at various depths was applied to bound-abrasive ground samples. We proposed a modified model of the relationship between surface roughness (R_Z) and SSD, which considered plastic and brittle deformation mechanisms and the material properties of different crystal orientations. The proposed model is expected to assess the subsurface damage depth by measuring the roughness of the surface (R_Z) during grinding. The following conclusions can be drawn:

1. Except for the D15A ground samples (surface roughness (R_Z) < R_{ZC}, $R_{Z<100>}$ < 1.5 μm, $R_{Z<100>}$ < 0.8 μm), where no cracks were observed on the subsurface, all the experimental results were within the theoretical prediction range. The relationship between SSD and surface roughness R_Z was shown to be a proportional function and in good accordance with the proposed model.
2. Grinding experiments showed that the subsurface damage depth in samples ground along the <110> crystal orientation was larger than that along the <100> crystal orientation in the same processing parameters, since the Si–Si covalent bond density on (100) plane is greater than (110) plane.
3. Whether it was grinding along the <100> or <110> direction, the trend of SSD changes with process parameters is shown as the depth of SSD increasing with increasing grit size and feed rate, which decreases with the wheel speed.

In summary, this paper proposed an anisotropic SSD model for monocrystalline silicon based on the SSD model of optical glass. Then, the MRF spot method was applied to measure SSD along the <100> and <110> orientations, which is in good accordance with the model. It could guide the next process like the CMP to remove the quantitative depth. This article does not have a quantitative study on the depth of plastic deformation subsurface defects caused by the D15A grinding wheel grinding, which needs to be further studied by the TEM method.

Author Contributions: The two authors contributed equally to this work. All authors have read and agreed to the published version of the manuscript.

Funding: The research was partially funded by the Foundation for Youth Talents of LFRC, CAEP (LFRC-PD012); the Foundation for Scientific & Technological Innovations of CAEP (CX2019025); and the National Natural Science Foundation of China (No. 52075462).

Acknowledgments: Thanks go to Huiyang Tang for his great help in the experiments.

Conflicts of Interest: The authors declare no conflict of interest.

Abbreviations

ψ	the sharpness tip angle of indenter
K_C	the fracture toughness of Mono-crystalline Silicon
E	the elastic modulus
(R_Z)	ten-point mean roughness
SSD	subsurface damage
R_{ZC}	the brittle-plastic transition critical value
$R_{ZC<100>}$	the brittle-plastic transition critical value along <100> orientation
$R_{ZC<110>}$	the brittle-plastic transition critical value along <110> orientation
μ	the depth ratio of removal depth to cutting depth
m	a dimensionless quantity
β	the elastic recovery coefficient

References

1. Suratwala, T. *Materials Science and Technology of Optical Fabrication*; Lawrence Livermore National Lab: Hoboken, NJ, USA, 2018; p. 94550.
2. Yin, J.; Bai, Q.; Li, Y.; Zhang, B. Formation of subsurface cracks in silicon wafers by grinding. *Nanotechnol. Precis. Eng.* **2018**, *1*, 172–179. [CrossRef]
3. Chen, J.; Jinyi, C.; Tao, W. Theoretical model of brittle material removal fraction related to surface roughness and subsurface damage depth of optical glass during precision grinding. *Precis. Eng.* **2017**, *48*, 421–427.
4. Yan, J.; Asami, T.; Kuriyagawa, T. Nondestructive measurement of machining-induced amorphous layers in single-crystal silicon by laser micro-Raman spectroscopy. *Precis. Eng.* **2008**, *32*, 186–195. [CrossRef]
5. Liu, W.; Deng, Z.; Shang, Y.; Wan, L. Effects of grinding parameters on surface quality in silicon nitride grinding. *Ceram. Int.* **2017**, *43*, 1571–1577. [CrossRef]
6. Tönshoff, H.; Karpuschewski, B.; Hartmann, M.; Spengler, C. Grinding-and-slicing technique as an advanced technology for silicon wafer slicing. *Mach. Sci. Technol.* **1997**, *1*, 33–47. [CrossRef]
7. Stephens, A. Technique for measuring the depth and distribution of damage in silicon slices. *J. Electrochem. Soc.* **1986**, *133*, 106–115.
8. Lundt, H.; Kerstan, M.; Huber, A.; Hahn, P. Subsurface damage of abraded silicon wafers. In Proceedings of the 7th International Symposium on Silicon Materials Science and Technology, Pennington, NJ, USA, October 1994; pp. 218–224.
9. Tang, F.; Zhang, L. Subsurface nanocracking in monocrystalline Si (0 0 1) induced by nanoscratching. *Eng. Fract. Mech.* **2014**, *124*, 262–271. [CrossRef]
10. Zarudi, I.; Zhang, L. Effect of ultraprecision grinding on the microstructural change in silicon monocrystals. *J. Mater. Process. Technol.* **1998**, *84*, 149–158. [CrossRef]
11. Gogotsi, Y.; Zhou, G.; Ku, S.-S.; Cetinkunt, S. Raman microspectroscopy analysis of pressure-induced metallization in scratching of silicon. *Semicond. Sci. Technol.* **2001**, *16*, 345–352. [CrossRef]
12. Bismayer, U.; Brinksmeier, E.; Güttler, B.; Seibt, H.; Menz, C. Measurement of subsurface damage in silicon wafers. *Precis. Eng.* **1994**, *16*, 139–144. [CrossRef]
13. Lambropoulos, J.C.; Jacobs, S.D.; Ruckman, J. Material removal mechanisms from grinding to polishing. *Ceram. Trans.* **1999**, *102*, 113–128.
14. Li, S.; Wang, Z.; Wu, Y. Relationship between subsurface damage and surface roughness of optical materials in grinding and lapping processes. *J. Mater. Process. Technol.* **2008**, *205*, 34–41. [CrossRef]
15. Shen, N.; Suratwala, T.; Steele, W.; Wong, L.; Feit, M.D.; Miller, P.E.; Dylla-Spears, R.; Desjardin, R. Nanoscratching of Optical Glass Surfaces Near the Elastic–Plastic Load Boundary to Mimic the Mechanics of Polishing Particles. *J. Am. Ceram. Soc.* **2016**, *99*, 1477–1484. [CrossRef]
16. Wojciechowski, S.; Nowakowski, Z.; Majchrowski, R.; Królczyk, G. Surface texture formation in precision machining of direct laser deposited tungsten carbide. *Adv. Manuf.* **2017**, *5*, 251–260. [CrossRef]
17. Xiao, G.; To, S.; Zhang, G. Molecular dynamics modelling of brittle–ductile cutting mode transition: Case study on silicon carbide. *Int. J. Mach. Tools Manuf.* **2015**, *88*, 214–222. [CrossRef]
18. Zhang, L.; Chen, P.; An, T.; Dai, Y.; Qin, F. Analytical prediction for depth of subsurface damage in silicon wafer due to self-rotating grinding process. *Curr. Appl. Phys.* **2019**, *19*, 570–581. [CrossRef]
19. Li, H.N.; Yu, T.B.; Da Zhu, L.; Wang, W.S. Analytical modeling of grinding-induced subsurface damage in monocrystalline silicon. *Mater. Des.* **2017**, *130*, 250–262. [CrossRef]
20. Model 80# is a Product of Changxing Diamond Abrasives Co., Ltd., China; the Others Are Manufactured by Winter Diamond Tools, Saint-Gobain Diamantwerkzeuge GmbH & Co., Germany. Changxing Diamond Abrasives Co., Ltd. Available online: http://www.cxtools.com.cn (accessed on 28 March 2021).
21. Zhang, Y.X.; Li, D.L.; Gao, W.; Kang, R.K. Experimental Investigation on the Detection Technique for Surface Layer Damage of Machined Silicon Wafers. *J. Synth. Cryst.* **2011**, *40*, 359–364.
22. Ohta, T.; Yan, J.; Kuriyagawa, T.; Kodera, S.; Nakasuji, T. Prediction of subsurface damage depth of ground brittle materials by surface profiling. *Int. J. Mach. Mach. Mater.* **2007**, *2*, 108–124. [CrossRef]
23. Helbawi, H.; Zhang, L.; Zarudi, I. Difference in subsurface damage in indented specimens with and without bonding layer. *Int. J. Mech. Sci.* **2001**, *43*, 1107–1121. [CrossRef]
24. Zarudi, I.; Zhang, L. Subsurface damage in single-crystal silicon due to grinding and polishing. *J. Mater. Sci. Lett.* **1996**, *15*, 586–587. [CrossRef]
25. Lu, W.K.; Sun, J.G.; Pei, Z.J. Subsurface damage measurement in silicon wafers with cross-polarisation confocal microscopy. *Int. J. Nanomanuf.* **2006**, *1*, 272–282. [CrossRef]
26. Korkh, Y.V.; Burkhanov, A.M.; Rinkevich, A.B. Scanning acoustic microscope for visualization of microflaws in solids. *Russ. J. Nondestruct. Test.* **2009**, *45*, 677–684. [CrossRef]
27. Abe, T.; Nakazato, Y.; Daito, M.; Kanai, A.; Miyashita, M. The ductile mode grinding technology applied to silicon wafering process. In *Semiconductor Silicon: Proceedings of the Seventh International Symposium on Silicon Materials Science and Technology*; The Electrochemical Society: Pennington, NJ, USA, 1994.
28. Gao, S.; Kang, R.K.; Guo, D.M.; Huang, Q.S. Study on the Subsurface Damage Distribution of the Silicon Wafer Ground by Diamond Wheel. *Adv. Mater. Res.* **2010**, *126*, 113–118. [CrossRef]

29. Randi, J.A.; Lambropoulos, J.C.; Jacobs, S.D. Subsurface damage in some single crystalline optical materials. *Appl. Opt.* **2005**, *44*, 2241–2249. [CrossRef] [PubMed]
30. Zarudi, I.; Zou, J.; Zhang, L.C. Microstructures of phases in indented silicon: A high resolution characterization. *Appl. Phys. Lett.* **2003**, *82*, 874–876. [CrossRef]
31. Zarudi, I.; Nguyen, T.; Zhang, L.C. Effect of temperature and stress on plastic deformation in monocrystalline silicon induced by scratching. *Appl. Phys. Lett.* **2005**, *86*, 011922. [CrossRef]
32. Gu, W.; Yao, Z.; Li, K. Evaluation of subsurface crack depth during scratch test for optical glass BK7. *Proc. Inst. Mech. Eng. Part C J. Mech. Eng. Sci.* **2011**, *225*, 2767–2774. [CrossRef]
33. Cook, R.F. Strength and sharp contact fracture of silicon. *J. Mater. Sci.* **2006**, *41*, 841. [CrossRef]

micromachines

MDPI

Article

Rapid and Non-Destructive Repair of Fused Silica with Cluster Damage by Magnetorheological Removing Method

Mingjie Deng [1,2,3], Ci Song [1,2,3,*], Feng Shi [1,2,3], Yaofei Zhang [1,2,3], Ye Tian [1,2,3] and Wanli Zhang [1,2,3]

[1] College of Intelligence Science and Technology, National University of Defense Technology, 109 Deya Road, Changsha 410073, China; dengmingjie19@163.com (M.D.); sf.wind@yahoo.com (F.S.); zhangyaofei18@nudt.edu.cn (Y.Z.); tianyecomeon@sina.cn (Y.T.); zhangwanli17@nudt.edu.cn (W.Z.)
[2] Hunan Key Laboratory of Ultra-Precision Machining Technology, Changsha 410073, China
[3] Laboratory of Science and Technology on Integrated Logistics Support, National University of Defense Technology, 109 Deya Road, Changsha 410073, China
* Correspondence: songci@nudt.edu.cn; Tel.: +86-135-7415-8421

Abstract: The damage repair of fused silica based on the CO_2 laser repair technique has been successfully applied in high-power laser systems in the controllable nuclear fusion field. However, this kind of repairing technique mainly focuses on large-scale laser damage with sizes larger than 200 μm, but ignores the influence of cluster small-scale damage with sizes smaller than 50 μm. In order to inhibit the growth of small-scale damage and further improve the effect of fused silica damage repair, this paper carried out a study on the repair of fused silica damage using the magnetorheological (MR) removing method. The feasibility of fused silica damage repairing was verified, and the evolution law of the number, morphology, and the surface roughness of small-scale damage were all analyzed. The results showed that the MR removing method was non-destructive compared to traditional repairing technologies. It not only effectively improved the whole damage repairing rate to more than 90%, but it also restored the optical properties and surface roughness of the damaged components in the repairing process. Based on the study of the MR removing repair law, a combined repairing process of 4 μm MR removal and 700 nm computer controlled optical surfacing (CCOS) removal is proposed. A typical fused silica element was experimentally repaired to verify the process parameters. The repairing rate of small-scale damage was up to 90.4%, and the surface roughness was restored to the level before repairing. The experimental results validate the effectiveness and feasibility of the combined repairing process. This work provides an effective method for the small-scale damage repairing of fused silica components.

Keywords: fused silica; small-scale damage; magnetorheological removing method; combined repairing process; evolution law

Citation: Deng, M.; Song, C.; Shi, F.; Zhang, Y.; Tian, Y.; Zhang, W. Rapid and Non-Destructive Repair of Fused Silica with Cluster Damage by Magnetorheological Removing Method. *Micromachines* **2021**, *12*, 274. https://doi.org/10.3390/mi12030274

Academic Editor: Martin Byung-Guk Jun

Received: 12 February 2021
Accepted: 1 March 2021
Published: 6 March 2021

1. Introduction

Due to its excellent optical properties, fused silica is often used as a diffractive optical element and a focusing optical lens in the terminal device of high-power laser systems [1,2]. As high-powered laser optics are difficult to fabricate and easy to damage during application, it is very difficult to meet the requirements only by manufacturing methods [3]. Therefore, methods of repairing and reusing damaged components are urgently needed [4].

Figure 1 shows the flow chart of the optical elements in the National Ignition Facility Project (NIF) system [5]. Three processing methods are proposed for damaged elements: firstly, the damaged area is covered; secondly, if it cannot be covered, it needs to be repaired; thirdly, if it cannot be repaired, it should be replaced [6]. As an important part of the component in the NIF system, damage repair has become key to ensure the stable operation of the whole system.

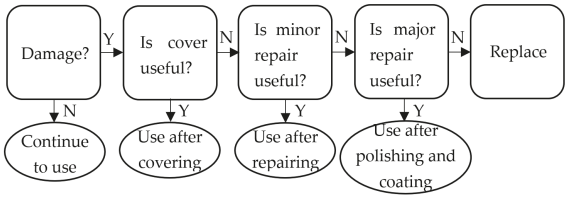

Figure 1. Flow chart of optical elements in the NIF system.

At present, the surface damage repairing methods of fused silica components include HF etching, femtosecond laser repairing, and CO_2 laser repairing, among others. CO_2 laser repairing is the most effective and reliable method and has been widely studied and developed [7–10]. Although CO_2 evaporation repairing has been used in engineering and has a good inhibition effect on damage growth, there are still some problems in practical application [11,12]. This method is mainly used to repair single point damage where sizes are larger than 200 μm, and the optical performance of the repairing point will be invalid after repairing [11,13]. A large number of small-scale damage points are difficult to repair with this method because the cost and time of repair are greatly increased [14].

Miller from the Lawrence Livermore National Laboratory, California, USA conducted an in-depth study on the law of damage occurrence and growth, as shown in Figure 2. The research showed that the probability of small-scale damage points with sizes less than 50 μm was more than 95%, and the probability of growth was very high. That is to say, a large number of small-scale damage points would lead to rapid deterioration, and ultimately affect the service life of components [15,16]. Miller used a new terminal optical component damage detection system called the Final Optics Damage Inspection (FODI), which can reliably detect damage sites larger than 50 microns in the repairing process. Then, the small damage points can be repaired and the service life of components can be improved by 40% [15]. Therefore, to the ability to repair small damage points and inhibit their further growth quickly and effectively is critical to improving the optical performance of fused silica optical elements [17].

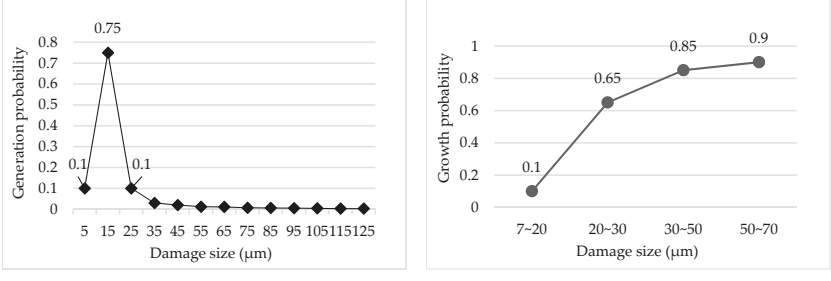

Figure 2. Probability of damage generation and growth.

In order to achieve batch and high-efficiency removal of the small-scale damage points without inducing new damage, this paper adopts the magnetorheological (MR) removing method to repair the damaged fused silica components. The MR removing method has the characteristics of high-efficiency removal, strong controllability, and good surface quality [18]. The biggest difference between the MR removing and traditional methods is that it is based on the shear removal. The process of repairing the original damage points of components mainly occurs in the elastic-plastic domain and does not induce new crushing defects [19].

Guo Zhongda of Northwestern Polytechnic University, Xi'an, China found that if the surface of the optical element is uneven and the magnetic field intensity in the depression

is positioned where the gradient magnetic field is relatively weak, the magnetic particles will move to the depression and reduce the extrusion of the optical parts, thus forming comet tail defects and degrading the surface quality [20].

Zhang Yaofei of the National University of Defense Technology, Changsha, China proposed a method of repairing cluster small-scale damage by using the MR removing method, and carried out a preliminary study on the evolution law of MR repairing damages on fused silica [21]. The results showed that MR repair produced a tail and worsened the surface quality. Follow-up research was carried out, and the feasibility of MR repairing damage was further analyzed. The evolution law of damage quantity, morphology change, and surface quality in the process of MR repairing was studied. Combined with the research results of the MR repairing, a set of perfect repairing process systems was summarized; finally the repairing of small-scale damage of fused silica components cluster was realized.

Based on the existing research, this paper studies the MR removing method as a repairing method to ensure the optical properties and surface quality are maintained, as well as to realize the efficient repairing of small-scale damage.

In the second section, the rule of the MR removing method is studied, and its feasibility and effectiveness are analyzed. The optimal repairing depth and the problems after repairing are summarized based on the damage repairing process.

In the third section, we carried out research on the optimization of the repairing process. By analyzing and solving the problems in the MR repairing process, a better MR repairing process is proposed. The main process includes three steps: 1. MR repairing of 4 μm; 2. computer controlled optical surfacing (CCOS) repairing of 700 nm; and 3. CCOS polishing of 200 nm. The repair effect and surface quality can meet the actual system index.

The fourth section focuses on the experimental verification of the optimized repairing process. The results show that the repairing rate of small-scale damage can be up to 90.4%, and the optical properties and surface quality of the components can basically return to the level before damage.

In general, the MR repairing technique can be used to repair small-scale damage of fused silica. The experimental results verify the effectiveness and feasibility of fused silica component repair. This new repairing method can bring new enlightenment to the existing repairing technology, and is conducive to improve the service life of fused silica high-intensity light components.

2. Experiment of MR Repairing Damage

2.1. Experimental Parameters

In order to verify the feasibility of repairing small-scale damage of fused silica with the MR removing method and study the evolution law of the number, morphology, and surface roughness of the small-scale damage points, two fused silica samples with size of 50 mm × 50 mm × 10 mm and the material of Heraeus 312 were used. The surface roughness of the component was 0.975 nm, which met the requirements of the actual system.

A pulsed laser with 355 nm wavelength and 7 ns pulse width was used to irradiate one the fused silica elements through three scans to prepare the damaged element, and the other fused silica element was not damaged. The average output energy of the laser was about 80 mJ, the spot area was about 1.5 mm^2, and the calculated energy density was about 5.4 J/cm^2 (the actual system is about 5 J/cm^2).

The KDUPF-700 MRF, which is made by National University of Defense Technology, Changsha, China, was used to remove the surface of damaged and non-destructive components evenly. Cerium oxide was used to remove the wear particles, and hydroxy iron powder was used as soft powder. The specific process parameters are shown in Table 1. After removing 1 μm each time, absolute ethanol was used to wipe the surface of the component. Then HF acid was used to remove the hydrolytic layer, and then it was cleaned and dried. Finally, the number and shape evolution of small-scale damage were measured by an ultra-smooth surface laser scattering defect detector, an ultra-deep hole microscope,

and an atomic force microscope. The surface roughness evolution of the experimental component was measured using a white light interferometer.

Table 1. Parameters of the MR process.

Item	Level
Wheel speed (r/min)	280
Flow rate (L/min)	120
Current (A)	8
Ribbon penetration depth (mm)	0.25

2.2. Evolution of the Number and Morphology of Small-Scale Damage

Using the laser scattering defect detector of super-smooth surface, which is made by ZC Optoelectronic Technologies, Ltd., Hefei, China, to measure the evolution of damage quantity in the process of the MR repairing, the dark field image was obtained, as shown in Figure 3. Table 2 shows the change of each size of damage points with the MR removal depth after image processing. Based on the comparison of the test results, the number of component damage points after MR repairing was significantly reduced. When the removal depth was up to 20 μm, the total number of damage points was reduced by 80%. The number of damage points with sizes larger than 20 μm were basically unchanged, but the small-scale damage points with sizes smaller than 50 μm were reduced by almost 90%. This showed that this method can effectively remove a large number of small-scale damage points.

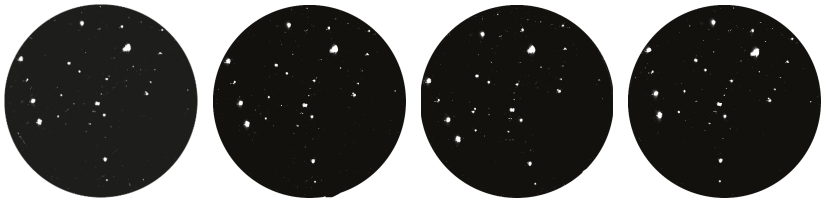

(**a**) Initial (**b**) Removal of 4 μm (**c**) Removal of 8 μm (**d**) Removal of 20 μm

Figure 3. Dark field results of damage with different sizes before and after MR repair.

Table 2. Quantity statistics of damage before and after MR repair.

Size (μm) \ Removal Depth	0–50	50–200	200–400	Larger Than 400
0 μm	673	86	21	24
4 μm	307	67	21	24
8 μm	180	55	21	24
12 μm	105	49	20	24
16 μm	78	46	20	24
20 μm	67	44	20	24

The curve of damage number with transverse sizes smaller than 50 μm variation with the MR removal depth were drawn, as shown in Figure 4. The results showed that the repairing efficiency was very high at the beginning, but the efficiency gradually reduced as the removal depth increased. When the removal depth was up to 20 μm, the overall removal rate of small damage points met the requirements.

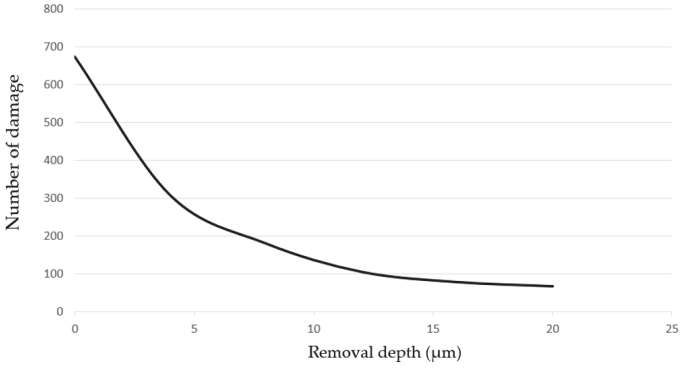

Figure 4. Variation of damage number where damage size was smaller than 50 μm with removal depth.

Variations in large-scale damage were also observed using the optical microscope, as shown in Figure 5. The results showed that there were clusters of small-scale damage around areas of large-scale damage before the MR repairing. When the removal depth was up to 2 μm, the number of the small-scale damage points were significantly reduced, but it was not completely repaired. When the removal depth was increased to 4 μm, the small-scale damage was basically repaired. However, it was clearly observed that the trailing phenomenon occurred at the damage point. The trailing phenomenon at the small damage points was completely removed in the MR repairing process, but the trailing phenomenon at the large damage points became serious.

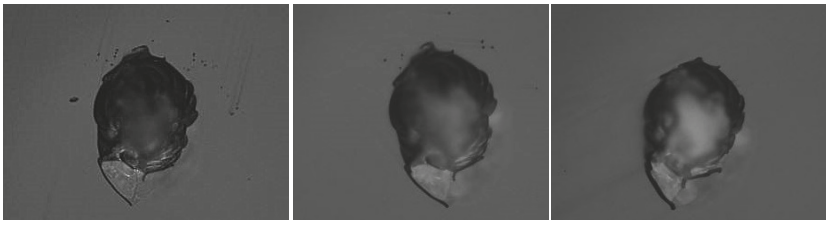

(**a**) Initial (**b**) Removal of 2 μm (**c**) Removal of 4 μm

Figure 5. Morphology variation of large-scale damage.

The atomic force microscope was used to randomly select small-scale damage and observe its repairing evolution process, as shown in Figure 6. Figure 6a is the initial image of the small-scale damage on the element. After removing 0.5 μm uniformly with the MR removing method, the measured results are shown in Figure 6b. The transverse size of the damage became smaller and the damage contour became more regular, as observed by comparing the two images. The profile of damage 1 measured along the MR scanning direction is shown in Figure 7. The width of the damage decreased from 7 μm ± 10% to 4.5 μm ± 10%, and the depth decreased from 620 nm to 120 nm. The depth was basically the same as the removal depth of MR, and the contour of the damage opening became smoother. The results showed that the variation of damage depth was consistent with the MR removing depth, and the repairing process did not cause damage to the bottom of the damage. This indicates that the MR removing method can effectively repair small-scale damage.

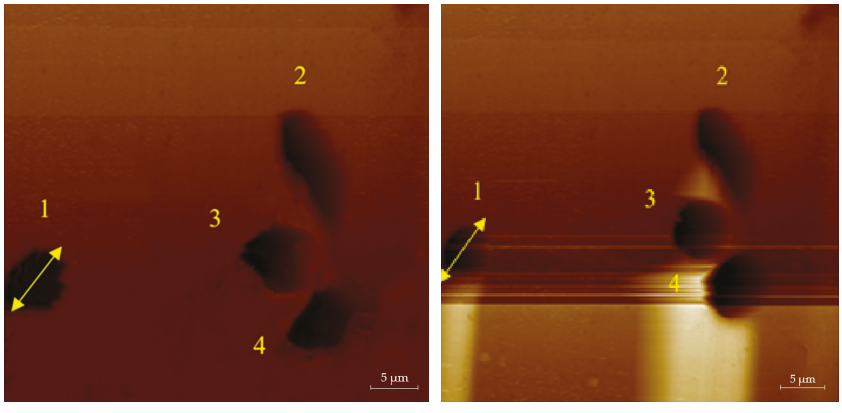

(**a**) Initial (**b**) Removal of 2 μm

Figure 6. Morphology evolution of small-scale damage before and after MR removal.

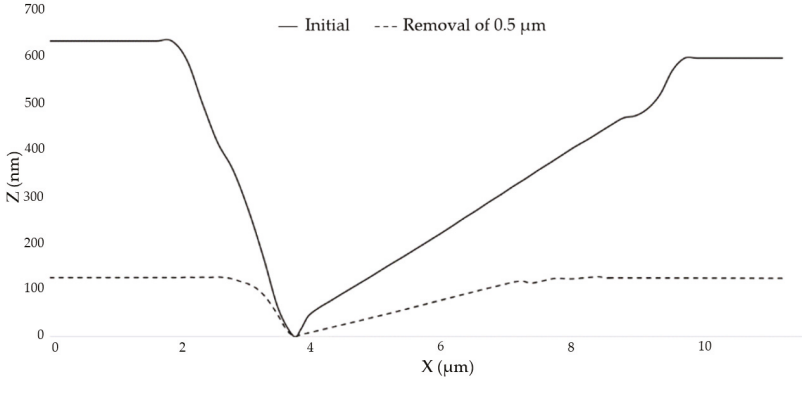

Figure 7. Profile evolution of damage before and after MR removal.

2.3. Evolution of Surface Roughness

After magnetorheological treatment of the non-destructive component, the white-light interferometers with removal depths of 0.5, 1, 2, 4 and 8 μm were selected. The measurement results are shown in Figure 8. A three-dimensional white light scanning interferometer (NewView 700) made by Zygo Corporation, Connecticut, United States, was used to measure the surface roughness of optical elements. The device is a non-contact instrument for measuring the surface roughness of optical elements. Its field of view is 0.94 mm × 0.70 mm, the longitudinal resolution is 0.1 nm, the transverse resolution is 0.36–9.50 μm, and the measurement repeatability Root Mean Square (RMS) is less than 0.01 nm [22].

According to the division of error frequency band by Lawrence Livermore National Laboratory (LLNL), an error with F > 8.33 mm−1 was considered a high-frequency error. In order to study the variation of errors in different frequency bands by the removal depth, mid-frequency errors of $F \leq 8.33\ mm^{-1}$ were filtered out in the measurement, and the variation results of surface roughness with the removal depth before and after filtering were plotted, as shown in Figure 9.

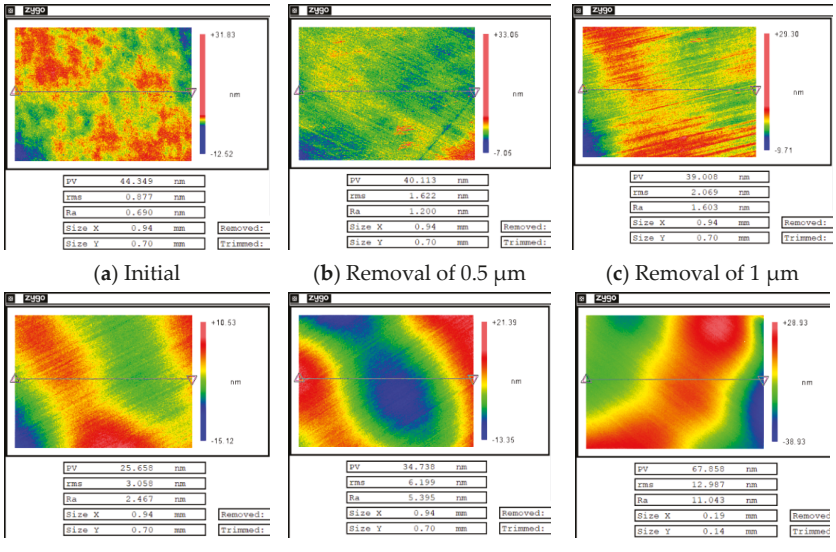

Figure 8. Results of surface roughness of a non-destructive component with different removal depths.

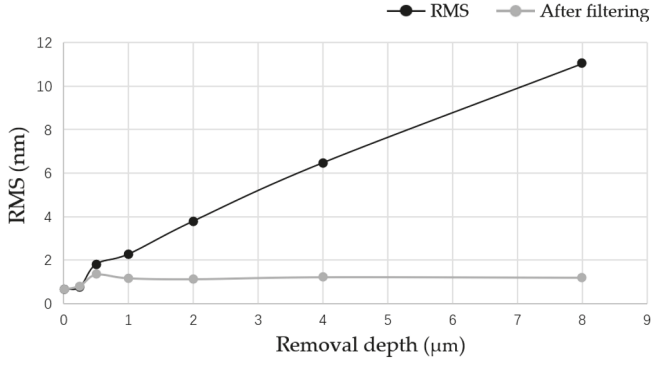

Figure 9. Evolution of surface roughness of a non-destructive component by removal depth.

The results show that the surface roughness of the non-destructive component increased linearly with the increase in the removal depth, and the high-frequency error of the components did not change with the removal depth. This indicates that the MR removing method leads to the increase in the mid-frequency and low-frequency error of the component, which are mainly caused by the convolution effect of the MR removing method. In addition, with the increase in the removal depth, the high-frequency error of the non-destructive element was found to first deteriorate and then tended towards stability, which was mainly determined by the initial surface roughness of the element and the characteristics of the removal function.

After MR repairing of the damaged component, white-light interferometers with removal depths of 0.5, 1, 2, 4, and 8 μm were selected. The measurement results are shown in Figure 10.

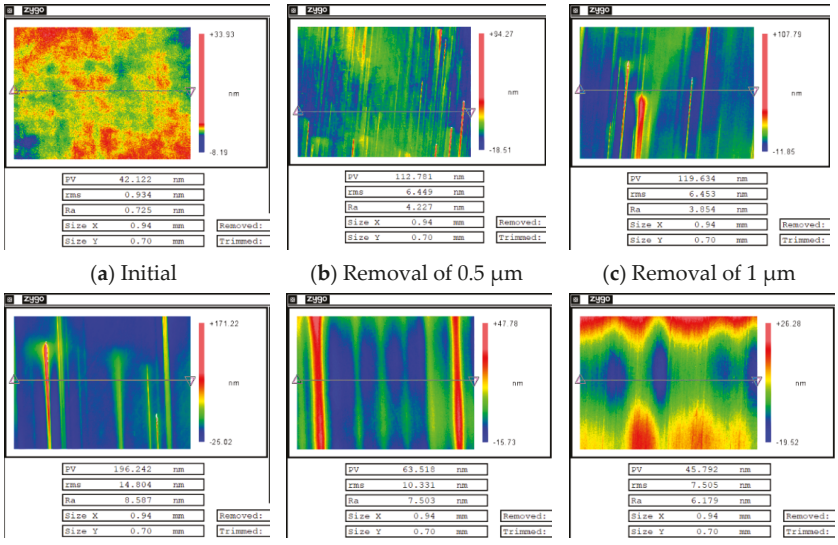

Figure 10. Results of surface roughness of damaged component with different removal depths.

The curves of surface roughness of the non-destructive component and damaged component with different removal depths are plotted together, as shown in Figure 11.

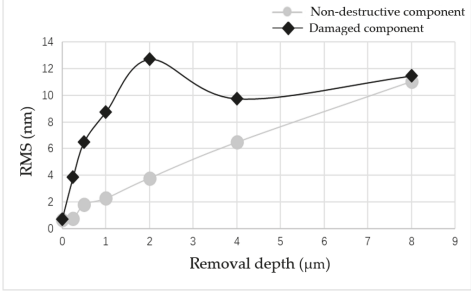

Figure 11. Comparison of surface roughness changes of the two components.

The results showed that when the repairing depth was smaller than 4 μm, the RMS increased rapidly and was is much higher than for the RMS of the non-destructive component. Then, with the increase in removal depth, RMS gradually decreased, and finally it became similar to the RMS of the non-destructive component. From the measurement results in Figure 10, it was found that during the rapid increase in RMS, many non-uniform strip tails were produced on the component surface, which gradually disappeared with the increase in the removal depth. The measurement results showed that in the process of the MR removing method, the existence of damage led to the tailing phenomenon, which was one of the reasons for the rapid deterioration of the surface quality of components. However, with the further increase in the removal depth, the influence of damage on the surface quality was gradually eliminated.

3. Repair Process Optimization Strategy

In the second part, the damage law of fused silica repaired by MR was studied, and the feasibility and effectiveness of the MR repairing were analyzed. The results showed

that MR repairing can effectively repair small damage points, and the removal rate can be more than 90%. At the same time, it will also lead to two problems: firstly, with the increase in the repairing depth, the surface roughness of component increases, which will not meet engineering needs; secondly, there will exist the tailing phenomenon in the process of repairing damage. In order to solve the series of problems induced by the MR repairing process, computer controlled optical surfacing (CCOS) was used to modify the repaired components, and a perfect combination repair process is achieved by combining with the MR repairing law.

According to the damage law of fused silica repaired by MR, with the increase in the MR repairing depth, the tailing of large-scale damage became deeper, and the surface roughness worsened. In order to eliminate tailing and restore the surface roughness as much as possible, the appropriate process parameters of MR and CCOS were selected.

This section studies the time required for CCOS to eliminate tailing and restore surface roughness under different MR repairing depths. The results are shown in Figure 12. The black curve in the figure shows the time required for CCOS to recover the surface roughness at different MR repairing depths, and the gray line shows the time required for CCOS to eliminate tailing under different MR repairing depths. The results show that when the MR repairing depth was 4 μm, CCOS repairing needed 70 min to eliminate the tailing and restore the surface roughness. At this time, the revolution speed of CCOS was 150 rotations per minute (rpm) and the diameter of polishing powder was 1.5 μm. Other process parameters are shown in Table 3, and the corresponding depth of 70 min was 700 nm.

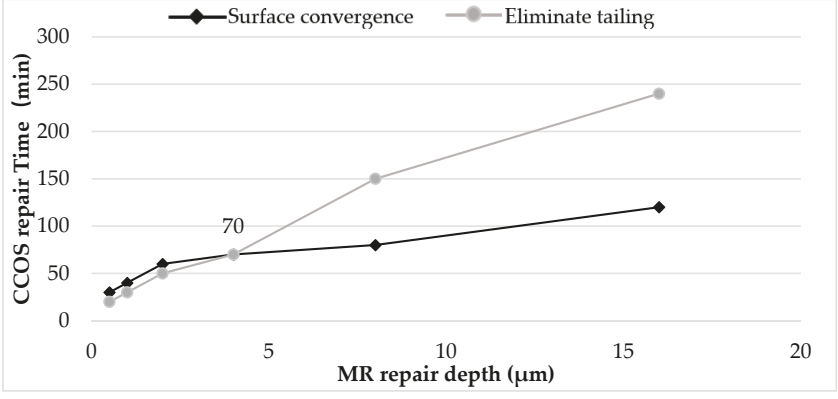

Figure 12. Relationship curves of MR and CCOS process parameters.

Table 3. Parameters of the CCOS process.

Item	Level
Polishing powder material	Cerium dioxide
Disc material	asphalt
Disc diameter (mm)	25
Rotation speed (rpm)	155
Eccentricity (mm)	5
Polishing pressure (KPa)	50

Finally, in order to further improve the surface smoothness and eliminate the subsurface defects, the combined process parameters were optimized based on the previous process research conclusions. The final repair process is shown in Figure 13. The combination process is as follows: MR repairing of 4 μm; CCOS repairing of 700 nm with revolution speed of 150 rpm and polishing powder diameter of 1.5 μm. After two cycles to achieve

the ideal repair effect, MR refinement was carried out. Finally, CCOS repairing of 200 nm with a revolution speed of 0 rpm and polishing powder diameter of 0.5 μm should be used. At this time, the damage repair effect and surface quality of components were able to meet the system index.

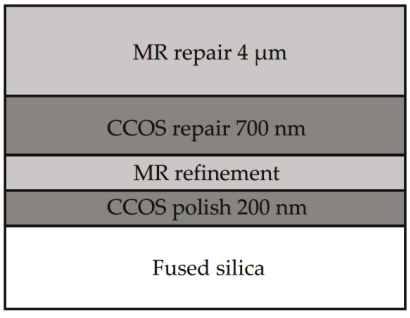

Figure 13. Material removal distribution of each process.

4. Experimental Verification of Repair Process

Figure 14 shows the flow chart of the whole repairing process. The repair of small-scale damage of fused silica was divided into three stages: the damage quantity and size distribution detection; the MR repairing of small-scale damage; and surface quality recovery. The specific process steps were as follows: (a) the initial damage detection was carried out on the existing fused silica damage elements and the distribution characteristics including the number and size of the damage was obtained; (b) the MR removing method was used to repair 4 μm, and CCOS with revolution speed of 150 rpm and polishing powder diameter of 1.5 μm was used to repair 700 nm. Two cycles were carried out until the removal rate of small-scale damage was of more than 90%; (c) MRF polishing was used, and then CCOS with a revolution speed of 0 rpm and polishing powder diameter of 0.5 μm was used to polish 200 nm until the surface roughness was better than 1 nm. Finally, the components were cleaned.

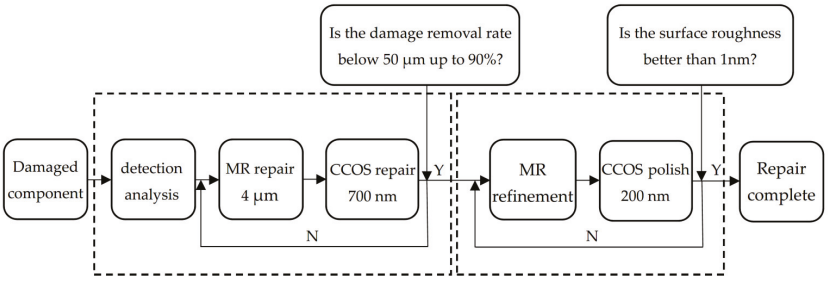

Figure 14. Repair flow chart.

In order to verify the effectiveness of the whole repairing process, the above repairing process was used to repair the fused silica damaged components produced by an actual system. The experimental sample was a fused silica damaged component of 50 mm × 50 mm × 10 mm. Three large-scale damages were directly observed on the surface of the component. The local image in the red frame was observed through the optical microscope, as shown in Figure 15. There were also clusters of small-scale damage on the surface of the components.

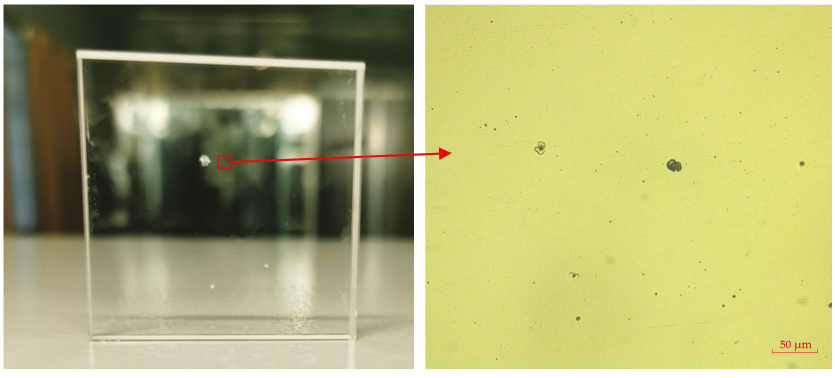

(**a**) Physical picture (**b**) Local micrograph

Figure 15. Physical and micrographs of damaged components.

The MR repairing method was used to repair 4 μm, and the CCOS was used to repair 700 nm. After the process was completed, the removal rate of small surface damage was more than 90%, and the removal depth was 23.5 μm. Figure 16 shows the comparison of dark field images before and after the MR repairing. Figure 17 shows the distribution of the number of damage points with different sizes. The results show that after the MR repairing, the number of damage points, especially damage points with sizes smaller than 50 μm, were significantly reduced, with a removal rate of 90.4%.

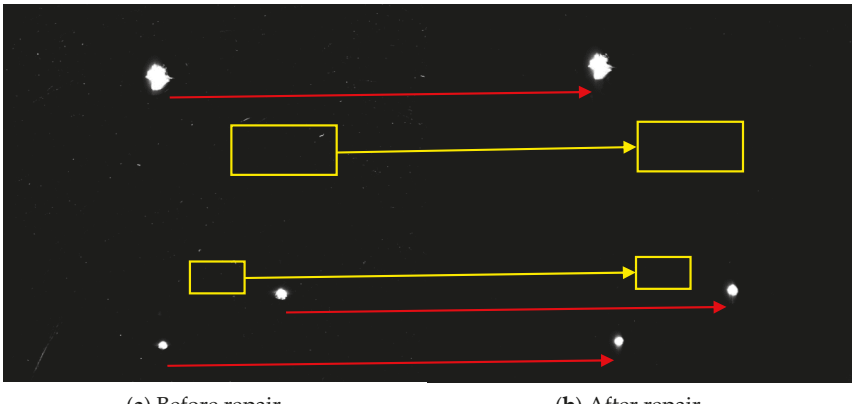

(**a**) Before repair (**b**) After repair

Figure 16. Dark field images of damaged components before and after repairing.

Figure 18 shows the evolution of the surface roughness during the repair process measured by the white light interferometer. The surface roughness of the repaired component was 1.625 nm, which did not meet the system index.

The surface roughness of the components was restored by combining MR refinement and CCOS polishing. Figure 19 shows the measurement result after the surface quality was restored. At this time, the surface roughness was 0.828 nm, which met the requirement that the surface roughness is better than 1 nm.

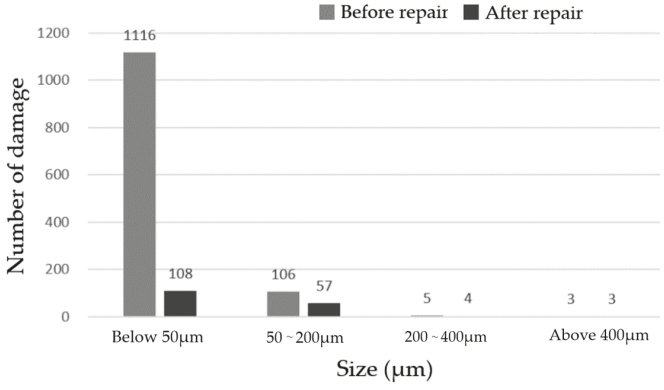

Figure 17. Number of different sizes of damage before and after repairing.

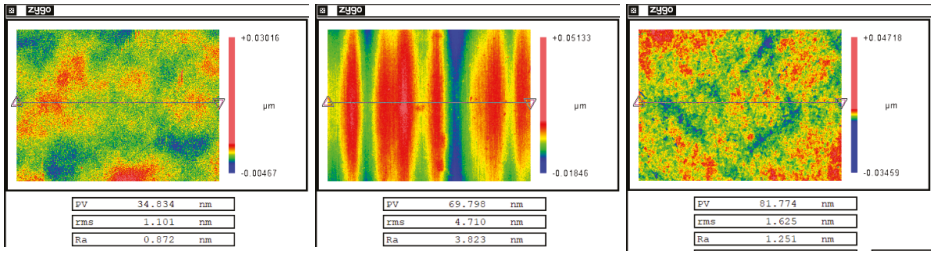

(**a**) Initial (**b**) After MR repair (**c**) After CCOS repair

Figure 18. Evolution of surface roughness during the process.

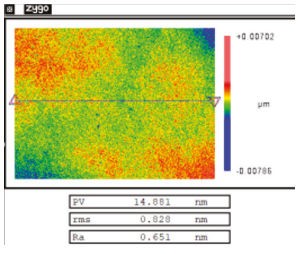

Figure 19. Result of surface roughness after refinement.

5. Conclusions

The research on the MR repairing fused silica damaged components was carried out, and the rapid repair of fused silica small-scale damage was successfully realized. The repairing rate of small-scale damage was more than 90%, and the optical properties and surface quality was able to reach the system index.

Firstly, it was found that the size and quantity distribution of the damage were key factors affecting the repairing process. The number of cluster small-scale damage, the morphology and depth of single small-scale damage, and the evolution law of fused silica component surface quality were studied. The feasibility of the MR removing method to remove the damage points was verified. The problems after repairing were analyzed, the causes of the problems were explored, and the solutions were summarized.

Secondly, the optimization of the restoration process was studied. By selecting the appropriate process parameters for MR and CCOS, the surface roughness was able to be

restored as much as possible, while eliminating the tailing caused by the MR removing method. Finally, the optimized repairing process parameters were obtained: MR repairing for 4 μm, CCOS repairing for 700 nm with revolution speed of 150 rpm and polishing powder diameter of 1.5 μm. After two process cycles, MR refinement was carried out. Finally, CCOS with a revolution speed of 0 rpm and a polishing powder diameter of 0.5 μm was used to polish 200 nm. The damage repair effect and surface quality of the components met the actual system index.

Finally, a repairing process validation experiment was carried out. The repairing results showed that the repair rate of small-scale damage can be up to 90.4%, and the optical properties and surface quality of the components can be restored to the level before damage. The experimental results verify the effectiveness and feasibility of MR repairing.

In sum, the MR removing method can be used to repair small-scale damage of fused silica components. This new repairing method can complement existing repair technology and is conducive to improving the service life of fused silica optical components.

Author Contributions: Conceptualization, F.S. and C.S.; methodology, M.D.; validation, Y.Z.; formal analysis, W.Z.; investigation, Y.Z. and M.D.; resources, Y.T.; data curation, M.D.; writing—original draft preparation, M.D.; writing—review and editing, C.S. and F.S.; visualization, Y.Z.; supervision, C.S.; project administration, Y.T.; funding acquisition, F.S. All authors have read and agreed to the published version of the manuscript.

Funding: This research was funded by National Natural Science Foundation of China (No. 51775551, No. 51675526), Strategic Priority Research Program of Chinese Academy of Sciences (Grant No. XDA25020317), The National Key Research and Development Program of China (No. 2020YFB2007504).

Informed Consent Statement: Informed consent was obtained from all subjects involved in the study.

Data Availability Statement: The data presented in this study are available on request from the corresponding author. The data are not publicly available due to the data also forms part of an ongoing study.

Conflicts of Interest: The authors declare no conflict of interest.

References

1. Campbell, J.H.; Hawley-Fedder, R.A.; Stolz, C.J.; Menapace, J.A.; Borden, M.R.; Whitman, P.K.; Yu, J.; Runkel, M.J.; Riley, M.O.; Feit, M.D.; et al. NIF optical materials and fabrication technologies: An overview. *Opt. Eng. Lawrence Livermore Natl. Lab. II Natl. Ignition Facil.* **2004**, *5341*, 84–101. [CrossRef]
2. Norton, M.A.; Donohue, E.E.; Hollingsworth, W.G.; Feit, M.D.; Rubenchik, A.M.; Hackel, R.P. Growth of laser initiated damage in fused silica at 1053 nm. *Boulder Damage Symp. XXXVI* **2005**, *5647*, 197–206. [CrossRef]
3. Gao, X.; Yao, K.; Luo, Y.; Yi, J.; Qiu, R.; Jiang, Y.; Zhou, Q.; Tang, S.; Zhou, G. Investigation on Laser Damage Probability of Fused Silica with Simultaneous Multi-wavelength Irradiation. *Plasmonics* **2017**, *13*, 617–622. [CrossRef]
4. Spaeth, M.L.; Manes, K.R.; Kalantar, D.H.; Miller, P.E.; Heebner, J.E.; Bliss, E.S.; Spec, D.R.; Parham, T.G.; Whitman, P.K.; Wegner, P.J.; et al. Description of the NIF Laser. *Fusion Sci. Technol.* **2016**, *69*, 25–145. [CrossRef]
5. Moses, E.I. The National Ignition Facility and the National Ignition Campaign. *IEEE Trans. Plasma Sci.* **2010**, *38*, 684–689. [CrossRef]
6. Spaeth, M.L.; Wegner, P.J.; Suratwala, T.I.; Nostrand, M.C.; Bude, J.D.; Conder, A.D.; Folta, J.A.; Heebner, J.E.; Kegelmeyer, L.M.; MacGowan, B.J.; et al. Optics Recycle Loop Strategy for NIF Operations above UV Laser-Induced Damage Threshold. *Fusion Sci. Technol.* **2016**, *69*, 265–294. [CrossRef]
7. Suratwala, T.I.; Miller, P.E.; Bude, J.D.; Steele, W.A.; Shen, N.; Monticelli, M.V.; Feit, M.D.; Laurence, T.A.; Norton, M.A.; Carr, C.W.; et al. HF-Based Etching Processes for Improving Laser Damage Resistance of Fused Silica Optical Surfaces. *J. Am. Ceram. Soc.* **2010**, *94*, 416–428. [CrossRef]
8. Haight, R.; Wagner, A.; Longo, P.; Lim, D. High resolution material ablation and deposition with femtosecond lasers and applications to photomask repair. *J. Mod. Opt.* **2004**, *51*, 2781–2796. [CrossRef]
9. Cao, Q.; Zhang, J.; Du, J.; Zhao, H.; Liu, S.; Peng, Q. Athermal repair of nanoscale defects in optical materials using a femtosecond laser. *Nanoscale* **2017**, *9*, 17233–17240. [CrossRef] [PubMed]
10. Fang, Z.; Zhao, Y.; Chen, S.; Sun, W.; Shao, J. Method of mitigation laser-damage growth on fused silica surface. *Appl. Opt.* **2013**, *52*, 7186–7193. [CrossRef] [PubMed]
11. Mendez, E.; Nowak, K.M.; Baker, H.J.; Villarreal, F.J.; Hall, D.R. Localized CO_2 laser damage repair of fused silica optics. *Appl. Opt.* **2006**, *45*, 5358–5367. [CrossRef] [PubMed]

12. Tan, C.; Zhao, L.; Chen, M.; Cheng, J.; Wu, C.; Liu, Q.; Yang, H.; Yin, Z.; Liao, W. Experimental and theoretical investigation of localized CO_2 laser interaction with fused silica during the process of surface damage mitigation. *Results Phys.* **2020**, *16*, 102936. [CrossRef]
13. Dai, W.; Xiang, X.; Jiang, Y.; Wang, H.J.; Li, X.; Yuan, X.; Zheng, W.; Lv, H.; Zu, X. Surface evolution and laser damage resistance of CO_2 laser irradiated area of fused silica. *Opt. Lasers Eng.* **2011**, *49*, 273–280. [CrossRef]
14. Wong, J.; Ferriera, J.; Lindsey, E.; Haupt, D.; Hutcheon, I.; Kinney, J. Morphology and microstructure in fused silica induced by high fluence ultraviolet 3ω (355nm) laser pulses. *J. Non-Cryst. Solids* **2006**, *352*, 255–272. [CrossRef]
15. Miller, C.F.; Kegelmeyer, L.M.; Nostrand, M.C.; Raman, R.N.; Cross, D.A.; Liao, Z.M.; Garcha, R.; Carr, C.W. Characterization and repair of small damage sites and their impact on the lifetime of fused silica optics on the National Ignition Facility. In Proceedings of the Laser-Induced Damage in Optical Materials 2018: 50th Anniversary Conference (SPIE), Boulder, CO, USA, 23–26 September 2018; Volume 10805, p. 108051D.
16. Negres, R.A.; Abdulla, G.M.; Cross, D.A.; Liao, Z.M.; Carr, C.W. Probability of growth of small damage sites on the exit surface of fused silica optics. *Opt. Express* **2012**, *20*, 13030–13039. [CrossRef] [PubMed]
17. Yan, C.; Liu, B.; Li, X.; Liu, C.; Ju, X. Photothermal spectroscopy study of fused silica irradiated by a 355 nm wavelength and 68 ns pulse duration laser. *Opt. Mater. Express* **2019**, *9*, 3439–3451. [CrossRef]
18. Xu, M.; Shi, F.; Zhou, L.; Dai, Y.; Peng, X.; Liao, W. Investigation of laser-induced damage threshold improvement mechanism during ion beam sputtering of fused silica. *Opt. Express* **2017**, *25*, 29260–29271. [CrossRef]
19. Shi, F.; Tian, Y.; Peng, X.; Dai, Y. Combined technique of elastic magnetorheological finishing and HF etching for high-efficiency improving of the laser-induced damage threshold of fused silica optics. *Appl. Opt.* **2014**, *53*, 598–604. [CrossRef] [PubMed]
20. Guo, Z.; Wang, X.; Yang, Z.; Hang, L.; Cheng, Z. Influence of plasticity on comet tail phenomenon in magnetorheological finishing. *J. Xi'an Technol. Univ.* **2010**, *30*, 112–116.
21. Zhang, Y.; Song, C.; Shi, F.; Tian, Y.; Lin, Z. Research on rapid repairing of surface laser damage of fused silica optics. In Proceedings of the Second Target Recognition and Artificial Intelligence Summit Forum, Shenyang, China, 28–30 August 2019; Volume 11427, p. 1142745. [CrossRef]
22. Wu, T.; Hui, Y.; Yan, Z.; Li, Z.; Li, Q. Zygo interferometer for the precious measurement of tiny refractive index change of two laser crystals. *Opt. Laser Technol.* **2017**, *89*, 196–199. [CrossRef]

MDPI
St. Alban-Anlage 66
4052 Basel
Switzerland
Tel. +41 61 683 77 34
Fax +41 61 302 89 18
www.mdpi.com

Micromachines Editorial Office
E-mail: micromachines@mdpi.com
www.mdpi.com/journal/micromachines

MDPI
St. Alban-Anlage 66
4052 Basel
Switzerland

Tel: +41 61 683 77 34
Fax: +41 61 302 89 18

www.mdpi.com

ISBN 978-3-0365-3863-1